Insight into Ca^{2+} Dependent Lipid Scrambling from the Crystal Structure of a TMEM16 Family Member

Dissertation

zur

Erlangung der naturwissenschaftlichen Doktorwürde

(Dr. sc. nat)

vorgelegt der

Mathematisch-naturwissenschaftlichen Fakultät

der

Universität Zürich

von

Janine Denise Brunner

von Ebnat-Kappel SG

Promotionskomitee

Prof. Dr. Raimund Dutzler (Leitung und Vorsitz)

Prof. Dr. Markus Grütter

Prof. Dr. Markus Seeger

Zürich, 2015

Dedicated to my mother

Yolanda Brunner

14. 06. 1956 - 16. 04. 2006

Acknowledgements

First, I would like to express my gratitude to Prof. Raimund Dutzler for giving me the opportunity to work on that great project on TMEM16 proteins. I am thankful to the members of my thesis committee for their interest, Prof. Markus Gruetter and Prof. Markus Seeger.

I would like to thank Alessia for her appreciated help during her master thesis, also for constant support with cupcakes. I am grateful to Stephan for a great time in the past five years, inside as well as outside of the lab, and for support throughout my PhD, for invaluable discussions on scientific topics while drinking our daily coffee and for introduction to the HEK expression system. I appreciated a lot our teamwork on shared projects. I would like to thank Sibylle for many funny hours throughout my PhD and for valued chats, making L24 a nice place. I would like to express my gratitude to Nita, always amiable, and usually finding each other working late in the lab, for mental support. I would like to thank Novandy for introduction to the yeast expression system. I would like to thank Yvonne for constant effort to organize the lab and make it a pleasant place.

I wish to express my gratitude to former members of the Gruetter lab and to the present members of the Jinek lab, who provided a good atmosphere inside and outside the lab, and who made the L-floor a pleasant place. Special thank goes to Michi, for his constant support and friendship in good times and in bad, Heidi, Georg and Cristopher for introduction to the insect cell expression system, for helpful discussions and valued chats. Also, I appreciated the introduction to the art of brewery through Cristopher.

I want to say thanks to the infrastructure of the Department of Biochemistry, especially Sascha for designing and constructing the HPL6 cell lyser, which made membrane preps a comfortable thing and for valued chats. I would like to express my gratitude to Sascha, Adi and Lukas from the workshop in general for support, and to Beat and Celine from the protein crystallization facility for constant support and valued chats, and to the IT team, Stefan, Steve and Jannik, for solving all kinds of computer problems.

I wish to express my deepest gratitude to my friends and family for endless support throughout the past years.

List of Figures

List of Tables

List of Abbreviations

aa	Amino acid
afTMEM16	TMEM16 homologue from the fungus *Aspergillus fumigatus*
Ala	Alanine
Asn	Asparagine
Asp	Aspartate
BLAST	Basic local alignment search tool
CaCC	Ca^{2+}- activated chloride channel
CC_{all}	Weighted correlation coefficient (between E_{obs} and E_{calc} weighted as $1/\sigma E$)
cmc	Critical micelle concentration
CFTR	Cystic fibrosis transmembrane conductance regulator
DDMβ	N-Dodecyl-β-D-Maltopyranoside
DOTAP	Trimethylammonium propane
EC_{50}	Half maximal effective concentration
EDTA	Ethylenediaminetetraacetic acid or 2-(2-(Bis(carboxymethyl) amino)) ethyl (carboxymethyl) amino) acetic acid
EGTA	Ethylene glycol tetraacetic acid or ethylene glycol-bis (2-amino ethylether) - *N*,*N*,*N*′,*N*′-tetraacetic acid
EGFP	Enhanced GFP
ER	Endoplasmic reticulum
E_{rev}	Reversal potential
FSEC	Fluorescent size exclusion chromatography
GalCer	Galactosylceramide
GFP	Green fluorescent protein
GHK	Goldman-Hodgkin-Katz
Gln	Glutamine
Glu	Glutamate
GluCer	Glucosylceramide
GPI	Glycosylphosphatidylinositol

gzeTMEM16	TMEM16 homologue from the fungus *Gibberella zeae*
HEK cells	Human embryonal kidney cells
His	Histidine
HPLC	High performance liquid chromatography
HRP	Horseradish peroxidase
LLO	Listeriolysin O
MALDI	Matrix assisted laser desorption/ ionization
M5-DLO	Man5GlcNAc2-PP-dolichol
MPD	Mannose-phosphate-dolichol
MR	Molecular replacement
MS	Mass spectrometry
mTMEM16A	TMEM16A from *Mus musculus*
NBD	7-nitrobenz-2-oxa-1,3-diazole
NCS	Non- crystallographic symmetry
nhTMEM16	TMEM16 homologue from the fungus *Nectria haematococca*
PC	Phosphatidylcholine
PCC	Protein crystallization center
PE	Phosphatidylethanolamine
PEG	Polyethylene glycol
PI	Phosphoinositides
PIP	Phosphatidylinositolphosphate
$PI(4,5)P_2$ or PIP2	Phosphatidylinositol-4,5-bisphosphate
PI4P	Phosphatidylinositol-4-phosphate
PL scramblase	Phospholipid scramblase
PLSCR	Phospholipid scramblase
PM	Plasma membrane
PMal	Phosphotidylmaltose
PMSF	Phenylmethanesulfonylfluoride
PS	Phosphatidylserine
PTriose	Phosphatidyltriose

SAD	Single anomalous dispersion
SBP	Streptavidin binding peptide
SDS-PAGE	Sodium dodecyl sulfate polyacrylamide gel electrophoresis
SEC	Size exclusion chromatography
Sf9, Sf21	Insect cell lines from *Spodoptera frugiperda*
SM	Sphingomyelin
SR	Sarcoplasmic reticulum
TIM-4	Phosphatidylserine receptor
TM	Transmembrane
TMEM16	Transmembrane protein of unknown function
UDMα	N-Undecyl-α-D-Maltopyranoside
VGLUT2	Vesicular glutamate transporter 2
vYFP	Venus yellow fluorescent protein
YPL	Yeast polar lipids

Abstract

In vertebrates the TMEM16 family of proteins consists of ten members, designated as TMEM16A-K (or anoctamin 1-10). TMEM16 proteins are found in all branches of life, except in bacteria. Interestingly, vertebrate TMEM16 proteins were linked to different functions. On the one hand, the TMEM16 family contains Ca^{2+}- activated chloride channels, of which TMEM16A is involved in the regulation of different processes such as epithelial fluid secretion, cardiac as well as neuronal excitability and potentially also nociception [1-6], while the closely related TMEM16B is expressed in the retina and olfactory epithelia and might be of importance for olfaction [7, 8]. For TMEM16F, besides a function in ion transport [9], a role in the translocation of lipids between the two leaflets of a membrane was proposed [10]. In the resting state of a cell, the plasma membrane is organized in an asymmetric manner with phosphatidylcholine and sphingomyelin localized in the outer leaflet, while phosphatidylserine (PS) and phosphatidylethanolamine (PE) are confined to the cytoplasmic side of the membrane. This is functionally important, since the breakdown of the lipid asymmetry serves as a signaling cue in different processes such as blood clotting and apoptosis. TMEM16F was associated with the Ca^{2+} dependent disruption of the lipid asymmetry (phospholipid scrambling) and exposure of PS to the outer leaflet in platelets, which is required to trigger efficient blood coagulation after vascular injury. Although the function of certain family members was previously investigated by electrophysiological methods, at the start of this thesis only limited structural information was available, based on the prediction of the molecular topology by epitope mapping and sequence analysis [11]. Clearly, detailed structural knowledge is mandatory to understand the role of TMEM16 proteins in ion conduction and lipid scrambling.

For this reason, it was the aim of this work to determine the first high-resolution structure of a family member, which would allow to obtain first insight at a molecular level into a novel protein architecture and also into the described transport processes. In the course of this work, eighty genes were selected based on various criteria. These were cloned into different expression plasmids and the gene products were assessed with respect to expression yields, solubility after extraction with detergents, and stability. To increase the likelihood that a particular protein is successfully expressed, different expression systems were evaluated. Accordingly, the expression properties of the entire pool of selected genes was investigated in human embryonal kidney cells (HEK), a subset of genes was evaluated in *Saccharomyces cerevisiae*, while few selected genes were probed for insect cell expression. This approach has led to the identification of proteins with suitable properties for crystallization. A homologue from the fungus *Gibberella zeae* (gzeTMEM16) was successfully crystallized after purification from either HEK, insect cells or *S. cerevisiae* thereby producing crystals with a resolution of 5 Å. However, the comparable low stability and poor yield of the protein complicated the improvement of these initial crystals. Using an assay that monitors the intrinsic stability of a protein, conditions could be established that stabilized gzeTMEM16 and other family members. By this method, a closely related TMEM16 homologue from the fungus *Nectria haematococca* (nhTMEM16) was sufficiently stabilized for crystallization. Initial crystals with a resolution of 14 Å were significantly improved by systematic screening of crystallization

additives. Based on these efforts, the diffraction in two crystal forms could be improved to 3.3 and 3.4 Å, respectively. The Single Anomalous Dispersion method was subsequently expoited to determine the structure of nhTMEM16 using crystals of seleno-methionine derivatized nhTMEM16.

The structure of nhTMEM16 reveals the novel architecture of TMEM16 proteins. As observed in the structure, nhTMEM16 forms dimers with ten transmembrane spanning helices per subunit and structured cytoplasmic amino- and carboxy terminal domains. The carboxy- terminus of the one subunits wraps around the amino- terminus of the other subunit, thereby providing a large interface for interaction. Within the structure, a region was identified that most likely plays a role in the function of TMEM16 proteins for ion and lipid transport. This region, termed the subunit- cavity, resembles a crevice, that spans the membrane like a spiral staircase in a diagonal direction. The surface of the subunit- cavity is highly hydrophilic, despite facing the hydrophobic environment of the membrane. Interestingly, this feature is conserved among many other TMEM16 family members. Residues that were previously identified in electrophysiological recordings to influence ion conduction in TMEM16A [12] and selectivity in TMEM16A and F [9], map to the subunit- cavity in the nhTMEM16 structure, thus underlining its role for protein function. The subunit- cavity is in accordance with a previously proposed model for scramblases, where a hydrophilic path would lower the large energy barrier associated with lipid flip- flop, by providing interactions with the polar head groups of the lipids, while the fatty acid chains diffuse through the hydrophobic core of the membrane [13, 14]. As revealed from the structure, a Ca^{2+} binding site is located in close proximity to the subunit- cavity, which is likely linked to Ca^{2+}-activation. Interestingly, the Ca^{2+} binding site is embedded within the transmembrane part of the protein at about one third of the membrane thickness from the cytosolic side, thus providing an explanation for the observed voltage- dependence of Ca^{2+} activation in certain TMEM16 family members. Six amino acids, of which five carry a negative charge, are involved in the coordination of two Ca^{2+} ions per binding site.

By means of protein reconstitution into liposomes, it was demonstrated in the course of this work that nhTMEM16 functions as a scramblase, which facilitates the movement of phospholipids such as PS and PE between the two leaflets of the bilayer in a Ca^{2+} dependent manner. Similarly to Ca^{2+}, Sr^{2+} but not Mg^{2+} is capable of activating nhTMEM16. It is noteworthy, that in the apparent absence of Ca^{2+} nhTMEM16 exhibited a much lower, but still measurable, scrambling activity. It is currently not clear, whether this residual activity is caused by traces of Ca^{2+}, binding to the Ca^{2+} binding site with high affinity, or whether this reflects a basal activity in the absence of Ca^{2+}. During this work, a further structure of nhTMEM16 was obtained using crystals grown in apparent Ca^{2+}- free conditions. The fact, that it still contained Ca^{2+} bound to the binding site supports the theory of the high affinity, but on the other hand doesn't refuse any potential basal activity. Mutations in the Ca^{2+} binding site significantly impaired lipid scrambling, although also in this case low residual activity was observed, that was no longer enhanced by Ca^{2+}.

The structure of nhTMEM16 permitted first insight into the molecular organization of the recently discovered TMEM16 protein family. Furthermore, the structure revealed for the first time the architecture of a lipid scramblase. In the structure the location of a conserved Ca^{2+} binding site within

the membrane was identified, that is essential for activation. In addition, evidence was provided that both, ion and lipid transport in different family members, likely occurs along the hydrophilic surface of the membrane spanning subunit- cavity. Thus, this work does not only serve as template for the study of ion conduction in TMEM16 proteins, it also forms the basis for the comprehension of lipid transport processes, that while characteristic for certain TMEM16 proteins may also apply to other types of scramblases.

Zusammenfassung

In Wirbeltieren umfasst die TMEM16 Proteinfamilie eine Gruppe aus zehn verwandten Proteinen, die TMEM16A-K, oder auch Anoctamin 1- 10, genannt werden. TMEM16 Proteine kommen in den meisten Lebewesen vor, nicht aber in Bakterien. Interessanterweise wurden diese Proteine in Wirbeltieren mit einer Reihe von verschiedenen Funktionen in Verbindung gebracht. So umfasst diese Proteinfamilie unter anderem Ca^{2+}-aktivierte Chlorid- Kanäle, von denen zum Beispiel TMEM16A an der Sekretion von Chlorid in Epithelzellen, der Erregbarkeit von Herzzellen und Neuronen und vielleicht auch an der Schmerzwahrnehmung beteiligt ist [1, 2, 4-6, 15], während TMEM16B in Riechepithelien vorkommt, wo es womöglich eine Rolle in der Geruchswahrnehmung spielt [7, 8]. TMEM16F wurde neben einer Funktion im Ionenhaushalt [9] auch mit einer Rolle im Lipidtransport zwischen den beiden Schichten der Membran assoziiert [10]. In der ruhenden Zelle sind die beiden Lipidschichten asymmetrisch aufgebaut, so dass Phosphatidylcholin und Sphingomyelin hauptsächlich in der äusseren Schicht, und Phosphatidylserin (PS) und Phosphatidylethanolamin (PE) in der dem Zellinnern zugewannten Seite lokalisiert sind. Diese Anordnung ist sehr wichtig für die Zelle, da die Dissipation dieses Gradienten so unterschiedliche Prozesse wie die Blutgerinnung und Apoptose auslöst. TMEM16F wurde mit der Aufhebung der Lipidasymmetrie und damit mit dem Transport von PS zur Lipidaussenschicht in Verbindung gebracht, ein Vorgang, der generell als Lipid-Skramblierung bekannt ist. Dieser Prozess spielt eine wichtige Rolle um nach einer Blutgefässverletzung die Blutgerinnung möglichst effizient zu induzieren. Obwohl einzelne Mitglieder der TMEM16 Proteinfamilie bereits funktionell vor allem mittels elektrophysiologischer Methoden charakterisiert worden sind, gab es bisher noch keine Informationen bezüglich ihrer strukturellen Organisation [11]. Um die Rolle dieser Proteine im Ionen- und Lipidtransport zu verstehen, ist ein detailliertes Verständnis ihres Aufbaus unerlässlich.

Das Ziel dieser Doktorarbeitet war es deshalb, über die Aufklärung der drei-dimensionalen Struktur eines TMEM16 Proteins, einen detaillierten Einblick in die Architektur dieser Familie und in die unterschiedlichen Transportvorgänge zu erlangen. Um diese Zielsetzung zu erreichen, wurden achtzig Gene von TMEM16 Proteinen in Genom-Datenbanken identifiziert. Diese Gene wurden in verschiedene Expressions-Plasmide kloniert, um die Expression des jeweiligen Proteins, sowie seine Löslichkeit und Stabilität nach der Extraktion in Detergenzien zu untersuchen. Um die Wahrscheinlichkeit für ihre Überexpression zu erhöhen, wurden verschiedene Expressionssysteme geprüft. So wurden alle Konstrukte in Humanen Embryonalen Nierenzellen (HEK) getestet, die Hälfte der Konstrukte wurde in Hefe und wenige ausgewählte Proteine in Insektenzellen exprimiert. Dieses Vorgehen erlaubte es, Proteine mit vielversprechenden Eigenschaften für strukturelle Studien zu identifizieren. Ein TMEM16 Homolog aus dem Pilz *Gibberella zeae* (gzeTMEM16), konnte erfolgreich aus HEK, Insekten- und Hefezellen aufgereinigt und kristallisiert werden. Die Kristalle waren aber mit einer Streuung bis maximal 5 Å nicht von ausreichender Qualität und konnten aufgrund der Instabilität dieses Proteins nicht verbessert werden. Obwohl trotz seiner vielversprechenden Eigenschaften gzeTMEM16 nicht zur Strukturaufklärung geeignet war, konnten mit Hilfe eines Stabilitäts-Assays Bedingungen gefunden werden, mit denen TMEM16 Proteine stabilisiert werden konnten. Diese Ergebnisse erlaubten es in der

Folge, dass ein anderes, eng verwandtes Protein aus dem Pilz *Nectria haematococca* (nhTMEM16) für die Kristallisation ausreichend stabilisiert werden konnte. Erste Kristalle von nhTMEM16 mit einer Auflösung von 14 Å wurden durch das systematische Screening von verschiedenen Additiven in Kristallisationsexperimenten signifikant verbessert. Dadurch konnte die Auflösung von zwei verschiedenen Kristallformen bis zu 3.3 Å und 3.4 Å erhöht werden. Die Struktur wurde daraufhin mit Hilfe anomaler Daten bestimmt, die von Kristallen aus Seleno-Methionin derivatisiertem Protein gesammelt wurden.

Die Struktur von nhTMEM16 zeigt die bisher unbekannte Architektur von TMEM16 Proteinen. nhTMEM16 bildet ein Dimer mit zehn transmembranen Segmenten und intrazellulären Termini, wobei der C-Terminus des einen Monomers mit dem N-Terminus des anderen Monomers interagiert. Die Struktur erlaubte die Identifikation einer Region, der ‚Subunit-Cavity', die wahrscheinlich für den Ionen- und Lipidtransport verschiedener TMEM16 Proteine eine wichtige Rolle spielt. Diese ‚Subunit- Cavity', ähnelt einer Furche mit hydrophilen Eigenschaften, die zur Membran exponiert ist, und die wie eine Wendeltreppe den hydrophoben Kern der Lipiddoppelschicht durchspannt. Dieses Merkmal ist in anderen TMEM16 Proteinen konserviert. Die ‚Subunit- Cavity' enthält Aminosäuren-Reste, die, wie frühere Studien zeigen, bei TMEM16A [12] und F [9] eine Rolle in der Ionenleitung und Selektivität spielen. Die ‚Subunit Cavity' bestätigt ein hypothetischen Modell zur Lipidtranslokation in Skramblasen, in dem postuliert wurde, dass Lipide die enorme Energiebarriere des Lipid Flip-Flops überwinden könnten, wenn ihre polaren Kopfgruppen entlang eines hydrophilen Pfads durch die Lipidschicht gleiten könnten, während die hydrophoben Fettsäuren durch den hydrophoben Kern der Membran diffundieren [13, 14]. In der Struktur von nhTMEM16 konnten auch gebundene Ca^{2+}-Ionen identifiziert werden. Diese Ca^{2+}-Bindungsstelle befindet sich in nächster Umgebung zur ‚Subunit-Cavity', welcher darum mit grosser Wahrscheinlichkeit eine Funktion in der Ca^{2+}- Aktivierung zukommt. Die Tatsache, dass sich die Ca^{2+}-Bindungsstelle im Transmembran-Bereich des Proteins befindet, liefert eine plausible Erklärung für die Spannungsabhängigkeit der Ca^{2+}-Aktivierung. In der Ca^{2+}-Bindungsstelle konnten sechs konservierte Aminosäuren-Reste lokalisiert werden, von denen fünf negativ geladen sind, welche allesamt mit den beiden gebundenen Ca^{2+}-Ionen interagieren.

Neben den strukturellen Untersuchungen konnte nach Rekonstitution in Proteo-Liposomen gezeigt werden, dass nhTMEM16 als Skramblase fungiert, welche in Abhängigkeit von Ca^{2+} unspezifisch Phospholipide wie PS und PE zwischen den zwei Lipidschichten hin und her bewegt. Erwähnenswert ist, dass nhTMEM16 in der vermeintlichen Abwesenheit von Ca^{2+} immer noch Skramblase-Aktivität aufweist, obwohl diese um Grössenordnungen niedriger als im voll aktivierten Zustand ist. nhTMEM16 kann ausserdem von Sr^{2+}, nicht aber von Mg^{2+} aktiviert werden. Des Weiteren verringern Mutationen in der Ca^{2+}-Bindungsstelle die Aktivität um ein Vielfaches, obwohl auch in diesem Fall noch immer eine Restaktivität zu beobachten ist. Ob diese Restaktivität durch die relativ hohe Affinität der Bindungsstelle für Ca^{2+} oder durch eine eventuell vorhandene Basalaktivität zu begründen ist, konnte bisher nicht schlüssig geklärt werden. Während dieser Arbeit konnte eine weitere Struktur von nhTMEM16 aufgeklärt werden, in der das Protein aus scheinbar Ca^{2+}-freier Lösung kristallisiert wurde. Die Tatsache,

dass immer noch Ca^{2+} gebunden vorliegt, unterstützt die Theorie der hohen Affinität, schliesst aber eine mögliche Basalaktivität nicht aus.

Die Struktur von nhTMEM16 gewährte einen ersten Einblick in die molekulare Organisation der vor kurzem entdeckten TMEM16 Protein Familie. Ausserdem zeigt die Struktur zum ersten Mal die Architektur einer Lipid-Skramblase. Mit dieser Arbeit wurde die Position der zur Aktivierung benötigten Ca^{2+}-Bindungsstelle im Protein sichtbar gemacht, die in allen Familienmitglieder konserviert ist. Anhand der Struktur scheint es wahrscheinlich, dass jedes Monomer zwei Ca^{2+}-Ionen koordiniert. Des Weiteren konnten Hinweise geliefert werden, dass sowohl der Ionen- als auch der Lipidtransport entlang der stark hydrophilen, membran-durchspannenden ‚Subunit- Cavity' stattfindet. Die vorliegende Doktorarbeit bildet deswegen nicht nur einen wichtigen Ausgangspunkt um Prozesse der Ionenpermeation in TMEM16 Proteinen besser zu verstehen, sie legt auch eine wichtige Grundlage für das Verständnis für Vorgänge des Lipidtransports, wie sie in der TMEM16 Protein Familie, aber womöglich auch in ähnlicher Form in anderen Skramblasen vorkommen.

1. Introduction

1.1. Lipids and proteins in biological membranes

Irrespectively of their origin from bacteria, plants or animals, the smallest functional unit in all organisms are cells, which work by conserved biochemical processes. Each cell corresponds to an enclosed and well organized system separated from its environment by the plasma membrane. The plasma membrane operates as a physical but selective barrier that allows the cell to enrich nutrients from its environment whereas other essential compounds that are required for its function can be retained within its boundaries. In eukaryotic cells the lipid membranes of organelles such as mitochondria, nucleus, endoplasmic reticulum (ER), Golgi apparatus or endo- and lysosomes fulfill a similar role as they separate the contents of each compartment from the cytosol. All membranes consist of lipids that maintain the fundamental and unique composition of molecules in the cytoplasm as well as within organelles, and membrane proteins that enable the directed but selective assimilation and disposal of substances across the membrane.

All biological membranes share a similar architecture, where the lipids are organized in a double layer, the lipid bilayer [16]. The formation of the lipid bilayer occurs spontaneously due to the amphiphilic properties of the lipids since they consist of a polar, hydrophilic head group and a hydrophobic tail. This chemical characteristic and their distinct shape drives the self-assembly of lipids in either micelles with the hydrophobic tails pointing inward or bilayers with the hydrophobic tails sandwiched between the hydrophilic head groups. In membranes the most abundant lipids are phospholipids. These possess a polar head group and two hydrophobic hydrocarbon chains. Phospholipids can be grouped into phosphoglycerides and sphingolipids. The phosphoglycerides contain a glycerol backbone, two fatty acid chains and a phosphate group that are all linked via ester bonds, and several types of head groups bound to the phosphate. The main constituents of the phosphoglycerides are phosphatidylcholine (PC), phosphatidylethanolamine (PE) and phosphatidylserine (PS). The less commonly occurring phosphatidylinositol and its phosphorylated derivatives, the phosphoinositides (PI), play an important role in trafficking, define organelle identity and function as second messenger. The most prominent sphingolipid, sphingomyelin (SM), is built from sphingosine, not from glycerol. A free hydroxyl group close to the choline head group enables the hydrogen bond formation with adjacent lipid head groups, with water or with membrane proteins. A virtually unlimited number of lipids is created from the combination of different head groups with fatty acid chains that vary in chain length and saturation grade and by modifying head groups or attaching sugar moieties to the phosphate groups. In Figure 1 the most prominent phospholipids and cholesterol are displayed.

In bilayers lateral diffusion occurs rapidly and a lipid changes place with its neighbors 10^7 times per second. In contrast, the sandwich organization of the bilayer prevents the migration of phospholipids between the two leaflets as it is energetically highly unfavorable for the polar head groups to diffuse across the hydrophobic core. Furthermore membranes of many cell types contain cholesterol and glycolipids. Cholesterol has the ability to modulate the properties of a bilayer, such as its fluidity, in a broad temperature range. At the plasma membrane high concentrations of cholesterol increase the barrier effect of phospholipids by a tighter packing of lipids, which makes the membrane less deformable while still allowing rapid lateral diffusion of the phospholipids.

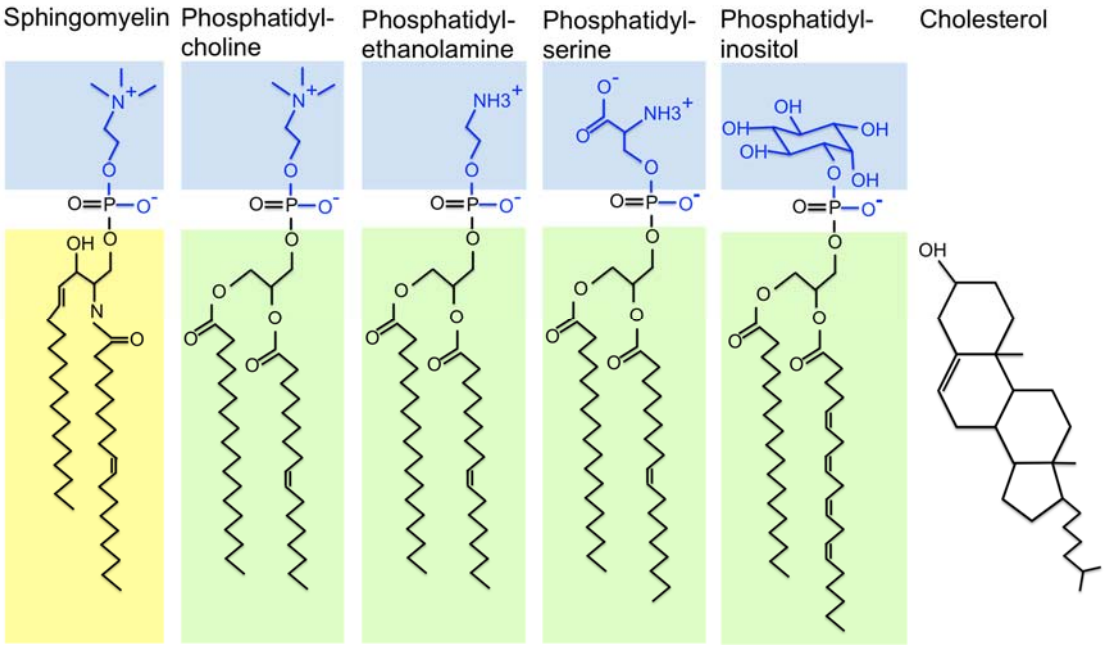

Figure 1 Phospholipids and cholesterol

The most prominent phospholipids and cholesterol are illustrated. The head groups of the phospholipids are highlighted with blue background. The glycerophospholipid backbone of phosphatidylcholine, -ethanolamine, -serine, and -inositol is marked in green and the sphingosine backbone of sphingomyelin in yellow. Phosphatidylinositol can be modified by the addition of one to three phosphate groups to the head group. Phosphatidylserine and phosphorylated derivatives of phosphatidylinositol carry a net negative charge. The fatty acid chains are displayed as 1-myristoyl-2-oleoyl (sphingomyelin, 14:0/ 18:1), 1-oleolyl-2-stearoyl (phosphatidylcholine, -ethanolamine and -serine, 18:1/ 18:0) or 1-stearoyl-2-arachidonyl (phosphatidylinositol, 18:0/ 20:4), but phospholipids with other types of fatty acid chains exist.

Although lipids are essential structural components of biological membranes most transport processes across the membrane are carried out by membrane proteins that are embedded within the lipid bilayer. Membranes of different organelles fulfill distinct tasks and therefore require different compositions of lipids and membrane proteins. While some membrane proteins allow the transmission of a signal from the outside to the inside of the cell, others, mostly multi-pass transmembrane proteins, provide a path for molecules to cross the lipid barrier. Like the surrounding lipids, membrane proteins are amphiphilic molecules, too. In a multi-pass protein hydrophobic regions span the membrane and interact with the acyl chains of the lipids to avoid the contact with water while hydrophilic moieties are exposed to water on either side of the membrane.

1.2. Lipid asymmetry in eukaryotic membranes

In eukaryots, the lipid composition varies between different membranes of distinct organelles. This property is functionally important since the cell uses this information for vesicle trafficking and to

distinguish between different compartments. Further, by the help of specific lipids that are characteristic for a certain organelle proteins are partially recruited to the target organelle [17].

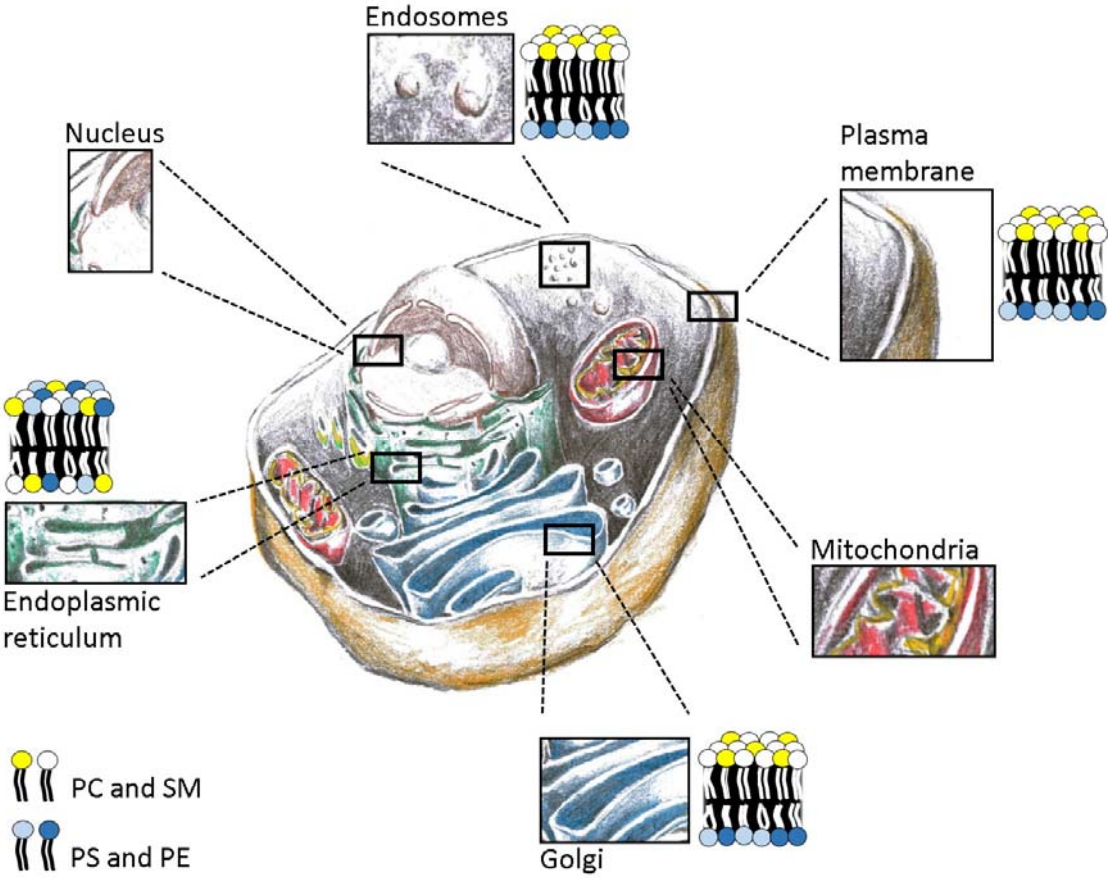

Figure 2 Membrane asymmetry in a eukaryotic cell

Membrane asymmetry in different compartments of a eukaryotic cell. While the lipid distribution is random in the endoplasmic reticulum, lipids are organized asymmetrically in the Golgi apparatus, late endosomes and at the plasma membrane. In asymmetric membranes PC and SM are localized to the outer or luminal leaflet, while PS and PE are confined to the cytoplasmic side. The lipid distribution of the nucleus and mitochondria is not discussed in this work. The lipid distribution (symmetric or asymmetric) in the organelles is exemplified within a small section of a schematic bilayer. PC: phosphatidylcholine, SM: sphingomyelin, PS: phosphatidylserine, PE: phosphatidyl-ethanolamine.

In many eukaryotic membranes the lipid composition of the two leaflets differs, as illustrated in Figure 2. Many lipid bilayers such as the plasma membrane, and membranes of late endosomes and the Golgi are organized in an asymmetric manner [18, 19]. An exception is the endoplasmic reticulum, where the lipid composition of both leaflets is similar [20]. In the asymmetrically organized lipid membranes phosphatidylcholine and sphingomyelin constitute the main lipids on the non-cytoplasmic leaflet, while phosphatidylethanolamine and phosphatidylserine are confined to the cytosolic side of the membrane. In contrast to phospholipids cholesterol can easily flip across the membrane and is not compulsory oriented

asymmetric. The lipid asymmetry is functionally relevant. It can induce membrane bending and curvature, since different types of phospholipids have distinct shapes depending on the size of the head group and the length and degree of saturation of the acyl chains [21, 22]. Membrane curvature is one essential requirement for cilium or vesicle formation and membrane fission [23]. At the apical side of epithelial cells, for example, glycosphingolipids are highly concentrated in the outer leaflet of the plasma membrane, where they protect the cell against low pH and proteases in the gut or stomach. The asymmetric distribution of the lipids, mainly the cytosolic localization of phosphatidylserine, causes the inner leaflet to be sufficiently negatively charged to attract and bind poly-cations and recruit proteins with clusters of positively charged amino acids [24, 25].

1.3. Breakdown of the lipid asymmetry in eukaryotic cells

Under physiological conditions the two leaflets of the plasma membrane and the membranes of certain organelles are organized in an asymmetric manner, which represents a prerequisite for the normal functioning of a cell. In response to certain stimuli this lipid asymmetry can be disrupted to equilibrate the distribution of the different types of lipids on either side of the membrane. Consequently, half of the phospholipids previously localized to the luminal or outer leaflet reach the cytosolic side, while phospholipids confined to the cytosolic side are suddenly transported to the outer leaflet. This process, resulting in the symmetrical distribution of lipids, is called scrambling. Depending on the type of cell that experiences loss of lipid asymmetry, the exposure of phosphatidylserine to the outer leaflet of the plasma membrane can initiate distinct processes. Two important processes that depend on the breakdown of membrane asymmetry are discussed below. Furthermore an example is given that describes, how cell clearance following the exposure of phosphatidylserine is exploited by pathogens for spreading.

1.3.1. Blood clotting

In vertebrates, platelet lipid asymmetry plays an important role in hemostasis. When due to vascular injury tissue factor gets in contact with the blood, platelet adhesion at the site of vascular injury is initiated. At the same time, a complex cascade, the coagulation cascade, is induced to produce small amounts of thrombin in the blood (see Figure 3a). Thereafter, an increase in intracellular Ca^{2+} in the cytosol of platelets causes their activation by disrupting the lipid asymmetry of the platelet plasma membrane (Figure 3b). As a result the lipid asymmetry is disrupted and phosphatidylserine is exposed to the outer leaflet. Due to its negative net-charge phosphatidylserine plays a dominating role in this process [26]. Phosphatidylserine recognition and subsequent attachment of different protein assemblies during the coagulation cascade [27] leads to the generation of even more thrombin [28]. Finally, as illustrated in Figure 3c, thrombin activation results in the clotting of platelets and the generation of a fibrin gel [29]. At the site of vascular injury these concerted processes ascertain the generation of an effective hemostatic plug. Importantly, the exposure of phosphatidylserine on the platelet plasma membrane provides a platform for the assembly of different coagulation factors to accelerate the plug formation by a factor of 2.4×10^6.

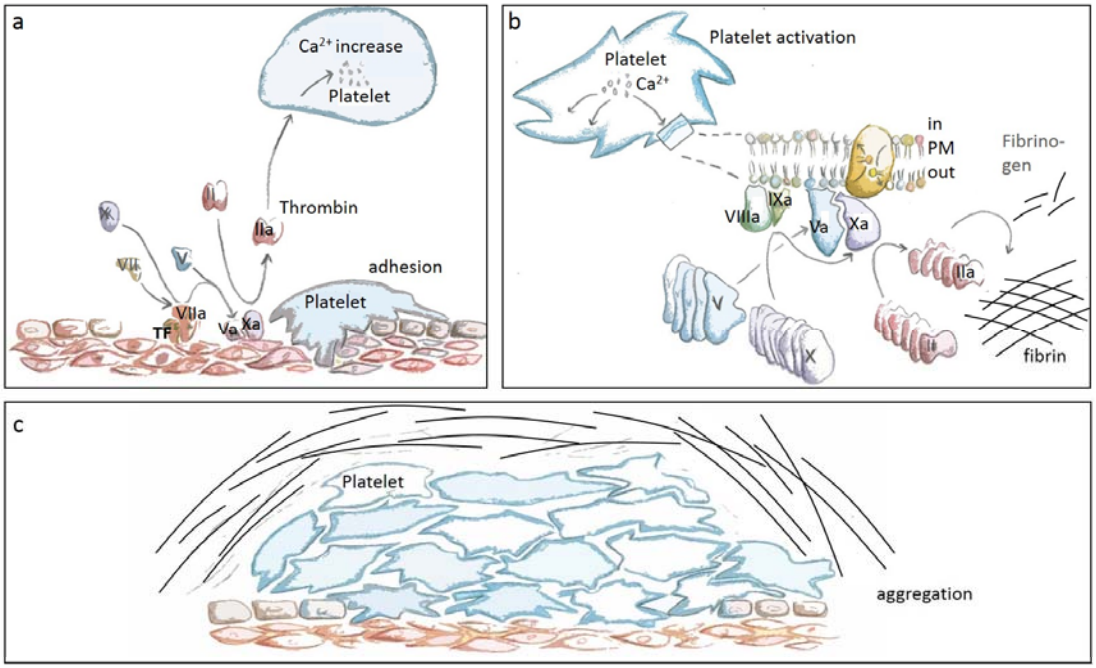

Figure 3 Events during blood clotting

A simplified description of the events that occur after vascular injury to form a hemostatic plug. Under normal conditions in blood vessels, platelet adhesion is inhibited. a, When the vessels are injured, the sudden exposure of sub-endothelial tissue factor to the blood causes platelets to adhere and to form an immediate but loose and inefficient thrombus at the site of injury. Tissue factor binds activated factor VII (VIIa) and mobilizes factor X (Xa). Xa forms a complex with activated V (Va), thereby generating factor IIa (thrombin). b, Thrombin in the blood stimulates platelet activation by an increase in intracellular Ca^{2+}. In the platelet, higher intracellular Ca^{2+} levels have manifold effects: In response to elevated Ca^{2+}, phosphatidylserine is exposed to the outer leaflet of the platelet plasma membrane. Extracellular phosphatidylserine is recognized by factor Va and VIIIa. Binding of factor IXa to VIIIa supports the generation of factor Xa that forms a complex with factor Va and phosphatidylserine. The factor Xa-Va complex then accelerates the formation of thrombin. c, Thrombin transforms fibrinogen into fibrin that enables rapid and tight gluing and cross-linking of platelets to plug the site of injury. Importantly, phosphatidylserine exposure on the platelet plasma membrane, which facilitates the assembly of different coagulation factors, accelerates the plug formation by a factor of 2.4×10^6.

1.3.2. Apoptosis

In many animal cell types, the lipid asymmetry is a critical determinant of survival or death of a cell. During the animal and plant development many extra cells are produced and need to be eliminated again in a precisely controlled manner to maintain organismal homeostasis. For example during the embryonic development hands and feet attain their shape because the cells between the developing fingers die. These cells are sorted out to commit suicide by starting an intracellular death program. Importantly, this happens as a completely controlled process, also known as apoptosis. During this process different pathways are switched on [30] and in combination with caspase cleavage of more than 500 target substrates [31, 32] the cell undergoes dramatic but characteristic morphological changes to complete

apoptosis. Caspase cleavage also induces the externalization of phosphatidylserine at the plasma membrane of the apoptotic cell as an 'eat me' signal to declare the apoptotic state [10, 33, 34]. This signal is immediately recognized by macrophages, that rapidly engulf the suicidal cells before they can spill their immunogenic content. The cellular components of the ingested cells are targeted to the lysosomes of macrophages to be degraded to nucleotides, fatty acids, amino acids and sugars for re-usage by the cell. Mature erythrocytes, for example, do not contain any nucleus whereas it's precursors, erythroblast, do. During the process of enucleation the nucleus is expelled from the erythroblast, and upon phosphatidylserine exposure the nucleus is recognized and engulfed by fetal liver macrophages [35].

Other processes that are dependent on the exposure of phosphatidylserine are the capacitation of sperm cells [36], myotube formation at cell-cell contact sites during development [37], myoblast fusion to build skeletal muscles [38] and host-pathogen interaction [39].

1.3.3. Cell-to-cell spread in *Listeria monocytogenes*

Dying cells are engulfed by macrophages through recognition of phosphatidylserine by TIM-4 [40, 41], a phosphatidylserine receptor located on the surface of macrophage cells. During infection of macrophages the bacterium *Listeria monocytogenes* excapes the phagosome and makes use of the process of phosphatidylserine mediated engulfment to facilitate cell-to-cell spread [42, 43]. *Listeria monocytogenes* ActA cell surface protein enables the modulation of actin-based motility in the interior of the macrophage leading most probably to membrane protrusion [39]. In combination with listeriolysin O (LLO), a pore forming toxin of *Listeria monocytogenes*, this results in membrane damage [44] that is locally restricted. Membrane damage by LLO is associated with Ca^{2+}-dependent loss of membrane asymmetry and therefore phosphatidylserine exposure [45, 46]. At the sites of membrane damage by LLO and protrusion formation, bacteria- containing membrane vesicles are released with exofacial phosphatidylserine [39]. Since they present phosphatidylserine these vesicles with bacterial content are in turn recognized by other macrophages through TIM-4 and ingested [39], and spread is continuing.

1.4. Proteins that modulate the lipid asymmetry in eukaryotes

In normal viable cells, the lipid distribution between the two leaflets of the plasma membrane and late endosomal and Golgi membranes is asymmetric. While phosphatidylcholine and sphingomyelin are localized in the outer leaflet, phosphatidylserine and –ethanolamine usually face the cytosolic side of a bilayer. The lateral diffusion of lipids of the bilayer is very fast, so that lipids permanently change their position within the plane. This gives the impression of a two-dimensional fluid where the constituents can move freely in the lateral direction. In contrast to that, the transbilayer movement of lipids occurs very rarely. Lipid flip-flop is highly unfavorable since the polar head groups of the phospholipids would have to cross the hydrophobic part of the lipid acyl chains. To overcome this energetic obstacle specific proteins are needed to catalyze the transbilayer movement of lipids.

1.4.1. Flippases and floppases

The lipid asymmetry of membranes of the Golgi, the late endosomes and plasma membranes is controlled by flippases, floppases and scramblases. The presence of these proteins was known for a long time, but the molecular identity of the responsible enzymes remained elusive until recently and is still debated for some candidate proteins. While flippases and floppases create and maintain the lipid asymmetry, scramblases randomize the lipid distribution after activation [47]. Figure 4 gives an overview on the concerted action of flippases, floppases and scramblases at the plasma membrane.

The preferred substrates of flippases comprise phosphatidylserine and phosphatidylethanolamine that are translocated from the outer or luminal leaflet to the cytoplasmic leaflet [48-50], but other substrates are reported as well [51-53]. Compared to flippases, floppases are rather slow and often facilitate the net transport of phosphatidylcholine from the cytoplasmic to the external leaflet, but exceptions exist. Other substrates of floppases include cholesterol and some ceramide derivatives. The membrane asymmetry is a result of the specificity of each of these translocators, thereby conferring distinct properties to membranes of different compartments needed for their respective biological function. The simultaneous action of both proteins and therefore the bidirectional lipid translocation is needed to prevent membrane imbalance and destabilization [54]. Importantly, the function of flippases and floppases depend in both cases on ATP- hydrolysis to transport lipids against the gradient [55, 56]. While flippases include members of the P4-type ATPase protein family [57, 58], floppases are predominantly constituted by members of the ABC transporter protein family with few exceptions [59-61].

Flippases are widely expressed and can be found in the membranes of intracellular compartments of the late secretory and endocytic pathways and in most plasma membranes of erythrocytes, platelets, lymphocytes, endothelial and epithelial cells, hepatocytes and spermatozoa [62-69]. Thus, the formation of lipid asymmetry is initiated in the late Golgi compartments and perpetuated at the plasma membrane by the action of distinct flippases. For their correct targeting and potentially even proper flippase function most P4-type ATPases need to associate with Cdc50 proteins [70-72].

Other P-type ATPase proteins, although structurally related, transport ions rather than lipids across the membranes. The best understood members include the Ca^{2+}-pump of the muscle sarcoplasmic reticulum (SR) that, after Ca^{2+} release to the cytosol to induce muscle contraction, pumps the ions back to the SR [73-76]. Another P-type ATPase, the Na^{+}- K^{+}- ATPase, establishes and maintains the gradient of potassium and sodium ions across the plasma membrane of all animal cells [77-80]. There, the intracellular potassium concentration is approximately 10-30 times higher than the external concentration, while it is the other way around for sodium.

All living organisms depend on the supply of nutrients from outside the cell and need to establish a way for disposal of unwanted products. ABC transporters constitute a large class of proteins that, besides lipid transport, are responsible to move substrate as different as inorganic ions, sugars, amino acids, peptides, proteins and therapeutics. Bacterial ABC transporters include both importers and exporters and have gained considerable attention since they partially account for antibiotic resistance [81-84]. ABC transporters in eukaryotes contribute to the antigen processing and presenting machinery [85] and were

associated with multidrug resistance in cancer cells [81-83, 86] or herbicide resistance in plants [87]. Some rather untypical ABC transporters, since they lack the transmembrane part, are involved in protein biosynthesis, while cystic fibrosis transmembrane regulator protein (CFTR), another ABC transporter [83, 88, 89], resembles rather a channel than a transporter that uses ATP hydrolysis for opening and closing [90].

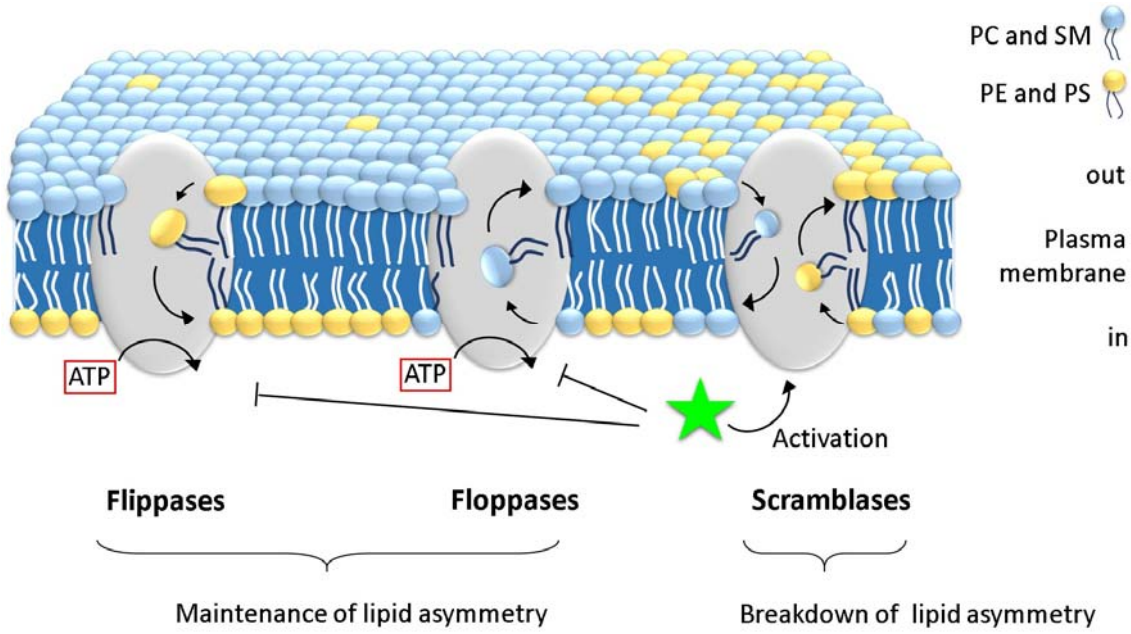

Figure 4 Maintenance and breakdown of the lipid asymmetry at the plasma membrane

In a healthy, resting cell, the membrane asymmetry at the plasma membrane is maintained by the collaborative operation of ATP-dependent flippases and floppases. Thus, phosphatidylserine and phosphatidylethanolamine suddenly located at the external leaflet are immediately transported back by flippases, while floppases support the net transport of phosphatidylcholine from the inner to the outer leaflet. The stimuli that lead to the activation of scramblases (green star) at the same time inhibit the function of the flippases and floppases. As a result of that and due to the unspecific performance of scramblases, rapid randomization of the different types of lipids between the two leaflets of the membrane occur.

1.4.2. Scramblases

The steady activity of flippases and floppases maintain the lipid asymmetry until scramblases are activated to randomize the lipid distribution. For efficient disruption of the lipid asymmetry the stimuli that mobilize scramblases at the same time inhibit the proper function of flippases and floppases [91-93]. Scramblase function is energy independent since they catalyze the down-hill movement of lipids along the concentration gradient. To equilibrate the lipid composition on both sides of the bilayer scramblases need to recognize their substrates in an unspecific manner. Therefore usually different kinds of phospholipids are transported. In the following different types of scramblases are delineated. This

description does not aim for completeness; instead the object is rather to give a short introduction to a few selected classes of scramblases that are involved in processes that couldn't be any different.

1.5. Scramblases of the endoplasmic reticulum

1.5.1. Phospholipid scramblase

Most glycerophospholipids are synthesized on the cytoplasmic side of the endoplasmic reticulum. To ascertain balanced growth of the membrane and to prevent the overload of newly synthesized lipids by this one-sided fabrication, the immediate compensation and randomization of these lipids is required. Since the rate of spontaneous flipping is slow in biogenic membranes, cells must have a strategy to enhance the lipid transbilayer movement. In the endoplasmic reticulum this function is carried out by a yet to be identified glycerophospholipid scramblase (PL scramblase) that secures the breakdown of the lipid asymmetry to balance the lipid density on either side [94, 95]. Since glycerophospholipids are synthesized continuously, this ER scramblase requires to be constantly active. As a result of that scramblase activity, phosphatidylserine is observed on both leaflets. If these lipids require to reach the plasma membrane by secretory vesicular transport, the lipid asymmetry thus must be established prior to fusion to avoid that phosphatidylserine is exposed to the external leaflet.

1.5.2. Glycolipid flipping

The modification of nascent peptide chains of secretory proteins by glycosylphosphatidylinositol (GPI) lipid anchors or by N-glycosylation occurs in the lumen of the endoplasmic reticulum. While the N-glycan is linked to a lipid platform, an oligosaccharide-diphosphate dolichol lipid, and is from there transferred to the protein, the GPI anchor is directly coupled to the protein. The N-glycan as well as the oligosaccharide-diphosphate dolichol and the GPI anchor need to be present at the luminal side of the endoplasmic reticulum. The N-glycan is assembled over several steps, and precursors and intermediate products such as Man5GlcNAc2-PP-dolichol (M5-DLO) and mannose-phosphate-dolichol (MPD) are formed on the cytoplasmic side of the endoplasmic reticulum [96]. Similarly, parts of the GPI anchor and the oligosaccharide-diphosphate are generated on the cytosolic side [96, 97]. Since parts of the synthesis of these lipids takes place on the cytoplasmic side, cells must come up with a mechanism to translocate them to the luminal side of the membrane, where they are required for protein modification. Furthermore, dolichol phosphate, one of the components of N-glycosylation, must be recycled to the cytosolic side for synthesis of the oligosaccharide-diphosphate dolichol. These flip-flop processes are ATP independent [96, 98] and occur bidirectional, but since the constituents are consumed at the luminal side of the ER, the process is directed. Since six unrelated classes of lipids need to be moved to the other side of the membrane, it appears likely that several scramblases are involved. All of these scramblases remain to be identified at the molecular level. Reconstitution with partially purified proteins of ER membranes revealed two distinct activities, termed M5-DLO- and MPD- flippase [99]. The term 'flippase' is actually misleading, but is nevertheless applied in this context here as well as in the literature,

but stands for an ER- scramblase. Recently Rft1 was proposed as the M5-DLO- flippase [100] and Dpm1 as the MPD- flippase [101], but both suggestions were subsequently questioned [98, 102-104].

1.6. Scramblases of the plasma membrane

Since many years researchers have characterized the flip-flop of distinct phospholipids at the plasma membrane of various cell types and cell lines. Phosphatidylserine exposure to the external leaflet is achieved by activation of two distinct pathways, either involving Ca^{2+} or apoptotic signaling [105].

1.6.1. Xk-related proteins and apoptosis

Virtually all types of cells need to be able to undergo apoptosis, not only during developmental stages, but also since cells become defective, senescent or toxic. Phosphatidylserine exposure on apoptotic cells is caspase cleavage dependent. Recently xkr8 of the xk-related protein family was identified as the scramblase that dissipates the membrane asymmetry at the plasma membrane of apoptotic cells, when activated by caspases through cleavage at its carboxy terminus [106]. Evidence was shown that other members of the xk-related protein family, such as xkr4 and xkr9, function as scramblases as well upon activation by caspase cleavage [107]. Mutations in the cleavage site abrogated cleavage and thus activation of these proteins by caspases and apoptosis induced phosphatidylserine exposure was prevented [106, 107]. At the same time, when these scramblases are activated by caspase cleavage, the flippases, which catalyze the lipid transport in opposite direction, are cleaved by caspases in a similar way. This leads to their inactivation [93]. Fibroblast of xkr8 knock-out mice were incapable of exposing phosphatidylserine on the outer leaflet as ‘eat-me’ signal [106]. Moreover, in cancer cell lines impaired phosphatidylserine exposure and disturbed apoptosis- induced cell clearance were associated with inadequate protein levels of xkr8, which could be attributed to hyper-methylation of the xkr8 promoter [106]. Furthermore CED-8, the *Caernohabditis elegans* homologue of xkr8, was shown to be functionally related and promotes phosphatidylserine exposure as well, although additional factors other than CED-8 seem to be involved in that process [106].

The xk-related protein family is only found in metazoans. The family constitute integral membrane proteins with a size of 400 to 700 amino acids. Hydropathy analyses predicted six to nine transmembrane spanning helices and cytosolic amino- and carboxy termini. The caspase cleavage site is localized at the amino- terminus in the case of CED-8, while most other xk-related proteins carry the caspase recognition site at the carboxy terminus.

1.6.2. TMEM16F and blood clotting

1.6.2.1. Phospholipid transport

In platelets, but also in other blood cells, elevated levels of Ca^{2+} lead to the breakdown of the lipid asymmetry and presentation of phosphatidylserine to the outer leaflet of the plasma membrane. In platelet this process triggers blood clotting in response to vascular injury.

Recently the responsible Ca^{2+}- activated scramblase was identified as TMEM16F [10], a member of the transmembrane proteins with unknown function 16 (TMEM16). Using blood cells the substrate specificity of this endogenous protein was investigated over many years without knowing the molecular identity of the responsible protein. It was demonstrated that, upon activation by Ca^{2+}, this particular (unknown) scramblase would transport fluorescently labelled derivatives of phosphatidylserine, phosphatidylethanolamine and phosphatidylcholine [108]. Phospholipid transport is supported by cations such as Ca^{2+} or Sr^{2+} but not Mg^{2+} [109]. Furthermore, phospholipids with a small sugar moiety such as phosphatidylgalactose, phosphatidylmaltose and galactosylceramide were translocated as well, although at lower rate [110]. Consistent with that, it was shown in a cellular assay that TMEM16F is able to transport fluorescent analogues of phosphatidylserine, phosphatidylethanolamine, phosphatidylcholine and galactosylceramide [10, 111, 112] in a Ca^{2+} dependent manner.

1.6.2.2. Pathophysiology

Patients with Scott-syndrome (named after the patient M. A. Scott 1939-1996) suffer from a rare congenital/autosomal recessive bleeding disorder marked with a deficiency in platelet procoagulant activity [105, 113]. In this disorder, blood cells, particularly platelets, fail to expose phosphatidylserine in response to an intracellular increase in Ca^{2+}, which is required for the efficient induction of blood coagulation [114-118]. The failure to expose phosphatidylserine is not a general phenotype in Scott-syndrome patients, since this signaling phospholipid can be moved to the outer leaflet of the plasma membrane during apoptosis [105]. After identification of TMEM16F as the putative Ca^{2+} - activated scramblase to facilitate platelet procoagulant activity, it was observed that in B-cell lines of Scott-patients TMEM16F is encoded by a mRNA that, due to aberrant splicing, lacks some part leading to a frame shift and premature termination of the protein [10]. In agreement with that, TMEM16F knock-out mice showed defective phosphatidylserine exposure and delayed blood coagulation [9].

In another TMEM16F knock-out mouse model skeletal deformations and a reduced skeleton size can be observed, but no prolonged bleeding during giving birth, which is a major problem in human Scott-patients [119]. The observed phenotype were explained by a defect in bone mineralization in osteoblasts, although morphologically these cells were intact [119]. Bone mineralization is a process found in osteoblasts, chondrocytes and odontoblasts to deposit hydroxyapatite to the extracellular space. There, the involvement of a Ca^{2+} dependent scramblase was expected [120]. Notably, osteoblasts of these TMEM16F knock-out mice exhibited impaired Ca^{2+} dependent phosphatidylserine scrambling [119].

1.6.2.3. Other candidate scramblases proposed

Before TMEM16F was proposed as the scramblase responsible for the Ca^{2+} dependent disruption of the lipid asymmetry in platelets and red blood cells, other proteins were considered. The protein PLSCR1 or phospholipid scramblase 1 was suggested as the Ca^{2+} induced phospholipid scramblase [121-123]. The expression level of this protein correlated with the observed Ca^{2+} dependent scrambling of phosphatidylserine [124]. Reconstitution of an isolated orthologue obtained from recombinant source confirmed the scramblase activity in response to Ca^{2+} [123]. Interestingly, mutations in a motif, that resembled an EF hand, abolished the scramblase activity [123]. However, PLSCR1 knock-out mice have normal blood clotting and normal phosphatidylserine exposure in response to elevated levels of Ca^{2+} [125] and none of the homologues of the PLSCR family is mutated in Scott-syndrome patients [126]. PLSCR is now thought to be involved in cell proliferation and differentiation, among other processes. In contrast to that, Scott- patients possess a truncated version of TMEM16F. Further evidence for a role of TMEM16F in scrambling processes was independently obtained from two knock-out mouse models, and one of these mouse models perfectly matched the phenotype of Scott- patients. Further, cells from both knock-out mice showed impaired phosphatidylserine exposure upon Ca^{2+} stimulation.

Nevertheless, despite the disagreement, TMEM16F is so far the most convincing candidate scramblase, that triggers the events during blood clotting in a Ca^{2+} dependent manner.

1.6.2.4. Ion transport

Before TMEM16F was linked to a scramblase function, other TMEM16 family members were classified as Ca^{2+}- activated chloride channels (see below). Efforts to characterize TMEM16F pinpointed thereafter to a role in ion transport. A report associated TMEM16F with a conductance for cations most selective for Ca^{2+} [9]. In this study, expression of TMEM16F in *Xenopus laevis* as well as axolotl oocytes and HEK cells gave rise to small conductance Ca^{2+}- activated nonselective cation currents that were also present in megakaryocytes of wild-type mice, but that were lacking in TMEM16 knock-out mice. TMEM16F seems to be permeable to monovalent as well as divalent ions, but slightly higher permeability has been seen for Ca^{2+}. A role of TMEM16F in ion transport is further supported by the identification of a glutamine (Q559) that, when replaced by a lysine, shifted the cation over anion selectivity towards a higher permeability for anions [9].

Therefore, it was proposed that TMEM16F acts as a regulator of phosphatidylserine scrambling, presumably forming a channel that, in response to Ca^{2+}, activates a scramblase downstream. Thus, for answering the question whether or not TMEM16F has a direct participation in the Ca^{2+} dependent lipid scrambling, it will be necessary to isolate and reconstitute the protein into liposomes to investigate the ability for scrambling and ion conduction.

1.7. TMEM16 proteins in mammals

TMEM16 proteins are found in all kingdoms of life, but they are absent in bacteria. Besides TMEM16F, nine other family members are found in mammals. The ten mammalian members are named TMEM16A to TMEM16K [127]. The sequence identity among the different members in mouse is generally between 25-65 %, whereas TMEM16H and K constitute the most divergent branch of this family.

1.7.1. TMEM16A and TMEM16B

For nearly 30 years researchers characterized Ca^{2+}- activated chloride channels (CaCC) at the plasma membrane of various cells and tissues such as *Xenopus laevis* oocytes [128, 129], Salamander photoreceptors [130], vascular, gut and airway smooth muscles [131], pulmonary artery endothelial and secretory epithelial cells [132] and hepatocytes [133] among others. CaCCs were correlated with a diverse range of functions including the fast block to polyspermy in *Xenopus laevis* oocytes, membrane excitability in neurons and cardiac muscles, fluid secretion in acinar cells as well as signal transduction in photoreceptor and olfactory cells [134]. By electrophysiological measurements different types of CaCCs could be discriminated. Proteins mediating a chloride current that is activated by Ca^{2+} are denoted as CaCCs, independent of the mechanism of activation and their molecular identity. The investigated CaCCs elicit chloride currents with a strong outward rectification at low levels of intracellular Ca^{2+}, meaning that chloride ions enter the cell, whereas this outward rectification disappears at higher intracellular Ca^{2+} concentrations [133, 135]. The Ca^{2+} sensitivity was observed to increase at positive membrane potential and was therefore described as voltage- dependent. The anion over cation selectivity with one sodium for 7-10 chloride ions is moderate. The permeability sequence was determined to be lyotropic, with a preference for larger over smaller anions: $SCN^- > NO_3^- > I^- > Br^- > Cl^- > F^-$ [136, 137], while the conductance was measured to be opposite and follow the sequence: $Br^- > Cl^- > I^- > SCN^-$ [136]. Ca^{2+} binding to TMEM16A was determined to be cooperative and involves at least 2 or 3 Ca^{2+} ions [1].

In 2008 three groups independently identified TMEM16A as the protein responsible for the described currents [4-6]. TMEM16A was the first member of this protein family with assigned function. It is therefore not surprising that many of the insights known to date were gained by studying TMEM16A using mainly electrophysiological methods. TMEM16A transmits chloride ions with low anion over cation selectivity and similar permeability for larger anions as preciously described for CaCCs. Moreover, TMEM16A is outwardly rectifying at low Ca^{2+}- concentrations, but not at higher Ca^{2+} concentrations [4-6]. Like CaCC currents, TMEM16A conductance could be inhibited by known chloride channel inhibitors [5, 6]. Furthermore, the Ca^{2+}-sensitivity is voltage-dependent as previously observed for CaCCs [5]. Consistent with the localization of CaCCs, a specific anti-TMEM16A antibody detected the protein in different tissues such as smooth muscle cells, airway endothelia, and salivary gland as well as pancreas acinar cells [2, 138].

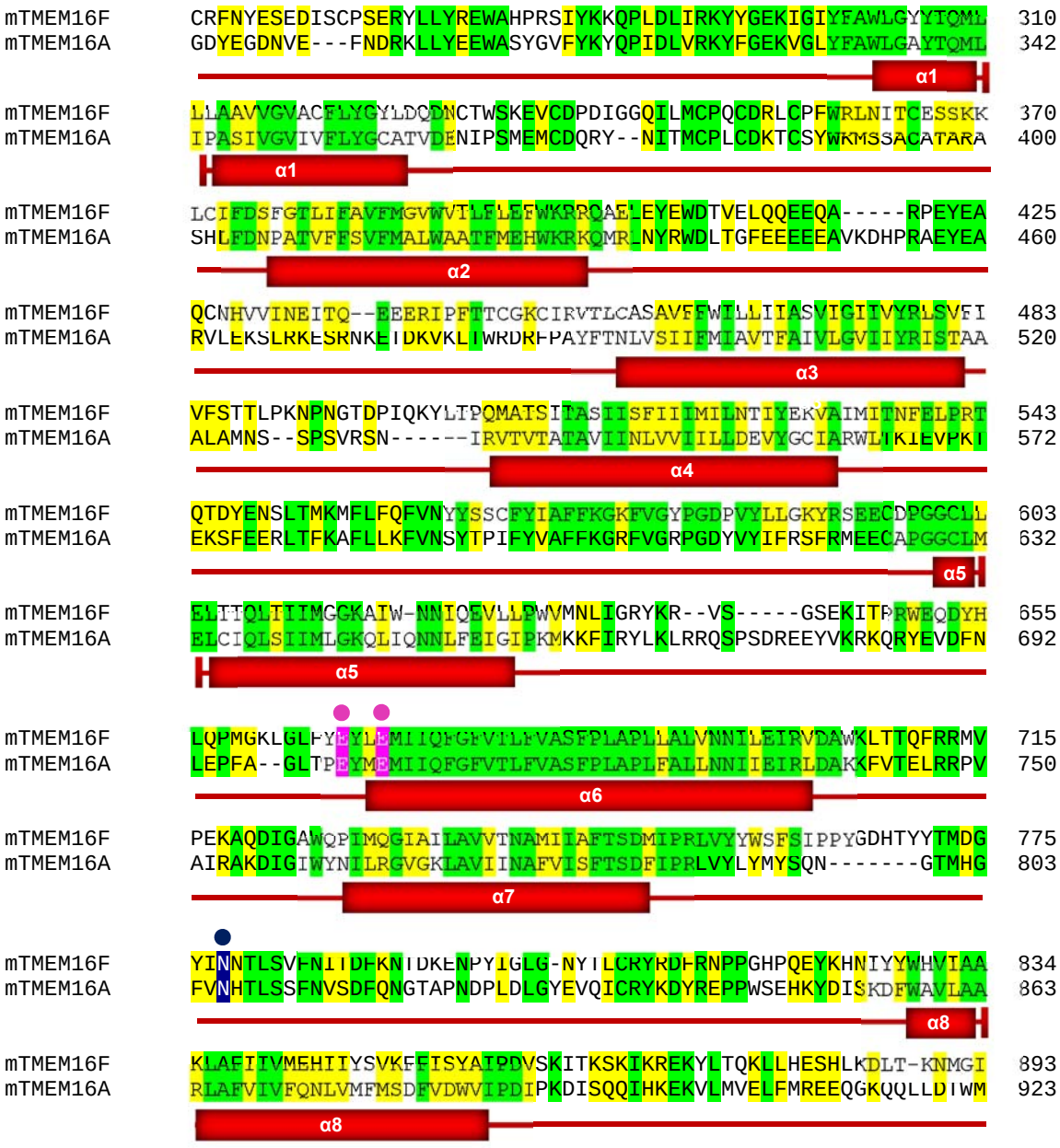

Figure 5 Alignment of murine TMEM16A with TMEM16F

The sequence of murine TMEM16A was aligned with murine TMEM16F using Clustal Omega [139]. Identical residues are labelled in green while similar residues are shown in yellow. Two residues that were demonstrated to be involved in Ca^{2+} sensing are marked in magenta. A conserved glycosylation site is indicated in dark blue. Predicted transmembrane domains are displayed by red helices. The amino- (first 300 amino acids) and carboxy (last 50 amino acids) termini are not shown.

Interestingly, TMEM16A can form a number of alternative splice variants (see Figure 6). The alternatively spliced segments concern regions in the amino- terminus and first intracellular loop and are termed a, b, c and d. Splice isoforms that naturally occur in mouse or human are TMEM16a (only in mouse), ac, abc, ad and acd [140, 141]. Pre-mRNA alternative splicing is widely used to increase proteome diversity and is thought to be the basis for tissue-specific regulation of expression [142] and

function [143-146]. TMEM16A alternative splicing is processed tissue dependent and Ca^{2+}- activated chloride currents of splice variants differ in their functional properties and kinetics. Exclusion of segment b for example increases the Ca^{2+} sensitivity 4- fold and segment c has an impact on channel kinetics by changing voltage- dependence of the currents in TMEM16A and B [141, 147, 148]. Alternative splicing also takes place in TMEM16B [149]. Whether alternative splicing occurs in other TMEM16 family members has not been described to date. Murine TMEM16A (mTMEM16A) shares 40% of the sequence with murine TMEM16F (mTMEM16F) with the highest identity found in the transmembrane part (Figure 5).

Similarly as TMEM16A, TMEM16B functions as Ca^{2+}-activated chloride channel [149-152], with altered kinetics of activation and different functional properties [149, 153-155]. Compared to TMEM16A the Ca^{2+} sensitivity is significantly lower [154], but a voltage- dependence was also shown in this case [148]. Its expression was reported in the retina [156] and in chemosensory neurons [157]. Due to the expression profile TMEM16B was proposed to be involved in olfactory and photoreceptor signal transduction (see also chapter 1.9.1 and 1.9.2) [7, 156].

1.7.2. Other TMEM16 proteins

Since the discovery of TMEM16A and B as Ca^{2+} -activated chloride channels, it was generally assumed that other family members would be functionally related. Today, there exists a number of controversial reports that suggested other TMEM16 family members besides TMEM16A and B, particularly TMEM16F, to have a function in ion transport [9, 158-160]. However, in these often contradicting studies TMEM16F was associated with different kinds of currents such as hyperpolarization- [161], volume- [162] and Ca^{2+}- activated chloride currents [158, 159, 163-165] while other groups do not measure chloride conductance at all [111, 166]. Moreover, TMEM16F was also proposed as Ca^{2+}-activated small conductance nonselective cation channel being most permeable for Ca^{2+} [9]. The described currents had different activation and inactivation kinetics and current-voltage relationships, and it seems implausible that a single protein can mediate these different types of currents [167-169]. Recent efforts provided substantial evidence for a direct or indirect involvement of TMEM16F in phospholipid scrambling [9, 10, 111, 112, 119, 170, 171].

Similarly as TMEM16F, other members of this protein family were suggested to function as Ca^{2+}-activated scramblases. For TMEM16C, D, F, G and J a scramblase activity was proposed where transport of various lipid substrates is catalyzed with different kinetics [111]. TMEM16G protein was reported to be expressed in prostate and prostate cancer cells [172] particularly in cell-cell contact regions [173]. According to another study TMEM16G mRNA was only detected in significant amounts in the stomach and intestine [111]. For TMEM16C a role in pain processing by modulation of the SlacK Potassium channel was suggested [174, 175]. Still many of the other TMEM16 family members, that are not describe here, have so far resisted any detailed characterization, particularly TMEM16H and K.

1.8. Biochemical characterization of TMEM16 proteins

Most molecular information on TMEM16 proteins was obtained by studying TMEM16A. Members of the TMEM16 protein family were predicted to contain cytosolic amino- and carboxy termini and to span the membrane eight times, while having a re- entrant loop between transmembrane six and seven [11, 176]. Since the first members identified in this family were associated with Ca^{2+} dependent chloride currents, the family was also referred to as anoctamins (for anion selective and eight predicted transmembrane domains) [6].

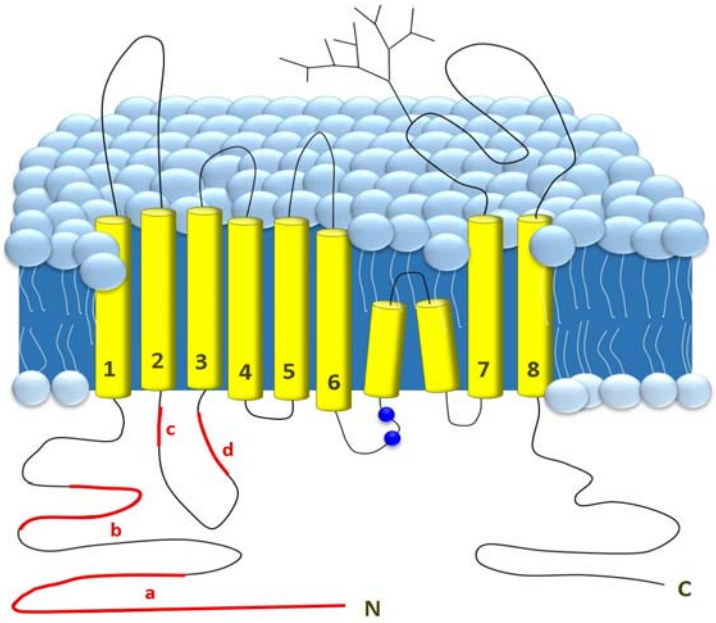

Figure 6 Predicted topology of TMEM16 proteins

Proposed topology of TMEM16 proteins. For simplicity, only one subunit of the dimer is displayed. Hydrophathy analysis has predicted eight transmembrane spanning helices with a re- entrant loop between transmembrane six and seven, and cytosolic amino- and carboxy termini. At least one glycoslylation site is present on the last extracellular loop in mammalian TMEM16 homologues. Dark blue dots indicate the presence of two residues involved in Ca^{2+} sensing (E702/E705 in TMEM16A). Red parts in the cytosolic loops represent alternative splice segments.

The proteins were shown to form dimers [177, 178], and dimerization was suggested to occur via intermolecular contacts at the amino- termini [179], although recently a functional form of TMEM16A was observed that lacks the region proposed to be involved in dimerization [180]. TMEM16 proteins form homodimers [112, 179], but TMEM16A and B may undergo hetero-dimerization [155, 179]. It was also shown that dimerization in TMEM16A occurs before the protein reaches the plasma membrane [177, 178]. Direct activation of TMEM16A by Ca^{2+} [181, 182] or indirect activation via Calmodulin [158, 183-185] was discussed controversially, until it was shown that purified TMEM16A lacking Calmodulin is sufficient for activation [186]. Furthermore, an isolated TMEM16 protein from the fungus *Aspergillus fumigatus* was attributed with a scramblase and ion conductance activity and demonstrated to be functional in the absence of Calmodulin [170]. Two residues (E702 and E705) were identified to be involved in Ca^{2+} sensing in TMEM16A [12]. The identification of these residues, that in the originally proposed topology model [176] were located at the extracellular side, permitted the correction of the topology model [12]. There is strong evidence that mammalian TMEM16 proteins are glycosylated [11,

156]. Figure 6 illustrates the proposed topology of the TMEM16 protein based on transmembrane predictions and biochemical analysis.

Several residues were related to the anion selectivity in TMEM16A [9, 187], notably K584 (corresponding to Q559 that in TMEM16F was previously shown be important for the cation over anion selectivity) and the recently identified amino acid residues at position R511, K599, R617 and R784 [188]. Several mutations influence the conductance of TMEM16A (G628, G529, M632, I636, Q637 and K645) [12]. Mutations in other residues turn TMEM16A into a constitutively active protein [189].

In the absence of a structure it is, however, difficult to comprehend the role of these residues for activation, selectivity and phospholipid scrambling or ion conduction in TMEM16 proteins.

1.9. Pathophysiology in TMEM16 proteins

Not much is known so far about diseases that are linked to TMEM16 proteins. Recent progress in this direction was made by knock-out mice and new-generation sequencing allowing correlation of some diseases with TMEM16 proteins.

1.9.1. TMEM16A related diseases and knock-out models

TMEM16A, the best investigated family member, was related to cancer [190-193]. The first report identified TMEM16A (also known as DOG1) as a marker for gastrointestinal stromal tumors [193]. A $TMEM16A^{-/-}$ knock-out mouse was available before TMEM16A was linked to CaCC function. Interestingly, within one month after birth, these mutant $TMEM16A^{-/-}$ mice died from tracheomalacia, that is the trachea exhibited gaps in the surrounding cartilage rings. Since TMEM16A is not expressed in the trachea, this effect was thought to be secondary and was attributed to a defect in muscle and endothelium smooth muscle cell organization. Thus, at that time TMEM16A was assigned a role as regulator in the organization of muscle and endothelium smooth muscle cells during mouse development [194]. Recently, a conditional $TMEM16A^{-/-}$ knock-out in acinar cells of the salivary gland was generated, owing to the TMEM16A expression pattern and functional relevance of this protein as CaCCs in these cells. The role of TMEM16A Ca^{2+}-activated chloride channel on salivation in adult mice was thereafter investigated. Two pathways exist that initiate salivary fluid secretion, a muscarinic or Ca^{2+} dependent and a β-adrenergic receptor-activated, cAMP dependent pathway. It was shown that salivary fluid production is regulated by TMEM16A in the Ca^{2+} dependent pathway, whereas loss of TMEM16A function doesn't change β-adrenergic salivation. Another conditional TMEM16A knock-out mouse model was generated to switch off expression of TMEM16A in the vomeronasal sensory neurons. In these cells TMEM16A specific detection and electrophysiological recordings indicated loss of TMEM16A expression and no CaCC currents could be measured, although expression of TMEM16B could still be confirmed [155]. The same type of cells derived from a TMEM16B knock-out mouse were deficient in CaCC currents as well [8]. These data could indicate that CaCC currents in vomeronasal sensory neurons are dependent on the formation of TMEM16A/B hetero-dimers [155]. There is evidence

that in the main olfactory epithelium TMEM16B alternative splicing produces isoforms that are, due to the lack of exon 4, not functional but are able to modulate the properties of TMEM16B currents [149]. However, the possibility remaines that different populations of neurons can have different TMEM16A and B expression profiles, potentially also involving distinct splice variants [155].

1.9.2. TMEM16B knock-out mouse model

In the olfactory signal transduction of vertebrates, amplification of the odorant signal was thought to be mediated by Ca^{2+}- activated chloride currents [195, 196]. TMEM16B is expressed in olfactory sensory neurons [197] and similarly as TMEM16A, TMEM16B displays Ca^{2+}- activated chloride currents [149-151] with slightly different functional properties [153]. A proteomic screen aiming for the identification of constituents of the olfactory signal transduction machinery identified all known components involved in that process including TMEM16B [152]. Hence, TMEM16B was proposed to be the candidate olfactory Ca^{2+}- activated chloride channel involved in amplification in olfactory signal transduction [7, 150, 152, 198]. In cells of the vomeronasal organ and the main olfactory epithelium from $TMEM16B^{-/-}$ knock-out mice no Ca^{2+} dependent chloride currents were detected anymore. However, in olfactory behavior tests these $TMEM16B^{-/-}$ knock-out mice did not show the expected phenotype, thus indicating that TMEM16B and Ca^{2+}- activated chloride currents, respectively, may not be required for smelling [8].

1.9.3. TMEM16E, F and K related diseases

A couple of mutations in TMEM16 family members were linked to diseases. Mutations in TMEM16E were implicated in autosomal recessive diseases such as muscular dystrophy, that manifests itself by muscle weakness [199], and gnathodiaphyseal dysplasia, a skeletal disorder, that is marked by bone fragility as well as deformation and by lesions of the jawbones [200-202].

The autosomal recessive bleeding disorder Scott-syndrome could be traced back to mutations of TMEM16F that lead to premature termination of the protein [10, 203]. One of the two available $TMEM16F^{-/-}$ knock-out mouse models exhibits defective phosphatidylserine exposure and impaired blood coagulation [9], similarly as patients suffering from Scott-syndrome [126]. Finally, mutations in TMEM16K were connected with cerebellar as well as gait ataxia, nystagmus, disarthrytic speech and secondary Q10 cofactor deficiency [204, 205].

1.10. TMEM16 proteins in *Xenopus laevis*

The frog *Xenopus laevis* is an invaluable model organism for molecular and cellular biology, embryology and development, since it is easy to manipulate single genes and entire embryos. *Xenopus laevis* oocyte production can be induced on demand upon application of chemicals to the frogs, and isolated oocytes are widely used to investigate ion transport by electrophysiological methods. Since the embryos develop outside of the animal, they can be studied before and directly after the fertilization process.

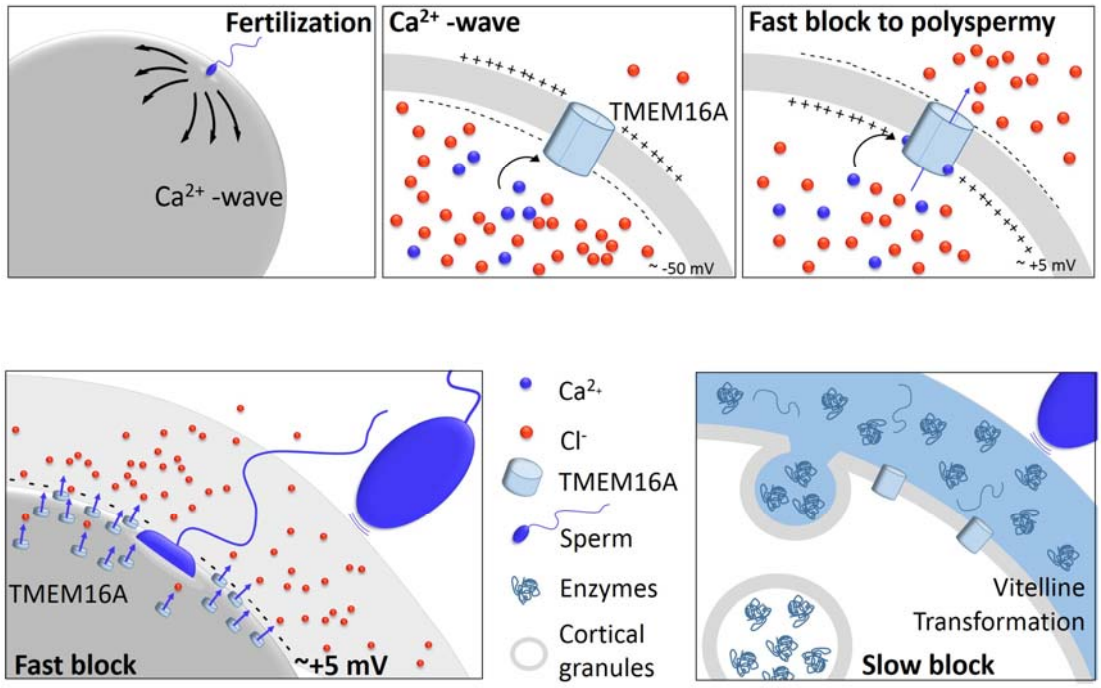

Figure 7 Block to polyspermy in *Xenopus laevis* oocytes after fertilization

The role of TMEM16A for the fast block to polyspermy after fertilization of *Xenopus laevis* oocytes is illustrated. Immediately after sperm entry, a Ca^{2+} wave is triggered within the egg. This sudden increase in intracellular Ca^{2+} has multifold effects. In response to Ca^{2+} TMEM16A is activated leading to a chloride efflux and the establishment of a membrane potential that is slightly positive. This positive membrane potential is thought to provide an electrical barrier that prevents the egg to fuse with more sperm cells. This membrane block is maintained for 15 min until the slow block to polyspermy is initiated by the fusion of cortical granules to physically change the vitelline layer on the surface of the egg.

For normal development and maintaining the ploidy, polyspermy must be efficiently prevented. At fertilization a Ca^{2+} wave in the cytoplasm simultaneously induces several Ca^{2+} dependent signaling events and cascades, generally referred to as egg activation [206, 207]. The Ca^{2+} signal can be measured over several minutes. Two major mechanism to block polyspermy are known. In many species elevated Ca^{2+} levels causes the fusion of cortical granules with the plasma membrane to reach the vitelline layer of the egg. The vitelline layer undergoes dramatic changes after fertilization. The cortical granules are filled with enzymes that modify the vitelline layer to prevent further sperm penetration. This mechanism is known as the slow block to polyspermy. In *Xenopus laevis* oocytes, but also other eggs, an additional 'fast' block to polyspermy exists, which happens prior to the cortical granule exocytosis. Within a few seconds after insemination the membrane is depolarized in a Ca^{2+} dependent manner to slightly positive values to establish an electrical block by largely unknown mechanisms [208]. This electrical block abolishes any further sperm entry [208, 209]. By addition of Ca^{2+} ionophores to eggs, it was shown that this electrical block can be reproduced and fertilization was suppressed [209]. Furthermore, it was demonstrated that fertilization is accompanied by a transient Ca^{2+} dependent chloride current [210]. It

was observed that with increasing extracellular Cl- concentration more eggs resulted to be polysperm. This effect was even more pronounced upon application of extracellular I- or Br- [209]. It was then shown that the membrane depolarization in the electrical block was established by Ca^{2+}- activated chloride channels [211-213]. Finally, TMEM16A was demonstrated to elicit currents resembling the endogenous *Xenopus* oocyte CaCC currents in voltage-dependence, anion selectivity and susceptibility to typical chloride channel inhibitors [5, 6]. Figure 7 illustrates the events occurring during the fast and the slow block to polyspermy in *Xenopus laevis* oocytes.

1.11. TMEM16 proteins in *Drosophila melanogaster*

Subdued is a *Drosophila melanogaster* TMEM16 protein that, similarly as TMEM16A and B, mediates Ca^{2+}-activated chloride currents [3, 214], is abundantly expressed. Subdued$^{-/-}$ knock-out flies are more sensitive to gut infections after ingestion of the bacteria *Serratia marcescens* and die significantly earlier [214]. Subdued was thus proposed to play a role in host defence. However, such a sensitivity phenotype might be attributed to defects in the gut epithelium or associated tissue during development [215, 216], which could be a side effect of the knock-out. The expression of the *Drosophila melanogaster* TMEM16 homologue Axs (aberrant X segregation), which is closest to TMEM16K, that in human plays a role in ataxia disorder, is needed for normal spindle assembly and cell cycle progression [217-219]. Axs was the first TMEM16 member to be described.

1.12. Fungal TMEM16 proteins

1.12.1. A TMEM16 protein of *Saccharomyces cerevisiae*

In *Saccharomyces cerevisiae* specific membranes of the endoplasmic reticulum (ER) associate with the plasma membrane (PM). These areas, termed cortical ER, are found at a distance of 33 nm from the plasma membrane [220, 221] and they establish micro-compartments that are devoid of ribosomes [221]. When membranes of two compartments come close enough together, membrane junctions can form as sites for ER-PM communication, lipid or Ca^{2+} transfer and intracellular signaling [222, 223]. In fungi, generally only one or two TMEM16 homologues are found. Unlike other TMEM16 proteins from fungal species, the *Saccharomyces cerevisiae* homologue, Ist2, plays a central role in the recruitment of endoplasmic reticulum compartments to the plasma membrane [224]. As illustrated in Figure 8, the targeting of Ist2 to the PM associated cortical ER requires the interaction with phosphatidylinositol-4,5-bisphosphate ($PI(4,5)P_2$) [225]. A cortical sorting signal at the very long and unstructured carboxy terminus consisted of a cluster of basic and a patch of hydrophobic amino acids allows the recognition of $PI(4,5)P_2$ at the cytosolic side of the plasma membrane [225-228], thereby determining the distance between the membranes of the compartment tether [224]. This distance of 33 nm in turn accounts for the inaccessibility of the ER-PM junction to the ribosomes [224]. Ist2 is further required for the recruitment of a protein (Sac1 phosphatase) to the cortical ER that regulates the amount of

phosphatidylinositol-4-phosphate (PI4P) at the cytosolic side of the PM. Thus the formation of the ER-PM tether by Ist2 is obligatory for proper PI4P signaling [229]. To date, no scrambling of lipids by Ist2 has been shown in cells, and even with purified and reconstituted protein no such activity could be observed [170].

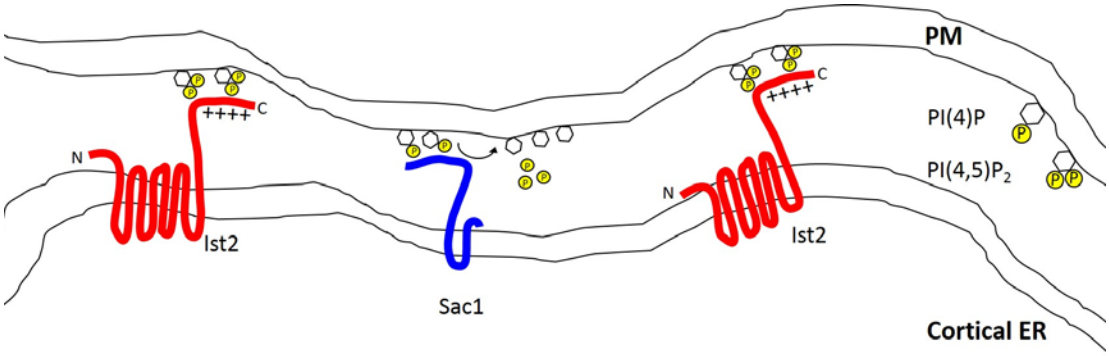

Figure 8 ER- PM tether by Ist2 in *Saccharomyces cerevisiae*

Ist2 mediated tether of the cortical ER to the PM. The tether is enabled trough recognition of $PI(4,5)P_2$ by a stretch of hydrophobic and positively charged residues located on the long, unstructured C- terminus of Ist2 TMEM16 protein. The space between cortical ER and PM is too small for ribosomes of the ER to access. The tether is required to recruit Sac1, a phosphatase that regulates the amount of PI(4)P at the PM.

1.12.2. A TMEM16 protein of *Aspergillus fumigatus*

Recently, the function of a TMEM16 family member of the fungus *Aspergillus fumigatus* (afTMEM16), that shares 25 % of the sequence with TMEM16F, was investigated. For this purpose the protein was obtained from recombinant sources, purified and reconstituted into liposomes. Since for some other members of the TMEM16 family a function as a channel was discussed, afTMEM16 was thus investigated for its role in ion conduction using planar lipid bilayer experiments and vesicular flux assays. For the flux assay, liposomes were loaded with high salt concentrations on their inside. A chloride sensitive electrode was used to monitor chloride efflux to the low chloride containing outside. Thus any chloride change is recorded upon initiation of ion transport. The results from the measurements in both systems indicated that afTMEM16 forms a channel with low ion selectivity that can be activated by Ca^{2+} [170]. Moreover, a Ca^{2+} dependent scramblase activity of the isolated and reconstituted protein was also confirmed [170]. Substrates that were tested for scrambling included the phospholipid derivatives NBD-PS, NBD-PE, NBD-PC and NBD-glucosylceramide, that all contained a fluorescent group for detection. Importantly, in this work both, the ion conductance and scramblase activity of a TMEM16 family member, were thus confirmed for the first time in a non-cellular system using purified and reconstituted afTMEM16. Furthermore, the fungal homologue was sufficient, and no down-stream effectors were needed to promote lipid scrambling. Thus, the direct involvement of afTMEM16 in lipid scrambling was demonstrated. However, the physiological function of afTMEM16 in its host, *Aspergillus fumigatus*, was not investigated and therefore remains elusive.

1.13. Summary

In mammals TMEM16 proteins constitute a family of ten proteins that appear to be relevant for a broad range of physiological processes. Proper functioning of TMEM16 proteins is required during development, for salivation, coordination, blood hemostasis and appropriate response to vascular injury. Malfunction or the lack of TMEM16 proteins is further linked to diseases of the muscle and skeletal apparatus. A role in the formation of cancer is discussed. Interestingly, the TMEM16 family contains members that were associated with phospholipid scrambling and phosphatidylserine signaling, whereas two other family members were unambiguously identified as subunits of the CaCCs investigated for more than 30 years. Although it appears that the family comprises proteins that, from a functional point of view, are not throughout related, they nevertheless share a high sequence identity of 25– 65%. A close structural and architectural relationship between the different family members can therefore be assumed [15, 167, 176, 230].

1.14. Aim of my thesis

The currents mediated by Ca^{2+}-activated chloride channels (CaCC) were investigated for decades by electrophysiological methods using *Xenopus laevis* oocytes and cells form other tissues, but the molecular identity of the responsible protein remained obscure for a long time. In 2008, three groups independently proposed that the ion conduction properties of CaCCs resembled currents obtained for the protein TMEM16A, when expressed in CaCC- free expression systems. Henceforward, in addition to electrophysiological studies, the knowledge about the molecular identity of CaCC allowed the manipulation and biochemical characterization of TMEM16 proteins. Shortly after that discovery, I started my PhD working with members of this protein family in 2010. At that time, only little data on the structural properties of the TMEM16 family was available, e.g. the localization of the termini was reported to be intracellular and a topology was proposed on the basis of sequence analysis and biochemical investigations including epitope accessibility studies. Clearly, the availability of detailed structural information would help to reveal the mechanism of ion transport and its mode of Ca^{2+} activation. Thus, I aimed for the determination of the first high-resolution crystal structure of a TMEM16 family member. In the course of my PhD, a family member, TMEM16F, was associated with a role in phosphatidylserine scrambling, which was shown to be required for efficient blood coagulation after injury. To assess and understand the role of TMEM16 family members in phospholipid scrambling, I have established a cell- free, liposome- based assay. With the structure determination of a fungal TMEM16 protein I have succeeded in revealing a novel protein architecture that is presumably general for this family. Since the investigated protein facilitates the translocation of lipids, my work has also provided the first mechanistic insight into this important class of lipid transport proteins.

2. Results

2.1. Sequence analysis

In mammals the TMEM16 family consists of ten members classified as TMEM16A to K. In order to identify genes of TMEM16 family members from a wide range of organisms, murine TMEM16A (mTMEM16A), a family member that was already functionally characterized as a Ca^{2+}- activated chloride channel, was initially used as query in a Blast search. By this attempt all available and annotated genomes were searched with the Blastp method using translated nucleotide sequences by applying default settings (see Methods for details). This first Blast search has identified a large number of genes, distributed among all eukaryotic branches of life. From this list a subset was selected for closer investigation. This first selection was broad and included genes from vertebrates and fungi likewise. After biochemical characterization of this first set of homologues further Blast searches (a total of 6) were performed using the sequences of homologues that showed advantageous biochemical properties from previous rounds of selections as queries. These novel searches predominantly focused on fungal homologues. The second and third Blast search was performed with the sequence of a family member from *Schizosaccharomyces pombe* (spoTMEM16). The fourth round has focused on members from thermostable organisms, but their biochemical properties turned out to be unsuitable. For the fifth selection the sequence of a member from *Pichia pastoris* (ppaTMEM16) was used and the sixth round of selection was carried out against the sequence of a homologue from *Giberella zeae* (gzeTMEM16) to finally identify nhTMEM16 of the fungus *Nectria haematococca,* from which the structure could be determined.

ID	species	origine	short name	NCBI accession o	length (aa)	identity %	identity %	homology %
1	*Acyrthosiphon pisum*	insect	apiTMEM16	XP_001944325	892	39.8		
2	*Ajelomyces capsulatus*	fungi	acaTMEM16	XM_001537152.1	743	25.1		
3	*Arthroderma benhamiae*	fungi	abeTMEM16	XM_003015597	784	24.4		
4	*Arthroderma otae*	fungi	aotTMEM16	XP_002849760.1	745	26.1		
5	*Aspergillus clavatus*	fungi	acl1TMEM16	XP_001274896.1	725	23.1		
6	*Aspergillus clavatus*	fungi	acl2TMEM16	XP_001274970.1	738	25.7		
7	*Aspergillus flavus*	fungi	afl1TMEM16	B8N5V7	823	27.4		
8	*Aspergillus flavus*	fungi	afl2TMEM16	XP_002377441.1	763	24.1		
9	*Aspergillus fumigatus*	fungi	afu1TMEM16	XP_746520.1	729	22.1	25	50
10	*Aspergillus fumigatus*	fungi	afu2TMEM16	XP_746483.1	735	26.6	29.9	49
11	*Ashbya gossypii*	fungi	agoTMEM16	Q75B72	926	23.3		
12	*Aspergillus nidulans*	fungi	aniTMEM16	CBF78946.1	715	24.7		
13	*Aspergillus niger*	fungi	anig1TMEM16	XP_001400927.1	734	27.1		
14	*Aspergillus niger*	fungi	anig2TMEM16	XM_001400785	734	22.2		
15	*Arabidopsis thaliana*	plant	athTMEM16	NP_177445.2	665	27.4		
16	*Aspergillus terreus*	fungi	ate1TMEM16	XP_001213993.1	741	25.5		
17	*Aspergillus terreus*	fungi	ate2TMEM16	XP_001211316.1	728	23.1		
18	*Bortryotinia fuckeliana*	fungi	bfuTMEM16	CCD55619.1	739	29.5		
19	*Bos taurus*	mammalian	btaTMEM16A	NP001179646.1	985	92.3	96.2	99
20	*Caenorhabditis elegans*	nematode	celTMEM16	?	1049	27.7		

Table 1 TMEM16 genes that were investigated in this work (part A)

The table summarizes basic characteristics of the genes encoding TMEM16 proteins and provides information about the species origin, which is reflected in a short name identifier (i.e. the gene from *Nectria haematococca* TMEM16 is named nhTMEM16). Either the NCBI accession number of the gene or protein (yellow) or the UniProt code (green) is specified leading to the sequence of the gene. The sequence length of each homologue is indicated as well, as number of amino acids (aa). The sequence identity between mTMEM16A and the respective homologues is noted (derived from Clustal Omega [231]). Additionally, the percentage of identical and similar residues in the transmembrane part between mTMEM16A and selected TMEM16 family members is shown.

21	*Candida albicans*	fungi	calTMEM16	XP_711758.1	952	23.4		
22	*Candida glabrata*	fungi	cglTMEM16	Q6FUD4	929	22.9		
23	*Chaetomium thermophilum*	fungi	cthTMEM16	G0S5G1	743	24.5		
24	*Ciona intestinalis*	ascidiae	cinTMEM16G	?	962	36.3		
25	*Coccidioides immitis*	fungi	cimTMEM16	XP_001241728.1	771	25.1		
26	*Cordiceps militaris*	fungi	cmiTMEM16	EGX94757.1	751	23.6		
27	*Danio rerio*	fish (Osteichthyes)	dreTMEM16A	NP_001155062.1	925	64	72.1	88
28	*Danio rerio*	fish (Osteichthyes)	dreTMEM16G	XP_684890.3	790	39.1	43.3	66
29	*Drosophila melanogaster*	insect	dmeTMEM16	Q9VDV4	1075	40.6		
30	*Equus caballus*	mammalian	ecaTMEM16A	XP_001493686.2	845	93.4	96.2	99
31	*Exophiala dermatitis*	fungi	edeTMEM16	EHY59986.1	739	24.1	25.5	45
32	*Fusarium oxysporum*	fungi	foxTMEM16	EGU84773.1	732	25.2		
33	*Gallus gallus*	bird	ggaTMEM16A	XP_421072.2	955	85.12	90.6	97
34	*Glomerella graminicola*	fungi	ggrTMEM16	EFQ27658.1	732	24.5		
35	*Giberella zeae*	fungi	gzeTMEM16	XP_389929.1	737	24.7	26.1	51
36	*Homo sapiens*	mammalian	hsaTMEM16Aa,ac,abc,acd,abcd	Q5XXA6	956,960,982,986,1008	92.1(a)	96.4	98
37	*Homo sapiens*	mammalian	hsaTMEMD	Q32M45	955	43.8	49.3	71
38	*Homo sapiens*	mammalian	hsaTMEMF	Q4KMQ2	910	39.7	44.2	67
39	*Homo sapiens*	mammalian	hsaTMEMJ	A1A5B4	782	34.3	39.4	64
40	*Homo sapiens*	mammalian	hsaTMEMK	Q9NW15	660			
41	*Kluyveromyces lactis*	fungi	klaTMEM16	Q6CVG2	857	20.6		
42	*Lachancea thermotolerans*	fungi	lthTMEM16	C5DIR7	890	22.5		
43	*Leptosphaeria maculans*	fungi	lmaTMEM16	CBX99755.1	646	23		
44	*Magnaporthae oryzae*	fungi	morTMEM16	XP_003714771.1	825	22.8		
45	*Metharhizium acridum*	fungi	macTMEM16	EFY92738.1	665	25.1		
46	*Mus musculus*	mammalian	mTMEM16A	Q8BHY3	960	100		
47	*Mus musculus*	mammalian	mTMEM16B	Q8CFW1	1002	59.1	71.4	88
48	*Mus musculus*	mammalian	mTMEM16G	Q14AT5	859	39.3	44.8	67
49	*Mus musculus*	mammalian	mTMEM16K					
50	*Nectria haematococca*	fungi	nhTMEM16	XM003045982.1	735	24.8	27	50
51	*Neurospora crassa*	fungi	ncaTMEM16	Q7S8J4	738	27.2		
52	*Neosartorya fischerii*	fungi	nfiTMEM16	XP_001262513.1	735	26.4		
53	*Paracoccidioides brasiliens*	fungi	pbrTMEM16	EEH43886.1	760	25.7		
54	*Penicillium chrysogenum*	fungi	pchTMEM16	XP_002558196.1	736	26.7		
55	*Penicillium marneffei*	fungi	pmaTMEM16	B6QU56	730	24.3		
56	*Phaeodactylum tricornutum*	protista	ptrTMEM16	B7G411	731	23.4		
57	*Physcomitrella patens*	plant	phpaTMEM16	A9RCS9	627	26.2		
58	*Phytophthora infestans*	fungi	pinTMEM16	D0MXY8	765	24.1		
59	*Pichia pastoris*	fungi	ppaTMEM16	XP_002491412.1	888	20.4	21.6	43
60	*Pyrenophora teres*	fungi	pteTMEM16	XM_003305265.1	721	24.12		
61	*Saccharomyces cerevisiae*	fungi	sceTMEM16	P38250	946	23		
62	*Scheffersomyces stipitis*	fungi	sstTMEM16	A3LWT2	887	20.7		
63	*Schizosaccharomyces pombe*	fungi	spoTMEM16	O13621	668	22.5		
64	*Sclerotinia sclerotiorum*	fungi	ssclTMEM16	XM_001585956.1	750	23.5		
65	*Sorghum bicolor*	plant	sbiTMEM16	SB03G032470	657	29.1		
66	*Sporotrychum thermophile*	fungi	sth1TMEM16	G2Q4S1	731	25.5		
67	*Sporotrychum thermophile*	fungi	sth2TMEM16	G2QG98	718	24.3		
68	*Sus scrofa*	mammalian	sscTMEM16A	?	885	82.1		
69	*Taeniopygia guttata*	bird	tguTMEM16A	H0Z4V6	952	86.1	91.7	97
70	*Talaromyces stipitatus*	fungi	tstTMEM16	B8MP59	730	25.1		
71	*Tetrahymena thermophila*	protista	tthTMEM16	TTHERM_0010718	847	22.2		
72	*Thalassiosira pseudonana*	protista	tpsTMEM16	XP_002291773.1	724	24.4		
73	*Trichoderma virens*	fungi	tviTMEM16	EHK43266.1	720	23.5		
74	*Uncinocarpus reesii*	fungi	ureTMEM16	C4JI53	733	25.9		
75	*Ustilago maydis*	fungi	umaTMEM16	Q4P618	951	24.2		
76	*Verticillum albo-atrum*	fungi	valTMEM16	XM_003003988.1	741	24.6		
77	*Vitis vinifera*	plant	vviTMEM16	D7U040	951	26.4		
78	*Xenopus laevis*	amphibia	xlaTMEM16A	B5SVV6	979	77.1	87.1	95
79	*Xenopus laevis*	amphibia	xlaTMEM16E	Q6DDQ3	896	41.1	45.7	69

Table 2 TMEM16 genes that were investigated in this work (part B)

The table summarizes basic characteristics of the genes encoding TMEM16 proteins and provides information about the species origin, which is reflected in a short name identifier (i.e. the gene from *Nectria haematococca* TMEM16 is named nhTMEM16). Either the NCBI accession number of the gene or protein (yellow) or the UniProt code (green) is specified leading to the sequence of the gene. The sequence length of each homologue is indicated as well, as number of amino acids (aa). The sequence identity between mTMEM16A and the respective homologues is noted (derived from Clustal Omega [231]). Additionally, the percentage of identical and similar residues in the transmembrane part between mTMEM16A and selected TMEM16 family members is shown.

A list of all the TMEM16 homologues that were obtained for this work is depicted in Table 1 and Table 2. The table assembles a total of 80 genes from 6 rounds of selections. *In silic*o characterization of the homologues

The genes were selected by based on sequence analysis *in silico*. Sequences were compared with respect to their length and number of predicted transmembrane helices (identified by kyte-doolittle based hydropathy analysis). Sequence alignments and disorder predictions (DISOPRED, PSIPRED of the protein sequence analysis workbench) indicated presumably disordered regions and secondary structure predictions.

2.1.1. Sequence length and origin

Figure 9 gives an overview on the relation of sequence length in amino acids (aa) and species origin. The sequences vary between 650 and 1050 amino acids with shortest sequences for members originating from plants and fungi. Fungal TMEM16 proteins range between 650 and 750 amino acids with some exceptions (*i.e. Pichia pastoris: 888 aa, Saccharomyces cerevisiae: 946 aa, Ustilago maydis 951 aa*).

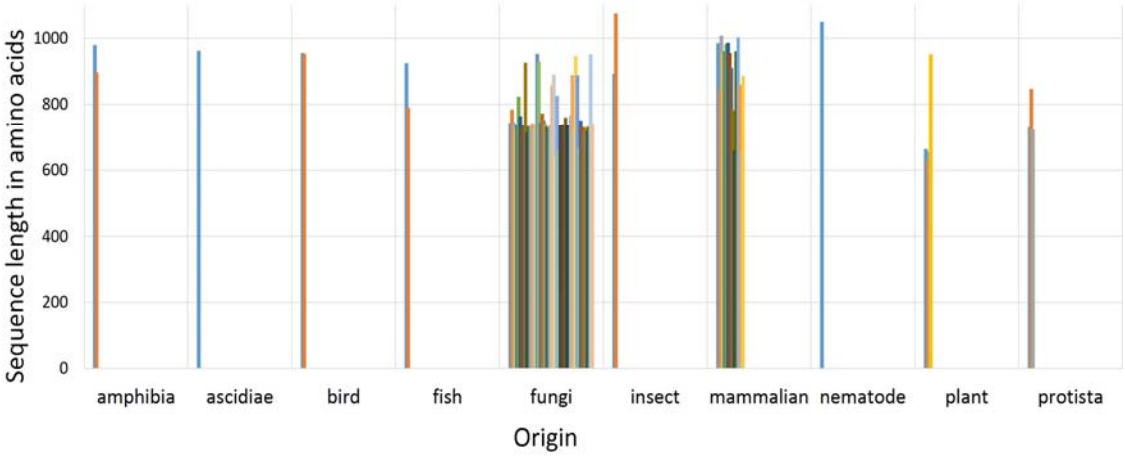

Figure 9 Origin and sequence length of the TMEM16 homologues

Chart describing the relation between the origin of the genes and sequence length of the TMEM16 family members used in this work. The origin of the genes arranged into different systematic groups is listed on the x axis, while the y axis contains information about the protein sequence length specified as amino acids.

Longer sequences around 900 to 1,000 amino acids frequently occur in mammalian TMEM16 proteins (except shorter TMEM16H and K containing 782 and 660 aa in human, respectively) but also in other species of phyla like amphibia, nematodes, birds, fish or insects. With 50 genes, the fungal homologues represent by far the majority of the genes included in this study, followed by 16 mammalian candidates, 3 genes from protists and plants, 2 from fish, birds, insects and amphibia and 1 representative from nematodes and ascidiae.

2.1.2. Relationship of mTMEM16A to other family members

Among the mouse proteins mTMEM16A is closest to mTMEM16B with an overall sequence identity of 59%. Within different species, mTMEM16A shares 66% overall sequence identity with *Danio rerio* TMEM16A (dreTMEM16A), 77% with *Xenopus laevis* TMEM16A (xlaTMEM16A) and 86% with *Taeniopygia guttata* TMEM16A (tguTMEM16A). These numbers imply that the relationship between equivalent TMEM16 proteins (i.e. xlaTMEM16A and mTMEM16A) is closer between different species than the relationship of TMEM16 family members of the same species (mTMEM16A-K) (Figure 10).

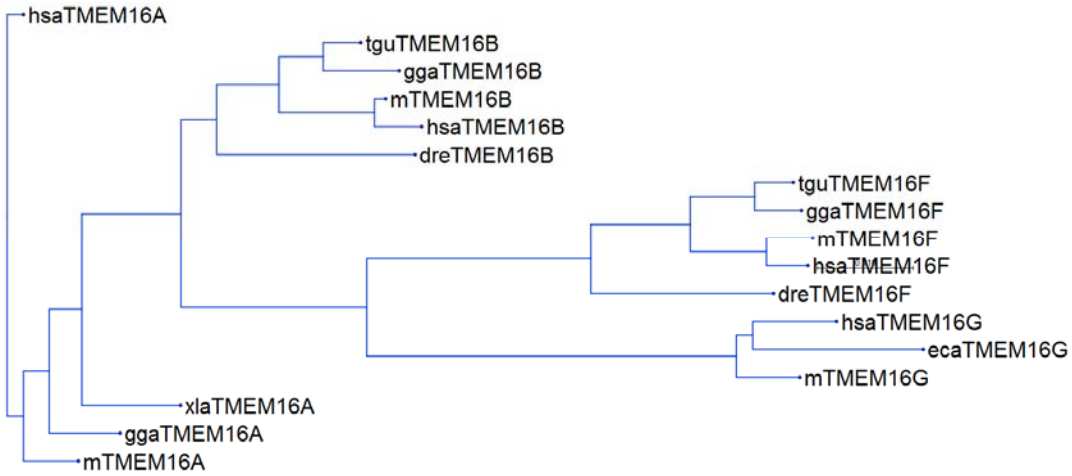

Figure 10 Relationship between selected TMEM16 members from vertebrates

The relationship of TMEM16A, B, F and G of TMEM16 proteins from vertebrates is shown by a phylogenetic tree. TMEM16A proteins are closer related within different species than for example murine TMEM16A with murine TMEM16B. And a similar relationship is observed for TMEM16B, F and G and other TMEM16 proteins.

In general, for the fungal candidates, the overall sequence identity compared to mTMEM16A was found to be on average between 20-30%. nhTMEM16 shares 25% of the sequence with mTMEM16A, but within the transmembrane part 27% of the residues are found to be identical and 50% (calculated as: number of similar residues/total number of residues in nhTMEM16) are related by similarity. In general, the candidates from fungi share slightly more homology with mTMEM16H and K than with mTMEM16A (see Figure 11).

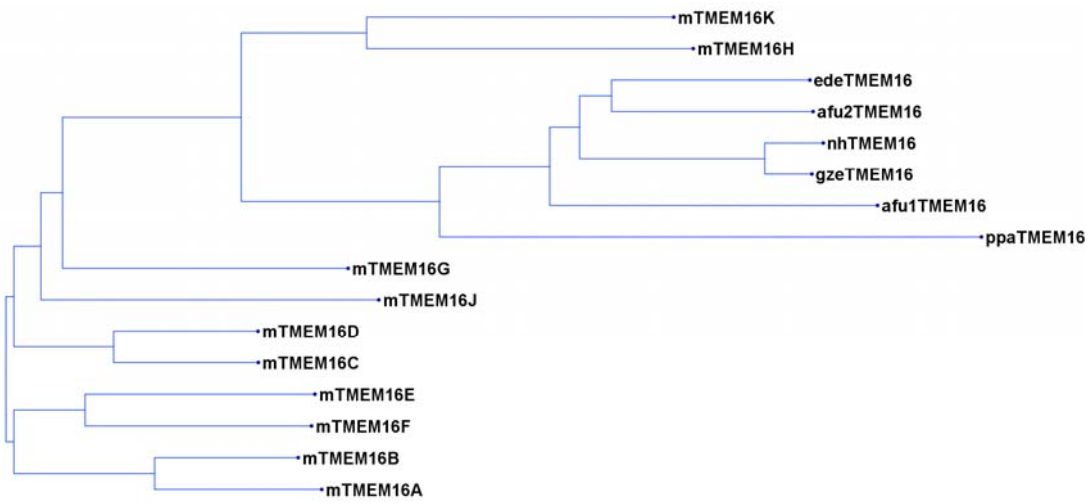

Figure 11 Relationship between fungal and murine TMEM16 proteins

The phylogenetic tree illustrates the relationship between fungal TMEM16 homologues and murine family members. mTMEM16H and K are rather distantly related to other murine TMEM16 proteins.

2.1.3. Sequence conservation in TMEM16 family members

2.1.3.1. Transmembrane part

Sequence alignments of various TMEM16 proteins have revealed that certain parts within the proteins are highly conserved. These parts largely coincide with the location of the eight transmembrane domains that were predicted by hydrophathy analysis using a kyte-doolittle based approach. The alignment depicted in Figure 12 illustrates the degree of conservation in the transmembrane part of selected murine TMEM16 proteins.

The sequence comparison underlines that, among different family members, the transmembrane part of the proteins shows the highest degree of conservation [230] and that the conservation in the amino- or carboxy termini between different TMEM16 proteins is weak. This characteristic is also found in other membrane protein families [232-234]. A high sequence conservation in certain regions of a membrane protein is often of functional relevance and underlies functional and structural conservation within the family [234]. The figure compares the location of the predicted with the actual transmembrane spanning helices observed in the nhTMEM16 structure. Whereas sequence based hydropathy plots predicted eight regions of increased hydrophobic character, presumably corresponding to the transmembrane spanning helices, it became obvious from the nhTMEM16 structure that the calculations of the boundaries failed to identify two additional transmembrane spanning entities. The actual transmembrane helix number 6 was not recognized at all by the software and helices α7 and α8 could not be discriminated as two separate helices.

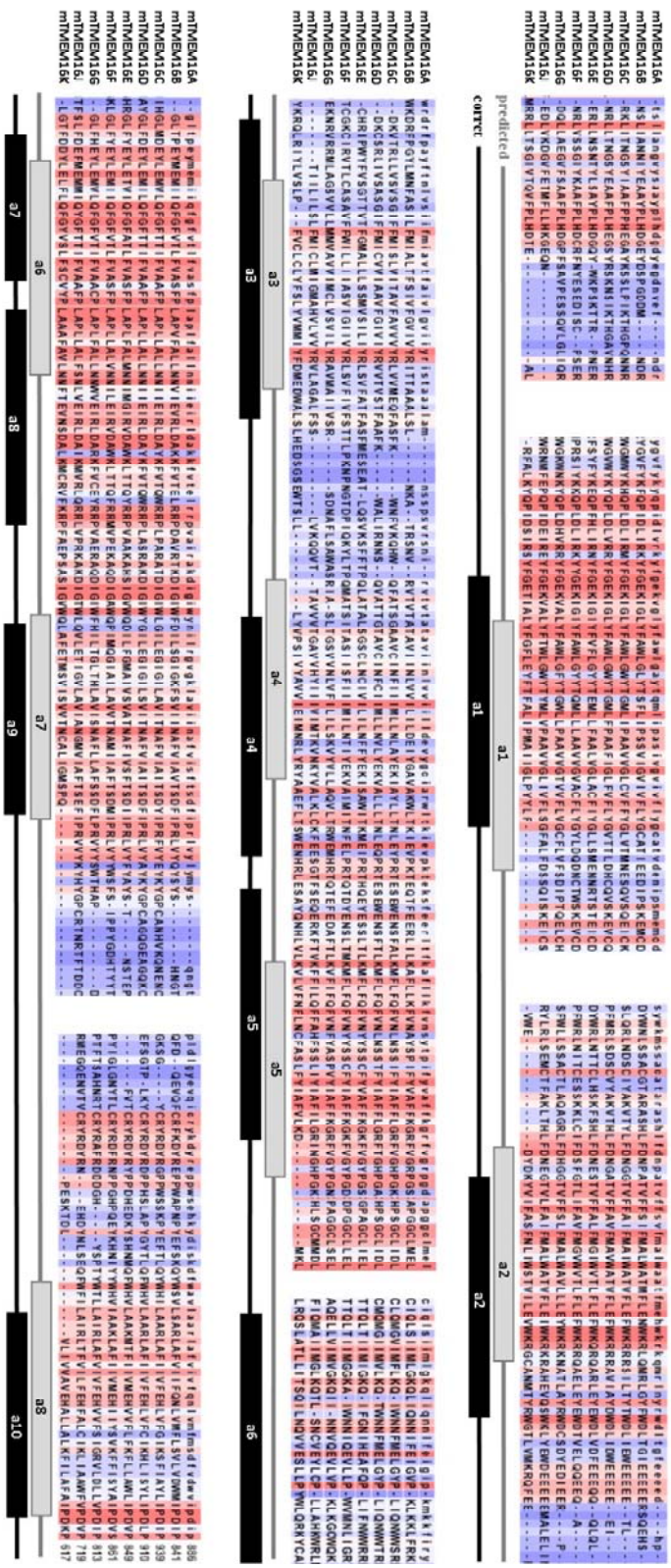

Figure 12 Sequence alignment of the TM part of murine TMEM16 proteins

The figure shows an alignment of murine TMEM16 homologues with the transmembrane spanning helices indicated as cylinders in grey (predicted) and black (structure based). The boundaries of the predicted transmembrane helices were obtained from a kyte-doolittle hydropathy plot. The sequence alignment highlights the degree of conservation between different TMEM16 members (red: identical, blue: not conserved) and reveals the regions of low and high relationship. While highly conserved parts of the proteins match the location of the transmembrane spanning helices, loop regions show a larger variability. Arrows indicate the position of the most homologous part of the N-terminus of TMEM16 family members, the sequences 'FPLHD' and 'FGEK'.

2.1.3.1. Amino- and carboxy terminus

While the carboxy terminus of TMEM16 family is comparably short with 50- 100 amino acids and is predicted to be unstructured, the amino termini underlie more variation in sequence length with N-terminal sequences ranging from 110- 370 amino acids and according to secondary structure prediction programs, it contains sections with alpha helices and beta strands.

Figure 13 Secondary structure elements in the N- terminus

Sequence alignment containing information about the location of predicted secondary structure elements (obtained from PSIPRED) and disordered regions (obtained from DISOPRED) in different TMEM16 family members compared to the secondary structure elements present in the structure of nhTMEM16. While predicted β- strands are displayed in yellow, expected alpha helices are colored grey. The longer insertions in mTMEM16A appear to be unstructured (red). The predicted location of α- helices and β- strands almost perfectly overlay with their actual position in the nhTMEM16 structure (black cylinders and black arrows). Vertical arrows indicate the position of two well conserved stretches, 'FPLHD' and 'FGEK' found in most TMEM16 homologues. A blue line indicates an alpha- helical element that was demonstrated to have a role in dimerization [179].

Although on the level of primary structure, the amino- termini are only weakly conserved, their secondary structure elements appear to be largely preserved. Figure 13 shows an alignment that compares

the predicted secondary structure elements in mTMEM16A containing a comparably long amino-terminus with the shorter N-termini of nhTMEM16 and edeTMEM16 from *Exophiala dermatitis*. Predicted alpha-helices and beta-strands are located at equivalent positions in N-termini of distantly related family members and these regions thus likely share a similar fold. Long insertions in mTMEM16A appear to be disordered. The location of predicted secondary elements in mTMEM16A almost perfectly match the observed positions in the nhTMEM16 structure.

On the level of primary structure, although generally weakly conserved, the amino- termini comprises two stretches of residues that appear to be characteristic for TMEM16 proteins as they are largely conserved from human to fungal homologues (Figure 14). These two sequences can be found at the end of the amino- terminus preceding the first transmembrane helix and consist in most cases of the amino acids 'FPLHD' and 'FGEK' or very similar sequences that are marked with an arrow (Figure 13 and Figure 14). Figure 14 displays the region of highest similarity found in the respective amino- termini and illustrates the large variability in size of the N-terminal region ranging from 110 to 370 amino acids. Comparably short amino termini are found in fungal TMEM16 homologues with few exceptions (i.e. umaTMEM16 from *Ustillago maydis*). As shown later, the structure of nhTMEM16 revealed that the transmembrane domain starts with two short α-helices that form a hairpin with amphiphilic properties. These alpha helices interact with the membrane on the cytosolic side and that contain the described conserved sequences 'FPLHD' and 'FGEK'.

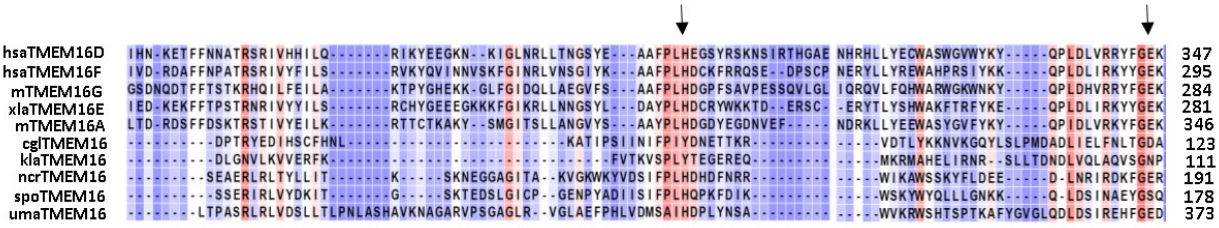

Figure 14 Sequence alignment of the N- termini of TMEM16 proteins

The last part of the N-terminus of selected TMEM16 family members of mammals and fungi is depicted. High sequence identity is marked in red and unrelated regions are colored in blue. Arrows indicate the position of the most homologous part of the N-terminus of TMEM16 family members, the sequences 'FPLHD' and 'FGEK'.

2.1.3.2. Loop regions

The length of selected sequences varies between 650 and 1050 amino acids with the shortest proteins originating from plants and fungi. The largest variation in sequence length between different family members is observed on their respective N- termini and in loop regions connecting the transmembrane spanning helices. The transmembrane part can be compact in cases where short loops connect the transmembrane spanning helices as found in many fungal homologues or larger with long loops between the transmembrane helices. Figure 15 shows an alignment of mTMEM16A, F and K in comparison with some fungal family members.

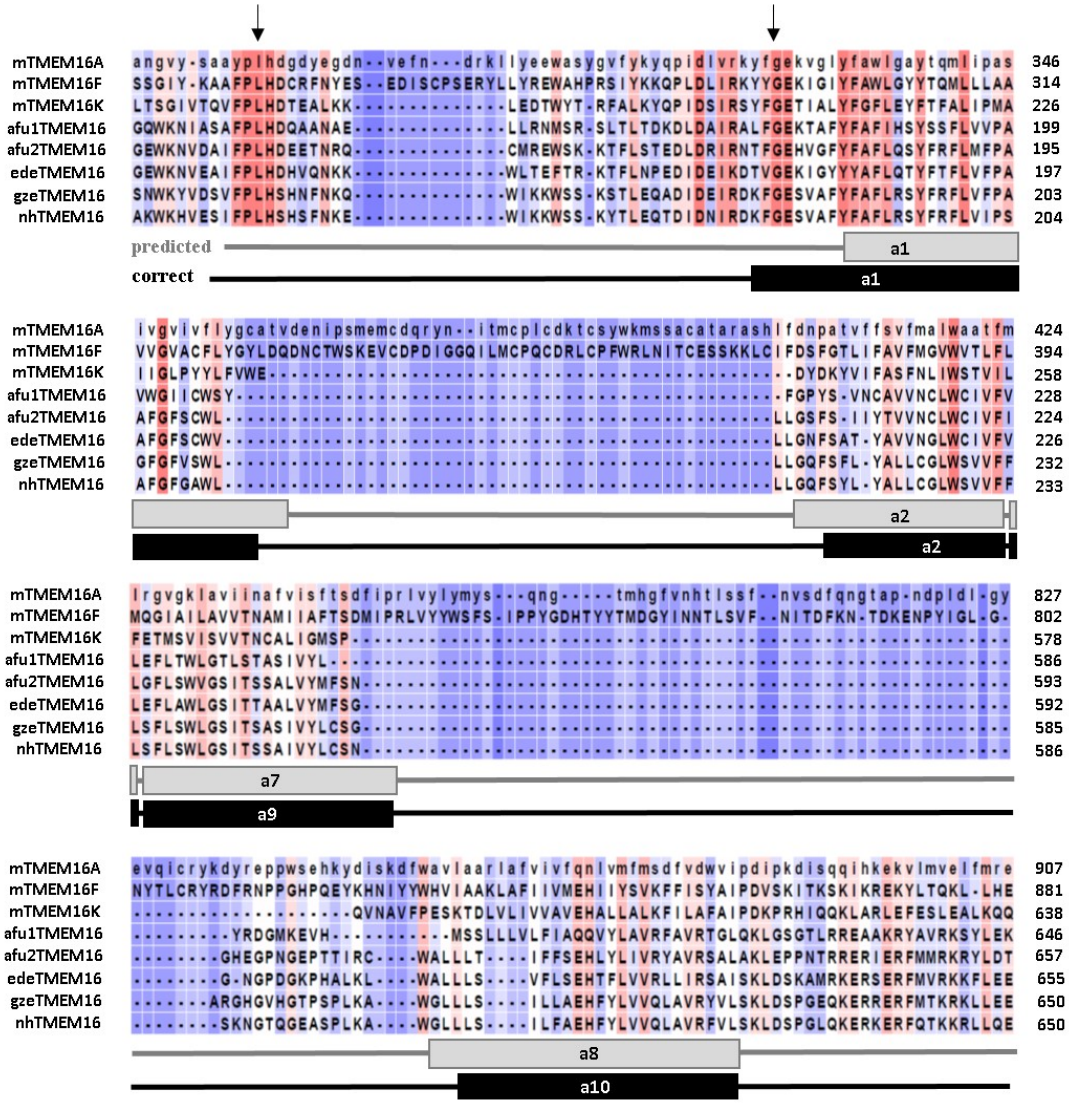

Figure 15 Sequence alignment of the loop regions of TMEM16 members

Alignment illustrating the variability in length of the loops connecting transmembrane helices α1 and α2 as well as α9 and α10 in the verified topology. These loops are considerably longer for most TMEM16 proteins in vertebrates and are suggested to be unstructured according to secondary structure and disorder predictions. In contrast to mammalian proteins, many of the homologues originating from fungi are distinguished by minimal loop lengths. Transmembrane spanning helices of the predicted and verified topology (grey and black) are shown as cylinders and numbered. The arrows indicate a homologous part at the amino terminus, 'FPLHD' and 'FGEK', that can be found in most TMEM16 family members from fungi to human.

The alignment illustrates that in some TMEM16 proteins the loops regions are long and poorly conserved, particularly in the loops connecting transmembrane helices α1 and α2 and transmembrane segments α9 and α10. According to secondary structure and disorder predictions it can be expected that these loop regions contain unstructured elements. It is generally assumed that long, presumably unstructured loops, are flexible and therefore potentially interfere with crystallization [235-238]. Moreover, long loops may be sensitive to contaminating proteases during expression and purification.

For structural investigation, TMEM16 proteins that adopt a more compact fold are therefore preferred over proteins that contain long loops.

2.1.4. Posttranslational modifications

It is likely that higher eukaryotic TMEM16 proteins are post- translational modified by glycosylation at multiple sites [11]. A glycosylation site that is conserved in TMEM16A-K is found on the last extracellular loop at amino acid 803 in mTMEM16A (isoform a) [176]. Interestingly, it appears that consistent with alignments and biochemical characterization no glycosylation sites are present in fungal homologues. As glycosylation is frequently found to be heterogenous and presumably interferes with crystallization. Therefore, he lack of this post-translation modification may be advantageous for the crystallization behavior of fungal TMEM16 proteins.

2.1.5. Selection criteria for TMEM16 candidates

The results of the Blast searches were analyzed based on the following criteria:

- Any protein longer than 1050 amino acids was rejected.
- Homologues that either appeared to be truncated at their respective termini or that lacked substantial part of the transmembrane domain were rejected.
- Preferably, sequences were included that appeared to be compact but not truncated. Selected genes should encode proteins that are complete but short, particularly in the loops regions.
- Sequences below a certain level of sequence identity (less than 20%) compared to mTMEM16A were not considered.
- Genes that did not include the two stretches 'FPLHD' and 'FGEK' or a similar sequence at their N-terminus were rejected.
- In addition, sequences of proteins that showed superior biochemical or crystallization properties (*i.e.* spoTMEM16, ppaTMEM16, gzeTMEM16) were used as a query for additional blast searches and close homologues were included in the screen.

Following these guidelines, predominantly fungal genes were selected. However, since the physiological role and function of the fungal homologues was unknown, close relatives of TMEM16A, the electrophysiologically well characterized Ca^{2+}- activated chloride channel, were included as well, despite their long and unstructured loops and termini. The selected candidates were subsequently characterized. They should exhibit appropriate biochemical properties such as adequate expression levels, proper folding and stability in detergent solution.

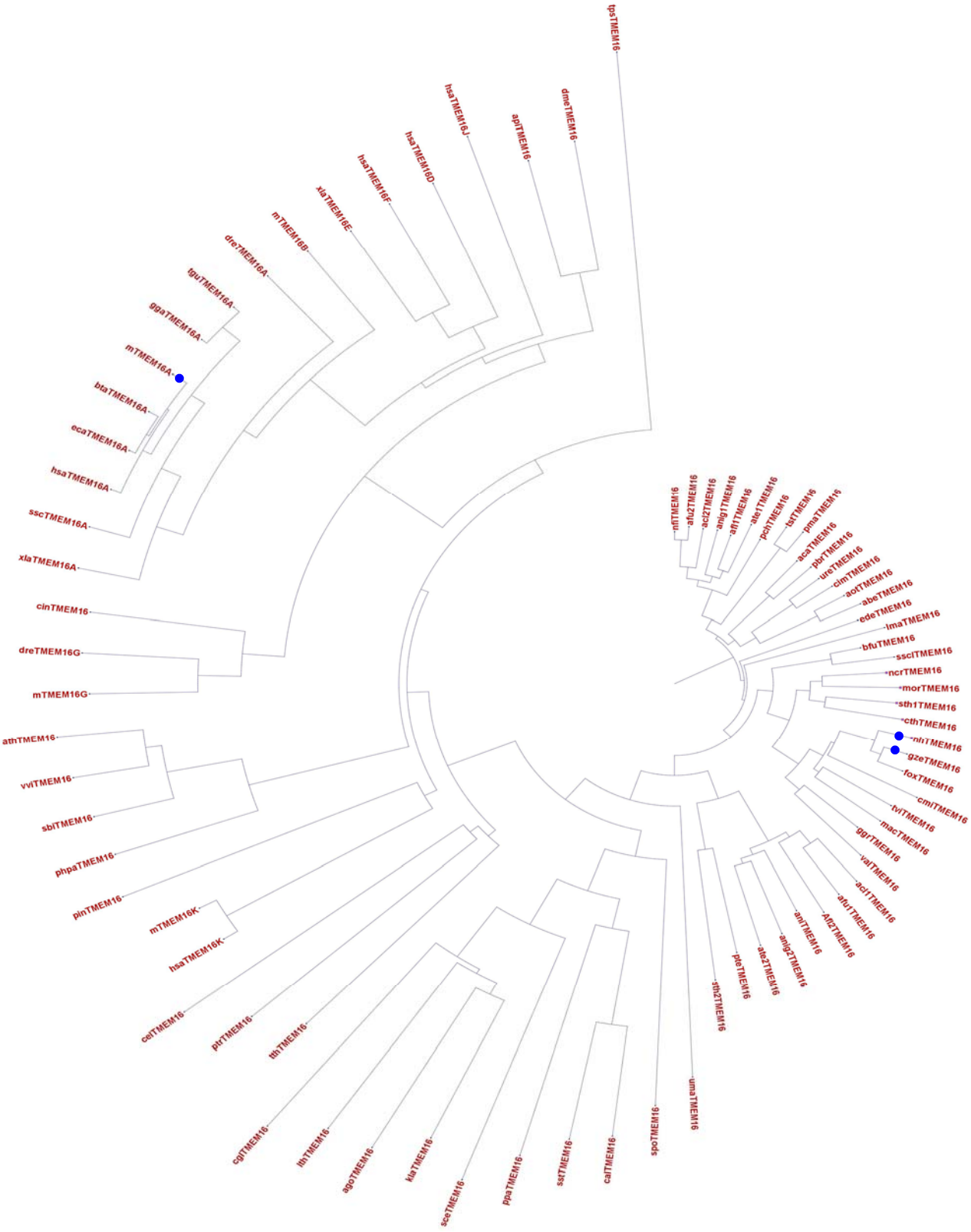

Figure 16 Circular phylogramm of all TMEM16 homologues used in this work

This tree illustrates the relationship between the TMEM16 family members investigated in this study. They derive from mammals, fish, amphibian, birds, fungi and protista. mTMEM16A, gzeTMEM16 and nhTMEM16 are indicated by blue dots. nhTMEM16 is closely related to gzeTMEM16, both proteins exhibited advantageous/favorable biochemical properties and were characterized in detail.

The broad initial screen of different candidates increased the likelihood to find suitable homologues that fulfill the biochemical criteria required in crystallography [238, 239]. In later stages of the project, TMEM16 proteins with desirable biochemical properties served as a query to identify closely related homologues with potentially similar characteristics. In summary, the pool of genes identified in the Blast searches was examined by alignments, secondary structure prediction and hydropathy analysis to select a total of 80 genes in six consecutive Blast searches that matched the relevant requirements on the DNA but also on the biochemical level (see Figure 16).

2.2. Cloning of the homologues

Genes that were available as cDNA clones were purchased from Imagene.com (now Source Bioscience) or Origene. Genes that did not contain any introns were cloned by Stephan Schenck from genomic DNA if the organism was available from DSMZ, the German Collection of Microorganisms and Cell Cultures (*Aspergillus nidulans, Kluyveromyces lactis, Lachancea thermotolerans, Neurospora crassa, Pichia pastoris*, *Saccharomyces cerevisiae*, *Schizosaccharomyces pombe* and *Ustilago maydis*). Any other genes were synthesized by GenScript without codon optimization. The genes were modified by PCR to carry 3' or 5' overhangs that contained a SapI cleavage site to allow sub-cloning into modified vectors for HEK, insect cell or *Saccharomyces cerevisiae* expression. The expression vectors were modified as described in the methods section and in [240].

2.3. Identifying stable TMEM16 proteins for structural characterization

2.3.1. A general perspective

It is often a difficult task to produce large quantities of recombinant membrane proteins for functional and structural studies, which is particularly challenging for eukaryotic membrane proteins [241, 242]. This difficulty is often overcome by searching for related bacterial homologues. Bacterial proteins lack post-translational modification, which usually allows their production in *E.coli* as host. Frequently, due to a smaller size, bacterial proteins seem to adopt a more compact fold, when compared to related eukaryotic proteins, and the connecting loops between the transmembrane helices tend to be shorter or less mobile, which facilitates crystallization [235, 238, 243, 244].

However, this approach was not possible in case of the TMEM16 family, that is only found in eukaryotic species [176, 245]. For structural studies with eukaryotic integral membrane proteins, the first difficulty to overcome concerns the amount of folded protein that can be produced [242, 246, 247]. Recombinant expression of eukaryotic integral membrane protein in bacteria often results in accumulation of improperly folded protein. This can be attributed to the inability of the bacterial system to carry out posttranslational modification such as the addition of sugar moieties or phosphorylation, for example [248]. In contrast to that, recombinant expression of eukaryotic membrane proteins in eukaryotic hosts

frequently leads to protein that retains activity and structural integrity. Since the production of well-folded protein in a functional state in milligram quantities is required for structural studies, it can be crucial to investigate different expression systems for recombinant expression to be able to choose the appropriate expression host [242, 249]. Therefore, the entire pool of selected genes was screened in HEK tsA201 cells, half of the genes in *Saccharomyces cerevisiae*, and for some selected TMEM16 members insect cell expression was investigated as well. One approach that proved to be helpful to find a promising homologue for structural studies is based on the screening of many proteins, commonly referred to as searching of crystallization space by cloning [236-238, 250]. Since it is difficult to predict the expression behavior of a particular protein, the initial screening of many different homologues makes the identification of potential candidate proteins more likely.

2.3.1. Fluorescence- based expression screening

The production of sufficient amounts of a particular membrane protein often requires the optimization of the expression conditions or improvement of the protein stability. A common approach in structural biology is to fuse the protein of interest to a fluorescence tag [251, 252]. This enables the continuous tracking of the fusion protein by quantifying the fluorescence and has several advantages over the conservative Western blotting technique, namely getting data rapidly and skipping the need to carry out time- consuming blots. The fluorescence can be monitored during expression to evaluate different strategies and optimize conditions to generate highest protein yields and quality. Moreover, the subcellular localization of the fusion protein can be monitored by microscopy in cellular systems that are large enough, as for example HEK cells. Protein extractability and solubility in detergent solution can be determined by a simple fluorescence measurement. To circumvent the need for protein purification at an early stage, the crude lysate can be subjected to a size exclusion column connected to a fluorescence detector to record the size exclusion profile of the fusion protein [253].

For these reasons, expression screening of full-length TMEM16 proteins was carried out with the use of fluorescent protein fusions. A fusion of the proteins to either venus yellow fluorescent protein (vYFP) for the constructs used in HEK expression or enhanced green fluorescent protein (EGFP) for yeast expression allowed tracking of the fluorescence in the screening procedure. The constructs used for HEK expression were additionally modified to include a Myc epitope for detection, an SBP purification tag and a 3C cleavage site for removal of the fusion tag after purification. The constructs employed for *Saccharomyces cerevisiae* expression contained a His_{10}- tag for purification and a 3C cleavage site to allow removal of the tags after purification. A scheme of the constructs used in HEK, insect cell and *Saccharomyces cerevisiae* expression is depicted in Figure 81.

In the following chapters, the results of the screening in HEK, insect and *Saccharomyces cerevisiae* cells is described which allowed the identification of promising constructs. A medium scale purification of promising homologues was subsequently carried out to estimate yields and stability. After that, the expression culture was scaled up for large scale to obtain sufficient material for first crystallization screens.

2.3.1.1. Screening in HEK cells

In recent years, human embryonal kidney (HEK) cells have attracted increasing attention as expression system for mammalian membrane proteins. These proteins often require a mammalian protein quality control system that is capable to carry out suitable glycosylation or the formation of disulfide bonds for proper protein maturation and folding [254, 255]. The choice of the expression host that is needed to produce a particular protein of interest, largely correlates with the complexity of the protein with respect to its folding process [256]. In this work, a substantial part of the proteins selected for overexpression are of mammalian origin and were reported to be modified by glycosylation [11, 176]. Thus, the entire pool of genes was screened in HEK tsA201 cells to determine their expression properties.

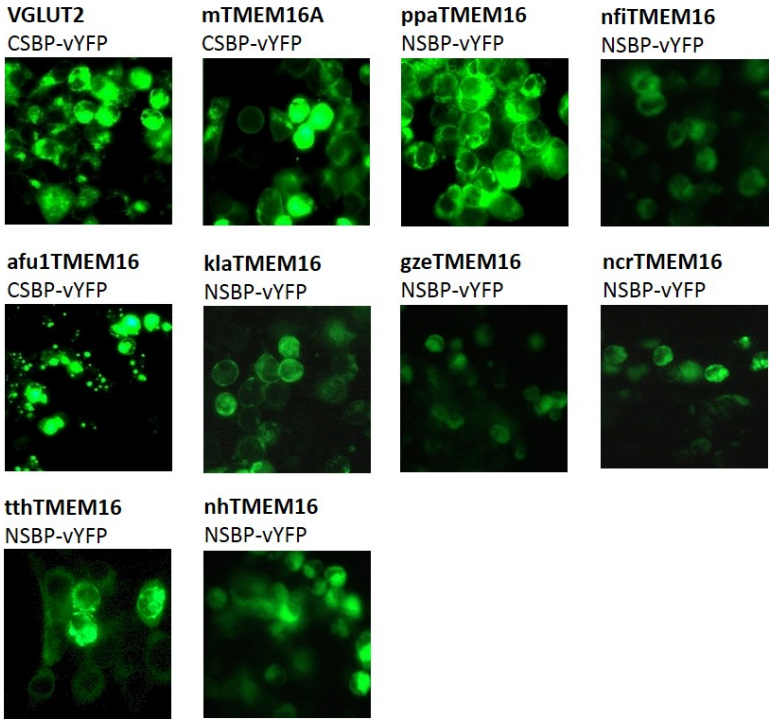

Figure 17 Compartment localization of TMEM16 family members in HEK cells

The expression level and the localization of TMEM16 proteins fused to vYFP was analyzed and a selection is depicted. As positive control vesicular glutamate transporter 2 from rat (VGLUT2 or VGluT2) was included in the screening process.

Since the expression screening of candidate proteins in HEK cells is facilitated by the use of vYFP [257] fusions in this work, a purification step after protein extraction was not required for the initial characterization. Moreover, transient transfection using the calcium phosphate precipitation method [258] in adherent HEK cell cultures allowed for a fast, reliable and high through-put screening. As one culture dish was usually sufficient per construct for an initial evaluation, many proteins could be screened in parallel.

Protein expression was under the control of the strong CMV promoter allowing for high expression levels of protein. 25- 40 h post transfection, the expression was usually complete. The expression pattern as well as the compartment targeting in whole cell HEK tsA201 was evaluated by fluorescence microscopy. Figure 17 illustrates the outcome for selected TMEM16 proteins fused to vYFP. It summarizes results obtained for selected constructs during the entire screening process. A strong variation of expression levels and protein distribution was observed for different TMEM16 family members. Only a few

constructs were targeted to the plasma membrane (i.e. ppaTMEM16, klaTMEM16, mTMEM16A), which makes them suitable candidates for electrophysiological characterization in HEK cells. Most other investigated TMEM16 vYFP fusion proteins target to different compartments and organelles in the interior of the cell. ppaTMEM16 targets mainly to the plasma membrane and is produced in comparably high yields. gzeTMEM16 and nhTMEM16 exhibit intermediate expression levels and vYFP- staining can be detected anywhere in the cell with diffuse expression pattern.

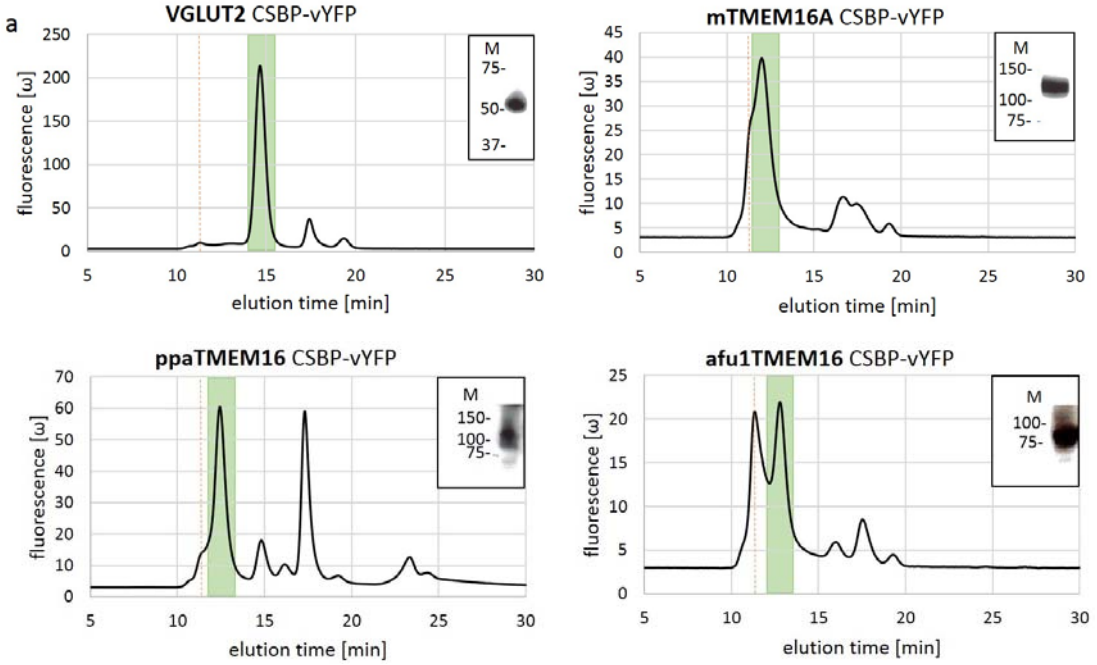

Figure 18 Expression screening (HEK cells) evaluated by FSEC (part a)

TMEM16 proteins fused to Venus-YFP were extracted from HEK cells and subsequently subjected to fluorescence size exclusion chromatography (FSEC). Samples were run on a G3000SWxl column. A peak at 12.5 min corresponds to stable and intact protein and is highlighted in green. The void volume corresponding to soluble aggregates is found at 11 min and is indicated as dashed line in red. The fluorescence was excited at 515 nm and measured at 530 nm. Positive controls, such as VGLUT2, were included. The cleared lysates were analyzed by Western blotting using a αMyc antibody.

Besides the cellular distribution, important parameters such as detergent stability and integrity of the protein were investigated. After extraction with the detergent n-Dodecyl-β-D-Maltopyranoside (DDMβ), the constructs were characterized with respect to their yield and homogeneity in detergent solution by subjecting the cleared detergent-solubilized extracts to fluorescent size exclusion chromatography. Figure 18 and Figure 19 show the elution profiles of a selection of candidate TMEM16 proteins that were obtained from HEK tsA201 cells. To confirm the homogeneity and molecular weight of the proteins a Western blot is displayed. Highest fluorescence levels could be measured for the positive control vesicular glutamate transporter 2 from rat (VGLUT2). Several peaks indicated the presence of multiple species originating from cleavage or degradation of the protein or expression of vYFP alone as observed in the case of ppaTMEM16. Furthermore, few homologues such as afu1TMEM16 or mTMEM16A showed a peak at the void volume of the column corresponding to aggregation besides the peak at the

expected elution time. Here, a selection of promising family members is shown, which had a peak at the expected elution time and were thus classified as proteins with potentially suitable properties. Screening was carried out as iterative process that involved 6 Blast searches and included novel proteins at different stages of the project. For this reason, various columns and screening protocols were applied, which makes it difficult to quantitatively compare fluorescence and absorption levels among the different constructs.

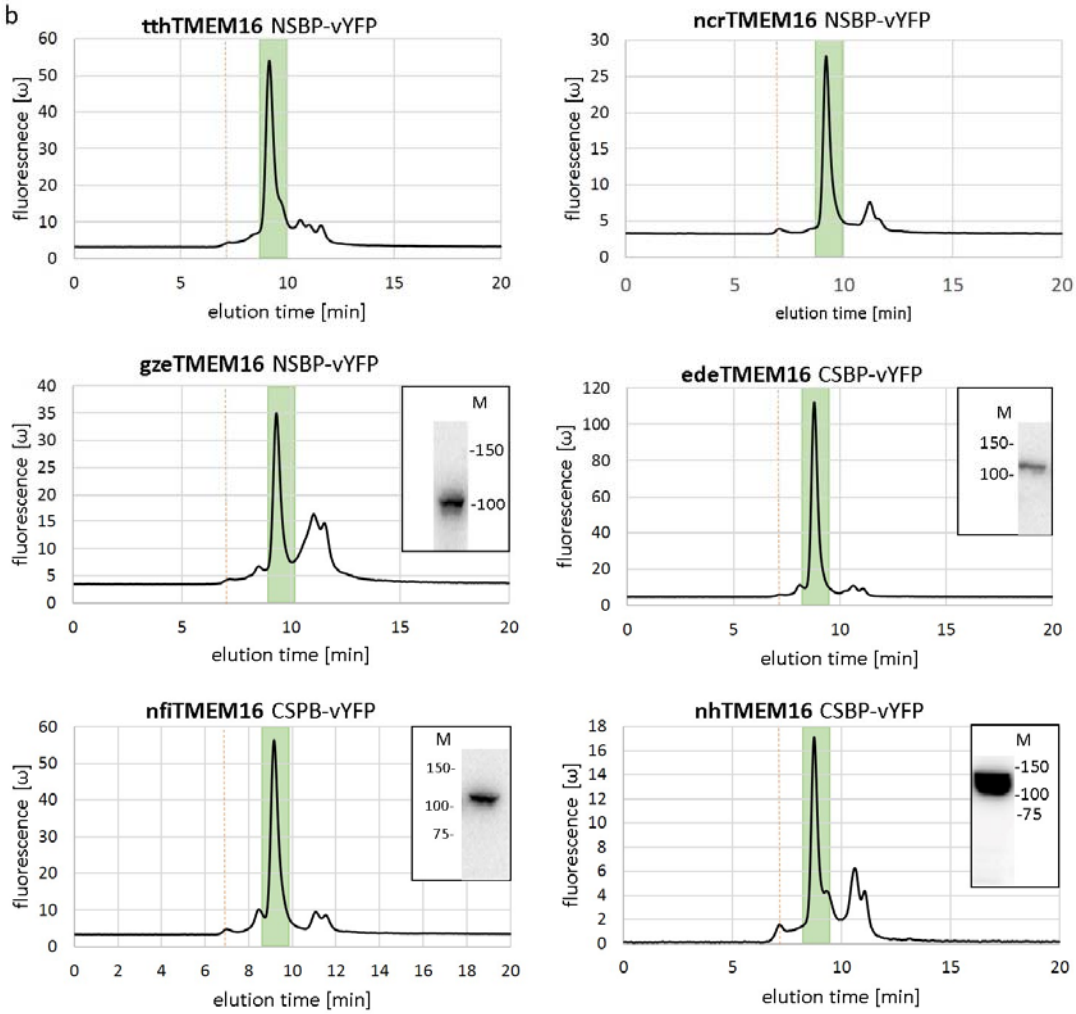

Figure 19 Expression screening (HEK cells) evaluated by FSEC (part b)

TMEM16 proteins fused to vYFP were extracted from HEK cells and subsequently injected to fluorescence size exclusion chromatography (FSEC) on a GF450 column. The peak at 9.5 min corresponding to intact protein is highlighted in green. The soluble aggregate at the void volume at 7 min is indicated by a dashed line in red. The fluorescence was excited at 515 nm and measured at 530 nm. The cleared lysates were analyzed by Western blotting using a αMyc antibody

TMEM16 proteins that were identified in the fluorescence-based screening to meet the requirements were first scaled up to medium scale before probing large scale expression. Increasing the expression volume is particularly laborious for transient HEK monolayer expression. Therefore, it was inevitable to be confident about the selection of the homologues before scaling up to large volumes. Hence, the

constructs were initially purified at a medium-scale of 100-200 dishes to evaluate the stability of the constructs and to exclude that the vYFP-tag caused the solubility of an otherwise instable protein. Thus, this medium scale purification served to ensure that the protein can be successfully purified. In later stages of the project, the fluorescence fusion proteins were only used to detect the compartment localization in intact cells, but not for screening. For screening, the proteins were affinity-purified in small scale from 1-5 dishes. The specificity of the SBP purification tag to its binding partner allowed for a one-step affinity purification that resulted in highly pure protein. The pure eluate was subsequently applied to size exclusion chromatography and detected by recording of its intrinsic fluorescence. The intrinsic fluorescence, mainly contributed by tryptophans but to some extent also by tyrosins and phenylalanines, was exploited to increase the sensitivity of detection compared to UV absorption during size exclusion chromatography. This approach made the medium scale purification unnecessary and allowed to estimate the stability of a protein during purification already in the small-scale purification step.

2.3.1.2. Screening of selected homologues in insect cells

An alternative expression system routinely used for recombinant expression of eukaryotic proteins is the baculovirus mediated insect cell expression system. This expression system gained considerable attention over the past years because it offers some advantages over the mammalian expression systems and for certain proteins it allows to obtain higher expression levels [259]. The baculovirus-mediated insect cell expression system exploits the ability of baculoviruses to infect mainly larval forms of moths such as *Spodoptera frugiperda*, of which isolated cells are used for insect cell expression in cell culture. The *Autographa californica* multiple nuclear polyhedrosis virus (AcMNPV) infection occurs following ingestion into the host stomach. Uncoating from the protecting and encapsulating polyhedrin matrix facilitates the release of the nucleocapsid and subsequent endocytosis of the virus into endosomes takes place. After escaping the endosomes nucleocapsids target to the nucleus to induce the viral replication and transcription. In the latest phase of infection, polyhedrin is produced in large amounts to occlude the new virus particles as a protection against the environment when they are released from lysed cells. Polyhedrin is the most common protein in AcMNPV, but under sterile conditions it is not required [260]. In the baculovirus mediated insect cell expression system the gene encoding polyhedrin, that normally occludes the virus in the protective matrix, is replaced by the gene of interest. Thus, the expression of the inserted gene is under control of the strong polyhedrin promoter. Neither the infection itself nor the replication depends on polyhedrin, therefore infected cells initiate virus production as well as overexpression of foreign proteins.

Despite allowing high recombinant protein yields using the insect cell expression system, a few drawbacks exist. First of all, the N-linked glycosylation is different in insect cells compared to mammalian cells and therefore it may be inadequate for some proteins [256]. This can negatively affect the functionality of the recombinant expressed glycoproteins [261]. A further drawback concerns the screening in insect cells, which is rather inefficient. Since the generation of virus is a time-consuming process, it is only advantageous if a particular construct doesn't need any further modifications. If a

construct requires to be optimized by truncations or removal of glycosylation sites to be more suitable for crystallization purposes, the screening for the optimal constructs would preferably be done in transient and adherent HEK cell cultures.

Selected homologues that were classified as hits from the HEK screening are potential targets for this expression system and were thus chosen to be tested in insect cells. The main reason to test insect cell expression was the limitation of HEK cells as an expression host to produce suitable amounts of TMEM16 protein needed for structural investigation. It was found that fungal TMEM16 proteins generally did not contain any glycosylation during HEK cell expression (data not shown), therefore these proteins were considered to be suitable targets for insect cell expression. The investigated proteins included ppaTMEM16, gzeTMEM16, nfiTMEM16, ncrTMEM16, afu1TMEM16 and tthTMEM16.

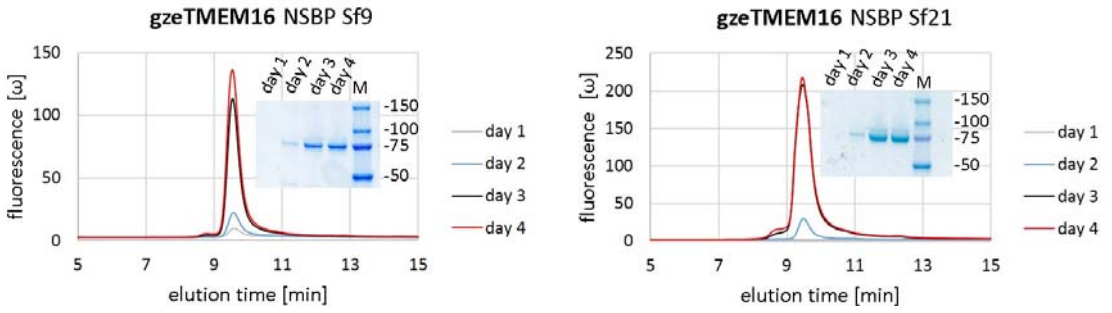

Figure 20 Small-scale purification of gzeTMEM16 expressed in insect cells

Fluorescent size exclusion profiles showing the increasing expression level of gzeTMEM16 purified in small scale from Sf9 and Sf21 cells at day 1 to 4. An increasing peak around 9.5 min from day 1 to 4 indicated the fraction of well-folded protein. The protein was run on a GF450 column and tryptophan fluorescence was recorded (excitation 280 nm, emission 310- 350 nm). The elution time of the void is around 7 min. The purity and quality of the protein was analyzed by SDS-PAGE.

The virus was generated as described in the Methods section and expression was carried out in Sf9 and Sf21 insect cells at suitable cell density for infection in suspension culture. Protein expression was controlled by the strong polyhedrin promoter. For each virus batch the best virus to insect cell ratio was determined in a number of small scale expressions. A fixed amount of cells was taken each day, and protein was affinity purified using the SBP tag and analyzed by fluorescent size exclusion chromatography. The expression of gzeTMEM16, for example, was maximal at day four as indicated by Figure 20. The average amount of gzeTMEM16 that could be produced was around 0.8 mg l^{-1} for Sf9 and approximately 2 mg l^{-1} for Sf21 cells. The addition of protease inhibitors to the expression media during expression was necessary to prevent degradation of the recombinant protein during the inevitable virus mediated lysis of the cells [259].

2.3.1.3. Screening in *Saccharomyces cerevisiae*

The *Saccharomyces cerevisiae (S.cerevisiae or S.ce)* expression system became available in the lab after my second PhD year. If a particular protein is suitable to be produced in this host, several advantages exist over mammalian and insect cell expression systems. Since yeasts are of eukaryotic origin their protein processing and quality control machinery is related to that found in higher eukaryotes. However, at the same time, *Saccharomyces cerevisiae* grows and reproduces relatively fast, comparable with *E.coli*. Thus, in relatively short time large cultures with high cell density can be obtained.

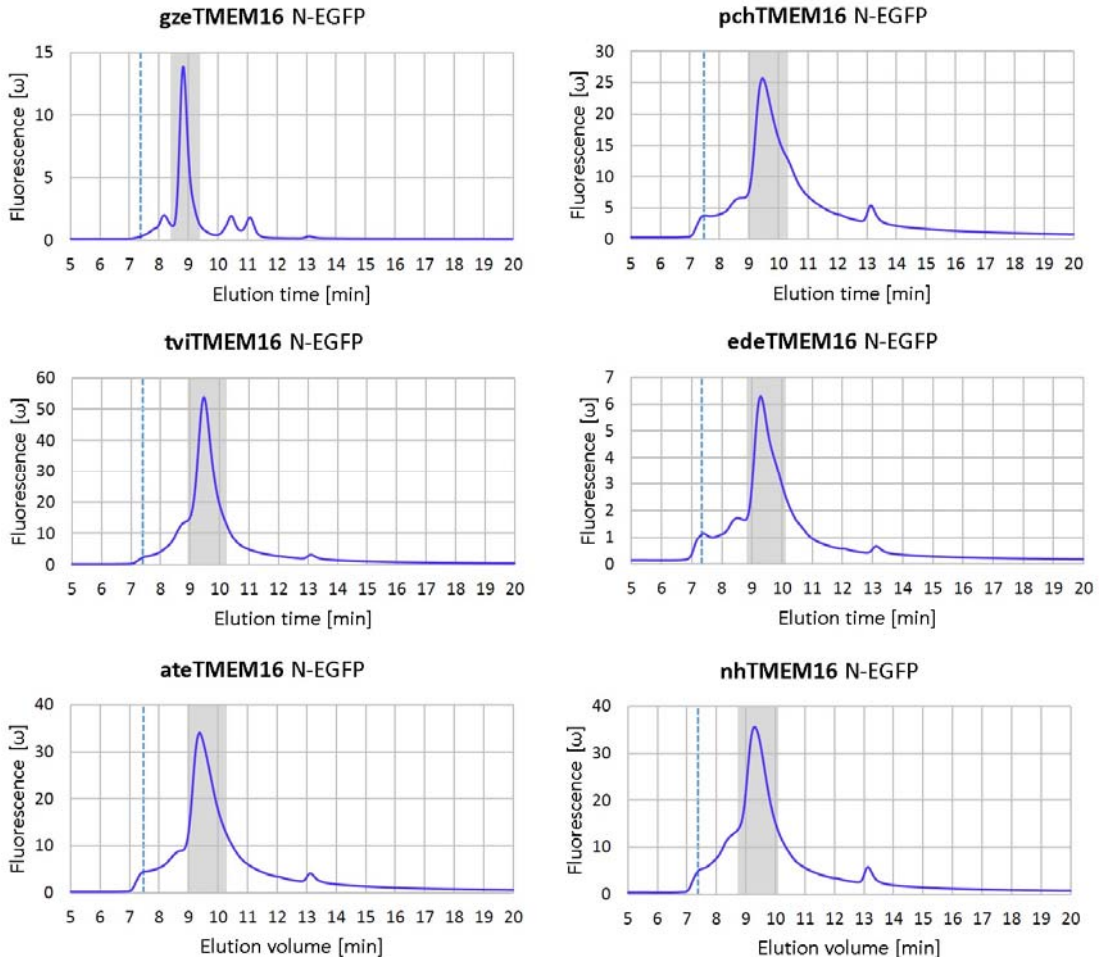

Figure 21 Expression screening (*S. cerevisiae*) evaluated by FSEC

Size exclusion profiles of selected TMEM16 family members. TMEM16 proteins fused to EGFP were extracted from membranes of *Saccharomyces cerevisiae* and the cleared supernatant was subsequently subjected to fluorescence size exclusion chromatography (FSEC). Samples were run on a GF-450 column, fluorescence was excited at 480 nm and emission detected at 515 nm. A peak around 9 min corresponds to stable and intact protein, marked in grey. The void volume corresponding to soluble aggregates at 7.2 min is indicated by a dashed line in cyan.

Expression screening was performed under the control of the GAL1 promoter in a volume of 50 ml in shaking flasks. Cells were lysed as described in the methods section and the supernatant was applied to ultracentrifugation for collecting the membranes. Membranes were extracted with DDMβ and the cleared lysate was subjected to size exclusion chromatography connected to a fluorescence detector. Figure 21 shows a selection of the gel filtration profiles of promising candidates. These were subsequently scaled up to 1 or 6 l in a medium scale purification.

2.3.2. Medium scale purification from HEK cells

Constructs that turned out as positive in the HEK cell screening were cloned such that they did not contain a vYFP fusion to further evaluate their properties. These constructs contained only an SBP- tag, a Myc-tag and a 3C- cleavage site. The lack of the vYFP coincidentally increased the expression levels.

For medium scale purification the cell pellet from 100-200 dishes was submitted to detergent solubilization and extraction. The protein of interest in the cleared lysate was thereafter affinity purified and subjected to a preparative size exclusion column to assess the quality and amount of the protein. Figure 22 and Figure 23 depict the medium scale elution profiles of selected TMEM16 homologues extracted from HEK cells.

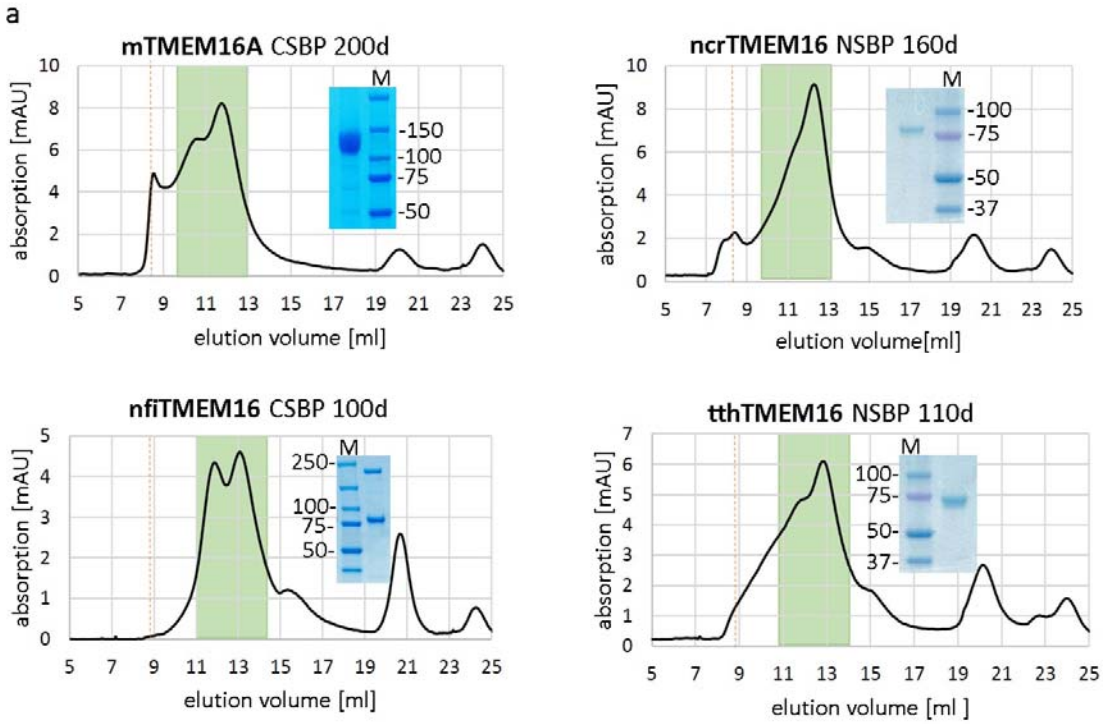

Figure 22 Medium scale purifications from HEK cell expression (part a)

Gel filtration profiles after a medium scale affinity purification of selected TMEM16 proteins expressed in HEK cell. 100- 200 dishes were used per medium scale purification with constructs containing an N- or a C- terminal SBP tag. The eluate from affinity purification was analyzed by SDS-PAGE before separation on a Superdex 200 column. While the expected retention time of the protein is highlighted in green, the elution time of soluble aggregates is marked by a dashed line in red.

Many of the constructs tested at medium scale exhibited unfavorable characteristics such as sample inhomogeneity or a tendency for forming soluble aggregates. While mTMEM16A eluted in more than one species on gel filtration, the SDS gel visualized a broad heterogenous sample distribution between 100-150 kDa reflecting its ability to be modified by glycosylation [176]. Similarly, nfiTMEM16 appeared to form two species and the eluate after affinity purification produced two distinct bands on SDS-PAGE. Mass spectrometric analyses confirmed the protein excised from both bands on the SDS-gel to correspond to full-length nfiTMEM16 indicating a very strong interaction in the dimer. This two species on the column and the low amount of protein, made this protein unsuitable for crystallization from HEK cell expression. Several constructs (i.e. tthTMEM16 and ncrTMEM16) produced a shoulder during size exclusion chromatography, indicating sample instability and aggregation. Only homologues producing a peak of significant height and at appropriate elution volume on gel filtration chromatography were investigated further.

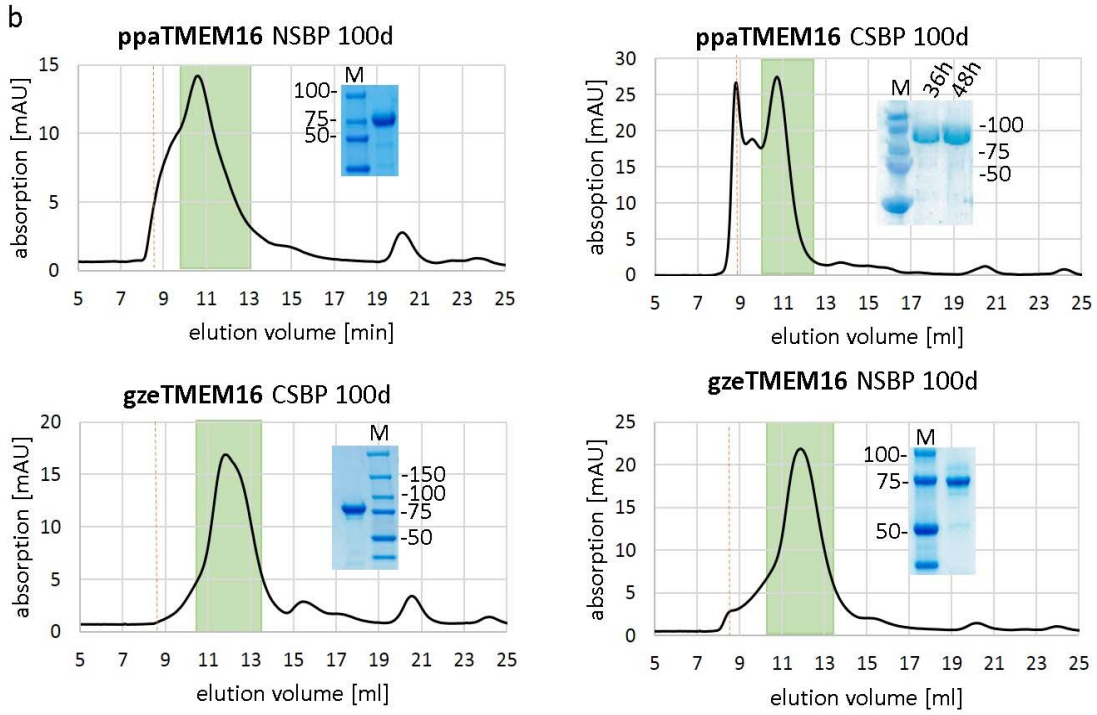

Figure 23 Medium scale purifications from HEK cell expression (part b)

Selected TMEM16 proteins from HEK cell expression cultures were purified from 100 to 200 dishes and run on a Superdex 200 gel-filtration column. The constructs contained an N- or C- terminal SBP tag. The expected elution time of well folded protein is highlighted in green. The retention time of the soluble aggregates is indicated by a dashed line in red. An SDS-gel shows the purity of the eluate after affinity purification.

ppaTMEM16 and gzeTMEM16 both fulfilled these criteria. Protein production was thus in both cases scaled-up for large scale purification and crystallization screening. It should be noted that both, screening and medium scale purifications in HEK cells were carried out before optimization of protein stability. It turned out at a later stage of the project, that TMEM16 proteins can be stabilized for purification to obtain higher protein yields.

2.3.3. Medium scale purification from *Saccharomyces cerevisiae*

To further investigate the stability of constructs that were previously identified as promising candidates from the screening in yeast, and to estimate the protein yield, a medium scale purification was carried out. Membranes of 1 or 6 l of shaking flask culture were extracted with DDMβ and affinity purified by IMAC. The eluted fraction from Ni-NTA resin was cleaved to remove the His- tag while lowering the Imidazole concentration by dialysis. After removing the fusion tag by a second IMAC step, the protein was concentrated and subjected to size exclusion chromatography to check for dispersity and protein yield. Figure 24 and Figure 25 summarize the size exclusion profiles of selected promising homologues expressed and purified from *S. cerevisiae*. Since the *Saccharomyces cerevisiae* expression system was explored comparably late in the project, most of the screening involved protocols that stabilize TMEM16 proteins. Thus, the protein from *Saccharomyces cerevisiae* appear to have properties more suitable for crystallization than previously observed from HEK cell expression.

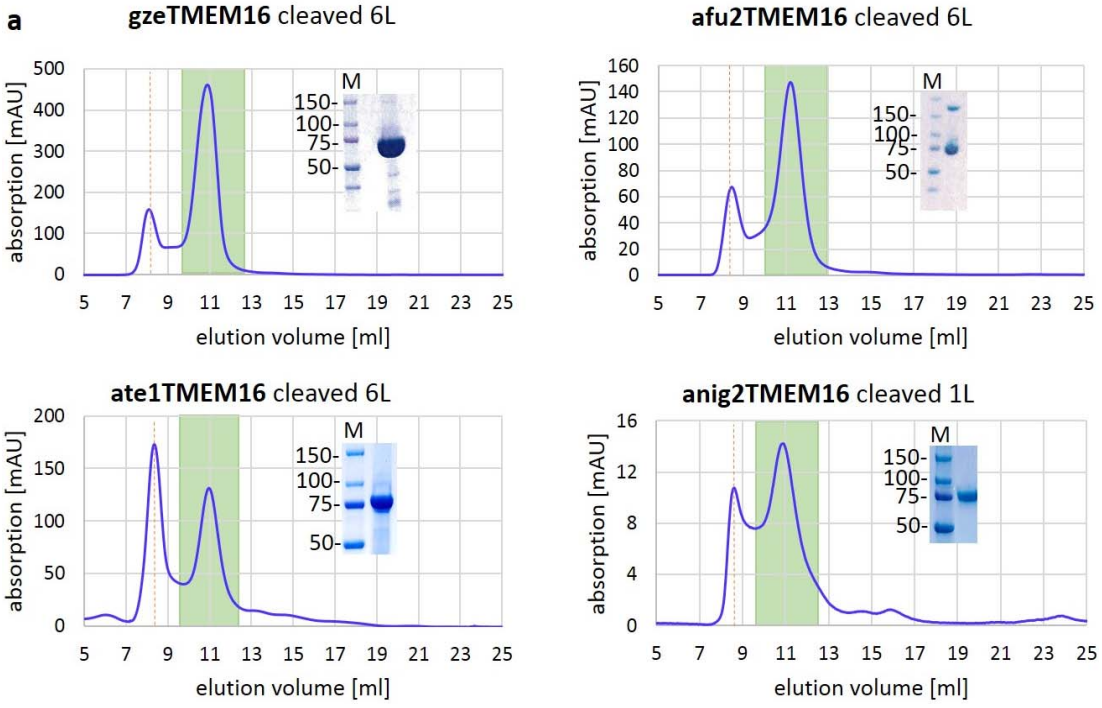

Figure 24 Medium scale purifications from *S. cerevisiae* expression (part a)

Homologues that in the small-scale GFP-fluorescence based screening proved to be extractable and homogenous in size exclusion chromatography were subsequently scaled to medium scale (1-6 l) to test the stability of the GFP-free proteins. The EGFP-His purification tag was cleaved and removed before subjecting to size exclusion (Superdex 200). An early peak at 7-8 ml corresponds to a fraction of the protein that forms soluble aggregates. A peak around 11-12 ml retention volume corresponds to protein of high quality. A sample of the concentrated peak fraction was run on SDS Page to confirm the purity. Note that afu2TMEM16 corresponds to afTMEM16, which was investigated in [170].

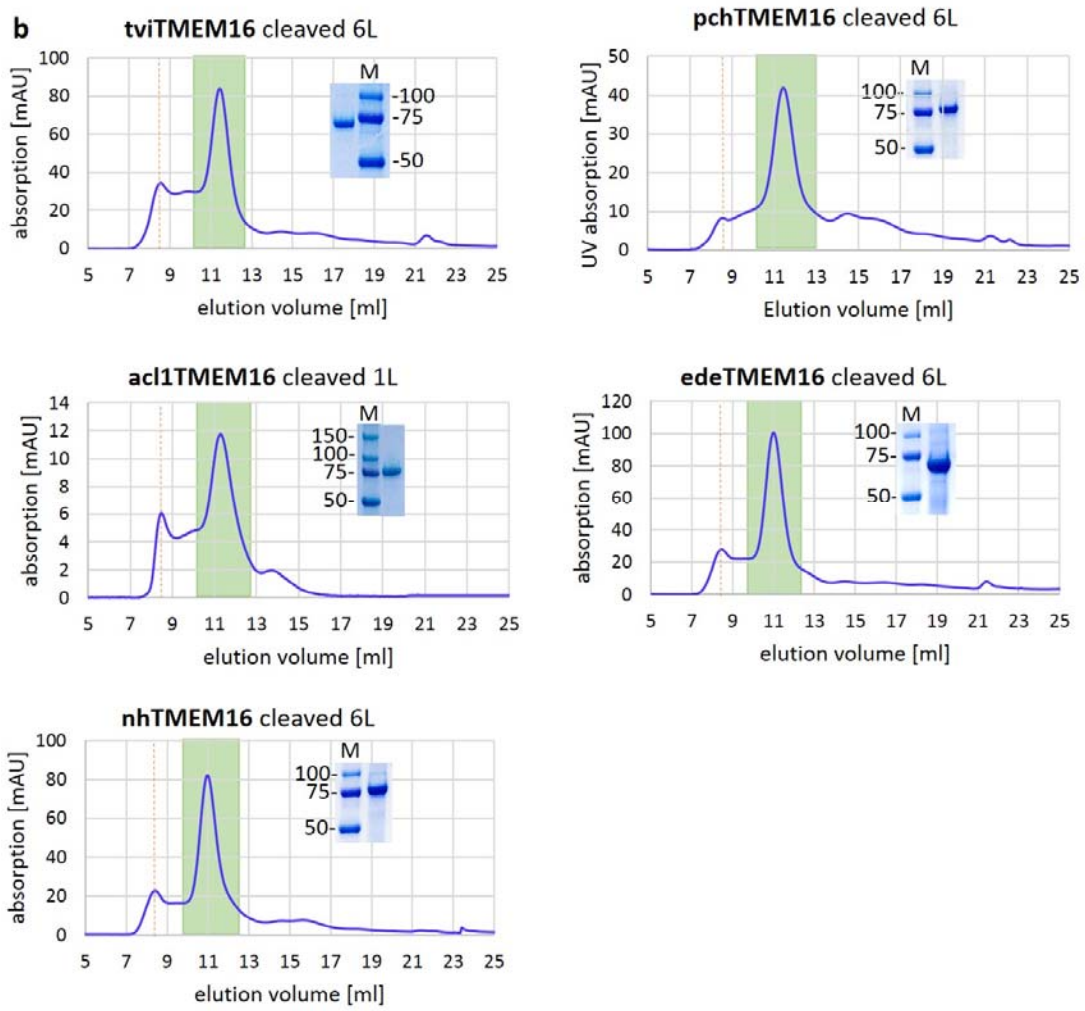

Figure 25 Medium scale purifications from *S. cerevisiae* expression (part b)

Homologues that during small-scale GFP-fluorescence based screening proved to be extractable and homogenous on size exclusion, were subsequently scaled up to medium scale (1-6 l) to test the stability of the GFP-free proteins. The EGFP-His purification tag was cleaved and removed before subjecting the sample to size exclusion chromatography (Superdex 200). A peak at 7-8 ml denotes a fraction of the protein that forms soluble aggregates. A peak around 11-12 ml retention volume corresponds to protein of high quality. An SDS Page of the concentrated peak fraction is shown as inset.

2.4. Crystallization screening of protein purified from HEK cells

During medium scale purification from 100-200 dishes promising TMEM16 proteins such as ppaTMEM16 and gzeTMEM16 were identified, presumably yielding sufficient amounts for further scale-up. Since expression was transient and carried out in adherent cell culture in 10 cm dishes, scale-up did not require any changes in the protocol. Thus in the following chapter the scale-up for both homologues from a large number of 10cm dishes is described. Protocols to stabilize TMEM16 proteins were not yet established.

2.4.1. ppaTMEM16

ppaTMEM16 is the only TMEM16 homologue found in the fungus *Pichia pastoris* (now *Komagataella pastoris*). 1,700 dishes of transient monolayer expression were collected for one large scale purification.

The protein was extracted using DDMβ and affinity-purified on streptavidin resin. The eluate contained 2.3 mg ppaTMEM16. The SBP- purification tag was cleaved as described in the method section. A size exclusion chromatography run served to separate different species. The size exclusion profile and an SDS- PAGE gel of purified protein are shown in Figure 26. In the gel filtration profile, two populations were observed, both presumably corresponding to well-folded protein. It is likely that these two populations represent a dimer-oligomer equilibrium. This behavior was already observed previously during the medium scale purification (Figure 23).

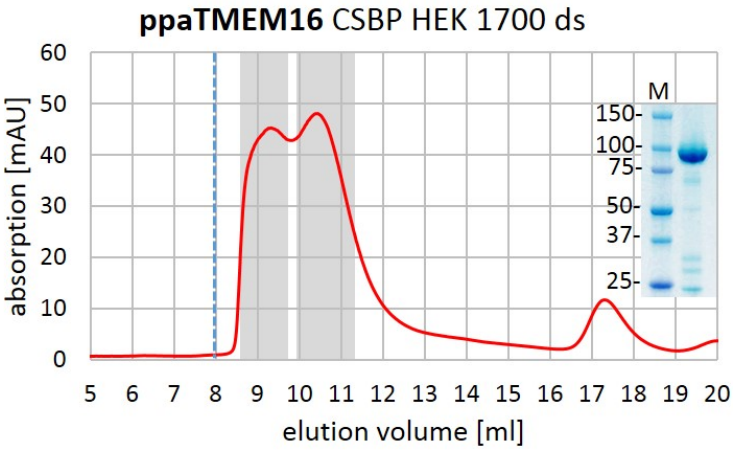

Figure 26 Size exclusion of a large scale purification of ppaTMEM16 from HEK cell culture

The size exclusion profile of protein purified from a large scale culture of 1700 dishes is shown. The grey frame indicates the elution volume of well folded protein. A dashed line in blue indicates the retention time corresponding to the void volume. Protein was detected by its absorption at 280 nm. An SDS-PAGE gel of the concentrate before setting up the protein for crystallization monitored the quality of the sample.

Both peaks were collected separately, concentrated to 2 mg ml^{-1} and subjected to robot-aided crystallization at a 2:1 ratio of protein to mother liquor. The protein- crystallization mix was prepared in 96 well crystallization plates at 4°C in sitting drops. For ppaTMEM16 no crystals were obtained in any of the tested conditions. Although approximately 600 different conditions were screened, only a small range of the virtually endless amount of possible conditions was covered. Protein crystallization is still an empirical process and no predictions can be made on the parameters (protein concentration, pH, salt, precipitant, temperature, ligand, crystallization technique among many others) needed for a particular protein to crystallize.

Importantly, the purification protocol for ppaTMEM16 from large-scale HEK cell culture deviated from the protocol described in the methods section as the buffer contained 1 mM EDTA in all solutions. As

discovered at a later stage of the project, this might have negatively affected the stability of the protein and its ability to crystallize, since Ca^{2+} is one of the components that have a stabilizing effect on TMEM16 proteins.

2.4.2. gzeTMEM16

Two TMEM16 homologues were annotated for the fungus *Gibberella zeae*, and one of them was selected for this work and termed gzeTMEM16. For gzeTMEM16 more than 10,000 dishes were harvested. The protein was purified in batches of 1500-2200 dishes. Although gzeTMEM16 was not the homologue of which the crystal structure was finally determined, I want to discuss my work with this family member in detail for two reasons: First, it was important for the project to identify gzeTMEM16 as hit during the initial screening in HEK cells and as promising target for crystallization. Due to the superior crystallization properties a Blast search was performed with the sequence of gzeTMEM16 as a query. As a result of this search, the closely related nhTMEM16 (85% sequence identity) was identified, of which crystals of sufficient resolution could be obtained for structure determination. Second reason for its importance is that all relevant protocols for purification were established working with gzeTMEM16. As described below, the purification of gzeTMEM16 was not straightforward, as it was essential to discover conditions to stabilize the protein, since the protein became very instable after extraction from the lipid environment of the membrane. All protocols established during the work with gzeTMEM16 could be directly transferred to nhTMEM16 (and other homologues) with similar results.

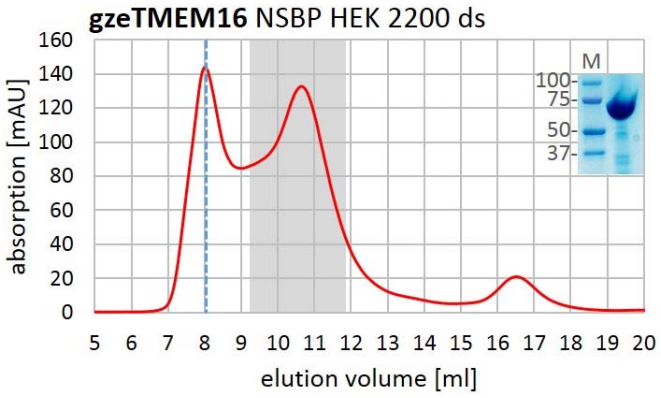

Figure 27 Size exclusion chromatography of a large scale purification of gzeTMEM16 from HEK cell culture

The figure illustrates the first size exclusion chromatogram for gzeTMEM16 purified from 2200 dishes HEK cell monolayer expression. A dashed line in blue indicates the void volume containing soluble aggregates. The protein that was still in a monodisperse state at expected molecular weight is highlighted in grey. Size exclusion chromatography was performed on a Superdex 200 column. An SDS-PAGE gel illustrates the purity of the concentrate before setting up for crystallization. The molecular weight of selected standard proteins is indicated.

gzeTMEM16 was extracted from HEK cells using the detergent DDMβ, insoluble parts were removed by ultracentrifugation and the protein was subsequently purified by binding to streptavidin resin. The elution fraction in the first large-scale purification contained 7.7 mg of gzeTMEM16. Gel filtration allowed to separate aggregates (see Figure 27). The fraction of well-folded monodisperse protein was comparably small compared to the total amount of the eluted protein obtained from affinity purification. In this fraction gzeTMEM16 was pure but underwent slight degradation, which was confirmed by mass spectrometry analysis. 0.8 mg of protein was obtained after size exclusion chromatography and was concentrated to 5 mg ml^{-1}. The protocols for stabilization of TMEM16 proteins were not yet established. The buffers used for extraction and affinity purification were still prepared with 1 mM EDTA, whereas the buffer used for gel filtration contained 0.5 mM Ca^{2+}. The crystallization plates were set up with 2 mM Ca^{2+} in sitting drops in a 2:1 ratio of protein to mother liquor and incubated at 4°C. Crystals grew in 4 different conditions, but in three of the conditions, they were not large enough to be used for X- ray diffraction analysis. One needle-like crystal grown in 50 mM Hepes pH 9.4, 50 mM Magnesium acetate and 15% PEG400 was successfully mounted, cryo-protected by a step-wise increase of the PEG concentration to 36% and flash-frozen in liquid propane.

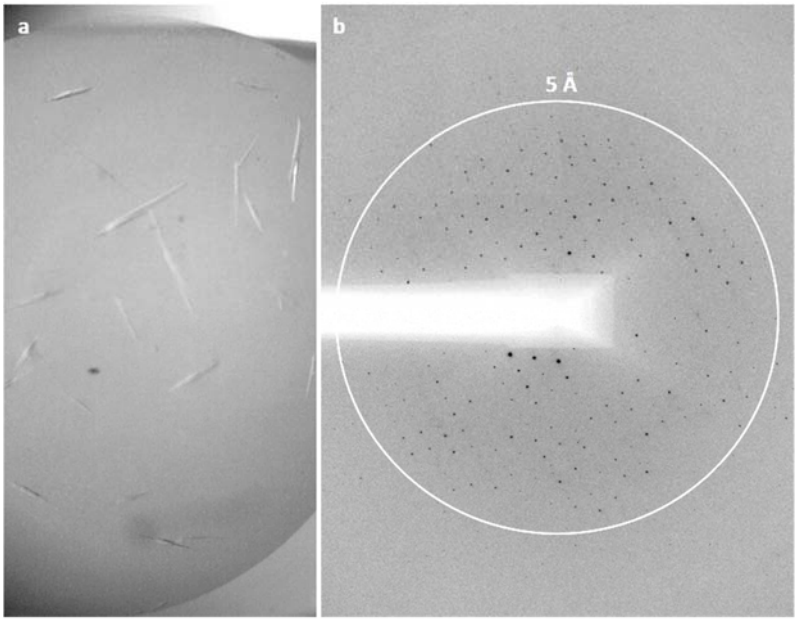

Figure 28 Diffraction of gzeTMEM16 crystals

a. Crystals grown from reservoir containing 50 mM Hepes pH 9.4, 50 mM Magnesium acetate and 15% polyethylene glycol 400. The crystals have a needle-like shape and were only a few micrometer in their longest direction. b. Diffraction pattern of crystals of space group P422. Diffraction could be detected beyond 5 Å (indicated by the white circle).

The crystal was subsequently analyzed at the MD-2 micro-diffractometer at the X06SA beamline of the Swiss Light Source (SLS) at a wavelength of 1 Å. It diffracted X-rays to 5 Å with a pattern that was well-ordered and that contained discrete spots. Diffraction images of few orientations were taken and only a small continuous wedge of data was collected, since due to the limited size of the crystal, radiation damage became apparent after few exposures. Processing of the data suggest that the crystals are of space group P422. Figure 28 illustrates the shape and the diffraction pattern for a gzeTMEM16 crystal.

In subsequent gzeTMEM16 purifications (in batches of 1500-2200 dishes) the crystallization conditions identified in the initial robot-aided crystallization screening were tried to be reproduced and improved

by manually setting up plates with larger volumes (1 µl) and by microseeding. However, the initial diffraction of 5 Å could not be improved. It was also not possible to collect a full data set.

The transient expression screening in adherent HEK cells has allowed the rapid assessment of a large number of TMEM16 family members in a relatively short time. The expression system proved to be scalable without technical limitations. Stable homologues could be identified and were successfully scaled up in the range of 1500-2200 dishes. Unfortunately, the expression in the best case was limited to 350 µg per 100 dishes. Due to the limitation in yield and the labor intensive production of gzeTMEM16 from HEK cells, the expression of selected TMEM16 homologues, particularly gzeTMEM16, was investigated in the insect cell lines Sf9 and Sf21.

2.5. Crystallization of gzeTMEM16 from insect cells

Although crystals could be obtained from transient HEK monolayer expression, the expression levels of the respective proteins (ppaTMEM16 and gzeTMEM16) was insufficient for frequent protein purifications. Although for the described results, large efforts were undertaken to harvest thousands of HEK monolayer dishes, alternative expression systems that required a less demanding procedure for protein production became attractive and were thus tried in parallel.

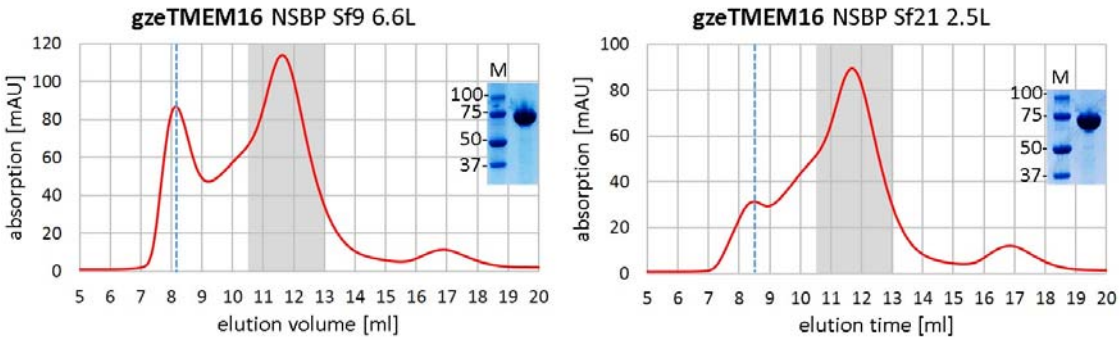

Figure 29 Gel filtration chromatograms of gzeTMEM16 purified from insect cell culture

The figure shows a size-exclusion chromatogram for gzeTMEM16 purified from either 6.6 L Sf9 or 2.5 L Sf21 suspension culture. A dashed line in blue indicates the void volume containing only soluble aggregates. The protein that was expected to be of good quality is marked in grey. Size exclusion chromatography was performed on a Superdex 200 column. An SDS- PAGE gel indicates the purity and intactness of the concentrate before setting up crystallization plates. The molecular weight of standard proteins is indicated.

The expression of gzeTMEM16 was scaled up for production in both, Sf9 and Sf21 cells. Purification was performed from a 6.6 l Sf9 and 2.5 l Sf21 suspension culture in a similar way as described for HEK cells. The fraction eluted after binding to streptavidin beads contained 4 mg of pure protein for either purification. Figure 29 displays the chromatogram from gel filtration of gzeTMEM16 obtained from Sf9 and Sf21 cells. The elution profiles showed similar characteristics compared to the chromatogram

obtained for protein purified from HEK cells. The peak fractions containing 0.6 mg protein each were concentrated to 3 and 4 mg ml^{-1}, respectively, and crystallization experiments were set up manually by mixing protein in a 2:1 ratio with mother liquor. The resulting crystals were harvested, cryo-protected and characterized at the X06SA beamline of the SLS. However, the resolution did not improve.

Similar to HEK cell culture, also in the case of purification from insect cells, the fraction of well-folded protein was expected to be larger than effectively obtained after size exclusion chromatography. A relative large part of the protein was lost during protein concentration before loading it to size exclusion, but also during protease cleavage of the affinity tag. This circumstance points to an inherent instability of the protein independently of the expression system used. All buffers used for extraction and affinity purification contained 1 mM EDTA. The presence of EDTA in the buffers was later shown to decrease the stability of the protein and thus to be disadvantageous for purification of TMEM16 proteins.

2.6. Stabilization of gzeTMEM16

During the first purifications from HEK, insect cells and *Saccharomyces cerevisiae* (data shown below) it appeared that during lysis gzeTMEM16 was sensitive to proteolysis and that it became instable during the process of purification, so that the final amount of purified protein was low. Since gzeTMEM16 had a tendency to aggregate and form degradation products, efforts were made to increase its stability.

2.6.1. Prevention of proteolytic degradation

At the start of a protein purification cells have to be lysed to make the protein of interest available for purification. Independent from the expression system that has been used for overexpression of the recombinant protein, during lysis endogenous proteases are released from the cytosol and get unrestricted access to each area of the broken cell. In the case of a membrane protein extracellular parts that previously did not face any proteases are suddenly exposed and accessible for proteolytic digestion.

Mass spectrometric analysis revealed that phenylmethanesulfonylfluoride (PMSF) did not sufficiently protect gzeTMEM16 from degradation during lysis and extraction. A significant improvement of the yields was thus achieved by the addition of a stronger protease inhibitor cocktail during the lysis of the cells. Importantly, addition of protease inhibitor was not only helpful during extraction but also during affinity purification of the protein to protect against proteases that were carried along during purification.

2.6.2. Thermal stability of a protein

The purification of an integral membrane protein requires the extraction of the protein from its natural membrane environment, which is composed of different types of lipids. The membrane spanning helices of such proteins have a predominantly hydrophobic signature and they insert well into the lipid environment of a membrane bilayer. For extraction of the membrane protein detergents are applied. These are amphiphilic substances that mimic the lipid composition of a biological membrane and that

are thus able to solubilize an integral membrane protein into an aqueous environment. Whenever possible, mild nonionic detergents such as DDMβ are applied for solubilization. However, such a treatment might nevertheless impair the integrity of a protein, since it is removed from its natural environment. This can be reflected in a loss of activity or a decreased stability [262].

For gzeTMEM16 a decreased stability was observed as > 97 % of the protein was lost during the purification. The thermal stability of gzeTMEM16 was measured by an assay that was adapted from Hattori et al [263]. Briefly, a fixed amount of purified protein was incubated for 10 min at temperatures ranging from 4 to 60°C. The emerging precipitate was removed by centrifugation and the supernatant was injected to fluorescent size exclusion chromatography to quantify the amount of protein that survived the treatment. Either the peak height or area are compared. In an attempt to stabilize gzeTMEM16, buffers were varied to cover a broad pH range and different salt concentrations. Furthermore, a variety of chemicals were added to the protein to assess a possible stabilizing effect. Thereafter the thermal stability was compared to the stability of gzeTMEM16 in the reference buffer.

Figure 30 and Figure 31 show the size exclusion profiles and processed data of a thermal stability assay performed in the (a) absence and (b) presence of glycerol and Ca^{2+} at 4, 30, 40, 50 and 60°C.

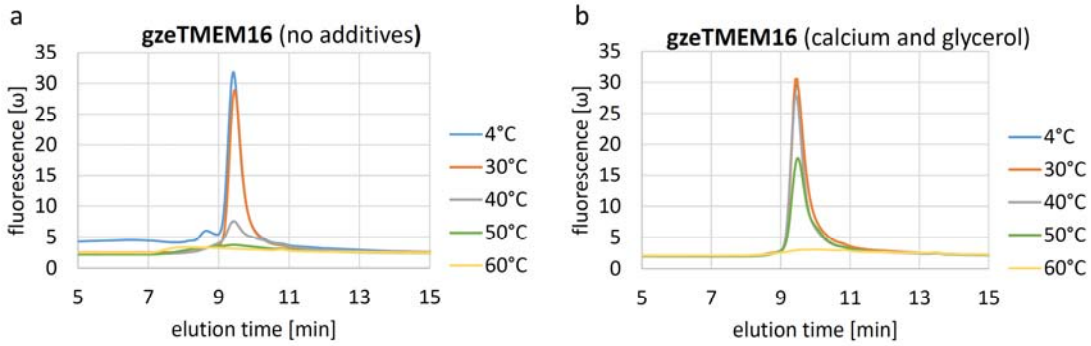

Figure 30 Thermal stability assay with gzeTMEM16 (raw data)

Size exclusion profiles of gzeTMEM16 after a 10 min incubation at various temperatures form 4 to 60 °C. The thermal stability was determined in the absence and presence of 10% glycerol and 5 mM Ca^{2+}. The elution time of the soluble aggregates was expected at 7 min and the peak around 9-10 min corresponded to well-folded protein. A GF450 column was used and tryptophan fluorescence was measured at 335 nm after excitation at 280 nm. The 'no additives'- sample was the reference sample, that did not contain any glycerol or Ca^{2+}.

The size exclusion chromatogram for the reference sample (no Ca^{2+}, no glycerol) indicated that within the given time range the protein was stable at 30°C, but upon increasing the temperature to 40°C or higher the protein precipitated. In contrast, when gzeTMEM16 was incubated with glycerol and Ca^{2+}, the sample only started to precipitate above 50°C. Figure 31 illustrates the observed effects after processing the raw data.

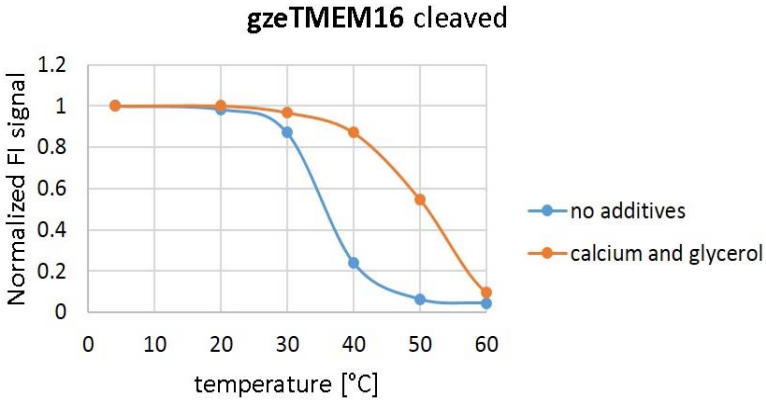

Figure 31 Thermal stability assay with gzeTMEM16

The graph illustrates the thermal stability of gzeTMEM16 as a function of normalized fluorescence (peak height) and temperature. The blue line represents the sample that did not contain any special additive (reference sample). The orange line plots the thermal stability of the protein mixed with 5 mM Ca^{2+} and 10% glycerol. The experiment was performed twice with similar outcome.

Variation of the pH (6.5 to 8.5) or salt concentration (60 mM to 500 mM sodium chloride) had no effect on the stability. The addition of unspecific CaCC (Ca^{2+} activated chloride channel) blocker had a negative effect on the stability (data not shown). Besides Ca^{2+} and glycerol, lipids like *E. coli* polar lipids or pig brain lipid extract had a stabilizing effect too (data not shown). Taken together, the thermal stability assay proved to be useful to identify additives like glycerol, lipids and Ca^{2+} that stabilized gzeTMEM16. The stabilization by Ca^{2+}, glycerol and lipids turned out to play a critical role in this project for structure determination of a related family member.

2.6.3. Purification of stabilized gzeTMEM16 from HEK cells

The newly acquired knowledge to improve the stability of the protein was thereafter applied on purifications from the previously discussed expression systems. Extractions were therefore carried out in the presence of a protease inhibitor cocktail and all purification steps were subsequently performed in the presence of 3-5 mM Ca^{2+} and 10 % glycerol. A purification from 2200 dishes HEK expression yielded 3.2 mg of pure protein after elution from the affinity column. The protein was cleaved, concentrated and loaded on gel filtration. The peak fraction containing 1.5 mg protein was concentrated and used for crystallization at a concentration of 8 mg/ml. The yield of pure protein at the end of the purification was 20% of the amount eluted from the affinity resin, which corresponds to at least 5 times more protein compared to previous purifications (see Figure 32).

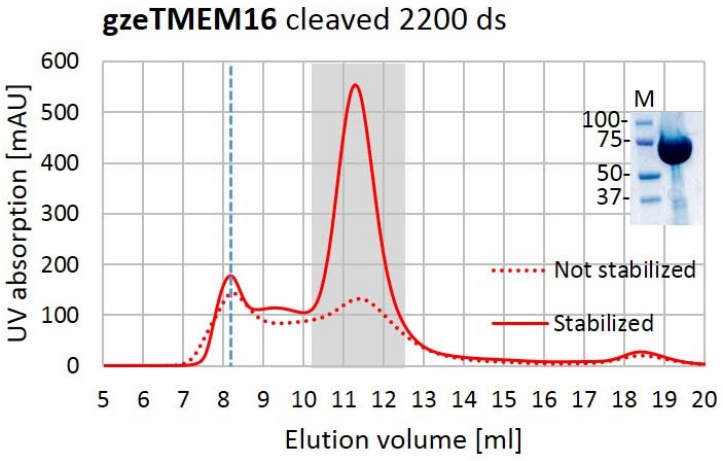

Figure 32 Stabilized vs. not stabilized gzeTMEM16 from HEK cells

A size exclusion chromatogram of gzeTMEM16 (2200 dishes) stabilized with 5 mM Ca^{2+} and 10 % glycerol is depicted and compared to a size exclusion profile, where gzeTMEM16 was not stabilized. Whereas well folded protein had an elution volume of 11-12 ml (highlighted in grey) the fraction of protein that contains misfolded protein or aggregates eluted at 8.7 ml (blue dashed line). An SDS-PAGE gel showed the purity of the concentrated peak fraction of the stabilized protein.

2.6.4. Crystallization of stabilized gzeTMEM16 from *S.cerevisiae*

gzeTMEM16 could also be successfully expressed and purified from *Saccharomyces cerevisiae* cells. While in the absence of glycerol and Ca^{2+} the protein was instable, the addition of glycerol and Ca^{2+} to the purification buffers increased the final yield significantly also for protein expressed in this system (Figure 33).

A 12 l fermentation culture of *S. cerevisiae* yielded approximately 16-20 g of membranes. Membranes were extracted in DDMβ and affinity purified by IMAC. The EGFP-His_{10} tag was cleaved by 3C protease digestion while dialyzing against buffers that did not contain imidazole. The fusion tag was removed by a second binding step to NiNTA and the protein was subsequently concentrated and injected on a size exclusion column. The peak corresponding to intact protein was concentrated to 8-14 mg ml^{-1} and the final yield of 1 mg per 3 g of membrane (or 0.5 mg per 1 l of culture) corresponded to 20% recovery of the amount of protein eluted from the Ni^{2+} beads, when stabilized by glycerol and Ca^{2+}. The protein was crystallized by robot-aided screening in small volumes with the same conditions used in the first broad crystallization screen with protein purified from HEK cells but, due to the higher yield, the concentration of the protein was much higher. 60 new crystal conditions could be identified in that way. These new crystals could either have grown because of the higher concentration or, more likely, because the protein was stabilized by high concentrations of Ca^{2+} and glycerol. Of these 60 new conditions the 25 most promising conditions were improved manually in subsequent purification and crystallization experiments. For the best diffracting crystals a full dataset at a resolution of 5 Å could be collected.

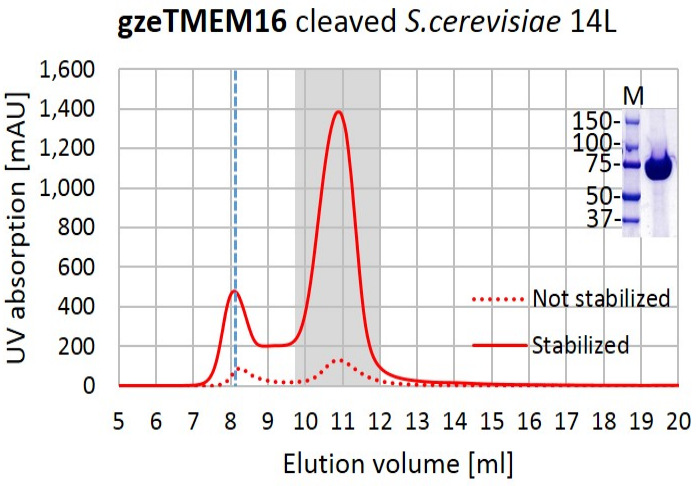

Figure 33 Stabilized versus not stabilized gzeTMEM16 from *S.cerevisieae*

gzeTMEM16 gel filtration profiles comparing stabilized and not stabilized protein derived from *S.cerevisiae*. Both purifications were carried out from a 14 l expression culture. Well-folded protein was eluted at a volume of 11-12 ml (highlighted in grey), while the fraction of protein that contained misfolded protein or aggregates eluted at 8.7 ml (blue dashed line). An SDS-Page gel indicated the purity of the peak fraction after concentration of the stabilized gzeTMEM16 protein.

2.6.5. Summary: Conditions that lead to stabilized gzeTMEM16

In previous purifications in the absence of Ca^{2+} but also in the presence of high concentrations of Ca^{2+} (0.5 mM) only 1- 4% of the initial amount of protein (calculated as final yield over the amount after affinity purification) could be recovered after gel-filtration chromatography and concentration. The stability of the protein during purification was low independent of the expression system. Protease inhibitors like PMSF did not efficiently prevent proteolytic degradation during extraction, as figured out by mass spectrometric analysis. Instead, it was necessary to include a protease inhibitor cocktail not only during extraction, but also during affinity purification for protection against proteolytic digestion. By screening for compounds and conditions, that in the thermal stability assay helped to make gzeTMEM16 more resistant to temperature, three promising conditions were identified. Glycerol and different kinds of lipids had a stabilizing effect on gzeTMEM16. Ca^{2+} had the potential to stabilize the protein as well, but interestingly only at high concentrations above 2 mM. The addition of these agents helped to improve the stability of the protein so that under these conditions a five to ten- fold higher amount of protein (around 20% recovery) was obtained after purification. In Table 3 statistics on the recovery of ppaTMEM16 and gzeTMEM16 in different conditions are summarized. These findings were essential to this work, since they could be successfully applied to other homologues, for example nhTMEM16, of which later the structure could be determined.

Protein	Expr. host	Volume	EDTA or Ca^{2+}	Recovery
ppaTMEM16	HEK	1700 ds	1 mM EDTA	5%
ppaTMEM16	HEK	1700 ds	1 mM EDTA	5%
gzeTMEM16	HEK	2200 ds	1mM EDTA, later steps 0.5- 2 mM Ca^{2+}	4%
gzeTMEM16	HEK	2000 ds	1mM EDTA, later steps 0.5- 2 mM Ca^{2+}	3%
gzeTMEM16	HEK	1600 ds	1mM EDTA, later steps 0.5- 2 mM Ca^{2+}	4%
gzeTMEM16	Sf9	6.6 l	1mM EDTA, later steps 0.5 mM Ca^{2+}	2%
gzeTMEM16	Sf21	2.5l	1mM EDTA, later steps 0.5 mM Ca^{2+}	4%
gzeTMEM16	*S. cerevisiae*	20 l	1mM EDTA, later steps 0.5- 2 mM Ca^{2+}	1%
gzeTMEM16	*S. cerevisiae*	20 l	1mM EDTA, later steps 0.5- 2 mM Ca^{2+}	2%
gzeTMEM16	*S. cerevisiae*	30 l	1mM EDTA, later steps 0.5- 2 mM Ca^{2+}	2%
gzeTMEM16	*S. cerevisiae*	20 l	1mM EDTA, later steps 0.5- 2 mM Ca^{2+}	1%
gzeTMEM16	*S. cerevisiae*	30 l	0.5- 2 mM Ca^{2+}	2%
gzeTMEM16	*S. cerevisiae*	30 l	0.5- 2 mM Ca^{2+}	2%
gzeTMEM16	*S. cerevisiae*	30 l	0.5- 2 mM Ca^{2+}	1%
gzeTMEM16	*S. cerevisiae*	30 l	0.5- 2 mM Ca^{2+}	2%
gzeTMEM16	*S. cerevisiae*	30 l	0.5- 2 mM Ca^{2+}	1%
gzeTMEM16	*S. cerevisiae*	30 l	0.5- 2 mM Ca^{2+}	2%
gzeTMEM16	HEK	1600 ds	10% glycerol, 3-5 mM Ca^{2+}	19%
gzeTMEM16	HEK	1500 ds	10% glycerol, 3-5 mM Ca^{2+}	22%
gzeTMEM16	HEK	2200 ds	10% glycerol, 3-5 mM Ca^{2+}	22%
gzeTMEM16	*S.cerevisiae*	12 l	10% glycerol, 3-5 mM Ca^{2+}	21%
gzeTMEM16	*S.cerevisiae*	12 l	10% glycerol, 3-5 mM Ca^{2+}	20%
gzeTMEM16	*S.cerevisiae*	20 l	10% glycerol, 3-5 mM Ca^{2+}	22%
gzeTMEM16	*S.cerevisiae*	20 l	10% glycerol, 3-5 mM Ca^{2+}	23%

Table 3 Statistics on the recovery of ppaTMEM16 and gzeTMEM16

The table compares different ppaTMEM16 and gzeTMEM16 purifications with respect to expression host, culture volume and the effect of different buffers on protein recovery. In light blue the purifications are shown, that were carried out using buffers that stabilized the protein. ds refers to 10 cm cell culture dishes containing 10 ml of medium.

2.7. Crystallization of nhTMEM16

The 6th blast search was performed with the sequence of gzeTMEM16 as query and identified close homologues of this fungal TMEM16 protein. These homologues were screened in HEK cells and *Saccharomyces cerevisiae* similarly as previously described. The expression screening was part of the Master Thesis of Alessia Duerst and identified nhTMEM16 as a promising candidate. The expression pattern in HEK cells of nhTMEM16 with a vYFP fusion is diffuse with nhTMEM16 being targeted to various different compartments.

nhTMEM16 shares 85% of the sequence with gzeTMEM16 and is the closest known homologue of this protein found in any of the sequenced fungal genomes available in 2012. Generally, nhTMEM16 displays similar biochemical properties as gzeTMEM16. It undergoes severe degradation and

precipitation in the absence of glycerol and Ca^{2+} independently of the expression system, but in the presence of these additives the thermal stability of nhTMEM16 is significantly improved, similarly as previously discovered for gzeTMEM16 (Figure 34).

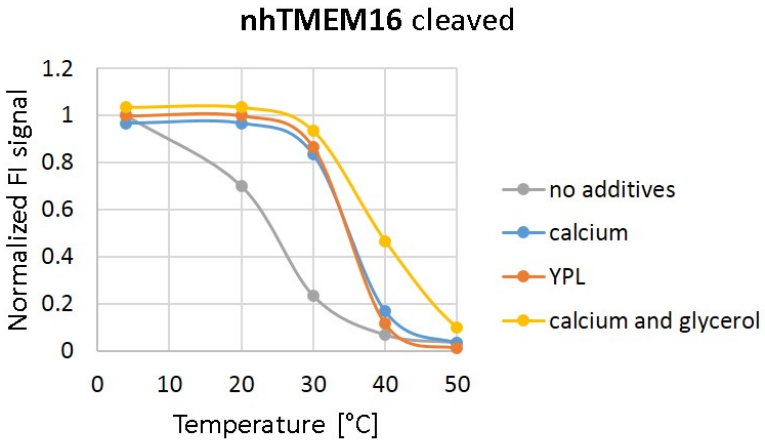

Figure 34 Thermal stability of nhTMEM16

Graph depicting the thermal stability of nhTMEM16. Different additives were investigated to test their effect on nhTMEM16. Peak height of the fluorescent signal from the size exclusion profiles were normalized to the reference sample (no additives). Incubation temperatures were set to 4, 20, 30, 40 and 50°C. Experiment was carried out once.

All purifications were carried out in the presence of glycerol and high concentrations of Ca^{2+}. nhTMEM16 was usually expressed in *Saccharomyces cerevisiae*. The construct used for crystallization contained an N-terminal His_{10}-tag followed by EGFP and a 3C cleavage site to remove the fusion and purification tag after affinity chromatography. A 35 l fermentation culture usually yielded around 40-50 g membranes and 4.5-5 mg of pure protein after purification. The membranes were solubilized by the detergent DDMβ, insoluble material was removed by ultracentrifugation and the protein in the supernatant was bound to NiNTA, washed and eluted as described in the methods section. The eluted fraction usually contained around 20- 25 mg protein. The tag was cleaved while dialyzing the protein against buffers lacking imidazole. A second IMAC step removed the fusion tag. The peak fraction after size exclusion chromatography shown in Figure 35 usually contained around 4.5-5 mg of pure protein and was concentrated to 8-14 mg ml^{-1} for crystallization. The size and purity of the protein was confirmed by SDS-PAGE. Crystallization experiments were prepared in sitting drops of 100 nl with the help of a crystallization robot to screen 800 conditions (from various full and sparse matrix screens). nhTMEM16 crystallized in 25 conditions. All conditions were refined manually in 1 µl drops by variation of PEG400 in 0.5% steps. Initial diffraction of crystals grown in a condition consisting of 50 mM Hepes pH 7.4, 100 mM Ammonium Sulfate and 21-23% PEG400 could be improved from 15 to 6 Å. In all cases the diffraction was anisotropic.

To change the micelle size and thus potentially influence crystal packing, different detergents, lipids and other additives were mixed to the concentrated protein at the end of the purification to test their impact on crystallization properties. In the first additive screening different detergents were tested for their effect (see Table 4). The DDMβ concentration in the final protein concentrate was estimated to be constant during protein concentration, since the DDMβ detergent micelle has a molecular weight of approximately

70 kDa and is therefore too small for being retained in a concentrator with cutoff of 100 kDa [264]. The amount of detergent used as additive was chosen based on the respective critical micelle concentration (cmc) and molar concentration.

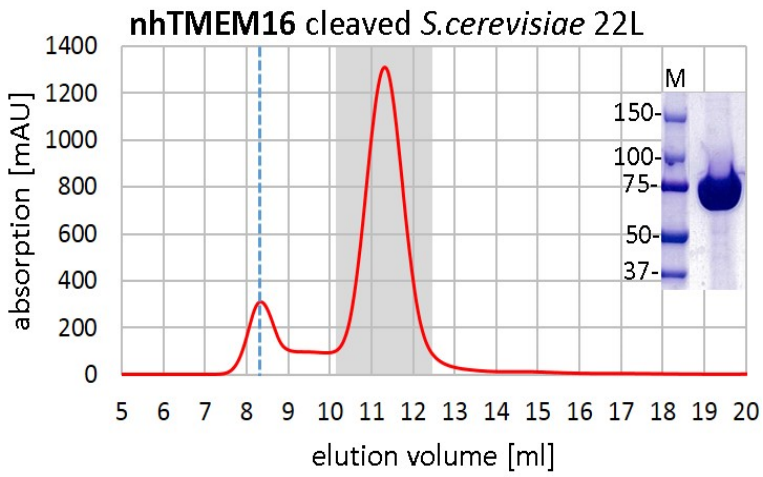

Figure 35 Gel filtration profile of nhTMEM16

Picture showing the gel filtration profile of nhTMEM16 using a Superdex 200 column. Well folded protein is expected at an elution volume of 11.5 ml while soluble aggregates are indicated by a small void peak around 8 ml. The SDS- gel of the concentrated peak fraction confirmed the purity of the protein.

	Detergent screening	x cmc	%	Exess detergent X over DDMβ
1	C12E8 (Polyoxyethylene (9) Dodecyl ether)	66	0.2	1
2	C12E9 (Octaethylene Glycol Monododecyl Ether)	41	0.2	7
3	Cymal-4 (4-Cyclohexyl-1-Hexyl-β-D-Maltoside)	0.6	0.2	10
4	Cymal-5 (5-Cyclohexyl-1-Hexyl-β-D-Maltoside)	1.6	0.2	10
5	Cymal-6 (6-Cyclohexyl-1-Hexyl-β-D-Maltoside)	7	0.2	10
6	N-Octyl-β-D Maltopyranoside	0.2, 1.1	0.2, 1	10, 42
7	N-Octyl-β-D-Glucopyranoside	0.4, 1.9	0.2, 1	20, 100
8	N-Nonyl-β-D-Maltopyranoside	0.7, 2.8	0.2, 0.8	10, 40
9	N-Nonyl-β-D-Thiomaltopyranoside	3.3	0.5	21
10	Decyl Glucopyranoside	0.7	0.05	4
11	Decyl Maltose Neopentyl Glycol	60	0.2	5
12	N-Decyl-α-D-Maltopyranoside	1.25, 2.5, 3.75	0.1, 0.2, 0.3	5, 10, 15
13	N-Decyl-β-D-Maltopyranoside	1.1, 3.3	0.1, 0.3	5, 15
14	N-Decyl-β-D-Thiomaltopyranoside	2.2, 6.6	0.1, 0.3	5, 15
15	N- Undecyl-α-D-Maltopyranoside	3.4, 6.8,10.3	0.1, 0.2, 0.3	5, 10, 15
16	N-Undecyl-β-D-Maltopyranoside	3, 6, 9	0.1, 0.2, 0.3	4, 8, 12
17	N-Tridecyl-β-D-Maltopyranoside	150	0.2	12
18	Sucrose Monolaurate	1	0.016	1
19	Lauryl Maltose Neopentyl Glycol	200	0.2	5

Table 4 Detergent additive screening for crystallization

The effect of different detergents on nhTMEM16 crystals was probed. The final detergent concentration used as additive is indicated as multiple of the critical micelle concentration (cmc) and in % (w/v).

	Lipid screening	final conc. [µg/ ml]
1	DOPC	50, 100
2	DOPS	50, 100
3	*E.coli* polar lipids	50, 100
4	pig brain lipids	50, 100
5	POPE	50, 100
6	Soy bean lipid	50
7	yeast polar lipids (YPL)	50, 100

Table 5 Lipid additive screening for crystallization

Different lipid additives that were included in the screening as secondary additives in combination with selected detergent additives are shown. The final concentration is indicated as µg ml^{-1}.

Usually a detergent concentration was chosen that was at least equimolar compared to the primary detergent DDMβ to allow for efficient replacement of DDMβ. But at the same time the detergent concentration of the additive was supposed to be at least three times above the critical micellar concentration to permit micelle formation (see Table 4).

Since in the thermal stability assays yeast polar lipids (YPL) had a stabilizing effect on nhTMEM16 lipids were included to the detergent screening. The best crystals from that screening were grown in the presence of the detergent UDMα in combination with YPL with a resolution of 3.5 Å and were isotropic. Crystals obtained in the presence of n-Undecyl-α-D-Maltopyranoside (UDMα) or YPL alone showed anisotropic diffraction to 4.5-6 Å or isotropic diffraction to 7 Å, respectively.

None of the investigated lipids shown in Table 5 improved the diffraction obtained in the presence of YPL. Further screening for a third additive, that was added to the protein in addition to UDMα (0.2%) and YPL (50 µg/ml), from a list shown in Table 6, identified 1,2,3-Heptantriol (2%) as molecule, which improved the diffraction to 3.4 Å. The final crystallization condition contained 50 mM Hepes pH 7.4, 100 mM Ammonium Sulfate, 21-23% PEG400, 0.2% UDMα, 50 µg ml^{-1} YPL and 2% 1,2,3-Heptantriol and was subsequently named crystal form 2 (CF2).

From the initial 25 conditions 10 conditions were refined again with a similar approach as described for CF2. This has allowed the improvement of crystals grown in another condition, which was: 100 mM Capso pH 9.4, 100 mM Magnesium Chloride, 100 mM Sodium Chloride, 21-23% PEG400, 0.2% UDMα, 50 µg ml^{-1} YPL and 2% 1,2,3-Heptantriol. Crystals grown in that condition could be refined to 3.3 Å, in the following denoted as crystal form 1 (CF1).

	Tertiary additive screening	final conc. mM or %
1	Acetone	4%
2	Benzamidine	4%
3	Betaine Hydrochloride	3 mM
4	1,2-Butandiol	3%
5	CadmiumChloride	2 mM
6	1,6-Diaminohexan	2%
7	1,5-Diaminopentan Dihydrochloride	2%
8	Dioxane	1%
9	DMSO	5%
10	D-sorbitol	3%
11	DTT	1 mM
12	Ethanol	3%
13	Ethylene Glycol	4%
14	D-+-Galactose	3%
15	D-+-Glucose	3%
16	glycerol	1%
17	1,2,3-Heptantriol	2%
18	1,6-Hexandiol	3%
19	2,5-Hexandiol	3%
20	Isopropanol	3%
21	Jeffamine	3%
22	L-Proline	3 mM
23	Manganese (II) Chloride Tetrahydrate	2 mM
24	Methanol	5%
25	2-Methyl-2,4-Pentanediol (MPS)	3%
26	Myoinositol	1%
27	Strontium Chloride	2 mM
28	Sucrose	3%
29	TCEP	5 mM
30	Toluol	3%
31	Urea	5 mM
32	Xylitol	3%

Table 6 Tertiary additive screening for crystallization

The table summarizes additives that were screened for their effect on nhTMEM16 crystals in combination with selected detergents and yeast polar lipids. The applied concentration is shown in % or mM.

Figure 36 illustrates crystals obtained from two different conditions and the corresponding diffraction pattern. Both crystallization conditions produced crystals of space group $P2_12_12_1$ (with unit cell dimensions of a= 96.5, b= 113.7, c= 235.7 Å with α= β= γ= 90°, CF1 and a= 115.9, b= 127.2, c= 180.1 Å with α= β= γ= 90°, CF2) each containing two copies of the nhTMEM16 subunit per asymmetric unit. While CF1 diffracted to 3.3 Å the resolution of CF2 was limited to 3.4 Å. Statistics on the data collection are displayed in Table 7. These native data sets were later used for the extension of initial experimental phases obtained from anomalous data collected from seleno- methionine containing crystals by NCS and cross-crystal averaging, model building and refinement.

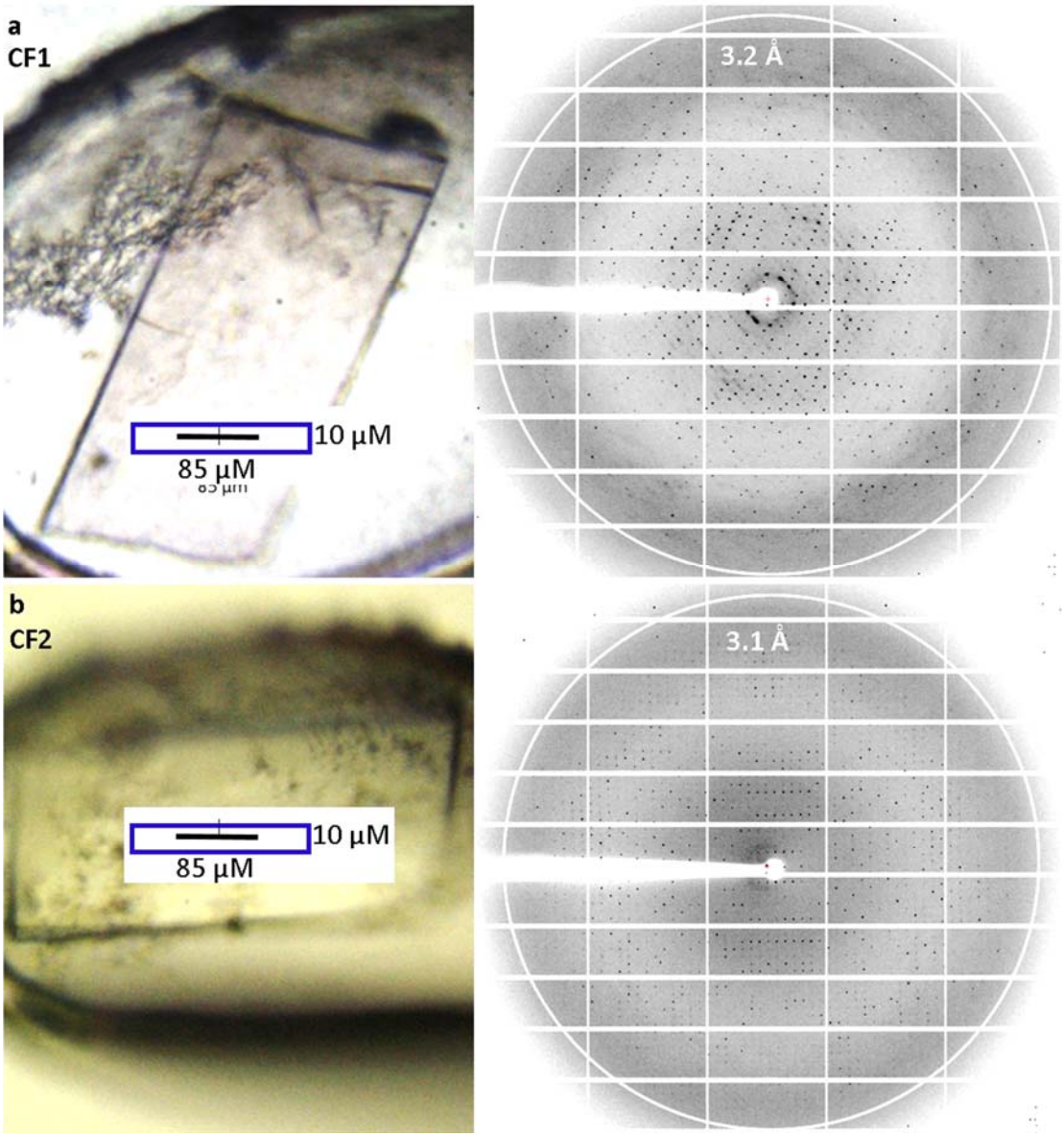

Figure 36 nhTMEM16 crystals and diffraction pattern

Crystals of nhTMEM16 and the corresponding diffraction pattern. a: Left side: Part of a rod-shaped crystal of space group $P2_12_12_1$ (crystal form 2, CF2) grown from solutions containing 50 mM Hepes pH 7.4, 100 mM Ammonium Sulfate, 23 % PEG400, 0.2 % UDMα, 50 µg ml^{-1} YPL and 2 % 1,2,3- Heptanetriol and mounted in a loop. The box indicates the size and shape of the X-ray beam. The corresponding diffraction pattern is shown right. The white circle indicates a resolution of 3.2 Å b: Left side: Plate-like crystals (CF1) of space group P212121 obtained from a condition containing 100 mM Capso pH 9.4, 100 mM Sodium Chloride, 100 mM Magnesium Chloride, 23 % PEG400, 0.2 % UDMα, 50 µg ml^{-1} YPL and 2 % 1,2,3- Heptanetriol. The corresponding diffraction pattern is shown on the right, a ring at a resolution of 3.1 Å is indicated.

	nhTMEM16/CF1	nhTMEM16/CF2
Data collection		
Wave length (Å)	0.9797	1
Space group	$P2_12_12_1$	$P2_12_12_1$
Cell dimensions		
a, b, c (Å)	96.5, 113.7, 235.7	115.9, 127.2, 180.1
(°)	90.0, 90.0, 90.0	90.0, 90.0, 90.0
Resolution (Å)	50-3.3 (3.4-3.3)	50-3.4 (3.5-3.4)
R_{merge}	8.3 (123.5)	6.5 (149.3)
I/σI	20.1 (2.6)	20.0 (1.7)
Completeness (%)	99.1 (99.8)	98.9 (87.9)
Redundancy	12.7 (12.7)	9.6 (8.6)
$CC_{1/2}$ (%)	99.3 (80.3)	99.9 (59.8)

Table 7 Data collection statistics of native data from CF1 and CF2

Data in parenthesis corresponds to highest resolution shell.

2.8. Summary of the entire screening procedure leading to structure determination

In this part of the thesis the selection of a suitable TMEM16 homologue and the improvement of crystals, that led to the structure determination of the protein are described.

A combination of described techniques and several approaches were combined to facilitate the screening of a large number of genes. This included several rounds of Blast searches with different query sequences, which allowed the selection of a broad range of target genes used for high throughput cloning. Cloning was simplified by the use of the FX method [240], that requires a single restriction enzyme to generate different constructs for all investigated homologues and plasmids. Furthermore, a fluorescence-based small-scale expression screening approach was employed to identify homologues with reasonably high expression levels. This screening was expanded to different eukaryotic expression hosts to chose the most suitable expression system depending on the investigated TMEM16 homologue. Initial purification was performed either at small or medium scale and size exclusion chromatography was applied to evaluate the stability and quality of the protein without a fluorescent fusion partner. Constructs that fulfilled the necessary requirements with respect to stability and yield were further scaled up, purified and investigated in a series of crystallization screening. With the help of a thermal stability assay, chemicals and conditions were identified that stabilized the constructs during purification and crystallization. Initial crystals were optimized by screening for further additives that improved the crystallization properties.

A flow chart shown below summarizes the relevant steps, techniques and strategies that led to the identification of nhTMEM16 and the growth of crystals diffracting to high resolution that were subsequently used for structure determination (Figure 37).

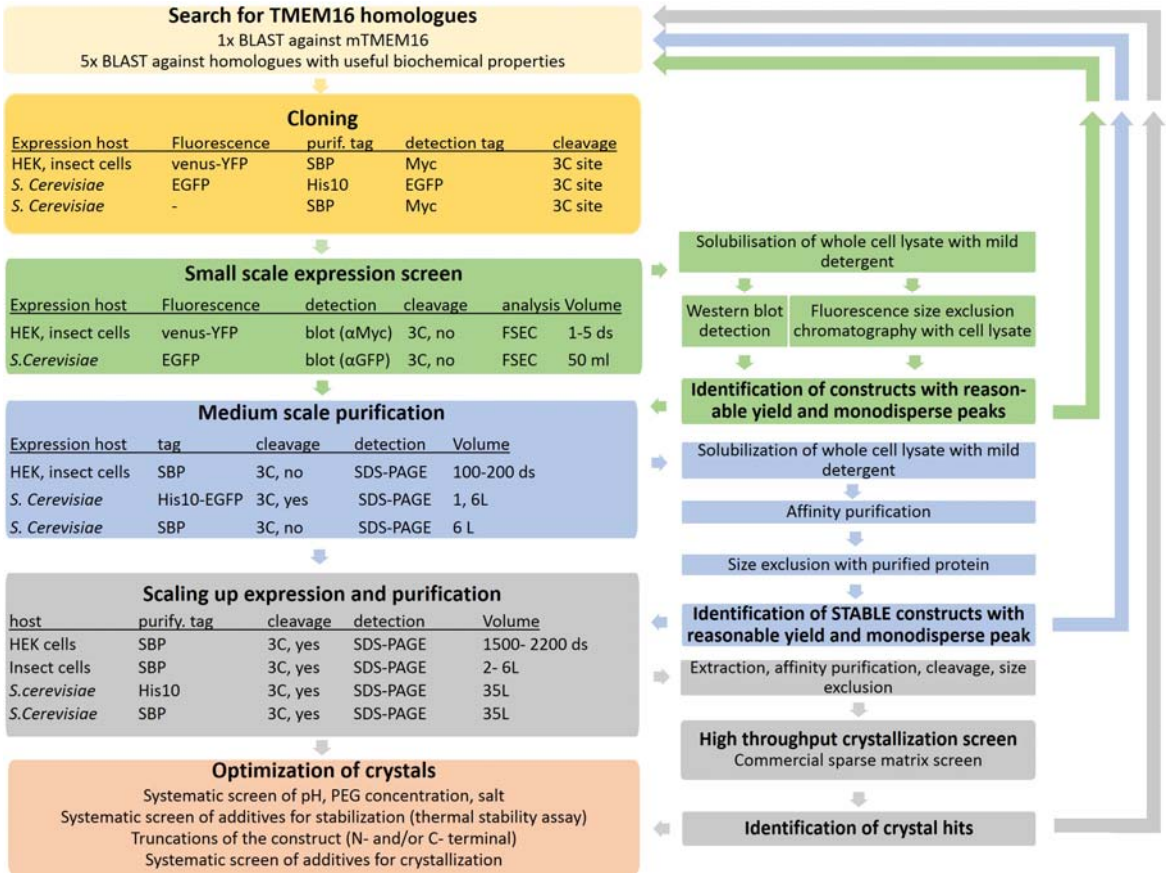

Figure 37 From BLAST search to high-resolution crystals: workflow

The flow chart summarizes the relevant steps, techniques and approaches used in this work leading to the growth of crystals, that finally allowed the structure determination of a TMEM16 protein. Same colors in the flow chart group techniques and steps according to the stage of the screening process. Yellow: Blast search and cloning, green: small-scale expression screen searching for constructs that express with reasonable yields, blue: small- or medium- scale purification to identify stable homologues, grey: large- scale purification and identification of initial crystal hits, orange: optimization of crystals. ds refers to 10 cm culture dishes of monolayer HEK expression.

2.9. Seleno- methionine derivatization of nhTMEM16 and structure determination by the SAD-method

The molecular picture we want to get from the protein that was crystallized is manifested in its electron density. The electron density can be determined from the structure factors using a Fourier transformation. The structure factors of a crystal are vectorial and contain information about the phase angles and the amplitudes of each reflection. The diffraction pattern of a crystal only reveals the structure factor amplitudes, but not the phases, a circumstance that is known as the 'phase problem' in crystallography. Since the phases contribute more to the electron density than the amplitudes, it is essential to acquire

accurate phases for structure determination. This can be achieved by different methods. If a structure from a homologous protein is available, it can serve as a phasing model by placing a model of the known protein into the unit cell of the unknown protein. In this case initial phases can be obtained from a Fourier transformation and combined with the measured amplitudes. Molecular Replacement thus exploits that similar structures contain similar amplitudes and phases, which can be transferred as initial estimates. Once the initial phases have been obtained an electron density of the protein, from which the structure needs to be solved, can be obtained.

However, Molecular Replacement is unsuitable if a structure of a homologous protein is not available. In this case, the phases need to be deduced experimentally by direct methods for very small molecules, or by Isomorphous Replacement or Anomalous Dispersion for larger molecules (> 500 atoms). In both methods used for large molecules, a small number of atoms is introduced to the protein in the crystal at identical places. All atoms in a protein crystal contribute to each reflection of the diffracted image, but the contribution is different for each reflection. Similarly, any introduced atom contributes to the diffraction depending on the number of electrons, which is manifested in small changes in the measured intensities. To maximize these small differences, the added atoms need to contain many electrons that diffract X-rays strongly. These heavy atoms in the crystal, all positioned at equivalent sites, can be looked at as a substructure, consisting only of few heavy atoms, which are placed at specific positions in the unit cell. Both methods, Isomorphous Replacement and Anomalous Dispersion, require knowledge of the structure factors (phases and amplitudes) of the heavy atom component. These can be calculated from the heavy atom substructure, which is determined using Patterson methods as a first step in a phasing procedure.

In a structure determination by Isomorphous Replacement, the crystals are usually prepared by soaking of a suitable heavy atom into the crystal followed by the collection of a heavy atom derivative data set. Importantly, the derivatized crystals require to be isomorphous to the native crystals, which means, that the protein component in both crystals must be perfectly congruent. Compared to the native data set, the diffraction pattern of the derivatized crystal and thus the structure factor amplitudes reveal slight changes occurring from the heavy atom diffraction. This discrepancy in the diffraction pattern can be calculated from the two data sets to calculate a Patterson function and determine the heavy atom substructure. The calculated structure factors of the heavy atom components is used in combination with the amplitude of each data set to calculate phases. With a single derivative this method would provide two possible solution for each phase angle, an ambiguity that can be resolved, if data from more than one derivative is available. A problem frequently encountered in Isomorphous Replacement is that the soaking with heavy atoms decreases the resolution of the data or slightly changes the protein arrangement in the crystal, leading to non-isomorphism.

In the Anomalous Dispersion method, isomorphism is not required because for structure determination the collection of a single heavy atom derivatized crystal is sufficient for phasing. The method exploits the heavy atoms properties to absorb X-rays at a particular wavelength and re-emit them with a phase change of 90° (anomalous scattering). The derivatized crystals are measured close to this absorption edge of the respective heavy atom. This effect is largest for heavy atoms which are strong scatterers, *e.g.*

selenium, but is barely measurable for lighter atoms such as sulfur. In Anomalous Dispersion the Friedel's law, that defines the symmetry of the structure factor amplitudes of a pair of reflections with indices hkl and -h-k-l, breaks down. The differences between such Friedel pairs can be measured and used for the determination of the heavy atom substructure. Phase information can be subsequently obtained by similar methods as described for Isomorphous Replacement.

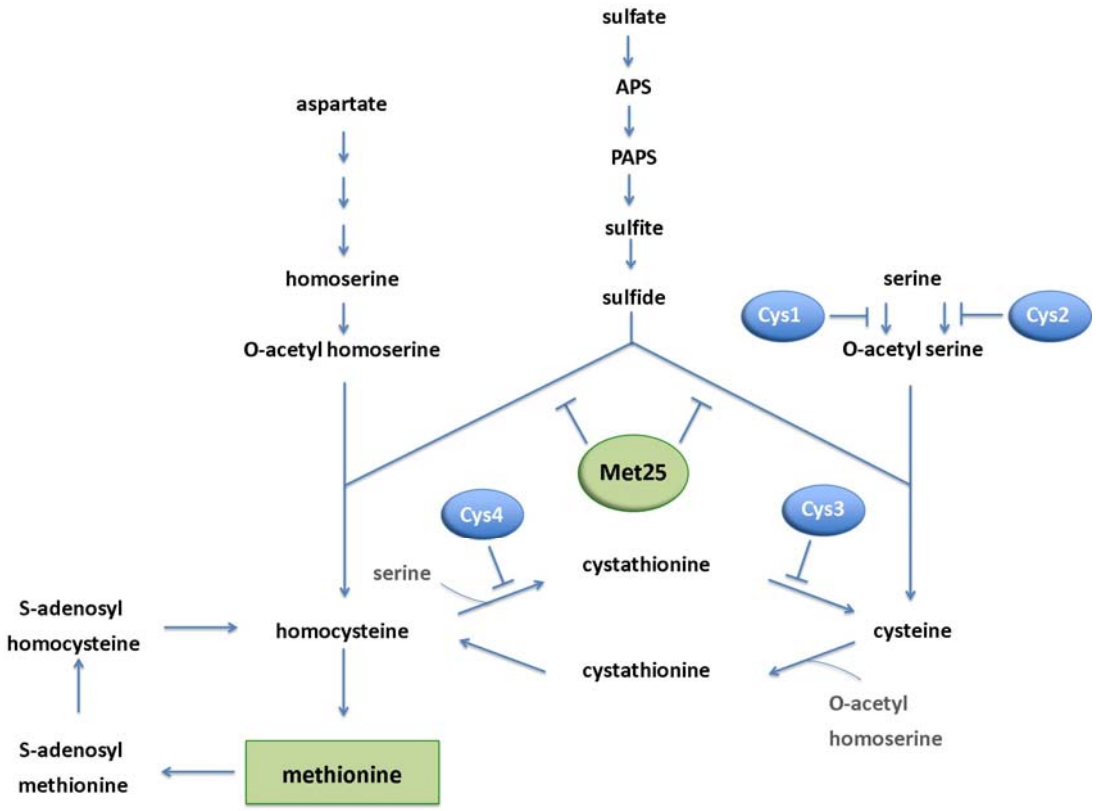

Figure 38 Methionine synthesis in *Saccharomyces cerevisiae*

Two major pathways exist in Saccharomyces cerevisiae to synthesize methionine. Both require the availability of inorganic sulfur that is used by O-acetyl homoserine-O-acetyl serine sulfhydrylase (met25) to build homocysteine, a direct precursor of methionine, and cysteine. Cysteine can be converted to methionine via several intermediate steps. Gene deletion of the met25 (also known as met15 or met17) thus prevents the biosynthesis of methionine and cysteine.

For experimental phasing methods heavy atoms can be either introduced into the crystal by soaking, or what is more frequently applied today, the protein is generated so that the sulfur containing amino acids methionine or cysteine are replaced by seleno- methionine (Se-Met) or seleno-cysteine (Se-Cys). Importantly, for efficient selenium labelling, the endogenous synthesis and incorporation of methionine (Met) or cysteine (Cys) is supressed or even disabled and selenium has to be added to the medium. The replacement of sulfur by selenium is often well tolerated, since only slight structural changes, if any, occur by the substitution of Met or Cys with Se-Met or Se-Cys in a protein. The first structure solved with Se-Met containing protein was described in 1990 [265]. Since then, Se-Met derivatized protein is

not only produced in *E.Coli*, but was also successfully obtained from eukaryotic cells [266-269]. In *Saccharomyces cerevisiae*, one strategy to obtain efficient replacement of Met with Se-Met requires that enzymes involved in methionine synthesis are turned off. In the BY4741 strain [270], which was used in this work, this is achieved by a gene deletion of the met25 gene (Figure 38). Like this, the main pathways for generation of methionine, but also cysteine, are interrupted. Therefore, during growth of the BY4741 strain and recombinant protein expression, Cys and Met (or Se-Met) need to be supplemented to the media. To find the optimal growth conditions for Se-Met labelled protein it might be crucial to evaluate different growth conditions.

2.10. Generation of seleno- methionine derivatized nhTMEM16

Including the first methionine at the beginning of the sequence, each nhTMEM16 monomer comprises 14 methionines in a 735 amino acid long protein chain, resulting in 28 methionines per asymmetric unit of the crystal form CF2.

For the Single Anomalous Dispersion method, this number of methionines is suitable for structure determination. For generation of Se-Met labelled protein in BY4741 cells, no protocols were available at the time of the experiments. For that reason, different strategies were tried to get sufficient amounts of the derivatized protein. Inoculation of a larger culture of Se-Met containing media with small amounts of BY4741 cells, which were grown in the presence of methionine was not successful. Cells stopped growing at low density, which was attributed to the toxicity of selenium [271]. Therefore BY4741 cells were grown to high density in media supplemented with methionine before protein expression was started. Prior to inducing protein expression with galactose, the cells were harvested sterile and regrown in media lacking methionine, until all of it was depleted. Then the media was supplemented with 100 µg ml^{-1} Se-Met and protein expression was initiated by addition of galactose. For optimal protein production addition of Se-Met to cells of different densities was investigated in small-scale cultures. The EGFP-tag was used to correlate the fluorescence detected in whole cells with the amount of protein.

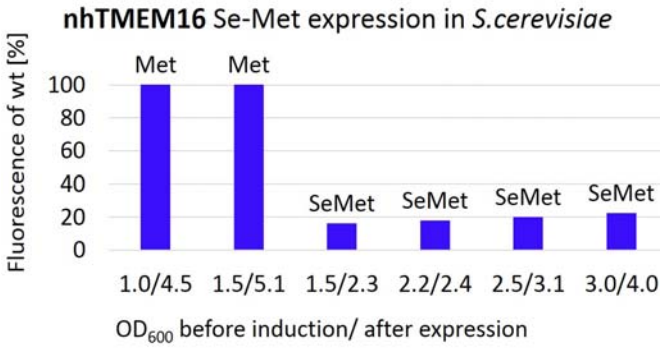

Figure 39 Optimizing expression conditions of Se-Met derivatized nhTMEM16

The expression levels of native and seleno-methionine derivatized nhTMEM16 in the *S. cerevisiae* strain BY4741 were compared and attempts were undertaken to optimize yields by induction of protein expression at different cell densities. The OD_{600} before induction and after expression are indicated below the blue bars.

Figure 39 compares the fluorescence of BY4741 cells expressing native nhTMEM16 in the presence of methionine with cells that produce the Se-Met labelled protein. The final fluorescence was slightly higher with increasing cell density at the point of Se-Met addition and induction. Se-Met incorporation into nhTMEM16 (and endogenous proteins) clearly inhibited growth of BY4741. Therefore the cells were grown to high density before addition of Se-Met and induction, which had an advantageous effect on expression. From the expression screening it was obvious that significantly lower protein expression can be obtained compared to native nhTMEM16.

For purification, 80 l of fermentation culture were grown by the described procedure and 60 g of membranes could be obtained. The fluorescence in whole cells was comparable to the values from small scale expression screening. The membranes were solubilized with DDMβ, cell debris was removed by ultracentrifugation and the protein was purified from the supernatant by incubation with NiNTA beads. nhTMEM16 was washed, eluted and subsequently dialyzed against buffer not containing any imidazole while cleaving the tag. The tag was removed by IMAC and the protein was concentrated before loading on a size exclusion column. The gel filtration profile of the Se-Met labelled protein is shown in Figure 40. The Se-Met protein produced more soluble aggregates than native nhTMEM16, presumably due to a decreased stability. The peak fractions were collected and concentrated to 5.6 mg/ml. Thereafter, the protein was supplemented with the additives that improved crystal quality and was subsequently used for crystallization in sitting drops with 1 µl volume. Only a few crystals grew. Crystals grown in CF2 were cryo-protected and data was collected at the X06SA beamline of the Swiss Light Source.

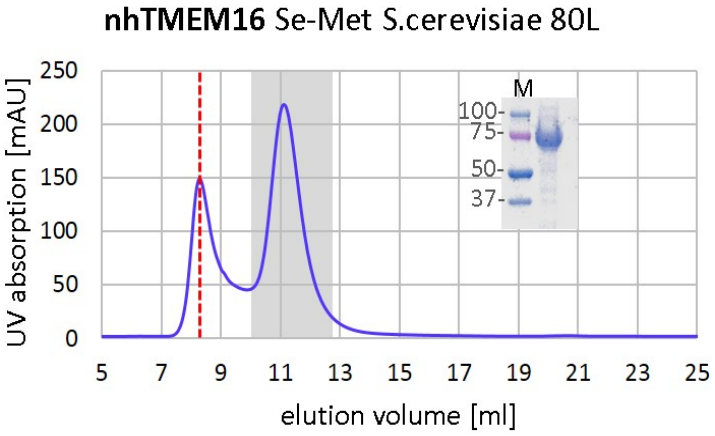

Figure 40 Gel filtration profile of Se-Met labelled nhTMEM16

The gel filtration profile of nhTMEM16 containing Se-Met instead of methionine is displayed. While the grey frame indicates the fraction of the well- folded protein at an elution volume of 11 ml, the red line at 8 ml marks protein that forms soluble aggregates. A gel of the concentrated peak fraction at 11 ml illustrates the purity and homogeneity of the sample.

A sample of the purified nhTMEM16 protein was investigated by mass spectrometry to quantify the amount of Se-Met labels in the protein. The protein was labelled inhomogeneously with 6 to 16 selenium atoms per subunit replacing sulfur. An average of 11 Se-Met residues per protein could be detected. Since nhTMEM16 contains maximally 14 Met the additional mass gain may potentially be derived from selenium atoms incorporated into seleno- cysteines (Se-Cys), since Met and thus presumably Se-Met can be converted to Cys and Se-Cys over several intermediated steps (see Figure 41 and Figure 38).

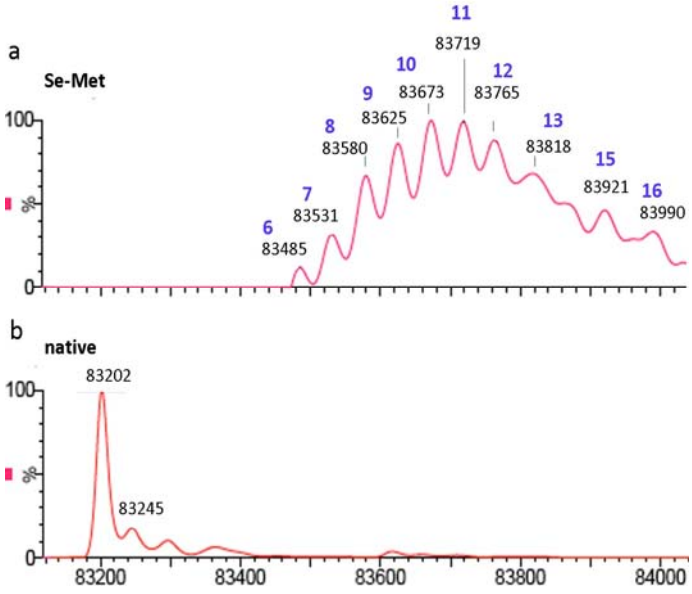

Figure 41 Se-Met incorporation revealed by mass spectrometric analysis

Se-Met derivatized and native protein were investigated by mass spectrometry. The X- axis denotes the mass to charge ratio (m/z). The mass difference between a selenium and a sulfur corresponds to 46.8 Dalton. a, Mass spectrum of the Se-Met derivative. An average of 11 Se-Met were confirmed per nhTMEM16 monomer, but the selenium incorporation was heterogenous with different protein species containing between 6 and 16 selenium atoms in place of sulfur, as indicated by the blue numbers. b, Native nhTMEM16, as reference sample, is composed of a single species (indicated by the uniform peak) and had a mass of 83202 Dalton.

2.11. Structure determination of nhTMEM16 by the Se-Met SAD method

Anomalous data of crystals of CF2 containing seleno- methionine derivatized protein was collected at the absorption edge of selenium, at a wavelength of 0.97972 Å. Since the crystal was comparably small, data collection was carried out carefully. To minimize the radiation damage, the beam was attenuated and highly redundant data was collected with 0.5° rotation increment per image. Data was collected from two non-overlapping regions of the crystal, which allowed the collection of two data sets. In total 2400 images were recorded, covering a total rotation of 1200°. XDS was used for indexing, integration and scaling [272]. Table 8 shows an overview of the statistics of the merged data set at different resolution shells. The crystals diffracted to a resolution of close to 4 Å at an I/σI of 2.27 at the highest resolution shell. The data was complete, had a 23-fold redundancy (with a 16-fold redundancy in the highest resolution shell, i.e. between 4.0-4.1 Å). SigAno, describing the anomalous differences over the measurement error, was 1.26 over the entire resolution range, had a value of 4.2 in the lowest resolution shell and decayed to 1.067 around 5.5 Å.

SUBSET OF INTENSITY DATA WITH SIGNAL/NOISE >= -3.0 AS FUNCTION OF RESOLUTION

RESOLUTION LIMIT	NUMBER OF REFLECTIONS OBSERVED	UNIQUE	POSSIBLE	COMPLETENESS OF DATA	R-FACTOR observed	R-FACTOR expected	COMPARED	I/SIGMA	R-meas	CC(1/2)	Anomal Corr	SigAno	Nano
20.00	7387	307	330	93.0%	3.8%	4.1%	7387	90.69	3.8%	100.0*	95*	4.235	111
10.00	51461	2310	2310	100.0%	4.0%	4.4%	51461	73.03	4.1%	100.0*	90*	3.633	994
8.00	57692	2500	2500	100.0%	5.0%	5.2%	57692	58.81	5.1%	100.0*	81*	2.768	1126
7.00	57399	2537	2537	100.0%	9.8%	9.4%	57399	34.66	10.0%	99.9*	64*	2.015	1166
6.50	46117	1924	1924	100.0%	16.8%	16.4%	46117	22.18	17.2%	99.7*	51*	1.543	889
6.00	63569	2603	2603	100.0%	22.9%	23.0%	63569	17.06	23.4%	99.4*	36*	1.220	1213
5.50	86097	3664	3664	100.0%	28.4%	28.6%	86097	13.73	29.0%	99.0*	25*	1.067	1716
5.00	121024	5219	5219	100.0%	34.0%	34.6%	121024	11.38	34.8%	98.6*	14*	0.916	2459
4.50	187522	7848	7848	100.0%	41.2%	41.7%	187522	9.68	42.1%	98.4*	8	0.856	3717
4.30	101874	4202	4203	100.0%	66.2%	66.6%	101874	6.29	67.6%	95.7*	3	0.819	1997
4.10	116904	5119	5119	100.0%	103.7%	104.8%	116904	3.88	106.1%	90.0*	-1	0.772	2441
4.00	46609	2936	2936	100.0%	137.9%	140.4%	46609	2.27	142.5%	71.1*	-3	0.723	1400
total	943655	41169	41193	99.9%	11.7%	12.0%	943655	18.39	12.0%	100.0*	32*	1.258	19229

Table 8 Statistics of crystals from seleno-methinine derivatized nhTMEM16

The figure shows the statistics of the anomalous data collected from seleno- methionine derivatized crystals. The resolution limit of the crystal at a given I/σI, the completeness of the data set, the corresponding R-factors and the anomalous signal (SigAno) are indicated.

SHELXC and D [273, 274] were used to determine the heavy atom substructure and identify the 28 selenium sites in the asymmetric unit in the anomalous difference Patterson map using Patterson superposition methods.

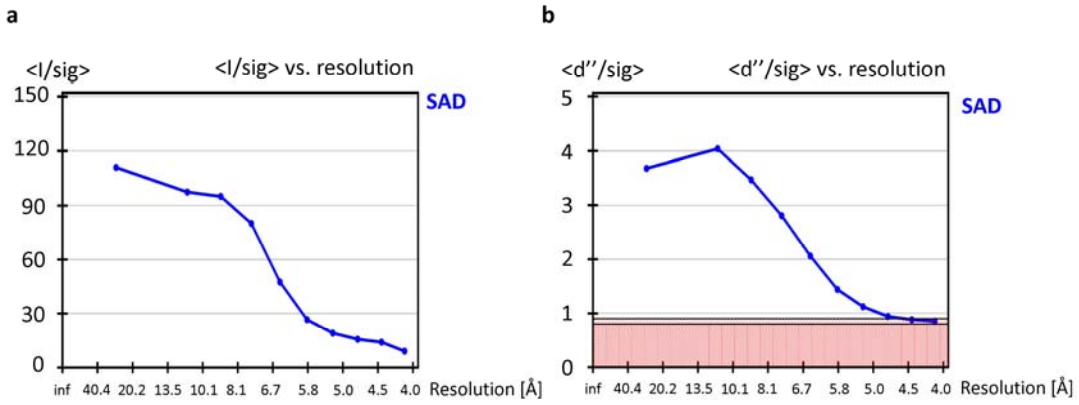

Figure 42 Statistics from SHELXC

I/σI and and the anomalous differences d''/σI are shown in dependence of the resolution. a, Total intensity data was cut below an I/σI of 2. b, The anomalous differences over background (d''/σI) is plotted against the resolution. As already seen during processing, the anomalous signal was predicted to extend to approximately 5.0 or 5.5 Å indicated by the drop to 1.

The resolution limit of the crystals was predicted to be around 4.1- 4.2 Å. The corresponding signal-to-noise ratio is depicted in Figure 42a. The drop of the data intensity and the anomalous signal with resolution is shown in Figure 42b. A measurable anomalous signal was detected to a resolution between 5.0- 5.5 Å.

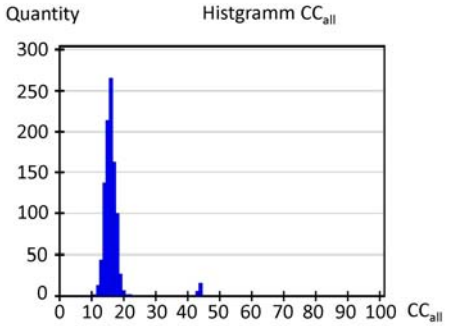

Figure 43 Solutions obtained with SHELXD

Histogram of possible solutions for the substructure calculated by SHELXD with 2000 trials. Most solutions were wrong as indicated by the low weighted correlation coefficient (between the normalized structure factors E_{obs} and E_{calc}) termed CC_{all}, with values of 10-20%, while only few solutions contained a higher CC_{all}, which predicted a correct solution for the substructure.

A correct solution for the heavy atom substructure is usually indicated by a correlation coefficient that is significantly higher (usually higher than 35%) than the distribution of wrong solutions. In this case the correct solution had a correlation coefficient of 45%, while wrong solutions were distributed around 20%. A likelihood distribution of all found solutions is illustrated in Figure 43. SHELXD was also used to assess the relative occupancies of the selenium sites (between 0 and 1) to separate reliably identified sites from sites that were found based on noise. Usually an occupancy over 0.25 (or 25%) is indicative for significant sites. According to this criterion, 23 selenium sites were reliable (Figure 44).

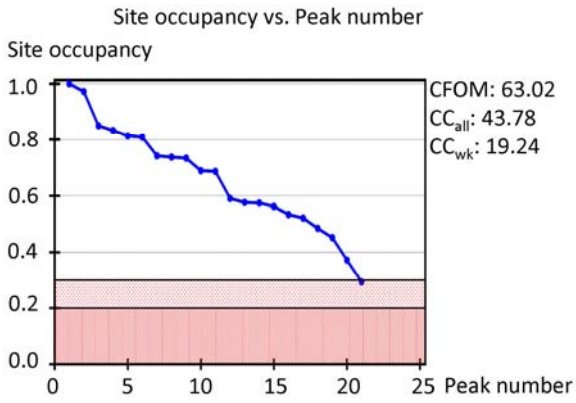

Figure 44 Statistical output of SHELXD: Selenium site occupancy

Significance of the calculated Se-Met sites analyzed by SHELXD. The site occupancy is plotted against the number of peaks.

An ambiguity arising from the substructure determination by the Patterson methods is the hand problem, which develops from losing the direction of the anomalous signal, thus the anomalous differences are the same for both solutions of the atomic substructure. This ambiguity was resolved in SHELXE, which performed density modification on a map calculated from a set of derived phases, which made it possible to distinguish between the two solutions, and select the correct hand of the heavy atom substructure over the wrong enantiomorphic solution. The correct solution was indicated by a higher contrast after density modification (Figure 45).

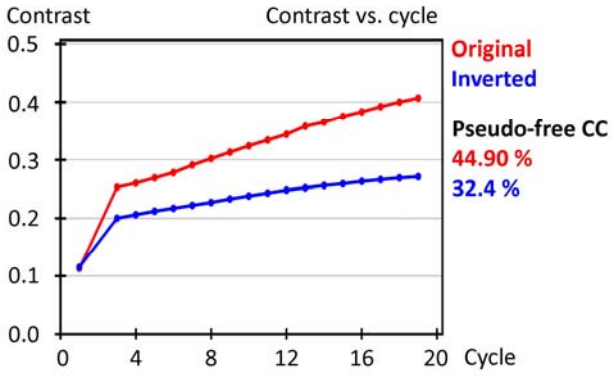

Figure 45 Density modification by SHELXE

The contrast of the electron density is mapped against the numbers of density modification cycles calculated by SHELXE. A higher contrast indicated the correct hand of the atomic substructure.

The substructure coordinates obtained from SHELXD were subsequently further refined resulting in selenium sites with improved values for the coordinates, B-factors, occupancies and initial set of SAD-phases to 5 Å were calculated with SHARP [275]. A first map was calculated after solvent flipping, but this map was not of sufficient quality and resolution to allow structure determination. To improve the map and extend the resolution, non- crystallographic symmetry (NCS) and cross crystal averaging was applied. The initial SAD phases were optimized and elongated to 4.0 Å in DM [276] by solvent flattening, histogram matching and NCS averaging between the two subunits present per asymmetric unit in CF2. NCS symmetry operators were obtained from NCS-related positions of the heavy atom substructure, and a mask covering the approximate extent of a subunit was calculated after the placement of helices in the electron density at low resolution, calculated after solvent flipping.

	nhTMEM16/CF1	**nhTMEM16/CF2**
Refinement		
Resolution (Å)	15- 3.3	15- 3.4
No. reflections	38985	36750
Rwork/ Rfree	23.8 (28.5)	24.8 (29.2)
No. atoms	10574	10574
Protein	10570	10570
Ligand/ ion	4	4
B-factors		
Protein	137	159
Ligand/ ion	104	146
R.m.s deviatios		
Bond lengths (Å)	0.003	0.002
Bond angles (°)	0.74	0.7

Table 9 Statistics of the refinement

Data in parenthesis corresponds to highest resolution shell.

The same procedure was also applied for the native crystals of CF2, for which data to 3.4 Å was collected and which were isomorphous to the Se-Met crystals. Significantly improved electron density allowed to

build a coarse model of the protein in O [277], mainly containing transmembrane helices. This model was subsequently used as search model for molecular replacement to localize the two copies in the asymmetric unit of CF1 using PHASER [278]. In a second density modification step employing cross-crystal averaging between the two crystal forms CF1 as well as CF2 and NCS averaging between the two subunits in the asymmetric unit of each crystal form, the phases were significantly improved and extended to 3.3 Å, which corresponds to the diffraction limit of the native data set of CF1. The improved electron density allowed the building of an atomic model using O and COOT [279], which was refined in CNS and PHENIX [280]. Table 9 summarizes the statistics of the refinement using CF1 and CF2. The quality of the electron density after refinement is illustrated in Figure 46, which shows a detail of the atomic model with $2F_o$-F_c electron density superimposed, that was built from the resulting electron density.

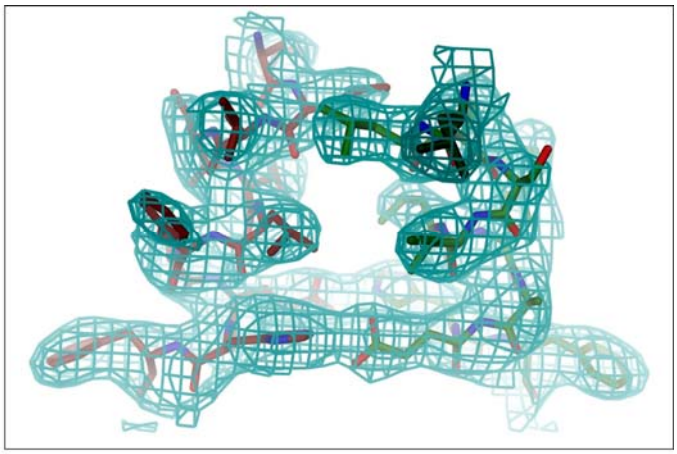

Figure 46 Electron density of the refined model

2Fo–Fc density of CF1 (calculated at 3.3 Å and contoured at 1σ after sharpening with b=50) in the transmembrane part of helices α10 is shown as cyan mesh superimposed on a stick model of the protein.

R and R_{free} were monitored throughout the refinement. R_{free} was calculated from 5% of the reflection data that were not included in the refinement. The model was initially built into experimental electron density for CF1 and later also refined against 3.4 Å- data of CF2. The final R/R_{free} values in CF1 were 23.7% and 28.2% respectively and no outliers were detected in the Ramachandran plot of the model. The conformation of the dimeric protein in both crystal forms is virtually identical. The final model contained 654 out of 735 residues per subunit. Residues 1-18, 130-140, 465-482, 586-593, 657-659, 685-691 and 720-735 could not be built due to lack of electron density. The structures of the two crystal forms can be found with PDB entry 4WIS and 4WIT in the PDB protein database.

2.12. Methionine mutants

The quality of the experimental electron density and knowledge of the Selenium positions allowed the assignment of a large part of the amino acids of the nhTMEM16 sequence in the atomic model. However, in some parts of the structure the electron density was poor and some regions of the model lacked native methionine and thus Se-Met positons as important checkpoints to confirm the correct register of the model. These poorly defined regions were mainly found in parts of the amino- and carboxy terminus and in certain loop regions of nhTMEM16. To introduce additional checkpoints in regions lacking native

methionine, methionine mutations were introduced to regions of the protein, where the sequence could not be assigned with certainty.

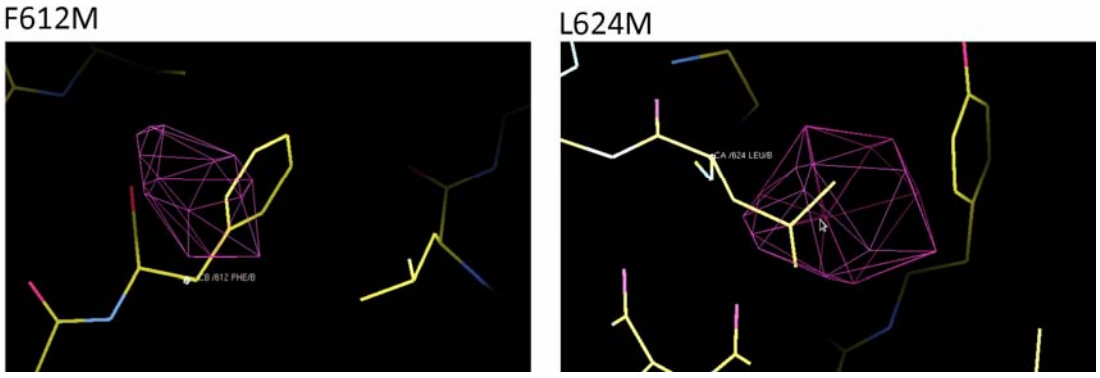

Figure 47 Anomalous difference density map of data collected from Met mutants

The anomalous difference density map of two methionine mutants, F612M and L624M, (calculated at 5.0 Å and contoured at 3.5 σ, magenta mesh) is displayed in relation to the nhTMEM16 model structure. The difference densities coincided with the side chains of the model structure.

Since the expression and growth of Se-Met derivatized crystals was challenging, attempts were made to identify the introduced methionine positions by exploiting the anomalous scattering of sulfur. Expression of the mutants was carried out by the standard methods resulting in comparable yields as obtained for WT. The protein was purified and crystallized as described in previous chapters. Since the anomalous scattering of sulfur is very small, the data was collected with very high redundancy and low beam intensity at a wavelength 1.95 Å, to maximize the anomalous signal. In two cases the anomalous difference map indicated the location of the additional sulfur site due to the insertion of methionines. In Figure 47, the anomalous difference map, that was obtained from data of two mutants in the C-terminal part of the transmembrane domain, F612M and L624M, is shown in relation to the model of nhTMEM16. Since positive difference density in both maps overlapped with the position of F612 and L624 respectively, it was concluded that the register of the model was correct. This approach was also used for several other sites at the N- and C-terminus, but due to the poor order in these regions, no difference densities could be observed.

2.13. Detecting the anomalous signal of Ca^{2+} to identify Ca^{2+} binding sites

The anomalous scattering properties of Ca^{2+} ions included in the crystallization buffers were exploited to determine the location of Ca^{2+} binding sites in the protein. Anomalous difference density of Ca^{2+} was calculated highly redundant from the WT protein at low beam intensity at a wavelength of 1.95 Å. The best data for that purpose was obtained for crystal form CF2. In the anomalous difference map two peaks of strong electron density were obtained for each Ca^{2+} binding site indicating the presence and binding of potentially two Ca^{2+} ions per subunit.

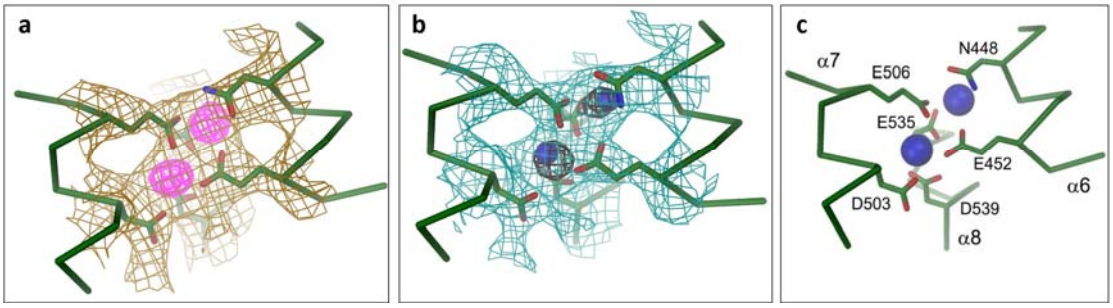

Figure 48 Ca^{2+} binding site

The anomalous scattering properties of Ca^{2+} were exploited to elucidate the localization of the Ca^{2+} binding site. The protein is shown as Cα-trace with side-chains of residues interacting with Ca^{2+} ions shown as sticks. a, View of the Ca^{2+} binding site in CF2. The $2F_o - F_c$ electron density (calculated at 3.5 Å, contoured at 1 σ, orange) is shown superimposed on the refined structure. Anomalous difference electron density (calculated at 3.8 Å, contoured at 5 σ) is shown in magenta. b, Ca^{2+} binding site in CF1. The $2F_o - F_c$ electron density (at 3.3 Å , 1 σ, cyan, 5 σ, black) is illustrated superimposed on the model of the refined structure containing Ca^{2+} ions (blue spheres). c, Model of the Ca^{2+} binding site. Residues and helices are appropriately numbered. Ca^{2+} ions are indicated by blue spheres.

2.14. Aiming for a Ca^{2+}-free conformation of nhTMEM16

Although the stability and thus the final yield of the protein decreased significantly during purification in the absence of Ca^{2+}, it was nevertheless possible to grow crystals in CF2. The purification was partially carried out in the presence of EGTA, but in crystallization solutions containing EGTA, no crystals were obtained. Thus for crystallization no EGTA was included. Crystals were cryo-protected, mounted, and highly redundant data was collected at 1.95 Å to detect residual Ca^{2+}, as described previously. The crystal grown in the absence of Ca^{2+} diffracted to a resolution of 4.2 Å. The data was complete with a redundancy of 18. Anomalous differences extended to 8 Å (Figure 49). The crystals were isomorphous to the crystal form grown in high Ca^{2+}, and a model of that crystal form not containing any Ca^{2+} ions refined well. The structure of the protein crystallized in the absence of Ca^{2+} was found to be very similar to the structure of crystals grown in the presence of high concentrations of Ca^{2+}.

RESOLUTION LIMIT	NUMBER OF REFLECTIONS OBSERVED	UNIQUE	POSSIBLE	COMPLETENESS OF DATA	R-FACTOR observed	R-FACTOR expected	COMPARED	I/SIGMA	R-meas	CC(1/2)	Anomal Corr	SigAno	Nano
20.00	6227	320	343	93.3%	5.8%	6.3%	6227	52.66	5.9%	99.8*	71*	1.758	117
10.00	43961	2403	2403	100.0%	5.9%	6.6%	43961	44.43	6.1%	99.9*	55*	1.391	1036
8.00	50229	2641	2641	100.0%	7.8%	8.1%	50229	35.91	8.0%	99.9*	24*	1.045	1193
6.00	142649	7386	7386	100.0%	24.8%	26.3%	142649	15.57	25.5%	99.5*	3	0.823	3420
5.00	171887	9251	9251	100.0%	60.5%	62.0%	171887	7.50	62.2%	97.2*	2	0.811	4351
4.40	197594	10308	10309	100.0%	90.3%	92.8%	197594	5.03	92.7%	95.3*	4	0.823	4889
4.30	42958	2326	2327	100.0%	181.3%	196.0%	42958	2.51	186.5%	80.7*	-1	0.692	1108
4.20	45224	2543	2543	100.0%	233.7%	252.9%	45224	2.04	240.6%	75.3*	-8	0.675	1211
total	700729	37178	37203	99.9%	15.2%	16.1%	700729	12.53	15.6%	99.8*	7	0.857	17325

Figure 49 Statistics on data collected in the apparent absence of Ca^{2+}

Data statistics of a crystal prepared without addition of Ca^{2+}.

However, residual positive F_o-F_c density at the Ca^{2+} binding site obtained after refinement of the model not containing Ca^{2+} ions and corresponding peaks in the anomalous difference density map indicated the presence of Ca^{2+} in the binding site, as shown in Figure 50. Due to the lower resolution of the crystal and the weaker anomalous signal compared to previous data sets obtained in the presence of Ca^{2+}, the electron densities are of lower resolution and thus less well resolved. While from these data, the number of Ca^{2+} peaks per binding site is no longer obvious, it is clear that there is still a substantial amount of Ca^{2+} bound.

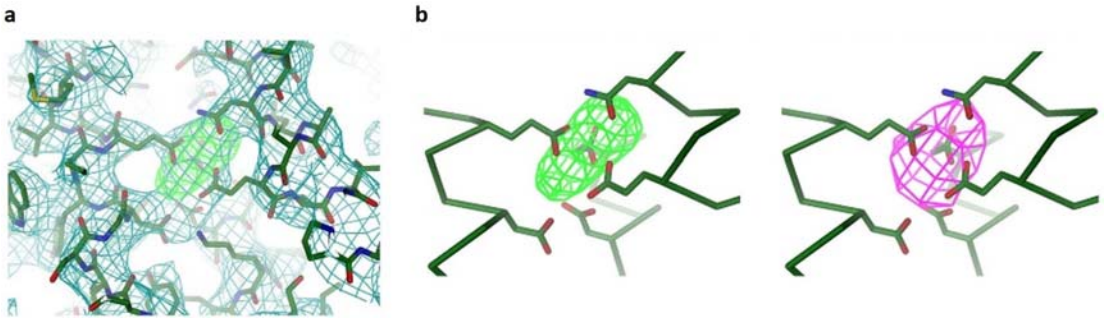

Figure 50 Electron density in the 'Ca^{2+}-free' structure

Close-up view of the Ca^{2+} binding site. a, The 2Fo – Fc electron density (cyan mesh, calculated at 4.2 Å and contoured at 1σ after sharpening with a b = 50) and the Fo – Fc density (contoured at 3σ, green) is superimposed on the refined model. No ions were included in the refinement. b, The F_o–F_c density (left, contoured at 3σ, green) and the anomalous difference density (right, calculated at 6 Å and contoured at 4σ, magenta) suggested the presence of bound Ca^{2+} ions.

2.15. nhTMEM16 as template for the architecture of TMEM16 proteins

Although members of the TMEM16 family show large differerences in their function and physiological roles, it can be assumed that TMEM16 homologues share a similar architecture [15, 167, 176, 230]. The sequence identity of TMEM16 proteins from distanly related organisms such as fungi and mouse is still as high as 25%, with higher identity between members of closely related organisms. Thus, structural information acquired for a fungal TMEM16 homologues applies also to other family members. The high-resolution crystal structure of a TMEM16 homologue from the fungus *Nectria haematococca*, nhTMEM16, was solved at 3.3 Å. This chapter does not aim for a detailed description of the structure (for a detailed description see chapter 2.18 X-ray structure of a calcium- activated TMEM16 lipid scramblase). Rather the most prominent and striking features of the stucture are briefly described here and are further discussed (chapter 3 Discussion).

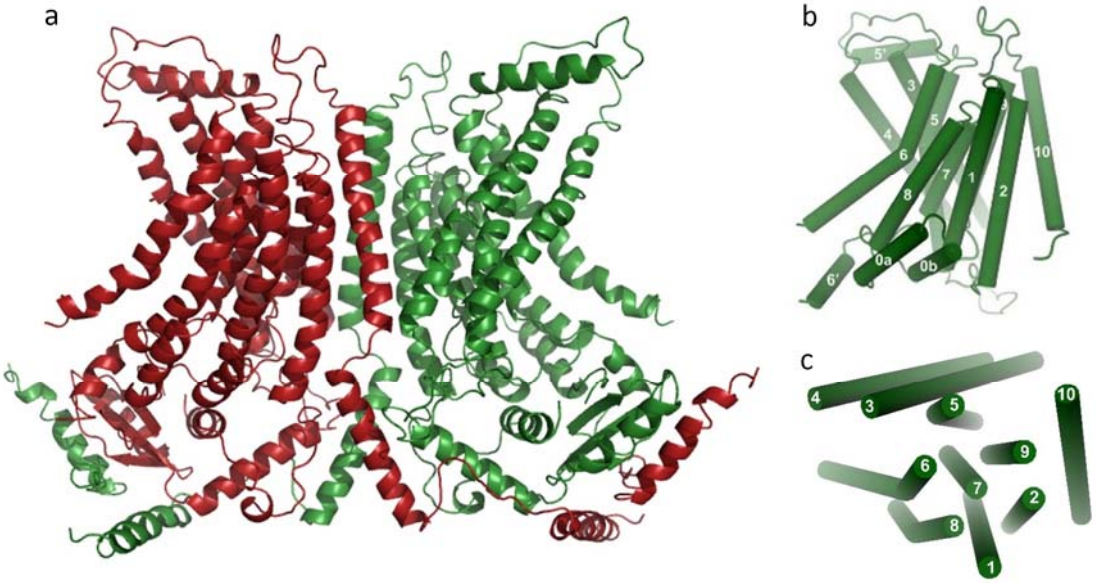

Figure 51 The structure of nhTMEM16

View of the nhTMEM16 crystal structure. a, The protein forms a homodimer (red/green) with ten transmembrane spanning helices per subunit. The amino- and carboxy termini are located on the cytoplasmic side. b and c, Helices of the transmembrane part of one subunit of the dimer are shown as cylinders and labeled with the corresponding numbers. b, front view as in a. c, Top view.

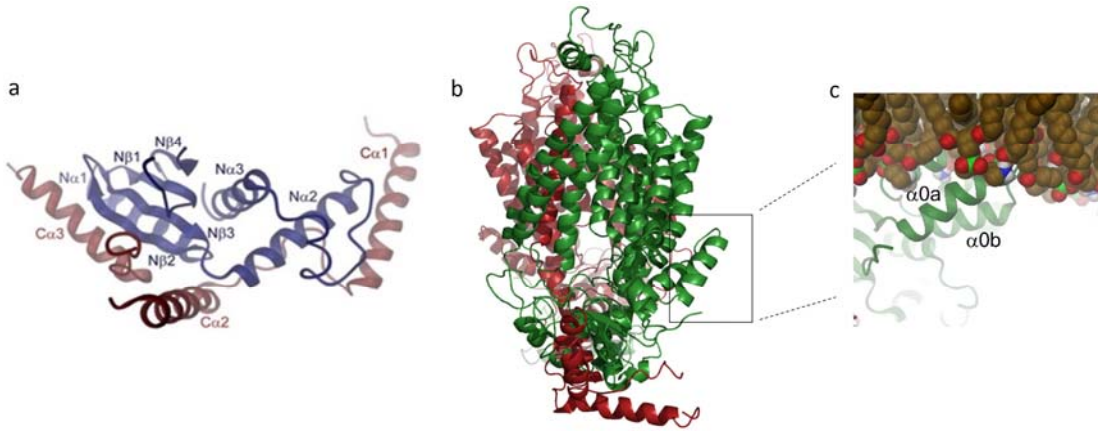

Figure 52 Features of the amino- and carboxy termini

a, In the dimer the C-terminus of one subunit (red) interacts with the N-terminus from the other subunit (blue) over a large area. The N-terminus adopts a ferredoxin-like fold. α-helices and β-sheets are labelled. b, Side view of the nhTMEM16 structure. A detail is framed and enlarged in c, showing two short α helices (α0a and α0b), which form a hairpin that most likely is in contact with the lipids of the membrane. Modelled lipids were obtained from http://www.lobos.nih.gov/mbs/coords.shtml.

As illustrated in Figure 51, nhTMEM16 forms a homodimer with ten transmembrane spanning helices per subunit (α1-10) and overall dimensions of approximatly 50 x 50x 130 Å. Both, the amino- and

carboxy termini are structured and point to the cytosol. The amino- terminus adopts a ferredoxin-like fold (Figure 52a) and the carboxy terminus of one subunit wraps around the amino- terminus of the neighboring subunit, thereby providing a large interface for interaction.

As shown in Figure 52b and c, the transmembrane part is preceeded by two short α-helices (α0a and α0b) that form a hairpin with amphiphilic properties. These contain the two motifs 'FPLHD' and 'FGEK' (Figure 13, Figure 14 and Figure 52) as the only consensus in the amino- terminus between distantly related TMEM16 proteins. Most likely, within a lipid bilayer these two helices may form a contact with the inner leaflet of the membrane, as seen in Figure 52c.

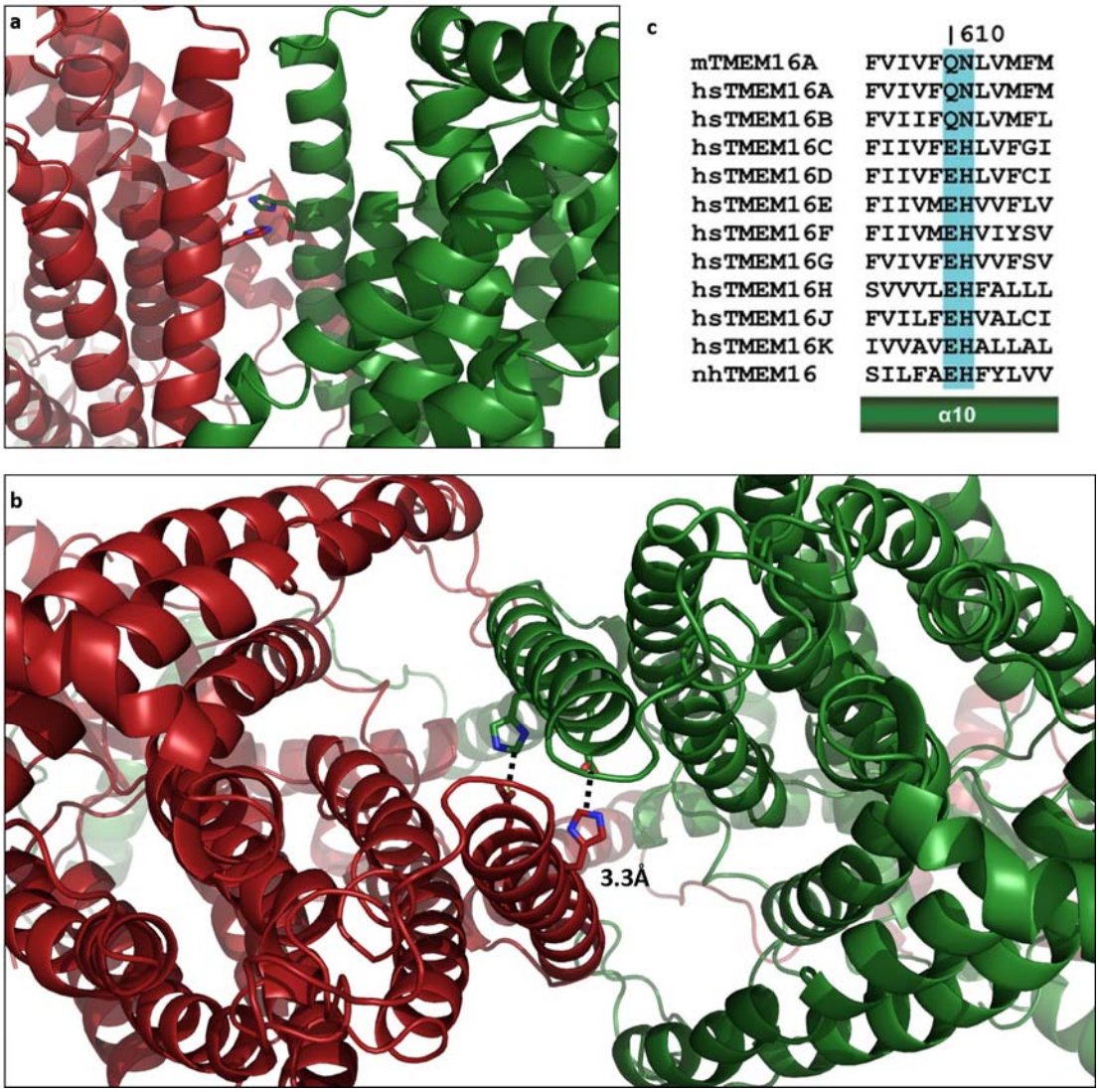

Figure 53 Mutual interaction between conserved glutamates and histidines

Intersubunit interactions between helices α10 and an alignment are depicted. A salt bridge is formed by a pair of glutamates and histidines of adjacent subunits. a, Front view of the nhTMEM16 structure. b, Top view. The distance between the respective glutamates and histidines was measured to be 3.3 Å. c, Sequence alignment of α10 of various TMEM16 family members. The interacting residues are marked in cyan.

Mutual interactions occur between transmembrane helices α10 involving equivalent residues of the two subunits in the dimer (Figure 53). There, the close location of a pair of glutamates and histidines allows the formation of two close-by saltbridges as shown in Figure 53. Importantly, this pair of salt bridges is conserved among most TMEM16 family members, except for TMEM16A and B homologues, where a glutamine and an asparagine is found instead at equivalent positions (Figure 53c).

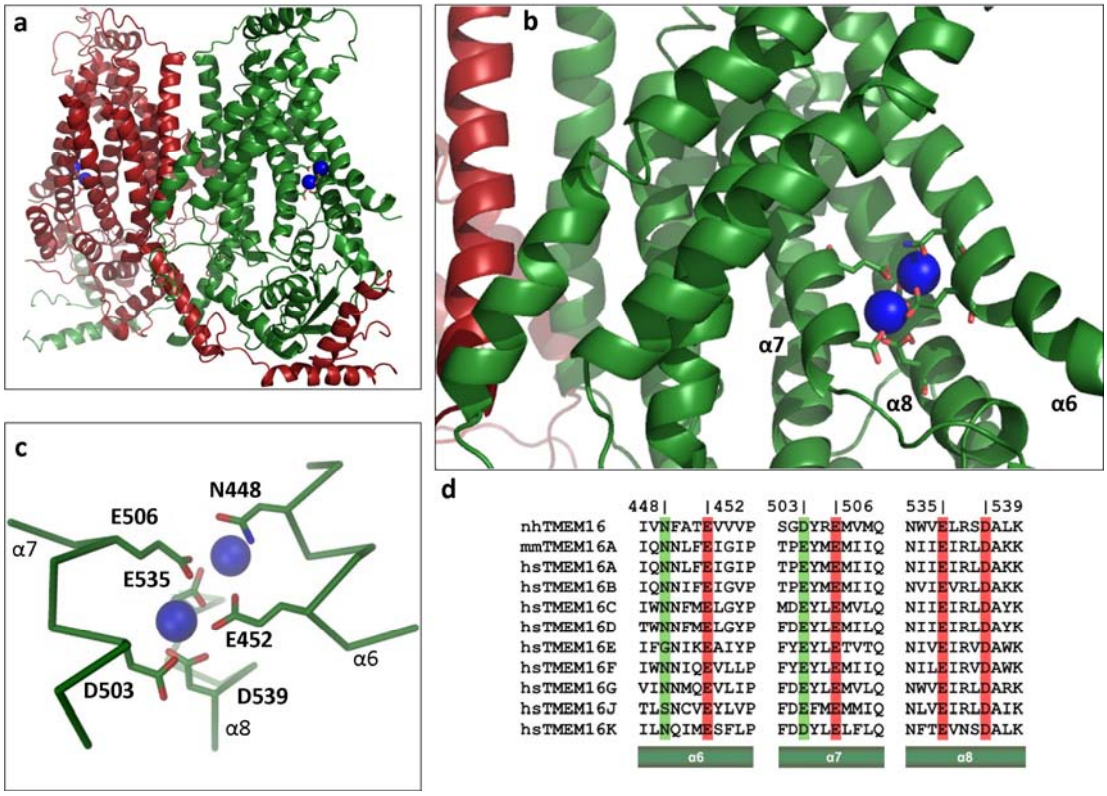

Figure 54 The Ca^{2+} binding site

Ca^{2+} binding site. The structure is shown as cartoon, and side chains of residues involved in Ca^{2+} coordination are displayed as sticks. The dimer is shown in red/ green and the Ca^{2+} ions are illustrated as blue spheres. a, The nhTMEM16 structure and b, region surrounding the Ca^{2+} binding site are depicted to indicate the location of the Ca^{2+} binding site. In b, the helices that are involved in Ca^{2+} binding are labeled. c, Stick model displaying the Ca^{2+} binding with bound Ca^{2+} ions with important residues and helices labelled. d, Sequence alignment of α-helices 6, 7 and 8 from various TMEM16 homologues underlining the conservation of residues involved in Ca^{2+} binding. Identical residues are marked in red and similar residues in green. The numbering is as in c.

The amomalous difference densitiy map collected at long wavelength revealed the location of a Ca^{2+} binding site in each subunit of the dimer and suggested that two Ca^{2+} ions may be bound to this site (Figure 54). The occupancy could not be determined with certainity from the crystallographic data, but simoultaneous occupation seems possible due to the large number of negative charges in the binding site. Furthermore, since during the refinement the B-factors didn't differ significantly from the B-factors of surrounding residues it appears that two Ca^{2+} are bound at the same time. Six residues, five of which carry a negative charge, control the coordination of the two Ca^{2+} ions placed at a distance of 4.2 Å from

each other. The residues invovled in Ca^{2+} binding are highly conserved among most TMEM16 family members (Figure 54d). Interestingly, the Ca^{2+} binding sites are embedded within the transmembrane part of the protein, and they consist of residues residing on transmembrane helices 6, 7 and 8.

In close proximity to the Ca^{2+} binding site a narrow cavity, 10-14 Å in width, spans the entire transmembrane part of the protein in the diagonal direction, comparable to a spiral staircase. This cavity, the subunit- cavity, is surrounded by transmembrane helices 3- 7 and 9 (Figure 55). Interestingly, although facing the hydrophobic environment of the membrane, the surface of the subunit- cavity is highly hydrophilic. Notably, it accomodates residues for which equivalent positions have been reported to be important for ion conduction in TMEM16A [12] and to influence the selectivity in TMEM16A [188] and TMEM16F [9]. Thus, according to these observations, it appears that the subunit- cavity would constitute the translocation path in both, channels and scramblases. However, the electron density of the data was not strong enough to confirm the location of lipids in the subunit- cavity.

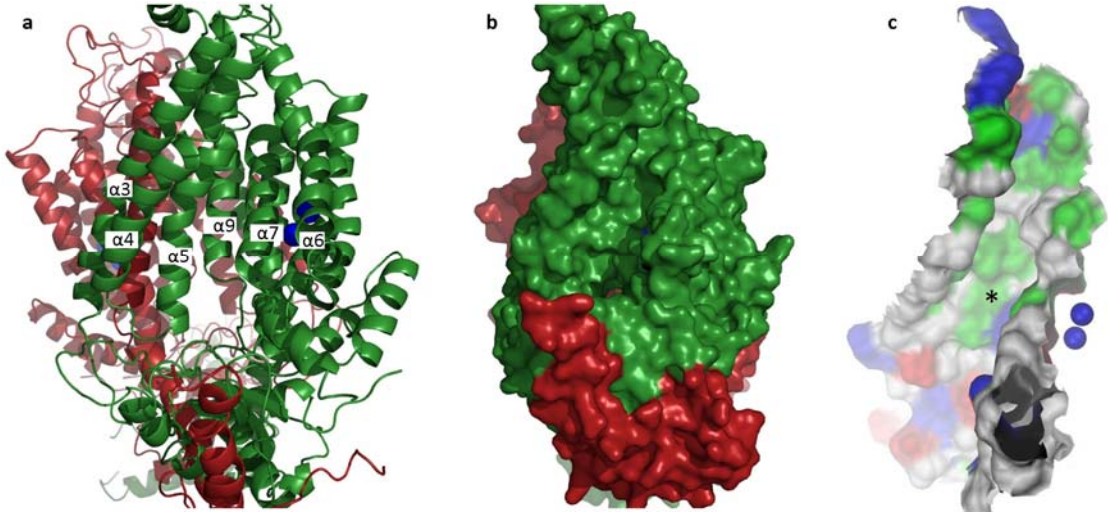

Figure 55 Subunit- cavity

Subunit- cavity of nhTMEM16. In a and b, the dimer is depicted in red and green. a, The protein is shown as cartoon. Ca^{2+} ions are indicated by blue spheres and the transmembrane helices contributing to the subunit- cavity are numbered accordingly. b, The solvent- accessible surface of the protein is shown with the same view as in a. c, The solvent-accessible surface of the subunit- cavity is colored according to the properties of contacting residues (blue, basic; red, acidic; green, polar). The Ca^{2+} ions bound to the Ca^{2+} binding site are displayed as blue spheres. A residue that was previously reported to influence the ion selectivity in TMEM16F is marked by an asterisk (*).

2.16. Investigating the function of nhTMEM16

The function of TMEM16A and B as Ca^{2+}-activated chloride channels was investigated thoroughly using electrophysiological methods [4-7, 155, 182, 187]. TMEM16F was characterized as non-selective, small-conductance cation channel [9] and was further proposed to be involved in phospholipid scrambling in a Ca^{2+} dependent manner [10]. Other members of this family were proposed to have a role in phospholipid scrambling as well [111]. Besides the *Saccharomyces cerevisiae* TMEM16 homologue, whose only known function is the tethering of the cortical ER to the plasma membrane [224], no other fungal

members of the TMEM16 family were examined until recently. afTMEM16 (termed afu2TMEM16 in this work) was successfully reconstituted into liposomes and its function was investigated with regard to its ion conductance and lipid scrambling properties [170]. In these studies afTMEM16 was characterized as a non-selective Ca^{2+}- activated ion channel using bilayer measurements and flux assays. Furthermore, by means of a scrambling assay using purified afTMEM16 reconstituted into liposomes, the transport of phospholipids was demonstrated and the activity of the protein was shown to be dependent on Ca^{2+} [170].

2.16.1. Phospholipid scrambling by nhTMEM16

The scrambling of TMEM16F was previously analyzed in a cellular system. In this cellular scrambling assay, fluorescently labelled 7- nitrobenz- 2- oxa-1, 3- diazole (NBD) lipids were incorporated into the outer leaflet of the plasma membrane. In the presence of a scramblase, e.g. TMEM16F, these NBD-lipids get rapidly equilibrated and therefore transported to the inner leaflet upon activation by Ca^{2+}. Fatty-acid free BSA was subsequently used to extract NBD- lipids, that remained in the outer leaflet, and thus the fraction of fluorescent lipids, that was translocated to the inner leaflet can be estimated. However, since a cellular system is very complex, it is often difficult to investigate individual components of a cell and thus conclusions about an observed functional phenotype need to be drawn carefully. Furthermore, it is assumed that the protein of interest targets to the plasma membrane, where the scrambling of fluorescent lipids is expected to occur in this assay.

A direct method to explore the function of membrane proteins involves the purification and reconstitution of the protein into artificial vesicular bilayers, so called liposomes. In such a cell- free system the function of a membrane protein can be studied without interference by other membrane components. For studying transport processes, since they are vectorial, a compartmentalized system is required where a membrane partitions two compartments. In such a setup transport can only occur through membrane proteins that are part of this system. The method to reconstitute membrane proteins for functional investigations was developed in the early 1970s [281, 282] and was subsequently expanded to be applicable to proteins solubilized in different detergents [283, 284].

Since the expression of nhTMEM16 in HEK cells is mainly intracellular (see Figure 17), the scrambling activity of nhTMEM16 could not be investigated in a cellular assay. Instead, nhTMEM16 was reconstituted into liposomes for functional analysis. The reconstitution method used in this work is adapted from Rigaud and Lévy [285] and Geertsma [286] (for details see chapter 4.11 Liposome preparation and scrambling assay). Ca^{2+}, necessary for activation, and small amounts of head-group labelled fluorescent NBD- lipids were included symmetrically during liposome preparation. The NBD-group is particularly suited as fluorophore, since it can be reduced by a reducing agent to abolish the fluorescence. In the scrambling assay used in this work, which was adapted from McIntyre et al, Williamson et al and Malvezzi et al [170, 287, 288], dithionite ($S_2O_4^{2-}$) application to the outside only affects the NBD- lipids that are contained in the outer leaflet of the liposome, while the NBD- lipids that are localized in the inner leaflet are not reduced. The addition of dithionite to protein- free liposomes therefore resulted in a 50% loss of fluorescence. Since, as previously shown [170], an activated

scramblase transports different types of lipids including NBD-lipids between the two leaflets of the liposome, the fluorescence would drop to zero after dithionite addition (Figure 56).

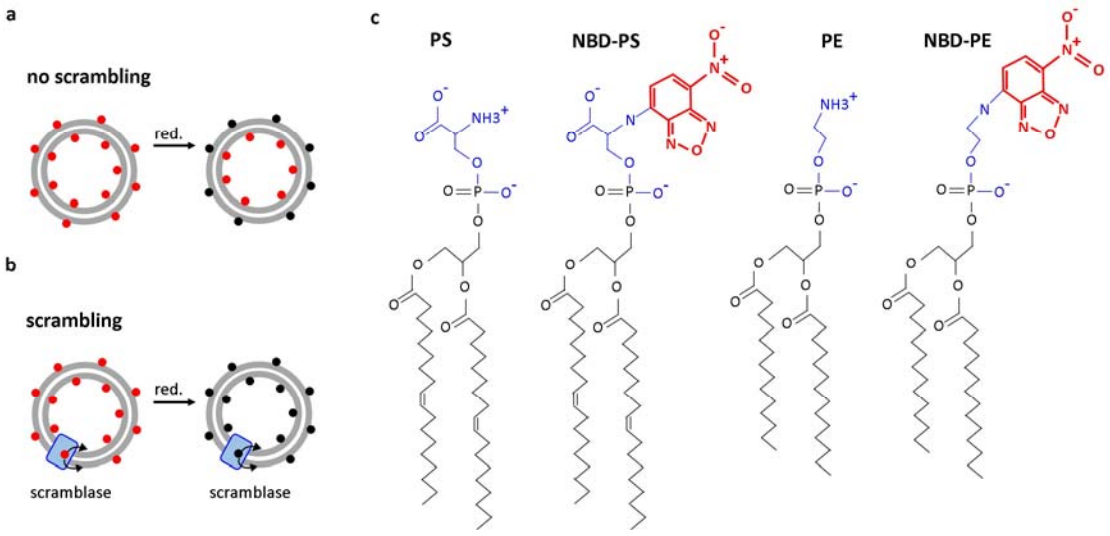

Figure 56 Scrambling assay in liposomes and NBD-lipids

a and b, Schematic representation of the scrambling measurements in liposomes. Fluorescently labelled 7-nitrobenz-2-oxa-1,3-diazole (NBD) lipids are incorporated symmetrically into liposomes (red dots). The application of a reducing agent (red.) from the outside leads to the elimination of the fluorescence on the outer leaflet of the membrane (black dots). a, Liposomes not containing protein. b, Liposomes reconstituted with a scramblase. c, NBD-lipids used in this work included head group NBD-labelled 1,2-dimyristoyl-sn-glycero-3-phosphoethanolamine (NBD-PE) and 1,2-dioleoyl-sn-glycero-3-phospho-L-serine-N (NBD-PS). PE and PS is illustrated for comparison. Lipids drawn with ChemDraw Pro 12.0.

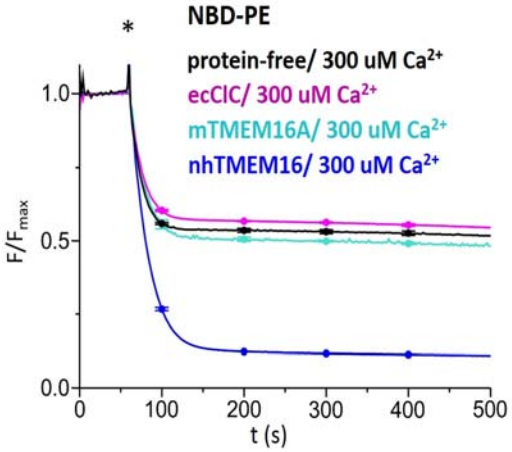

Figure 57 Scrambling of NBD-PE by nhTMEM16

The scrambling of NBD-PE by nhTMEM16 was investigated using a fluorescence- based assay. The fluorescence decay (excitation 470 nm, emission 530 nm) was compared between protein-free liposomes (black trace) and proteoliposomes containing nhTMEM16 (blue trace) or different chloride transport proteins, that are unable to scramble phospholipids (cyan and magenta trace). 300 µM free Ca^{2+} was present in all buffers. Addition of 30 mM dithionite after 60 seconds is marked by an asterisk (*). The fluorescence decay is denoted as F/F_{max}, calculated as the measured fluorescence at time point t(s) divided by the fluorescence detected before addition of dithionite (F_{max}). The average of 3 to 4 measurements is shown and standard deviations are indicated at time points 100, 200, 300 and 400 seconds. Experiments were repeated 3 times from independent reconstitutions with similar outcome.

To assess the scrambling activity of nhTMEM16, different types of NBD-lipids were included into liposomes, such as head group NBD-labelled 1,2-dimyristoyl-sn-glycero-3-phosphoethanolamine (NBD-PE) and 1,2-dioleoyl-sn-glycero-3-phospho-L-serine-N (NBD-PS). For maximal activation of nhTMEM16 liposomes were routinely prepared in the presence of 300 µM free Ca^{2+}. As shown in Figure 57, the loss of most of the fluorescence shortly after dithionite addition indicates that nhTMEM16 catalyzed the transbilayer movement of NBD-PE between the two leaflets of the liposomes in the presence of Ca^{2+}. Negative controls were included such as protein-free liposomes and proteoliposomes containing the well characterized ClC proton/chloride antiporter from *Escherichia coli* (ecClC or ClC-ec1) and the murine Ca^{2+}- activated chloride channel TMEM16A (mTMEM16A). No scrambling of NBD-PE could be detected for the negative controls, which is denoted by a fluorescence drop of only 50%, due to the reduction of the fluorophore on the outer leaflet of the membrane. For both proteins, ecClC and mTMEM16A, no evidence for phospholipid scrambling was reported so far [111, 112, 170] (and present work).

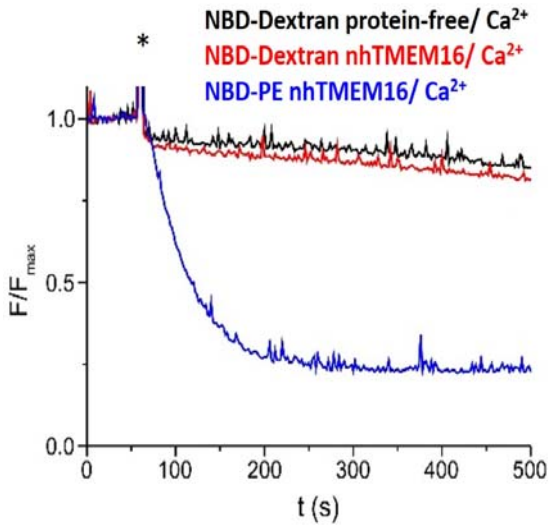

Figure 58 No dithionite permeation through nhTMEM16

The question was addressed, whether nhTMEM16 was permeable for dithionite. Liposomes contained soluble NBD-dextran in the inside of the vesicle instead of NBD-lipids in the membrane and were reconstituted with and without nhTMEM16. A permeability of nhTMEM16 to dithionite would be indicated by a total loss in fluorescence. A similar minimal loss of fluorescence was observed in preparations with and without protein after addition of 2.5 mM dithionite (red and black trace), which was marked by an asterisk (*). The same amount of dithionite was added to proteo-liposomes containing nhTMEM16 prepared with NBD-PE for comparison (blue trace). 300 µM free Ca^{2+} was present in all buffers. The fluorescence decay is denoted as F/F_{max}. A representative trace of 3 measurements is shown. Experiments were repeated with three 3 different reconstitutions with comparable outcome.

Since, besides phospholipid scrambling, some members of the family were associated with a conductance for ions [9, 170], the possibility had to be ruled out, that nhTMEM16 is permeable to dithionite and that the fluorescence decay was caused by dithionite reduction in the inside of the liposomes. For this purpose, liposomes were prepared to contain soluble NBD-dextran in the inside and were reconstituted with and without nhTMEM16 for comparison in the presence of 300 µM Ca^{2+}. As illustrated in Figure 58, using these liposomes the fluorescence remained nearly constant after dithionite addition for both, protein free and protein containing vesicles. Thus, dithionite did not reduce the NBD-dextrose trapped in the inside of the liposomes, because the fluorophore was inaccessible to dithionite. Since nhTMEM16 was

demonstrated to be impermeable for dithionite, it was concluded that the observed effect in Figure 57 was due to scrambling of NBD- phospholipids.

Next, the Ca^{2+} dependence of phospholipid scrambling by nhTMEM16 was investigated using NBD-PE. Liposomes were prepared in the absence or in the presence of defined concentrations of Ca^{2+}. The amount of Ca^{2+} and EGTA required in the buffer to reach a particular free Ca^{2+} concentration was calculated using MAXCHELATOR (**http://maxchelator.stanford.edu/CaMgATPEGTA-TS.htm).** Remarkably, in the absence of Ca^{2+}, although reasonable amounts of EGTA were added, the fluorescence dropped slightly with time, implying that scrambling of NBD-PE by nhTMEM16 was still happening at low rates. To date it is still unclear, whether this remaining activity originates from a residual activity of the protein, or whether traces of Ca^{2+} may still be bound to the Ca^{2+} binding site due to a high affinity to the binding site (see also chapter 2.14 Aiming for a Ca^{2+}-free conformation of nhTMEM16). Compared to the apparent Ca^{2+}- free samples, a gain in activity was already observed at Ca^{2+} levels as small as 250 nM, with a gradual increase with rising Ca^{2+} concentrations (Figure 59).

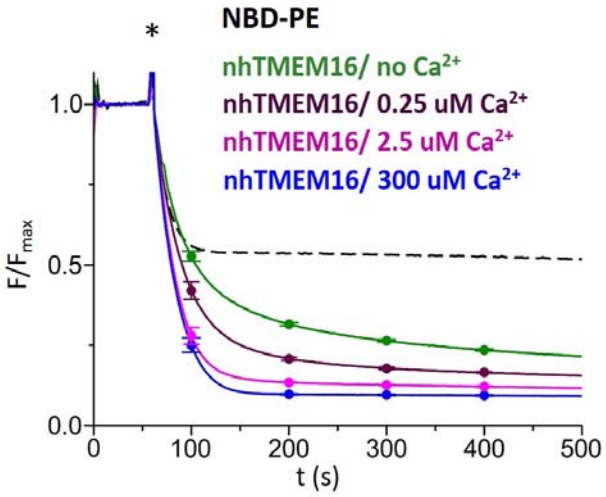

Figure 59 Ca^{2+} dependent scrambling of NBD-PE

The Ca^{2+} dependence of NBD-PE phospholipid scrambling was inspected in the absence and presence of defined Ca^{2+} levels. The asterisk (*) indicates addition of 30 mM dithionite. The fluorescence decay is denoted as F/F_{max}. The average of 3 to 4 measurements is shown and standard deviations are indicated at time points 100, 200, 300 and 400 seconds.

Similar to NBD-PE, NBD-PS is a substrate of nhTMEM16 with similar kinetics (Figure 60). However, NBD-PS showed a strong tendency to stick to the adsorbing bio-beads during detergent removal, probably due to the long and partially unsaturated fatty acid chains (18:1) (Figure 56). For this reason usually much less total fluorescence was observed than in the case of NBD-PE and thus fluctuations were comparably larger, as shown in Figure 60. Hence, scrambling experiments were generally performed using NBD-PE, that contained shorter, saturated chains (14:0), where this problem did not occur.

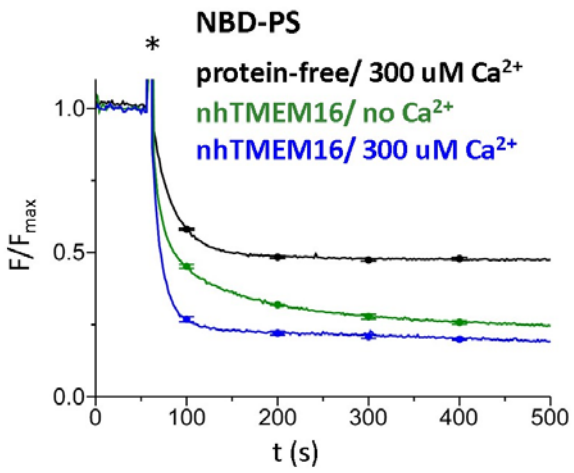

Figure 60 NBD-PS scrambling by nhTMEM16

The substrate specificity of nhTMEM16 was further investigated with the scrambling assay using NBD-PS. As asterisk (*) indicates addition of 30 mM dithionite. The fluorescence decay is denoted as F/F_{max}. The average of 3 to 4 measurements is shown and standard deviations are indicated at time points 100, 200, 300 and 400 seconds. The experiment was repeated twice, from two independent reconstitutions.

As Ca^{2+} binding sites often recognize related divalent cations, the effect of other divalent alkaline earth metal ions on the activation of NBD-PE scrambling by nhTMEM16 was investigated and compared to the activity of Ca^{2+} induced scrambling (Figure 61). Similarly as Ca^{2+}, Sr^{2+} is capable of activating scrambling with similar kinetics. In contrast to that, Mg^{2+} did not enhance activity, since the traces look similar as observed in the absence of Ca^{2+}.

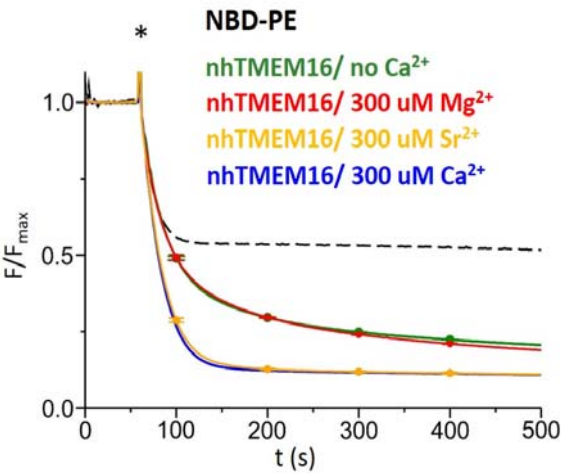

Figure 61 Activation of nhTMEM16 by divalent cations

Different divalent cations were included during purification and reconstitution of nhTMEM16 and their ability to activate nhTMEM16 was investigated in the scrambling assay. As asterisk (*) indicates addition of 30 mM dithionite. The fluorescence decay is denoted as F/F_{max}. The average of 3 to 4 measurements is shown and standard deviations are indicated at time points 100, 200, 300 and 400 seconds. The experiment was carried out with a single reconstitution.

It was found that TMEM16A [112, 289] and TMEM16F [112] can be inhibited by substances from red wine and green tea such as tannic acid (TA) and epigallocatechin-3-gallate (EGCG). To further characterize the properties of phospholipid scrambling by nhTMEM16 and potential inhibition of it, liposomes were prepared to contain either one of the potential inhibitors at reasonable concentrations. Since TA interfered with dithionite during the assay, liposomes were only loaded with the inhibitors on the inside, while the buffers outside of the liposomes were devoid of it. The resulting data illustrated in Figure 62 suggest that while EGCG had no obvious effect, tannic acid seemed to change the scrambling properties of nhTMEM16. At the applied concentration of 100 µM TA, the fluorescence dropped to a final value of 28% after 500 seconds compared to 10% using EGCG or 9% without any inhibitor at

activating Ca^{2+} levels of 300 µM. The kinetics of the fast reduction together with the final fluorescence value of 28% in the case of TA allows three conclusions:

First, it appears that the orientation of nhTMEM16 in liposomes was close to symmetric with half of the proteins having the cytosolic domains facing the inside of the liposomes and half pointing out.

Second, the inhibitor can only access one half of the proteins, but it is currently not known, which orientation of the protein would be affected.

Third, the fast reduction of the fluorescence of the red trace as judged from the decay, resembled the kinetics of the fully activated protein with comparable slope but was not similar to nhTMEM16 that is not fully activated in the absence of Ca^{2+}. This may indicate, that while one half of the proteins was functional, the other half with opposite orientation was fully inhibited.

However, even with half of the protein active, a drop in the fluorescence to low levels as observed in nhTMEM16 in the absence of an inhibitor would be expected, unless per liposome one nhTMEM16 dimer is contained. In liposomes of 100 nm size two nhTMEM16 dimers are expected per liposomes (the molecular weight of phosphatidylcholine is 760 g mol^{-1}, lipids and protein are prepared at a concentration of 25 mM and 0.6 µM (dimer), respectively, while a liposome of 100 nm size contains 80'000 lipids). The cause of the premature stop of the reaction will still have to be investigated.

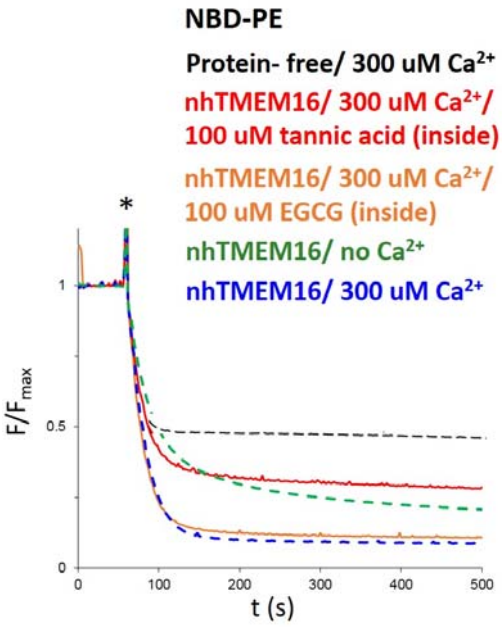

Figure 62 Inhibition of nhTMEM16 scrambling by tannic acid

The scrambling of NBD-PE was investigated in the presence of potential inhibitors such as tannic acid (TA) and epigallocatechin-3-gallate (EGCG) in the inside of liposomes. An asterisk (*) indicates addition of 30 mM dithionite. The fluorescence drop is denoted as F/F_{max}. The average of 3 to 4 measurements is shown. Only one experiment was carried out.

In the structure of nhTMEM16 the location and composition of the Ca^{2+} binding site was revealed. In this site, six residues, of which five contain a negative charge, were identified to coordinate two Ca^{2+} ions. In other TMEM16 proteins, equivalent residues are found at appropriate positions as indicated by a sequence alignment. Supporting these data, two out of these five negatively charged residues were previously proposed to be involved in Ca^{2+} sensing in TMEM16A [12], and were subsequently shown to play a similar role in TMEM16F [9] and afTMEM16 [170]. The impact of mutations in the Ca^{2+} binding

site of nhTMEM16 was analyzed using the scrambling assay. The three negatively charged amino acids that were identified in this study, E452, E535 and D539, were replaced by glutamines and asparagines and the resulting triple mutant was reconstituted into liposomes, that were prepared to either contain or lack Ca^{2+}. As shown in Figure 63, a gradual slow drop in the fluorescence indicated that the triple mutant exhibited a strongly reduced scrambling activity for NBD-PE compared to the wild-type protein (WT). The measured fluorescence decay for mutant nhTMEM16 is very similar in the presence and absence of Ca^{2+}, suggesting that the activity of the triple mutant cannot be enhanced anymore, even though 300 µM $Ca^{2+}$was applied.

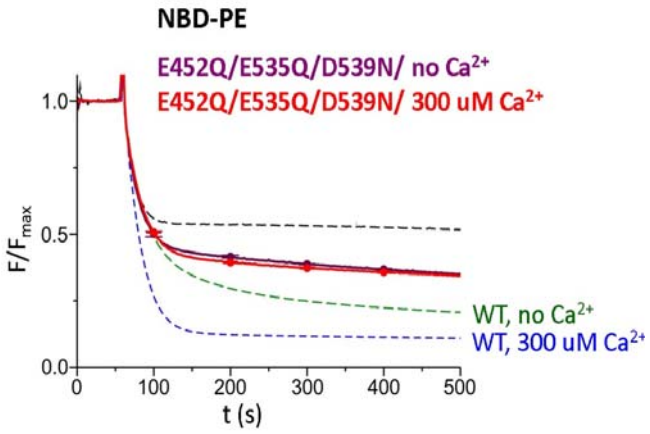

Figure 63 Decreased scrambling activity by a nhTMEM16 binding site mutant

The scrambling assay was used to monitor the activity of a triple mutant of nhTMEM16, containing the conservative mutations E452Q, E535Q, D539N. Activity was recorded in the presence and absence of Ca^{2+}. Dashed lines correspond to scrambling observed by wild-type nhTMEM16 in the presence and absence of Ca^{2+} (blue and green) or in protein- free liposomes (black dashed line). As asterisk (*) indicates addition of 30 mM dithionite. The fluorescence drop is denoted as F/F_{max}. The average of 3 to 4 measurements is shown and standard deviations are indicated at time points 100, 200, 300 and 400 seconds. Only one experiment was carried out.

2.16.2. Summary

The function of nhTMEM16 as a scramblase was studied in a cell-free system using isolated protein in an assay that records the reduction of fluorescence after addition of a reducing agent to the outer leaflet of the liposomes. The time-course of the fluorescence drop indicates the scrambling activity for a particular NBD-lipid. It was demonstrated that nhTMEM16 could be purified and reconstituted in a functional state, since the protein strongly enhanced the transport of phospholipids such as (NBD-labelled) PE and PS between the leaflets of the liposomes, and thus confirmed that nhTMEM16 is a scramblase. Some basal activity for the transbilayer movement of the investigated phospholipids was observed in the absence of Ca^{2+}, but this activity was strongly enhanced in the presence of even nano-molar concentrations of Ca^{2+}. In addition, evidence was brought that Sr^{2+} but not Mg^{2+} could substitute Ca^{2+} in the assay with similar results concerning activation and kinetics of scrambling. Two possible inhibitors were evaluated for their potential to block nhTMEM16. It was observed that tannic acid had a

strong inhibitory effect. However, a suitable negative control such as protein-free liposomes containing this particular inhibitor at similar concentrations will still have to be investigated and the lack of such a control currently makes any interpretation ambiguous. Based on the structure, a triple mutant was generated combining mutations of residues of the Ca^{2+} binding site that were identified in the present work. The mutant nhTMEM16 exhibited considerably reduced scrambling, underlining the significance of these three residues of the Ca^{2+} binding site for activation of nhTMEM16.

2.18. X-ray structure of a calcium- activated TMEM16 lipid scramblase

ARTICLE

doi:10.1038/nature13984

X-ray structure of a calcium-activated TMEM16 lipid scramblase

Janine D. Brunner[1], Novandy K. Lim[1], Stephan Schenck[1], Alessia Duerst[1] & Raimund Dutzler[1]

The TMEM16 family of proteins, also known as anoctamins, features a remarkable functional diversity. This family contains the long sought-after Ca^{2+}-activated chloride channels as well as lipid scramblases and cation channels. Here we present the crystal structure of a TMEM16 family member from the fungus *Nectria haematococca* that operates as a Ca^{2+}-activated lipid scramblase. Each subunit of the homodimeric protein contains ten transmembrane helices and a hydrophilic membrane-traversing cavity that is exposed to the lipid bilayer as a potential site of catalysis. This cavity harbours a conserved Ca^{2+}-binding site located within the hydrophobic core of the membrane. Mutations of residues involved in Ca^{2+} coordination affect both lipid scrambling in *N. haematococca* TMEM16 and ion conduction in the Cl^- channel TMEM16A. The structure reveals the general architecture of the family and its mode of Ca^{2+} activation. It also provides insight into potential scrambling mechanisms and serves as a framework to unravel the conduction of ions in certain TMEM16 proteins.

The TMEM16 or anoctamin family constitutes a class of membrane proteins that is only expressed in eukaryotic organisms. In vertebrates the family encompasses ten members with high sequence conservation[1]. Despite their close relationship these proteins combine different functions as some members are Ca^{2+}-activated ion channels while others work as Ca^{2+}-activated scramblases[2], which catalyse the shuffling of lipids between the inner and outer leaflets of the bilayer in an ATP-independent manner. In 2008 three groups independently identified TMEM16A (or Ano1) as the long sought-after Ca^{2+}-activated chloride channel (CaCC)[3–5]. After this discovery the name anoctamin was coined, synonymous for anion selectivity and the eight transmembrane spanning helices that were predicted by hydropathy analysis[3]. It has been shown that TMEM16A and TMEM16B (Ano2) share similar characteristics, although with different tissue distribution[3,5,6]. Whereas TMEM16A contributes to diverse physiological processes, such as epithelial chloride secretion, electrical signalling in smooth muscles and potentially also nociception[7,8], TMEM16B is expressed in the retina and in olfactory epithelia and might have a role in olfaction[6,9]. In further studies TMEM16F (Ano6) was shown to act as Ca^{2+}-activated small-conductance cation channel[10], possibly also as Cl^- channel[11] and to have a role in Ca^{2+}-activated lipid scrambling by facilitating the exchange of phosphatidylserine from the inner to the outer leaflet of the bilayer in blood platelets[10,12]. Similarly, TMEM16C, D, G and J (Ano3, 4, 7 and 9, respectively) were suggested to work as scramblases, although with variable lipid preference[13]. Recently a fungal TMEM16 homologue from *Aspergillus fumigatus* (afTMEM16) was found to scramble lipids as well after its purification and reconstitution into liposomes[14]. Besides its function as scramblase, afTMEM16 was also proposed to form non-selective ion channels with high conductance[14]. It is still a matter of debate how these closely related proteins can accommodate such a diversity of functional phenotypes[2,15].

Despite the functional breadth, characterized family members appear to share a similar mode of Ca^{2+} activation. This behaviour has been most thoroughly investigated for the chloride channel TMEM16A[3,16,17]. In TMEM16A Ca^{2+} activates the channel from the intracellular side at sub-micromolar concentrations with a half-maximum effective concentration (EC_{50}) that is voltage-dependent and decreases upon depolarization. Two conserved glutamate residues have been discovered to be involved in the Ca^{2+} activation of ion conduction in TMEM16A[18,19] and TMEM16F[10] and scrambling in afTMEM16[14], thus indicating the conservation of this regulatory mechanism within the family.

Although we have by now gained considerable insight into the functional properties of certain family members, their architecture and its relation to mechanisms of action are still unknown. Here we present the X-ray structure of a TMEM16 homologue from *Nectria haematococca* (nhTMEM16). The dimeric protein shows a novel fold with ten membrane-spanning segments per subunit. The transmembrane domain contains a highly conserved region that is embedded within the hydrophobic core of the membrane comprising a Ca^{2+}-binding site. Ca^{2+} binding by six residues, five of which carry a negative charge, controls the activation of scrambling in nhTMEM16 and ion conduction in TMEM16A. Our results thus have revealed a conserved structural framework that supports diverse functional properties within the family.

Functional characterization of nhTMEM16

To gain insight into the architecture of the TMEM16 family we screened 80 members in *Saccharomyces cerevisiae* and HEK tsA201 cells for overexpression and detergent stability, and were able to identify a homologue from the fungus *Nectria haematococca* (nhTMEM16), exhibiting the desired biochemical properties. The protein shares 48% of identical residues with the previously characterized afTMEM16 (with >70% homology within the transmembrane domain) (Extended Data Fig. 1a). Among mammalian proteins the relationship is closest to TMEM16H and K (Ano8 and 10) but it is still close to the more distantly related chloride channel TMEM16A (with homologies in the transmembrane region ranging between 39% and 42%), thus suggesting that all family members share a similar structural organization (Extended Data Fig. 1b,c). Unlike its mammalian counterparts, nhTMEM16 is not glycosylated. The solubilized protein is a dimer, as quantified by multi-angle light scattering, suggesting that the oligomeric organization is preserved in detergent solution (Extended Data Fig. 2a). To characterize its functional properties we have reconstituted the protein into liposomes and found, with respect to its scrambling activity, a very similar behaviour as described for the related afTMEM16. The function as lipid scramblase

[1]Department of Biochemistry, University of Zurich, Winterthurerstrasse 190, CH-8057 Zurich, Switzerland.

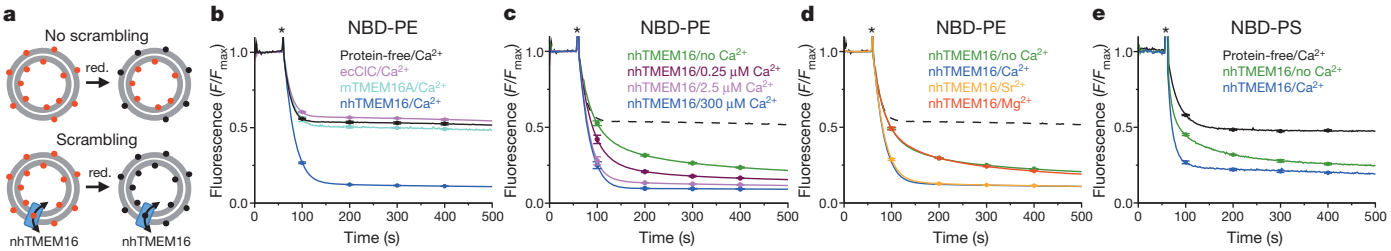

Figure 1 | Phospholipid scrambling by nhTMEM16. **a**, Scheme of the assay depicting the reduction of NBD-labelled phospholipids in the outer leaflet of the bilayer upon addition of dithionite (red.). **b**, Scrambling of NBD-PE. Traces of protein-free liposomes and proteoliposomes containing either nhTMEM16, the *E. coli* ClC transporter (ecClC) or mTMEM16A are shown. Asterisk marks addition of dithionite. **c**, Ca^{2+} dependence of NBD-PE scrambling by nhTMEM16. **d**, Influence of other divalent cations on NBD-PE scrambling by nhTMEM16. In **c** and **d**, protein-free liposomes (dashed lines) are shown for comparison. **e**, Scrambling of liposomes containing NBD-PS. Traces of protein-free liposomes and proteoliposomes containing nhTMEM16 in the absence and presence of Ca^{2+} are shown. **b**–**e**, Traces show averages of 3–4 measurements, standard deviations are included for selected time points. Unless stated otherwise, solutions contain 0.3 mM of the indicated free divalent cations. Scrambling experiments were replicated three times with similar results.

was investigated by an assay that monitors the reduction of fluorescently labelled lipids by sodium dithionite on the outer leaflet of liposomes[14,20] (Fig. 1a, Extended Data Fig. 2b–d). Our results demonstrate that nhTMEM16 catalyses the movement of nitrobenzoxadiazole-phosphatidylethanolamine (NBD-PE) and NBD-phosphatidylserine (NBD-PS) between the two layers of the liposome membrane (Fig. 1b, e). The observed effect is not due to permeation of dithionite through the protein (Extended Data Fig. 2b). Furthermore, we found that this catalytic function is enhanced by Ca^{2+} at submicromolar concentrations (Fig. 1c). Besides Ca^{2+}, we also observed activation for Sr^{2+} but not for Mg^{2+} (Fig. 1d). Scrambling in nhTMEM16 containing proteoliposomes measured under Ca^{2+}-free conditions may either be due to constitutive activity of the ligand-free scramblase or originate from traces of Ca^{2+} still bound to the protein (Supplementary Discussion, Extended Data Fig. 2d). To investigate whether nhTMEM16 would also function as ion channel, we have attempted to study ion conduction from proteoliposomes fused to artificial lipid bilayers and by patch-clamp electrophysiology of HEK293T cells expressing the protein. However, in neither case did we find any convincing evidence for ion channel activity (Extended Data Fig. 3 and Supplementary Discussion).

nhTMEM16 structure

For structure determination, nhTMEM16 was crystallized in two different crystal forms (CF1 and CF2), each containing a dimer in the asymmetric unit, for which we have collected data at 3.3 and 3.4 Å resolution respectively (Extended Data Fig. 4a). Initial phases, obtained by the Se-Met single-wavelength anomalous dispersion method, were improved and extended by non-crystallographic symmetry and cross-crystal averaging. The resulting electron density was of high quality and allowed the unambiguous interpretation by an atomic model (Extended Data Figs 4 and 5). The structure of the dimer is depicted in Fig. 2a. Both subunits are related by twofold symmetry and show very similar conformations. When viewed from the extracellular side the dimer has a rhombus-like shape with about 130 Å in the long and 40 Å in the short dimension (Extended Data Fig. 6). The topology of the nhTMEM16 subunit is shown in Fig. 2b. Both termini are structured and located on the cytoplasmic side of the membrane. The α-helices and β-strands of the amino-terminal domain are organized in a ferredoxin-like fold. The three α-helices of the carboxy terminus are wrapped around the N-terminal domain of the adjacent subunit, thereby constituting a large part of the subunit interface (Fig. 2c). The transmembrane domain starts with two short α-helices (α0a and α0b), followed by ten membrane-spanning segments (α1–α10). The two initial helices form a hairpin with amphiphilic properties, with its hydrophobic side interacting with α-helices 1 and 8. A model of the protein embedded in a lipid bilayer suggests that both helices only peripherally interact with the inner leaflet of the membrane (Extended Data Fig. 7a, b). Helices α1–α10, in contrast, all traverse the entire membrane with some of them being bent and tilted

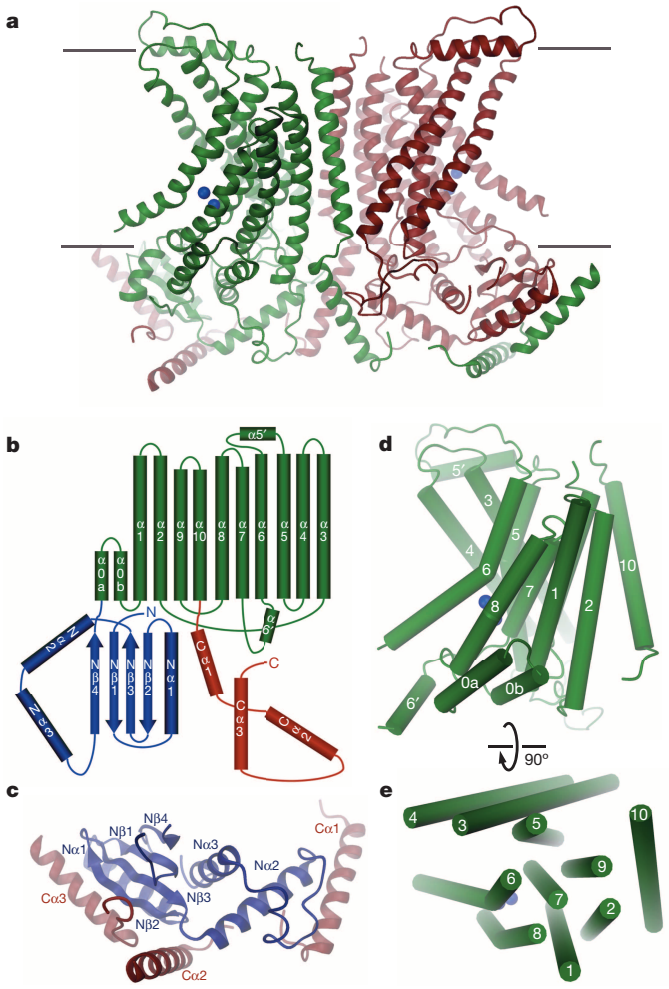

Figure 2 | nhTMEM16 structure. **a**, Ribbon representation of the nhTMEM16 dimer. The view is from within the membrane. Bound calcium ions are shown as blue spheres. The membrane boundary is indicated. **b**, Topology of the nhTMEM16 subunit. The transmembrane domain is coloured in green, the N- and C-terminal domains in blue and red, respectively. **c**, View of the cytoplasmic domains. The interaction of the N-terminal domain with the C-terminal domain of the adjacent subunit is shown. **d**, Transmembrane domain with α-helices shown as cylinders and labelled. The view is as in **a**. **e**, Organization of transmembrane helices. The view is from the extracellular side. Loop regions are omitted for clarity. Figures 2–4 and 6 were prepared with DINO (http://www.dino3d.org/) and show the structure determined in crystal form 1 (CF1) unless stated otherwise.

with respect to its plane (Fig. 2d, e). The transmembrane segments are connected by loop regions of variable length, two of which contain short helical regions (named α5′ and α6′, according to the preceding transmembrane region), on the extracellular and cytoplasmic side, respectively. The arrangement of α-helices does not follow any obvious symmetry or show any relationship to known membrane protein structures.

Dimer interface and dimer cavity

The dimeric organization of nhTMEM16 is reflected in the extended interface between the two subunits, which buries 9,650 Å^2 of the combined molecular surface. The largest part of this interface is contributed by interactions between the N- and C-terminal domains, whereas the contact area of 1,520 Å^2 between the transmembrane domains is comparably small. In the transmembrane region the dimer interface is formed by interactions of residues in the N-terminal part of α-helix 10 at the extracellular side close to the symmetry axis and interactions between α-helices 3 and 10 at their cytoplasmic end (Fig. 3a, b). Mutual interactions between residues of α-helices 10 involve hydrophobic contacts and a pair of salt bridges between a glutamate and a histidine side-chain that are conserved within the family, except for TMEM16A and B (Extended Data Fig. 7c). The arrangement of helices close to the dimer interface generates a large pore-like structure across the transmembrane region, the dimer cavity, which contains two separate 15 Å wide entrances at the extracellular side and which merges to one big, about 30 Å wide vestibule, at the intracellular half of the membrane (Fig. 3b, Extended Data Fig. 7d, e). Although on the inside this large cavity is confined by residues of the cytoplasmic domains, several fenestrations create access to the cytoplasm. In the transmembrane region the dimer cavity is accessible to the outer leaflet of the membrane via two v-shaped gaps framed by α-helices 3 and 10 from adjacent subunits (Fig. 3b, Extended Data Fig. 7e). Within the membrane, the vestibule is predominantly composed of hydrophobic and aromatic residues, which are conserved within the protein family, whereas there are several polar and charged residues found at the intracellular part outside of the predicted membrane region (Extended Data Fig. 7d, e). We thus suppose that the dimer cavity may be packed with lipids. The inside of this large cavity contains excess electron density, which is, however, not sufficiently ordered to be attributed to either solvent, or detergent and lipids (Extended Data Fig. 7f). It is currently not clear whether this region has a critical role for protein function.

Subunit cavity and Ca^{2+}-binding region

With respect to function, the most remarkable feature is found on the surface opposite to the dimer interface. Here a narrow crevice that spans the entire membrane is formed by α-helices 3–7 of the same subunit (Fig. 3c, Extended Data Fig. 8). These α-helices surround an 8–11 Å wide cavity that is twisted like a 'spiral staircase' and on one side is exposed to the membrane. In contrast to the dimer cavity the surface of the subunit cavity is strongly hydrophilic, despite its exposure to the lipid environment (Fig. 3c). Furthermore, it harbours residues for which equivalent positions have previously been shown to be involved in ion conduction in TMEM16A[18] and to influence ion selectivity in TMEM16A and F[10]. These observations make this region a prime candidate for the translocation path in both channels and scramblases. Within the hydrophobic core of the membrane, at a distance corresponding to about one third of its thickness from the intracellular side, the subunit cavity is lined by residues of α-helices 6 and 7, which are part of a conserved Ca^{2+}-binding site (Fig. 4a, b and Extended Data Fig. 8d). In the crystal structure, we have detected bound Ca^{2+} ions by anomalous scattering. Two peaks of strong anomalous difference density were found in each subunit at equivalent places (Fig. 4c, d). These peaks are separated by a distance of 4.2 Å and they are surrounded by three glutamates, two aspartates and an asparagine located on α-helices 6, 7 and 8 (Fig. 4e). Although from our data we cannot tell with certainty whether one or two Ca^{2+} ions are bound at the same time, simultaneous occupancy seems possible owing to the high density of negative charge in this region. All residues involved in Ca^{2+} binding are highly conserved within the TMEM16 family, which strongly supports a common Ca^{2+} binding and activation mode.

Functional investigation of the Ca^{2+}-binding region

Since the nhTMEM16 structure has allowed the identification of a conserved Ca^{2+}-binding site, we were interested to investigate the relevance of these interactions for activation in nhTMEM16 and TMEM16A. The two glutamates located in α-helix 7 have previously been shown to play an important role in the activation of TMEM16A[18], F[10] and afTMEM16[14] by Ca^{2+}. A Ca^{2+}-binding site triple-mutant of nhTMEM16 combining mutations of residues involved in Ca^{2+} coordination identified in this study (that is, E452Q, E535Q and D539N) shows only weak scrambling activity that is not enhanced by Ca^{2+} (Fig. 5a). To probe the importance of the same residues for the activation of ion conduction in murine TMEM16A (mTMEM16A), we have expressed the protein in HEK293T cells and monitored the Ca^{2+}-dependence in binding site mutants by patch-clamp electrophysiology. As previously shown Ca^{2+} activates mTMEM16A in a voltage-dependent manner with an apparent affinity that is higher at positive than at negative potentials[3] (Fig. 5b). At 80 mV Ca^{2+} activates the wild-type protein with an EC_{50} of 0.36 μM and a Hill coefficient of 2.3, which indicates a cooperative process that involves the binding of more than one ion. Single mutants of each residue contributing to the observed interactions in the Ca^{2+}-binding region

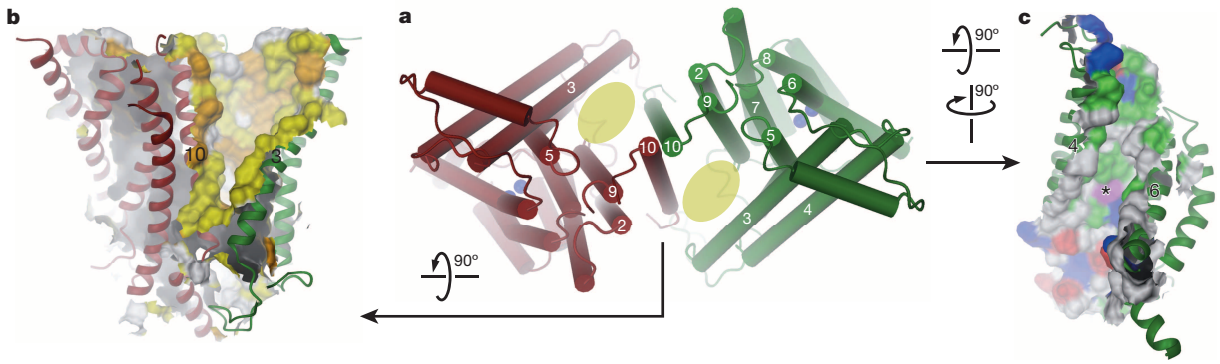

Figure 3 | Dimer interface and subunit cavity. a, Transmembrane domain of the nhTMEM16 dimer viewed from the extracellular side with yellow ovals indicating the location of the dimer cavity. Helices are represented as cylinders. **b**, Dimer cavity viewed from within the membrane. Helices of both subunits lining the cavity are displayed. The solvent-accessible surface of the cavity is shown with locations of hydrophobic and aromatic residues coloured in yellow and orange, respectively. **c**, Subunit cavity viewed from within the membrane. The solvent-accessible surface is coloured according to the properties of contacting residues (red, acidic; blue, basic; green, polar). A position that was shown to influence the ion selectivity in TMEM16A and TMEM16F is coloured in magenta and labelled with an asterisk.

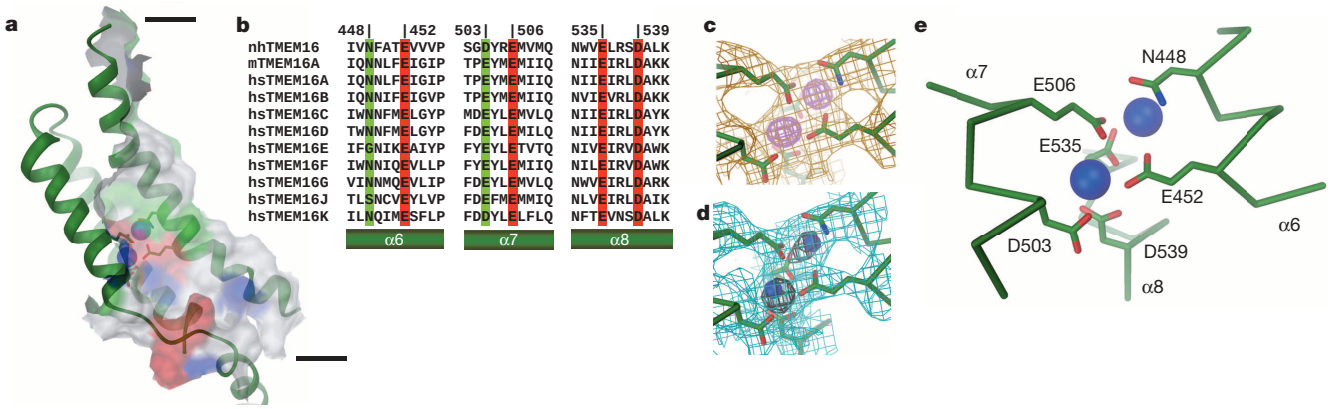

Figure 4 | Ca^{2+}-binding site. **a**, Location of the Ca^{2+}-binding site in relation to the subunit cavity. The view is from within the membrane, the colour coding as in Fig. 3c. **b**, Sequence alignment. Conserved amino acids of the Ca^{2+}-binding site are highlighted in red (identical) and green (homologous). hs, *Homo sapiens*. **c**, View of the Ca^{2+}-binding site in the refined structure of CF2. The $2F_o - F_c$ electron density (at 3.5 Å, contoured at 1σ, orange) is shown superimposed on the model. Anomalous difference electron density (at 3.8 Å, contoured at 5σ) is shown in magenta. **d**, View of the Ca^{2+}-binding site in the refined structure of CF1. The $2F_o - F_c$ electron density (at 3.3 Å, 1σ, cyan, 5σ, black) is shown superimposed on the model containing Ca^{2+} ions (blue spheres). **e**, Model of the Ca^{2+}-binding site.

shift the EC_{50} to higher Ca^{2+} concentrations (Fig. 5c and d, Extended Data Figs 9 and 10). The strongest effect was observed for Glu 654, where we have not observed any activation for E654Q and only low currents at high Ca^{2+} concentration for E654A, despite the strong plasma membrane expression of the channel (Extended Data Fig. 10h). Similar results were reported in a recent study that was based on the mutation of conserved acidic residues[21]. Taken together, our functional experiments on nhTMEM16 and mTMEM16A suggest that Ca^{2+} binding by equivalent residues regulates both functional branches of the family by a common mechanism.

Discussion

The structure of nhTMEM16 has revealed a framework for the TMEM16/anoctamin family. Whereas its homodimeric organization is consistent with previous investigations of TMEM16A, B, F and afTMEM16[14,22–24], a direct interaction between the N termini, which was proposed to be involved in dimerization of TMEM16A, is not observed[24]. In nhTMEM16, each subunit contains ten membrane-spanning helices, which differs from the eight transmembrane segments predicted from hydropathy analysis[3,25] (Extended Data Fig. 1c). It is however noteworthy that a recent study, which has revised the originally proposed topology, has correctly identified residues of the Ca^{2+}-binding site and the extracellular entry to the putative pore region[18]. The structure harbours two regions that are presumably in contact with the membrane; the dimer cavity, a large and predominantly hydrophobic structure at the dimer interface, and the subunit cavity, a hydrophilic membrane-spanning crevice contained within each subunit that resembles a spiral staircase. Whereas the functional relevance of the dimer cavity is currently unclear, the subunit cavity is linked to Ca^{2+} activation and probably also to catalytic properties of the protein (Fig. 3, Extended Data Fig. 8).

As a scramblase nhTMEM16 has provided first structural insight into an important class of transport molecules. These proteins catalyse the passive movement of lipids between the two leaflets of a bilayer, a process that is essential for membrane biogenesis in the endoplasmic reticulum[26] and the shuffling of lipids in several processes, including blood coagulation[10,12], apoptosis[27], glycosylation[28] and the assembly of the bacterial cell wall[29]. To lower the large intrinsic energy barrier associated with lipid flipping, it was proposed that scramblases would provide a hydrophilic path to facilitate the movement of the polar headgroups across the bilayer[26,30]. The subunit cavity of nhTMEM16 would ideally meet these requirements, as it is hydrophilic, accessible to the membrane and of sufficient dimensions to accommodate a phospholipid headgroup (Fig. 6a). These properties would also be consistent with the broad range of lipids that have been shown to be translocated by afTMEM16[14] and other Ca^{2+}-activated lipid scramblases[31]. Proteins with scrambling function belong to various families[13,20,27,29], some of which are still disputed[32] or have not yet been identified on a molecular level. It will thus be interesting to see to which extent structural and mechanistic features proposed in our work are shared by unrelated scramblases and whether still unassigned scrambling processes would be catalysed by TMEM16 proteins.

In TMEM16A, B and F, the subunit cavity may constitute the ion conduction pore, as suggested by the influence of point mutations of

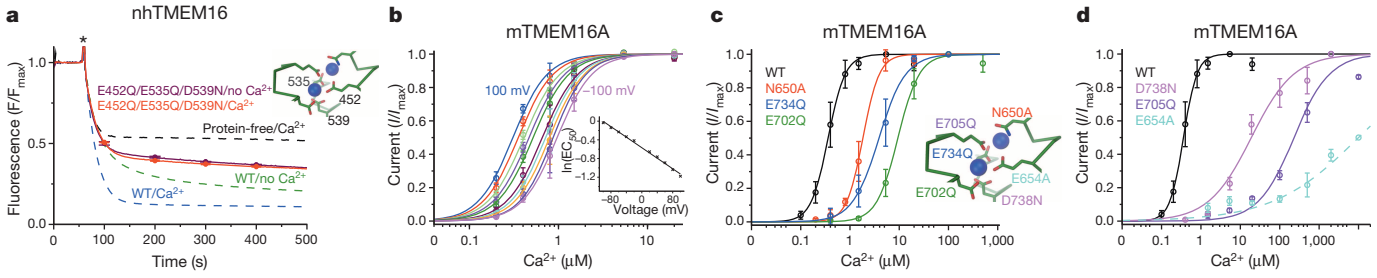

Figure 5 | Functional properties of Ca^{2+}-binding site mutants. **a**, Scrambling of the nhTMEM16 mutant E452Q/E535Q/D539N. Data of proteoliposomes containing NBD-PE and the triple mutant in absence and presence of 0.3 mM free Ca^{2+} are shown. Traces and statistics are as in Fig. 1 with dashed lines shown for comparison. Inset indicates the position of the mutations. WT, wild type. **b**, Voltage dependence of Ca^{2+} activation in mTMEM16A measured from excised inside-out patches. Currents were normalized to the maximum, lines show a fit to a Hill equation. The voltage dependence is shown as inset. **c**, **d**, Activation of Ca^{2+}-binding site mutants. Data were recorded at 80 mV and normalized to the maximum. Lines show a fit to a Hill equation (the fit for E654A was estimated). Numbers in inset correspond to mTMEM16A. Data in **b**–**d** are averages from 3–4 independent measurements, errors are s.d.

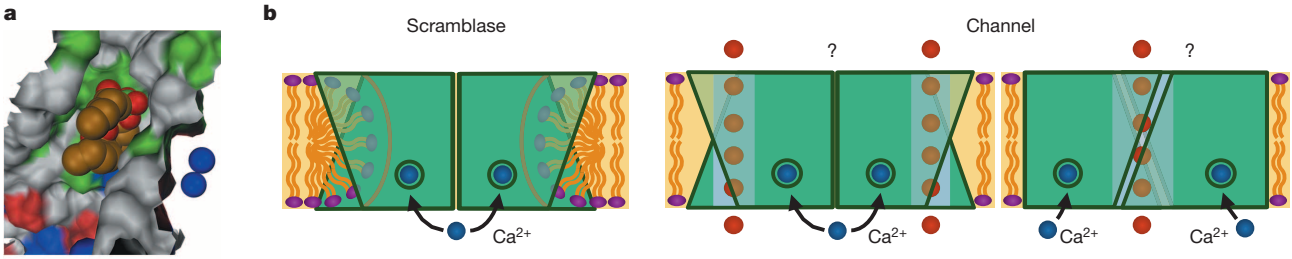

Figure 6 | Mechanism. a, Model of phosphatidylcholine in the subunit cavity. The acyl chains have been truncated for clarity. Bound Ca^{2+} ions are shown as blue spheres. **b**, Scheme illustrating the potential relationship between scramblases and ion channels within the TMEM16 family. Two distinct dimeric arrangements of TMEM16 channels are shown with one resembling the nhTMEM16 structure (centre) and the other formed by monomers that interact via the subunit cavities (right).

residues facing the subunit cavity on ion selectivity and conductance[10,18]. In TMEM16A and B, it is still puzzling how the subunit cavity might provide the aqueous environment required for ion conduction and, conversely, how lipid scrambling would be precluded in these proteins[13,14,33] (Fig. 1b). This distinction could be accomplished by local structural differences in an assembly as observed in nhTMEM16. Alternatively, it is tempting to speculate that in TMEM16 channels, the monomers might be turned by 180° and interact via their subunit cavities to form an enclosed pore. These different dimer assemblies would provide a plausible explanation for the functional dichotomy in TMEM16 proteins and are largely compatible with the structure of the monomer (Fig. 6b). Whereas the arrangement that is similar to nhTMEM16 would contain two potentially independent pores, as seen in the ClC family[34], the latter would probably result in a single ion conduction path.

For scramblases it will be important to investigate whether lipid movement locally distorts the membrane and whether ions can pass through the bilayer by binding to the polar headgroups of lipids that are in the process of being scrambled, which could potentially give rise to the small ion conductance observed in TMEM16F[10]. The large channels observed in afTMEM16[14] may be distinct from the described process and no such property has so far been detected for the closely related homologue investigated in this study. Similarly, a potential chloride-selective ion conductance of TMEM16F[11], which was proposed to be independent of its role in scrambling[35] and a similar function in other TMEM16 proteins[36] still requires closer investigation. The coexistence of ion channels and lipid scramblases in the TMEM16 family is somewhat reminiscent of P-type ATPases[37], which include primary active ion pumps and ATP-driven lipid flippases with similar molecular architecture. Also in this family both transport functions were proposed to localize in the same area. In flippases polar headgroups are thought to interact with a hydrophilic groove during bilayer passage[38], thereby facing a similar environment to that found in the subunit cavity of nhTMEM16.

Despite the breadth of functional behaviours, both branches of the TMEM16 family share the mechanism by which their activity is regulated by Ca^{2+}. The nhTMEM16 structure reveals a conserved Ca^{2+}-binding site contained within each subunit that is positioned within the hydrophobic core of the bilayer in proximity to the subunit cavity. Although this site potentially harbours two Ca^{2+} ions, it is currently not known whether binding of one or two ions is required to activate the protein. The location of this region within the membrane provides an explanation for the voltage-dependence of Ca^{2+} activation observed in TMEM16A[3,5], B[39] and TMEM16F[10]. This effect probably originates from the fact that the ion has to cross a fraction of the transmembrane electric field to reach the binding site[40], a model that was already proposed in an early study on CaCC activation[41]. While in our structure Ca^{2+} ions are buried within the protein, their entry from the cytoplasm via the subunit cavity or another path that becomes accessible in the ligand-free protein appears plausible (Fig. 4a, Extended Data Fig. 8). Ca^{2+} binding may either induce a conformational change in the protein that underlies its activation or modify the electrostatics in the close-by subunit cavity and in that way regulate the conductive properties of this region. Although the mechanism described is probably common for this protein family, there may be additional modes of regulation in certain TMEM16 proteins[42–46]. Our study has shed light on the unique properties of the TMEM16 protein family that does not resemble known classes of membrane proteins with respect to structure nor function. While detailed mechanisms of action are still unknown, the structure of nhTMEM16 has provided a template that will guide the future investigation of structure–function relationships.

Online Content Methods, along with any additional Extended Data display items and Source Data, are available in the online version of the paper; references unique to these sections appear only in the online paper.

Received 3 June; accepted 20 October 2014.
Published online 12 November 2014.

1. Milenkovic, V. M., Brockmann, M., Stohr, H., Weber, B. H. & Strauss, O. Evolution and functional divergence of the anoctamin family of membrane proteins. *BMC Evol. Biol.* **10,** 319 (2010).
2. Pedemonte, N. & Galietta, L. J. Structure and function of TMEM16 proteins (anoctamins). *Physiol. Rev.* **94,** 419–459 (2014).
3. Yang, Y. D. *et al.* TMEM16A confers receptor-activated calcium-dependent chloride conductance. *Nature* **455,** 1210–1215 (2008).
4. Caputo, A. *et al.* TMEM16A, a membrane protein associated with calcium-dependent chloride channel activity. *Science* **322,** 590–594 (2008).
5. Schroeder, B. C., Cheng, T., Jan, Y. N. & Jan, L. Y. Expression cloning of TMEM16A as a calcium-activated chloride channel subunit. *Cell* **134,** 1019–1029 (2008).
6. Pifferi, S., Cenedese, V. & Menini, A. Anoctamin 2/TMEM16B: a calcium-activated chloride channel in olfactory transduction. *Exp. Physiol.* **97,** 193–199 (2012).
7. Ferrera, L., Zegarra-Moran, O. & Galietta, L. J. Ca^{2+}-activated Cl^- channels. *Compr. Physiol.* **1,** 2155–2174 (2011).
8. Huang, F., Wong, X. & Jan, L. Y. International Union of Basic and Clinical Pharmacology. LXXXV: calcium-activated chloride channels. *Pharmacol. Rev.* **64,** 1–15 (2012).
9. Billig, G. M., Pal, B., Fidzinski, P. & Jentsch, T. J. Ca^{2+}-activated Cl^- currents are dispensable for olfaction. *Nature Neurosci.* **14,** 763–769 (2011).
10. Yang, H. *et al.* TMEM16F forms a Ca^{2+}-activated cation channel required for lipid scrambling in platelets during blood coagulation. *Cell* **151,** 111–122 (2012).
11. Martins, J. R. *et al.* Anoctamin 6 is an essential component of the outwardly rectifying chloride channel. *Proc. Natl Acad. Sci. USA* **108,** 18168–18172 (2011).
12. Suzuki, J., Umeda, M., Sims, P. J. & Nagata, S. Calcium-dependent phospholipid scrambling by TMEM16F. *Nature* **468,** 834–838 (2010).
13. Suzuki, J. *et al.* Calcium-dependent phospholipid scramblase activity of TMEM16 protein family members. *J. Biol. Chem.* **288,** 13305–13316 (2013).
14. Malvezzi, M. *et al.* Ca^{2+}-dependent phospholipid scrambling by a reconstituted TMEM16 ion channel. *Nature Commun.* **4,** 2367 (2013).
15. Kunzelmann, K. *et al.* Molecular functions of anoctamin 6 (TMEM16F): a chloride channel, cation channel, or phospholipid scramblase? *Pflugers Arch.* **466,** 407–414 (2014).
16. Kuruma, A. & Hartzell, H. C. Bimodal control of a Ca^{2+}-activated Cl^- channel by different Ca^{2+} signals. *J. Gen. Physiol.* **115,** 59–80 (2000).
17. Ni, Y. L., Kuan, A. S. & Chen, T. Y. Activation and inhibition of TMEM16A calcium-activated chloride channels. *PLoS ONE* **9,** e86734 (2014).
18. Yu, K., Duran, C., Qu, Z., Cui, Y. Y. & Hartzell, H. C. Explaining calcium-dependent gating of anoctamin-1 chloride channels requires a revised topology. *Circ. Res.* **110,** 990–999 (2012).
19. Terashima, H., Picollo, A. & Accardi, A. Purified TMEM16A is sufficient to form Ca^{2+}-activated Cl^- channels. *Proc. Natl Acad. Sci. USA* **110,** 19354–19359 (2013).
20. Menon, I. *et al.* Opsin is a phospholipid flippase. *Curr. Biol.* **21,** 149–153 (2011).
21. Tien, J. *et al.* A comprehensive search for calcium binding sites critical for TMEM16A calcium-activated chloride channel activity. *eLife* **3,** e02772 (2014).
22. Fallah, G. *et al.* TMEM16A(a)/anoctamin-1 shares a homodimeric architecture with CLC chloride channels. *Mol. Cell. Proteomics* **10,** M110.004697 (2011).

23. Sheridan, J. T. *et al.* Characterization of the oligomeric structure of the Ca^{2+}-activated Cl^- channel Ano1/TMEM16A. *J. Biol. Chem.* **286,** 1381–1388 (2011).
24. Tien, J., Lee, H. Y., Minor, D. L. Jr, Jan, Y. N. & Jan, L. Y. Identification of a dimerization domain in the TMEM16A calcium-activated chloride channel (CaCC). *Proc. Natl Acad. Sci. USA* **110,** 6352–6357 (2013).
25. Hartzell, H. C., Yu, K., Xiao, Q., Chien, L. T. & Qu, Z. Anoctamin/TMEM16 family members are Ca^{2+}-activated Cl^- channels. *J. Physiol. (Lond.)* **587,** 2127–2139 (2009).
26. Sanyal, S. & Menon, A. K. Flipping lipids: why an' what's the reason for? *ACS Chem. Biol.* **4,** 895–909 (2009).
27. Suzuki, J., Denning, D. P., Imanishi, E., Horvitz, H. R. & Nagata, S. Xk-related protein 8 and CED-8 promote phosphatidylserine exposure in apoptotic cells. *Science* **341,** 403–406 (2013).
28. Sanyal, S. & Menon, A. K. Stereoselective transbilayer translocation of mannosyl phosphoryl dolichol by an endoplasmic reticulum flippase. *Proc. Natl Acad. Sci. USA* **107,** 11289–11294 (2010).
29. Mohammadi, T. *et al.* Identification of FtsW as a transporter of lipid-linked cell wall precursors across the membrane. *EMBO J.* **30,** 1425–1432 (2011).
30. Zwaal, R. F., Comfurius, P. & Bevers, E. M. Scott syndrome, a bleeding disorder caused by defective scrambling of membrane phospholipids. *Biochim. Biophys. Acta* **1636,** 119–128 (2004).
31. Dekkers, D. W., Comfurius, P., Bevers, E. M. & Zwaal, R. F. Comparison between Ca^{2+}-induced scrambling of various fluorescently labelled lipid analogues in red blood cells. *Biochem. J.* **362,** 741–747 (2002).
32. Sham, L. T. *et al.* Bacterial cell wall. MurJ is the flippase of lipid-linked precursors for peptidoglycan biogenesis. *Science* **345,** 220–222 (2014).
33. Suzuki, T., Suzuki, J. & Nagata, S. Functional swapping between transmembrane proteins TMEM16A and TMEM16F. *J. Biol. Chem.* **289,** 7438–7447 (2014).
34. Miller, C. Open-state substructure of single chloride channels from *Torpedo electroplax*. *Phil. Trans. R. Soc. Lond. B* **299,** 401–411 (1982).
35. Kmit, A. *et al.* Calcium-activated and apoptotic phospholipid scrambling induced by Ano6 can occur independently of Ano6 ion currents. *Cell Death Dis.* **4,** e611 (2013).
36. Tian, Y., Schreiber, R. & Kunzelmann, K. Anoctamins are a family of Ca^{2+}-activated Cl^- channels. *J. Cell Sci.* **125,** 4991–4998 (2012).
37. Baldridge, R. D. & Graham, T. R. Identification of residues defining phospholipid flippase substrate specificity of type IV P-type ATPases. *Proc. Natl Acad. Sci. USA* **109,** E290–E298 (2012).
38. Vestergaard, A. L. *et al.* Critical roles of isoleucine-364 and adjacent residues in a hydrophobic gate control of phospholipid transport by the mammalian P4-ATPase ATP8A2. *Proc. Natl Acad. Sci. USA* **111,** E1334–E1343 (2014).
39. Pifferi, S., Dibattista, M. & Menini, A. TMEM16B induces chloride currents activated by calcium in mammalian cells. *Pflugers Arch.* **458,** 1023–1038 (2009).
40. Woodhull, A. M. Ionic blockage of sodium channels in nerve. *J. Gen. Physiol.* **61,** 687–708 (1973).
41. Arreola, J., Melvin, J. E. & Begenisich, T. Activation of calcium-dependent chloride channels in rat parotid acinar cells. *J. Gen. Physiol.* **108,** 35–47 (1996).
42. Xiao, Q. *et al.* Voltage- and calcium-dependent gating of TMEM16A/Ano1 chloride channels are physically coupled by the first intracellular loop. *Proc. Natl Acad. Sci. USA* **108,** 8891–8896 (2011).
43. Vocke, K. *et al.* Calmodulin-dependent activation and inactivation of anoctamin calcium-gated chloride channels. *J. Gen. Physiol.* **142,** 381–404 (2013).
44. Yu, K., Zhu, J., Qu, Z., Cui, Y. Y. & Hartzell, H. C. Activation of the Ano1 (TMEM16A) chloride channel by calcium is not mediated by calmodulin. *J. Gen. Physiol.* **143,** 253–267 (2014).
45. Tian, Y. *et al.* Calmodulin-dependent activation of the epithelial calcium-dependent chloride channel TMEM16A. *FASEB J.* **25,** 3 1058–1068 (2011).
46. Jung, J. *et al.* Dynamic modulation of ANO1/TMEM16A HCO_3^- permeability by Ca^{2+}/calmodulin. *Proc. Natl Acad. Sci. USA* **110,** 360–365 (2013).

Supplementary Information is available in the online version of the paper.

Acknowledgements This research was supported by a grant from the European Research Council (no. 339116, AnoBest) and by the Swiss National Science Foundation through the National Centre of Competence in Research TransCure. We thank the staff of the X06SA beamline for support during data collection, B. Blattman and C. Stutz-Ducommun of the Protein Crystallization Center at UZH, for their support with crystallization, B. Dreier for help with MALS experiments, A. Szydelko for providing ecClC as negative control in the scramblase assay and D. Drew for the FGY217 yeast strain. All members of the Dutzler laboratory are acknowledged for help in all stages of the project.

Author Contributions J.D.B. screened homologues, purified and crystallized nhTMEM16 and performed scrambling experiments. N.K.L. screened and crystallized homologues, performed electrophysiological recordings and did the MALS measurement. S.S. started the project, made expression vectors and aided in cell culture. A.D. screened homologues. R.D. assisted J.D.B. and N.K.L. during structure determination. J.D.B., N.K.L., S.S. and R.D. jointly planned experiments, analysed data and wrote the manuscript.

Author Information Coordinates and structure factors have been deposited in the Protein Data Bank under accession codes 4WIS (nhTMEM16 CF1) and 4WIT (nhTMEM16 CF2). Reprints and permissions information is available at www.nature.com/reprints. The authors declare no competing financial interests. Readers are welcome to comment on the online version of the paper. Correspondence and requests for materials should be addressed to R.D. (dutzler@bioc.uzh.ch).

METHODS

Cloning. The gene encoding nhTMEM16 from *Nectria haematococca* (PubMed accession number XM_003045982) was synthesized by GenScript and the gene encoding murine TMEM16A (mTMEM16A, isoform a) was obtained from ImaGenes (Clone IRAVp968B10135D). Expression vectors were modified to be compatible with FX-cloning[47]. For expression in *S. cerevisiae* nhTMEM16 was cloned into a modified pYES2/CT plasmid (Life Technologies) as C-terminal fusion to a cassette encoding EGFP, preceded by a His_{10}-tag and followed by a HRV 3C cleavage site (crystallization construct) or as N-terminal fusion to a cassette containing a streptavidin-binding peptide (SBP) tag[48] preceded by a Myc tag and a HRV 3C cleavage site (scramblase assay construct). For expression in tsA201 cells, nhTMEM16 and mTMEM16A were cloned into a modified pcDNA3.1 vector (Invitrogen), bearing a 5′ UTR (untranslated region) of hVEGF (from pcDNA4/HisMax, Invitrogen) upstream of the start codon. nhTMEM16 as well as mTMEM16A (isoform a) contained a C-terminal HRV 3C cleavage site, a Myc- and an SBP tag (scramblase assay constructs). For expression in HEK293T cells mTMEM16A (isoform ac) as well as nhTMEM16 were expressed with a C-terminal fusion encoding a Venus-yellow fluorescent protein (YFP)[49], a Myc- and an SBP tag[50] (defined as mTMEM16A–YFP, nhTMEM16–YFP; used in electrophysiological recordings). The mTMEM16Aac isoform used in patch-clamp experiments was generated by PCR. All point mutations were introduced by site-directed mutagenesis.

Protein expression. For expression of nhTMEM16 and its mutants, the pYES2/CT vectors carrying the respective genes were transformed into *S. cerevisiae* FGY217 cells carrying an *URA* deletion for positive selection as described[51]. Cells were grown at 30 °C in fermentation culture in yeast nitrogen base (without amino acids, Sigma) supplemented with Synthetic Complete drop-out medium without uracil (Formedium) and 0.1% glucose. Protein expression was induced with 2% galactose for 40 h at 25 °C at an OD_{600} of 0.8. For generation of selenomethionine labelled protein, BY4741 cells (*MAT**a** his3Δ1 leu2Δ0 met15Δ0 ura3Δ0*) were grown at 30 °C to an OD_{600} of 2–3, centrifuged and washed to remove residual methionine before induction. The cells were subsequently suspended in yeast nitrogen base without amino acids (Sigma), supplemented with Synthetic Complete drop-out medium without Met/uracil (Formedium), 0.01% raffinose and 100 mg l^{-1} Selenomethionine (Acros Organics), grown for 1 h, induced and expressed as described for wild type (WT). For expression in mammalian cells, tsA201 cells (catalogue no. 96121229, Sigma-Aldrich) with a confluency of 40–60% were transfected with plasmid DNA containing nhTMEM16 or mTMEM16A as described[50], except that the transfection buffer was prepared with 2.8 mM Na_2HPO_4. Expression was carried out in 10-cm dishes (Corning) at 37 °C and 2.2% CO_2 for 1–2 days. For electrophysiology HEK293T cells were transfected with the respective plasmids containing WT or mutant mTMEM16A (isoform ac, 5 μg of DNA per 3.5-cm dish) by similar protocols.

Protein purification. *S. cerevisiae* expressing WT nhTMEM16 was harvested by centrifugation and resuspended in buffer A (50 mM HEPES pH 7.6, 150 mM NaCl) containing 0.5 mM $CaCl_2$, protease inhibitors (Complete, Roche), DNase I, and 1 mM $MgCl_2$ and lysed in a custom-made pressure-based cell disruptor at 40,000 p.s.i. Cell debris was removed by low-spin centrifugation. Membranes were harvested by ultracentrifugation with a 45 TI rotor (Beckmann) at 40,000 r.p.m. for 1.5 h. All steps were carried out on ice or at 4 °C. Protein was extracted in buffer A containing 0.5 mM $CaCl_2$, 1% *n*-dodecyl-β-D-maltopyranoside (DDM, Anatrace) and protease inhibitors (Roche) for 1.5 h. Insoluble parts were removed by centrifugation for 30 min at 40,000 r.p.m. with a 45 TI rotor (Beckmann). After addition of 15 mM imidazole the protein was bound in batch to NiNTA for 1.5 h, washed with buffer B (10 mM HEPES pH 7.6, 150 mM NaCl, 5% glycerol, 0.025% DDM) containing 5 mM $CaCl_2$ and 50 mM imidazole and eluted in buffer B containing 5 mM $CaCl_2$ and 400 mM imidazole. The eluted fraction was cleaved with HRV 3C protease for 2 h and dialysed against buffer B containing 5 mM $CaCl_2$. The GFP–His_{10} fragment was removed by binding to NiNTA resin, the flow-through was concentrated (Amicon) and applied to a Superdex 200 column (GE healthcare) equilibrated in buffer C (5 mM HEPES pH 7.6, 150 mM NaCl, 0.025% DDM) containing 3 mM $CaCl_2$. The peak fraction was concentrated to 8–14 mg ml^{-1}. Prior to crystallization 0.2% *n*-undecyl-α-D-maltopyranoside (Anatrace), 50 μg ml^{-1} yeast polar lipid extract (solubilized in 1% DDM, Avanti Polar Lipids) and 2% 1,2,3-heptanetriol were added to the protein. The addition of additives was essential to remove the anisotropy of diffraction and improve the resolution from 6 to 3.3 Å. A 35 l fermentation culture harvested at an OD_{600} of 4.5 typically yielded about 5 mg of pure protein. Details concerning the purification and crystallization of nhTMEM16 in Ca^{2+}-free conditions are described in the Supplementary Discussion.

For reconstitution into liposomes WT nhTMEM16 and the triple mutant containing an SBP tag were either purified from *S. cerevisiae* or HEK tsA201 cells with similar results. mTMEM16A was expressed in HEK tsA201 cells by the same protocol. HEK tsA201 cells or membranes of *S. cerevisiae* expressing the respective protein were collected and treated with buffer A containing 5 mM EDTA, 5% glycerol, protease inhibitors and 2% DDM. Cell debris was removed by centrifugation. The supernatant was incubated with streptavidin resin (Pierce Streptavidin plus UltraLink) for 1.5 h and washed with buffer B. Protein was eluted with buffer B containing 2 mM biotin. The purity of the protein was confirmed by SDS–PAGE (Extended Data Fig. 2c). Initially, the protein was cleaved to remove the purification tag and subjected to size-exclusion chromatography on a Superdex 200 column before reconstitution. In later stages, the protein was reconstituted after affinity purification at 1 mg ml^{-1} with very similar results. For reconstitution, an 18 l fermentation culture of *S. cerevisiae* typically yielded 400 μg of pure protein. All buffers used during reconstitution were made with Ca^{2+}-free water (Merck Milipore) and chemicals extra low in Ca^{2+}. Multi-angle light scattering (MALS) experiments were carried out at 20 °C on a HPLC (Agilent 1100) connected to an Eclipse 3 system equipped with a miniDAWN TREOS MALS detector and an Optilab T-rEX refractometer (Wyatt Technology). 50 μg of purified nhTMEM16 (1 mg ml^{-1}) were injected onto a Superdex S200 column equilibrated in buffer B and eluted protein was detected online. The molecular weight was calculated at each time point during elution using a combination of ultraviolet absorbance, light scattering and differential refractive index measurements with the Astra software package (Astra 6.0, Wyatt Technology). The determined molecular weight of the protein of about 145 kDa compares well with the predicted 166 kDa of the dimer.

Crystallization and structure determination. WT nhTMEM16 (containing two additional residues on the N terminus remaining from the protease cleavage site) was crystallized in sitting drops at 4 °C. Crystals were prepared by mixing protein at a concentration of 8–14 mg ml^{-1} in a 1:1 ratio with reservoir containing either 100 mM Capso pH 9.4, 100 mM $MgCl_2$, 100 mM NaCl and 21–23% PEG400 (CF1) or 50 mM HEPES pH 7.4, 100 mM ammonium sulphate, 21–23% PEG400 (CF2). Crystals were harvested after 2–3 weeks (CF1) or 1 week (CF2), cryoprotected by increasing the PEG400 concentration to 36% and flash-frozen in liquid propane.

All data sets were collected on frozen crystals on the X06SA beamline at the Swiss Light Source (SLS) of the Paul Scherrer Institut (PSI) on a PILATUS 6M detector (Dectris, Extended Data Fig. 4a). The data were indexed, integrated and scaled with XDS[52] and further processed with CCP4 programs[53]. Both crystal forms are of space group $P2_12_12_1$ and each contains a dimer of the protein in its respective asymmetric unit (Extended Data Fig. 4a). The structure of the nhTMEM16 (CF2) was determined by the single-wavelength anomalous dispersion (SAD) method with data collected from crystals containing selenomethionine-derivatized protein. The Se-sites were identified with SHELX C and D[54,55] and refined in SHARP[56]. Initial phases at low resolution were improved by solvent flattening and twofold NCS averaging in DM[57]. A coarse model was built in O[58] and used as search model for molecular replacement in CF1 with PHASER[59]. Phases were subsequently extended to 3.3 Å by NCS and cross-crystal averaging with DM. Models were built with O and COOT[60]. The correct register of the protein was confirmed with the help of 13 methionine positions defined in the SeMet data set and from sulphur anomalous data collected for mutants F612M and L624M where methionine residues were inserted in regions of the protein that lack this amino acid. The structure was initially refined maintaining strict twofold NCS constraints in CNS[61]. In later stages, the strict constraints were loosened and restraint individual B-factors and TLS parameters were refined in PHENIX[62]. R and R_{free} were monitored throughout. R_{free} was calculated by selecting 5% of the reflection data that were omitted in refinement. The final model (CF1) contains 654 out of 735 residues per subunit, has R/R_{free} values of 23.8% and 28.5%, good geometry and no outliers in the Ramachandran plot (Extended Data Fig. 4a). Regions not defined in the electron density include residues 1–18, 130–140, 465–482, 586–593, 657–659, 685–691 and 720–735. The structure of nhTMEM16 in CF2 was refined in PHENIX as described for CF1. Both structures show very similar conformations. Ca^{2+} positions were identified from data collected at 1.95 Å to improve the anomalous scattering of the bound ions and included in the refinement (Extended Data Fig. 4a).

Liposome preparation and scrambling assay. Liposomes were prepared as 3:1 mixture of *Escherichia coli* polar lipids/egg PC (Avanti Polar Lipids). For scramblase assays lipids were supplemented with either 0.5% 1,2-dimyristoyl-*sn*-glycero-3-phosphoethanolamine-*N*-(NBD) or 1,2-dioleoyl-*sn*-glycero-3-phospho-L-serine-*N*-(NBD) (Avanti Polar Lipids). For control experiments approximately 20 μM NBD-dextran (prepared following manufacturers instruction, Life technologies) was added during liposome preparation instead of NBD-labelled lipids. Liposomes were suspended in buffer D (20 mM HEPES pH 7.4, 300 mM KCl) containing either 2 mM EGTA (for Ca^{2+}-free conditions), or 2 mM EGTA and the concentration of Ca^{2+} or other divalent cations (made from the respective nitrate salts) as calculated by MAXCHELATOR (http://maxchelator.stanford.edu/CaMgATPEGTA-TS.htm) to reach the indicated free divalent ion concentration. Liposomes were prepared as described[63]. Briefly, liposomes were subjected to three freeze-thaw cycles, subsequently extruded through a 400-nm polycarbonate filter (Avestin) and destabilized with Triton-X-100. Purified protein (5 μg per mg lipid) was added and detergent was removed by stepwise addition of SM-2 adsorbent biobeads (Bio-Rad). Proteoliposomes were formed at 4 °C under gentle agitation, incubated for 40 h, collected

by ultracentrifugation, resuspended in buffer D containing the above-mentioned concentrations of EGTA and divalent ions at a lipid concentration of 20 mg ml^{-1}, flash-frozen in liquid N_2 and stored at –80 °C. All buffers were prepared with Ca^{2+}-free water (Merck Millipore) using highly pure chemicals low in Ca^{2+}. The scramblase assay was performed similarly as previously described[14]. After three freeze-thaw cycles and extrusion (400-nm filter), 20 µl of proteoliposome suspension was diluted in 2 ml buffer D (with HEPES pH 7.4 concentration increased to 60 mM) containing either 2 mM EGTA, or 2 mM EGTA and the calculated concentrations of divalent ions, in a stirred cuvette at 23 °C. Sodium dithionite (Sigma) was added after 1 min to a final concentration of 30 mM unless stated otherwise and fluorescence decay was recorded on a Fluoromax-4 spectrofluorometer (Horiba, excitation 470 nm, emission 530 nm). For analysis the fluorescence intensity was normalized to F/F_{max}.

Patch-clamp electrophysiology. For electrophysiology mTMEM16A–YFP and nhTMEM16–YFP were expressed in HEK293T cells. Cells expressing either protein were identified by the fluorescence of the C-terminal Venus–YFP tag and used for patch-clamp experiments within 36 h after transfection. Experiments were conducted at room temperature (20–22 °C) with fire-polished borosilicate glass patch pipettes (4–8 MΩ). Currents were recorded in either whole-cell configuration or from excised patches in the inside-out configuration with an Axopatch 200B amplifier, digitized at 10 kHz, filtered at 1 kHz and analysed using Clampfit (MDS Analytical Technologies). Solutions were prepared as described[16]. Standard external solution contained: 140 mM NaCl, 4 mM KCl, 2 mM $CaCl_2$, 1 mM $MgCl_2$, 10 mM glucose, and 10 mM HEPES (pH 7.4). Ca^{2+}-free intracellular slution contained 146 mM $CsCl_2$, 2 mM $MgCl_2$, 5 mM EGTA, 10 mM sucrose, and 8 mM HEPES (pH 7.4), adjusted with *N*-methyl-D-glucamine. High Ca^{2+} solution contained 5 mM Ca^{2+}-EGTA (resulting in a free Ca^{2+} concentration of 20 µM). Intermediate Ca^{2+} solutions were prepared by mixing Ca^{2+}-free and high-Ca^{2+} solutions in corresponding ratios. Solution containing free Ca^{2+} concentrations higher than 20 µM were prepared by addition of the corresponding amounts of $CaCl_2$. In these cases EGTA was replaced by Br_2-BAPTA (5,5′-dibromo-1,2-bis(2-aminophenoxy)ethane-N,N,N′,N′-tetraacetic acid, 3.5 mM; Invitrogen). Solutions were applied with a double-barrelled theta tubing with a tip diameter of 400 µm attached to a piezo-bimorph (Siskiyou). The Ca^{2+} dependence of mTMEM16A and its mutants was measured in excised inside-out patches. Whereas the observed maximum current was similar to WT in mutants N650A, E702Q and E705Q, it was generally smaller in mutants E734Q, D738N and E654A. Currents generally saturated at high Ca^{2+} concentration except for E654A and D738N, where they continue to increase even at concentrations up to 10 mM Ca^{2+}. Activation in D738N shows a biphasic behaviour with an apparent saturation of currents around 100 µM and a subsequent increase above 500 µM Ca^{2+}. (Extended Data Fig. 9 and 10). A decrease of the response at increasing Ca^{2+} concentrations indicates rundown. For analysis of dose–response relationships, the current-response at different Ca^{2+} concentration recorded at a holding potential of 80 mV, was fitted to a Hill equation. Responses in D738N were only considered up to a Ca^{2+} concentration of 500 µM. The averages in the EC_{50} from 3–4 independent recordings (Extended Data Fig. 9 and 10) show shifts in the EC_{50} towards higher Ca^{2+} concentrations for all investigated mutants (WT, EC_{50} 0.36 µM, n 2.5; N650A, EC_{50} 1.8 µM, n 2.6; E702Q, EC_{50} 9.5 µM, n 2.1; E705Q, EC_{50} 231 µM, n 1.0; E734Q, EC_{50} 4.0 µM, n 1.6; D738N, EC_{50} 20.0 µM, n 0.84, where *n* is the Hill coefficient). To demonstrate the statistical significance of this increase, EC_{50} values were log-transformed for one-way ANOVA and subsequently compared to WT values using Tukey's post-hoc test for significance. Values were considered significantly different if $P < 0.05$. The analysis revealed that all shifts in the EC_{50} of Ca^{2+}-binding site mutants are statistically significant. The voltage dependence of WT suggests that Ca^{2+} crosses about 18% of the transmembrane electric field to reach its binding site (Fig. 5b).

Planar lipid bilayer experiments. For recording in planar lipid bilayers, nhTMEM16 was purified and reconstituted similarly as for the scramblase assay at lipid to protein ratios of 100:1 or 200:1, except that no NBD lipids were added. The incorporation of the protein into liposome was confirmed by freeze-fracture electron microscopy as described[64]. Proteoliposomes containing nhTMEM16 were fused to bilayers formed from 1-palmitoyl-2-oleoyl-*sn*-glycero-3-phosphoethanolamine and 1-palmitoyl-2-oleoyl-*sn*-glycero-3-phospho-(1'-*rac*-glycerol) (in ratio of 1:3 w/w, Avanti) and recorded with a horizontal planar lipid bilayer system as described[65,66]. In recordings under symmetric ion concentrations, both chambers contained 10 mM HEPES pH 7.4, 150 mM NaCl (buffer) and either no or 300 µM $CaCl_2$. In recordings under asymmetric conditions the NaCl concentration in one chamber was reduced to 15 mM. Electrodes were connected to the respective bath solutions via salt bridges. Currents were recorded with an Axopatch 200B amplifier, digitized at 10 kHz, filtered at 1 kHz and analysed using Clampfit.

47. Geertsma, E. R. & Dutzler, R. A versatile and efficient high-throughput cloning tool for structural biology. *Biochemistry* **50,** 3272–3278 (2011).
48. Keefe, A. D., Wilson, D. S., Seelig, B. & Szostak, J. W. One-step purification of recombinant proteins using a nanomolar-affinity streptavidin-binding peptide, the SBP-tag. *Protein Expr. Purif.* **23,** 440–446 (2001).
49. Nagai, T. *et al.* A variant of yellow fluorescent protein with fast and efficient maturation for cell-biological applications. *Nature Biotechnol.* **20,** 87–90 (2002).
50. Schenck, S., Wojcik, S. M., Brose, N. & Takamori, S. A chloride conductance in VGLUT1 underlies maximal glutamate loading into synaptic vesicles. *Nature Neurosci.* **12,** 156–162 (2009).
51. Drew, D. *et al.* GFP-based optimization scheme for the overexpression and purification of eukaryotic membrane proteins in *Saccharomyces cerevisiae*. *Nature Protocols* **3,** 784–798 (2008).
52. Kabsch, W. Automatic processing of rotation diffraction data from crystals of initially unknown symmetry and cell constants. *J. Appl. Crystallogr.* **26,** 795–800 (1993).
53. The Collaborative Computational Project, Number 4. The CCP4 suite: programs for X-ray crystallography. *Acta Crystallogr. D* **50,** 760–763 (1994).
54. Schneider, T. R. & Sheldrick, G. M. Substructure solution with SHELXD. *Acta Crystallogr. D* **58,** 1772–1779 (2002).
55. Pape, T. & Schneider, T. R. HKL2MAP: a graphical user interface for phasing with SHELX programs. *J. Appl. Crystallogr.* **37,** 843–844 (2004).
56. de La Fortelle, E. & Bricogne, G. in *Methods in Enzymology* Vol. 276 (eds Carter, C. W. & Sweet, R. M.) 492–494 (Academic, 1997).
57. Cowtan, K. 'dm': An automated procedure for phase improvement by density modification. *Joint CCP4 and ESF-EACBM Newsletter on Protein Crystallography* **31,** 34–38 (1994).
58. Jones, T. A., Zou, J. Y., Cowan, S. W. & Kjeldgaard, M. Improved methods for building protein models in electron density maps and the location of errors in these models. *Acta Crystallogr. A* **47,** 110–119 (1991).
59. McCoy, A. J. *et al.* Phaser crystallographic software. *J. Appl. Crystallogr.* **40,** 658–674 (2007).
60. Emsley, P. & Cowtan, K. Coot: model-building tools for molecular graphics. *Acta Crystallogr. D* **60,** 2126–2132 (2004).
61. Brünger, A. T. *et al.* Crystallography & NMR system: a new software suite for macromolecular structure determination. *Acta Crystallogr. D* **54,** 905–921 (1998).
62. Adams, P. D. *et al.* PHENIX: building new software for automated crystallographic structure determination. *Acta Crystallogr. D* **58,** 1948–1954 (2002).
63. Geertsma, E. R., Nik Mahmood, N. A., Schuurman-Wolters, G. K. & Poolman, B. Membrane reconstitution of ABC transporters and assays of translocator function. *Nature Protocols* **3,** 256–266 (2008).
64. Garcia-Celma, J., Szydelko, A. & Dutzler, R. Functional characterization of a ClC transporter by solid-supported membrane electrophysiology. *J. Gen. Physiol.* **141,** 479–491 (2013).
65. Accardi, A., Kolmakova-Partensky, L., Williams, C. & Miller, C. Ionic currents mediated by a prokaryotic homologue of CLC Cl^- channels. *J. Gen. Physiol.* **123,** 109–119 (2004).
66. Zimmermann, I. & Dutzler, R. Ligand activation of the prokaryotic pentameric ligand-gated ion channel ELIC. *PLoS Biol.* **9,** e1001101 (2011).
67. Sievers, F. *et al.* Fast, scalable generation of high-quality protein multiple sequence alignments using Clustal Omega. *Mol. Syst. Biol.* **7,** 539 (2011).

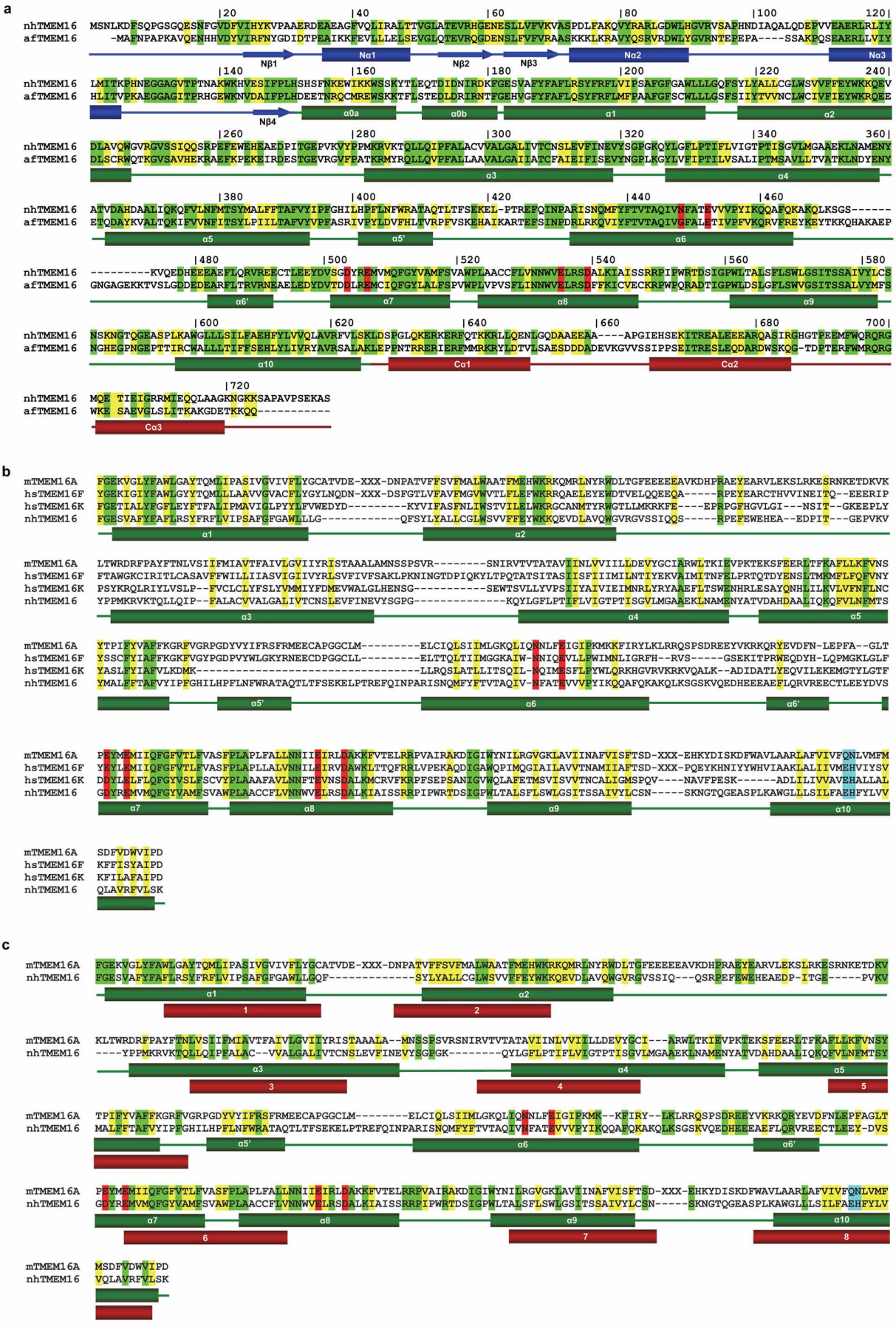

Extended Data Figure 1 | Structure-based sequence alignment. Sequences were aligned with Clustal Omega[67] and edited manually. Identical residues are highlighted in green, homologous residues in yellow and residues of the Ca^{2+}-binding site in red. Secondary structure elements are shown below. **a**, Comparison of nhTMEM16 and afTMEM16. The numbering corresponds to nhTMEM16. **b**, Comparison of the membrane domains of selected TMEM16 proteins, m refers to murine, hs to human proteins. Long insertions in loop regions of mammalian family members (indicated by -xxx-) are not shown in the alignment. The positions of residues in α-helix 10 involved in an inter-subunit salt bridge at the dimer interface are highlighted in cyan. **c**, Comparison of the observed and predicted topology of TMEM16 proteins. Sequence alignment of the membrane spanning regions of mTMEM16A and nhTMEM16 with the observed (green) and predicted topology[25] (red) indicated. Identical residues are highlighted in green, homologous residues in yellow, residues of the Ca^{2+}-binding site in red and the inter-subunit salt bridge at the dimer interface in cyan. The difference between the predicted and observed transmembrane segments is due to the failure of sequence-based approaches to identify the correct boundaries of several helices and to detect α-helix 6 at all and helices 7 and 8 as separate entities.

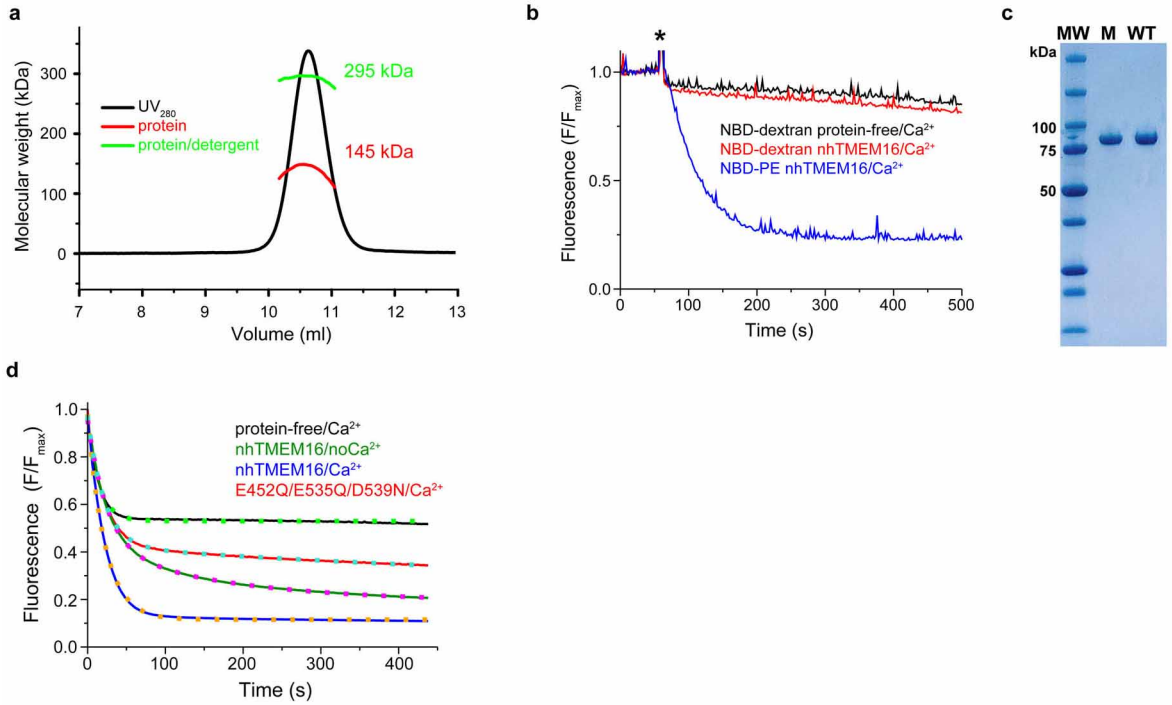

Extended Data Figure 2 | Multi-angle light scattering and lipid scrambling. **a**, Gel filtration and light scattering results for nhTMEM16 in the detergent DDM. The continuous black trace corresponds to the absorption at 280 nm. Molecular weights of the protein and the protein-detergent complex are shown in red and green, respectively. **b**, Inaccessibility of NBD groups trapped within liposomes. Dithionite is incapable of reducing the soluble NBD-dextran trapped in the interior of proteoliposomes containing nhTMEM16. Traces of proteoliposomes containing nhTMEM16 and empty liposomes are shown in red and black respectively. Traces from proteoliposomes of nhTMEM16 containing NBD-PE at equivalent dithionite levels are shown for comparison (blue). Asterisk marks addition of 2.5 mM dithionite. **c**, SDS–PAGE gel of the Ca^{2+}-binding site triple-mutant E452Q/E535Q/D539N (M) and nhTMEM16 (WT) used for reconstitution illustrating the purity of the sample. The molecular weight marker (MW) is shown on the left with selected bands labelled. **d**, Analysis of phospholipid scrambling. Time dependent fluorescence decrease of NBD-PE upon reduction by 30 mM dithionite ($t = 0$). The traces are as in Figs 1b–d and 5a. A fit to a single exponential decay is shown as dotted lines for protein-free/Ca^{2+} and nhTMEM16/Ca^{2+} with time constants of 15 s and 22 s, respectively. A fit to a sum of two exponential functions is shown for nhTMEM16/no Ca^{2+} and E452Q/E535Q/D539N/Ca^{2+} with time constants of 25 and 21 s for the fast component and 175 and 803 s for the slow component, respectively.

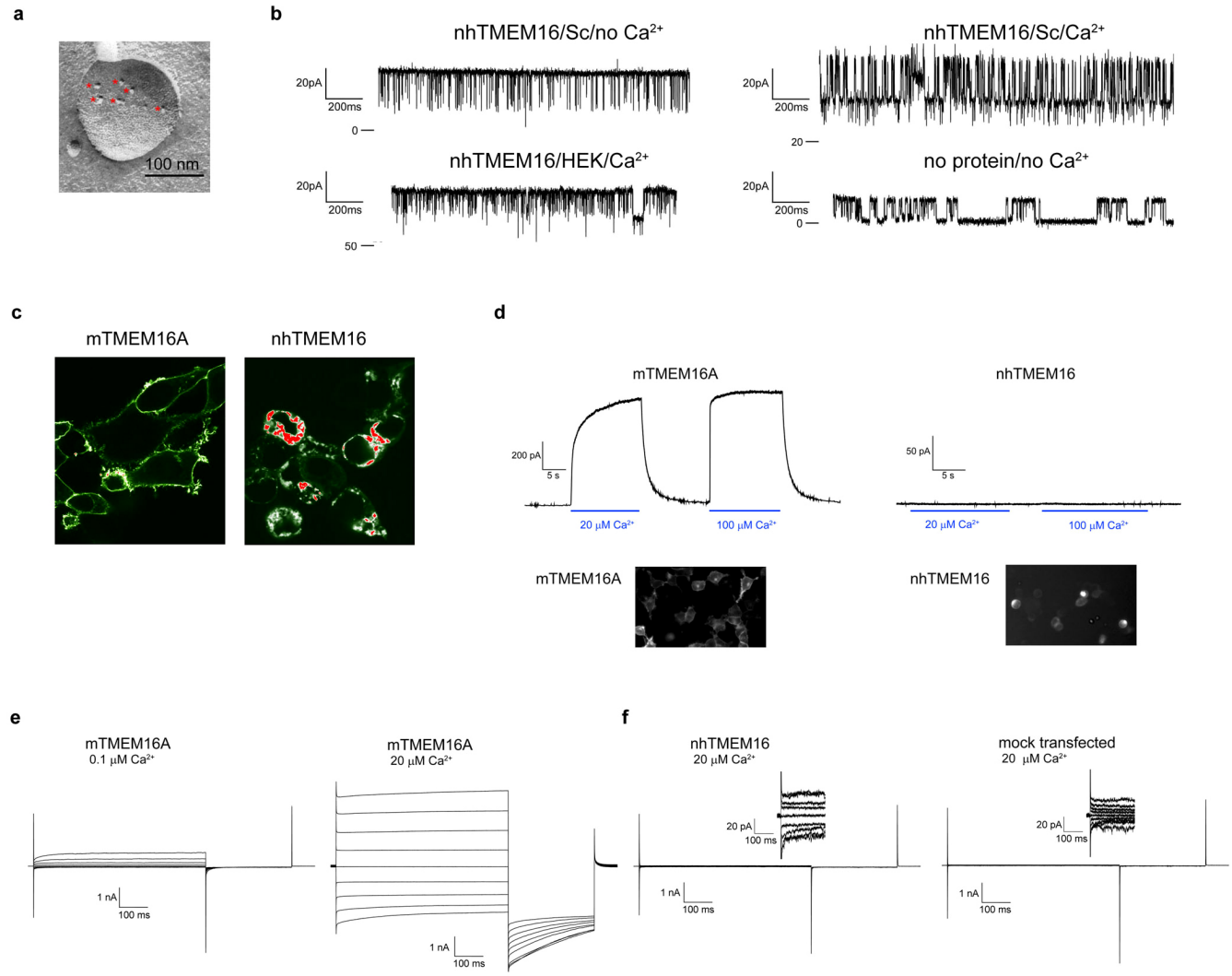

Extended Data Figure 3 | Search for ion channel activity in nhTMEM16. **a**, Freeze-fracture electron microscopy image of a proteoliposome containing nhTMEM16 formed from a 3:1 mixture of *E. coli* polar lipids/egg PC. Reconstituted proteins are labelled with red asterisks. **b**, Planar lipid bilayer experiments. Currents recorded after fusion of proteoliposomes containing nhTMEM16 expressed and purified from *S. cerevisiae* (Sc) in the absence of Ca^{2+} (top, left), with 300 μM Ca^{2+} added on both sides of the bilayer (top right) and of proteoliposomes containing nhTMEM16 expressed and purified from HEK tsA201 cells in the presence of 300 μM Ca^{2+} added on both sides of the bilayer (bottom left). Currents recorded after fusion of liposomes of the same lipid composition not containing any protein are shown for comparison (bottom right). Displayed traces were recorded at a holding potential of 100 mV in symmetric solutions containing 150 mM NaCl and 10 mM HEPES pH 7.4. Selected current levels (in pA) are indicated on the left. **c**, Fluorescence confocal microscopy images of HEK tsA201 cells expressing a mTMEM16A–YFP fusion construct (left) or a nhTMEM16–YFP fusion construct (right). **d**, Recordings from excised inside-out patches. Representative current response in a membrane patch excised from cells expressing a mTMEM16A–YFP fusion construct upon rapid exchange into solutions containing the indicated amount of Ca^{2+} (left) and equivalent recordings from patches that were excised from cells expressing a nhTMEM16–YFP fusion protein (right). The voltage was clamped at 80 mV. The fluorescence of transfected cells expressing mTMEM16A–YFP used for recording is shown below. No activity of nhTMEM16–YFP was observed in any of more than 30 patches. **e**, Patch-clamp recording in the whole-cell configuration. Representative currents from a HEK293T cell expressing a mTMEM16A–YFP construct recorded from a solution containing either 0.1 μM (left) or 20 μM (right) free Ca^{2+} in the patch pipette. **f**, Representative currents from a cell expressing a nhTMEM16–YFP fusion protein recorded from a solution containing 20 μM free Ca^{2+} in the patch pipette (left). Current response from mock-transfected cells recorded under the same conditions is shown for comparison (right). Insets show part of the traces with magnified current scale.

a

Table Data collection and refinement statistics

	nhTMEM16/CF1	nhTMEM16/CF2	nhTMEM16/SeMet	nhTMEM16/anom	nhTMEM16/no Ca^{2+}
Data collection					
Wavelength (Å)	0.9797	1.0	0.9797	1.95	1.95
Space group	$P2_12_12_1$	$P2_12_12_1$	$P2_12_12_1$	$P2_12_12_1$	$P2_12_12_1$
Cell dimensions					
a, *b*, *c* (Å)	96.5, 113.7, 235.7	115.9, 127.2, 180.1	113.7, 124.8, 177.4	115.2, 124.8, 177.4	115.2, 127.1, 179.7
(°)	90, 90, 90	90, 90, 90	90, 90, 90	90, 90, 90	90, 90, 90
Resolution (Å)	50-3.3 (3.4-3.3)*	50-3.4 (3.5-3.4)	50-4.0 (4.1-4.0)	50-3.5 (3.6-3.5)	50-4.2 (4.3-4.2)
R_{merge}	8.3 (123.5)	6.5 (149.3)	11.7 (137.9)	10.2 (116.5)	15.2 (233.7)
$I/\sigma I$	20.1 (2.6)	20.0 (1.7)	18.4 (2.3)	16.5 (1.8)	12.5 (2.0)
Completeness (%)	99.1 (98.8)	98.9 (87.9)	99.0 (100)	99.9 (100.0)	99.9 (100)
Redundancy	12.7 (12.7)	9.6 (8.6)	22.9 (15.9)	12.2 (7.0)	18.8 (17.8)
$CC_{1/2}$ (%)	99.9 (80.3)	99.9 (59.8)	100.0 (71.1)	99.8 (69.5)	99.8 (75.3)
Refinement					
Resolution (Å)	15-3.3	15-3.4		15-3.5	15-4.2
No. reflections	38985	36750		32709	19356
R_{work}/ R_{free}	23.8 (28.5)	24.8 (29.2)		23.7 (28.5)	23.0 (27.2)
No. atoms	10574	10574		10574	10570
Protein	10570	10570		10570	10570
Ligand/ion	4	4		4	0
B-factors					
Protein	137	159		147	199
Ligand/ion	104	146		123	-
R.m.s deviations					
Bond lengths (Å)	0.003	0.002		0.003	0.003
Bond angles (°)	0.74	0.70		0.90	0.78

*Highest resolution shell is shown in parenthesis.

b

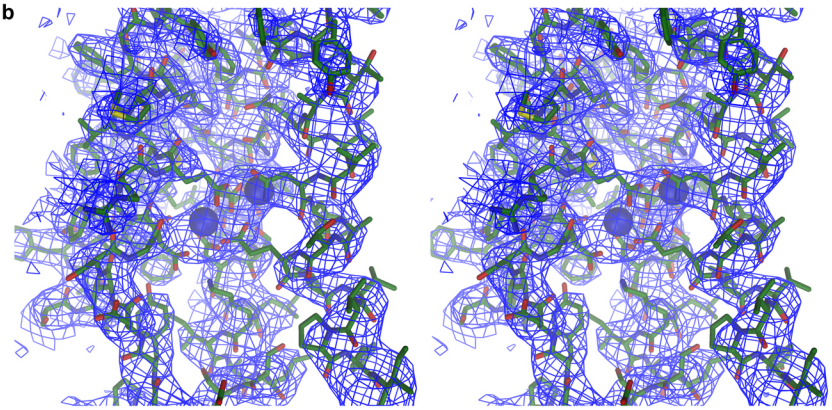

Extended Data Figure 4 | Crystallography. a, Table describing data collection and refinement statistics of five data sets presented in this study. nhTMEM16/CF1 and nhTMEM16/CF2 are data sets used for the building and refinement of the crystal structures of CF1 and CF2 respectively that have been deposited in the PDB. nhTMEM16/SeMet, a data set of a selenomethionine derivative collected at the Se anomalous absorption edge, was used for obtaining initial phases of CF2. nhTMEM16/anom is a data set used for the identification of the Ca^{2+}-binding site by anomalous scattering and nhTMEM16/no Ca^{2+} is from a protein purified in the presence of EDTA and crystallized without addition of Ca^{2+}. **b**, Stereo view of the Ca^{2+}-binding region in CF1. The model of the protein displayed as sticks is shown with experimental electron density superimposed. The map was calculated at 3.3 Å with Se-Met SAD phases that were improved by solvent flattening, cyclic twofold NCS and cross-crystal averaging (blue mesh, contoured at 1σ). Ca^{2+} ions are shown as blue spheres.

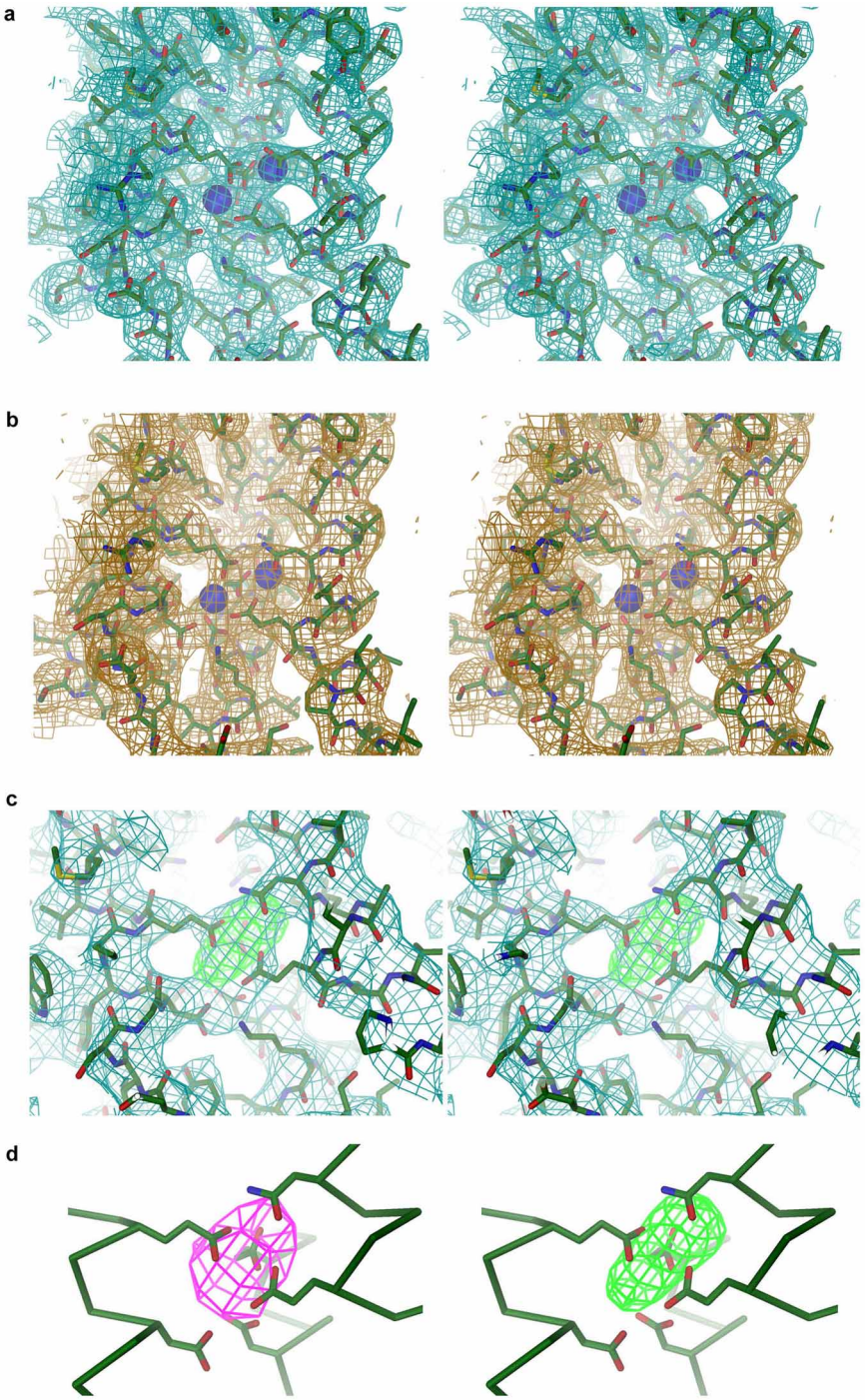

Extended Data Figure 5 | Electron density. **a**, Stereo view of the Ca^{2+}-binding region in CF1. The model of the protein displayed as sticks is shown with $2F_o - F_c$ electron density superimposed (cyan mesh, contoured at 1σ after sharpening with $b = 50$). The density at 3.3 Å was calculated with phases from the refined model. Ca^{2+} ions are shown as blue spheres. **b**, $2F_o - F_c$ electron density of the Ca^{2+}-binding region in CF2 (calculated at 3.4 Å and contoured at 1σ after sharpening with $b = 50$, orange) superimposed on the refined model. **c**, Stereo view of the Ca^{2+}-binding region of a structure obtained from protein purified in the presence of EDTA and crystallized in CF2 without addition of Ca^{2+}. $2F_o - F_c$ electron density (cyan mesh, calculated at 4.2 Å and contoured at 1σ after sharpening with a $b = 50$) and $F_o - F_c$ density (contoured at 3σ, green) is superimposed on the refined model. No ions were included in the refinement. **d**, Close-up of the Ca^{2+}-binding site. Anomalous difference density (left, calculated at 6 Å and contoured at 4σ, magenta) and $F_o - F_c$ density (right, contoured at 3σ, green) indicates the presence of bound Ca^{2+} ions.

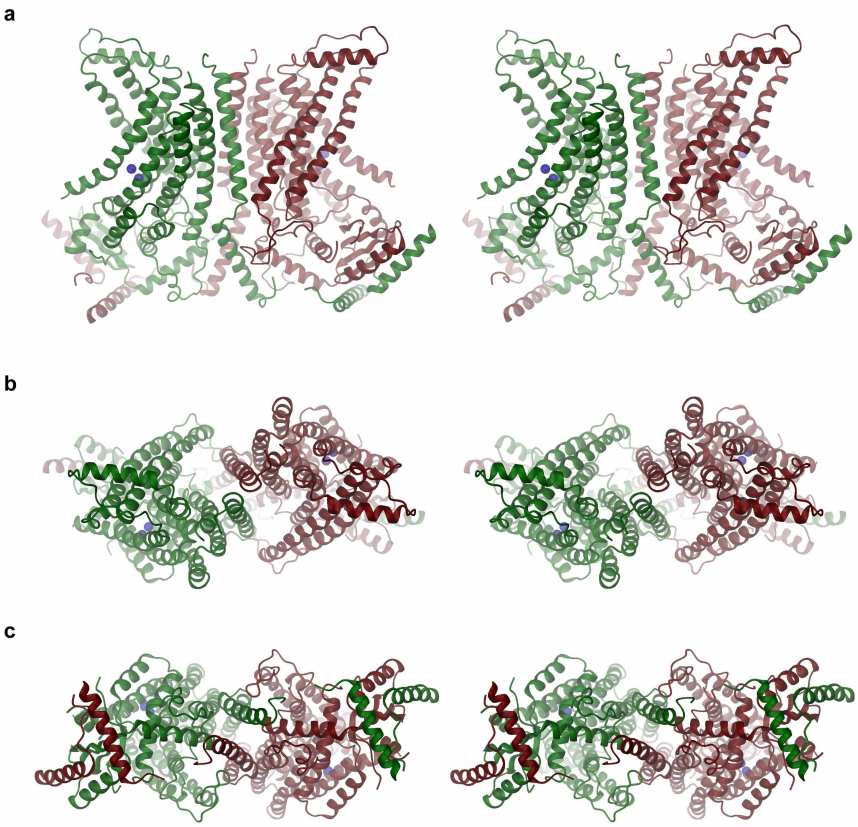

Extended Data Figure 6 | nhTMEM16 dimer. Stereo views of a ribbon representation of the dimeric protein. Bound Ca^{2+} ions are shown as blue spheres. **a**, View from within the membrane; **b**, view from the extracellular side; **c**, view from the cytoplasm.

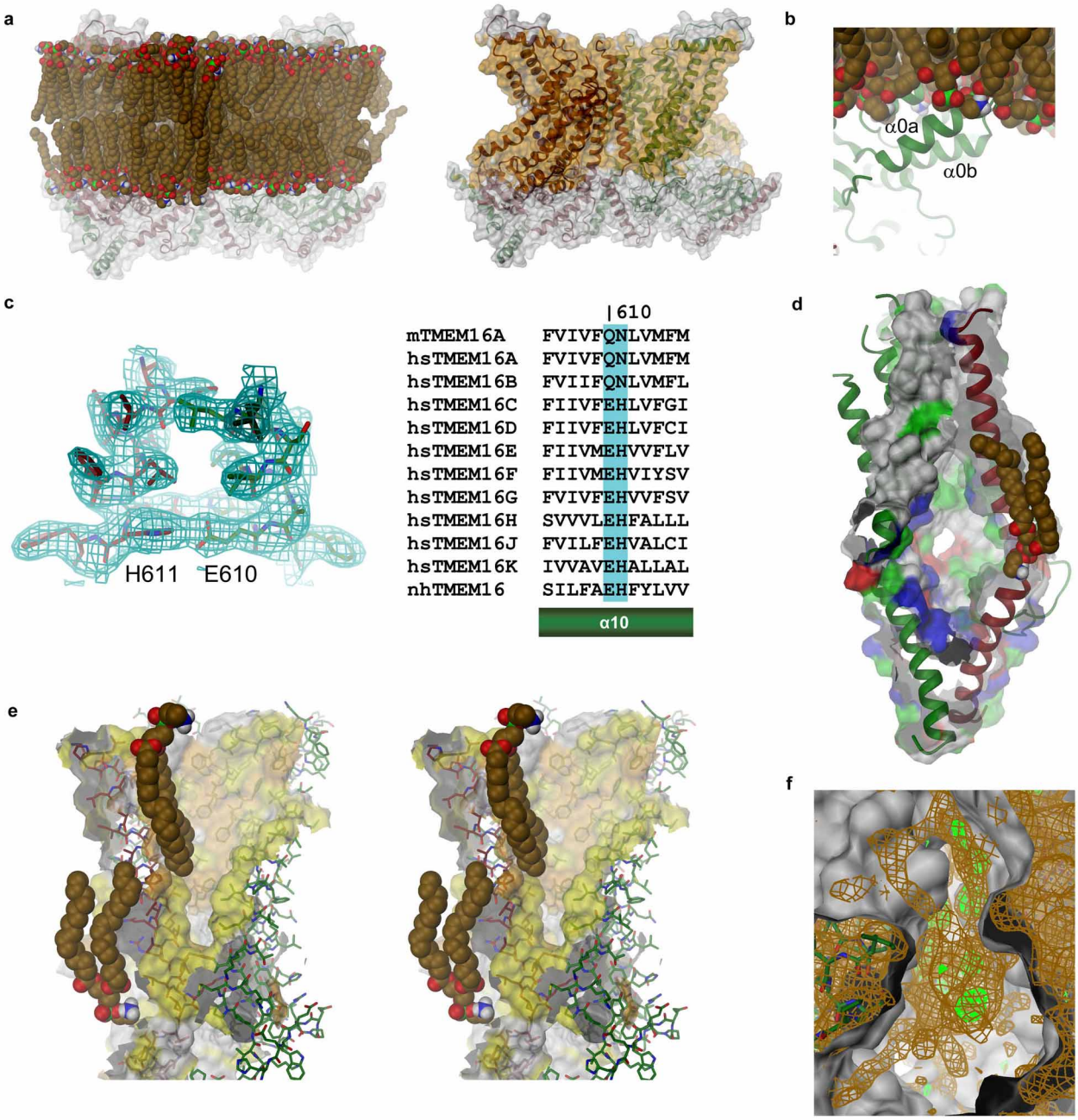

Extended Data Figure 7 | Model of lipid interactions and dimer cavity. **a**, Model of nhTMEM16 embedded in a lipid membrane (left). The protein was positioned within the model of a PC bilayer (obtained from http://www.lobos.nih.gov/mbs/coords.shtml). A ribbon representation of the protein and the molecular surface are shown. Lipids are displayed as CPK models. Same view of the protein with regions on the surface presumably in contact with the membrane coloured in orange (right). **b**, Putative location of α-helices 0a and 0b relative to the lipid bilayer. **c**, Inter-subunit interactions between residues of α-helix 10. The protein is shown as sticks with $2F_o - F_c$ density (CF1, calculated at 3.3 Å and contoured at 1σ after sharpening with $b = 50$, cyan mesh) superimposed (left). A sequence alignment of the corresponding region underlines the conservation of interacting residues. Amino acids of the salt bridge in nhTMEM16 are highlighted in cyan, the numbering corresponds to nhTMEM16. **d**, View on the dimer cavity from the dimer interface. The molecular surface is coloured according to the properties of contacting residues (red, acidic; blue, basic; green, polar). A modelled lipid indicates the boundary of the inner leaflet of the bilayer. **e**, Stereo view of the cleft between α-helices 3 and 10. The protein is shown as stick model. The molecular surface is coloured according to the properties of contacting residues (yellow, hydrophobic; orange, aromatic). Lipids indicate the membrane boundary. **f**, Residual density in the dimer cavity. The molecular surface is coloured in white. $2F_o - F_c$ density (CF2, contoured at 1σ after sharpening with $b = 50$, orange) and $F_o - F_c$ density (contoured at 3σ, green) are shown. The view is as in **d**.

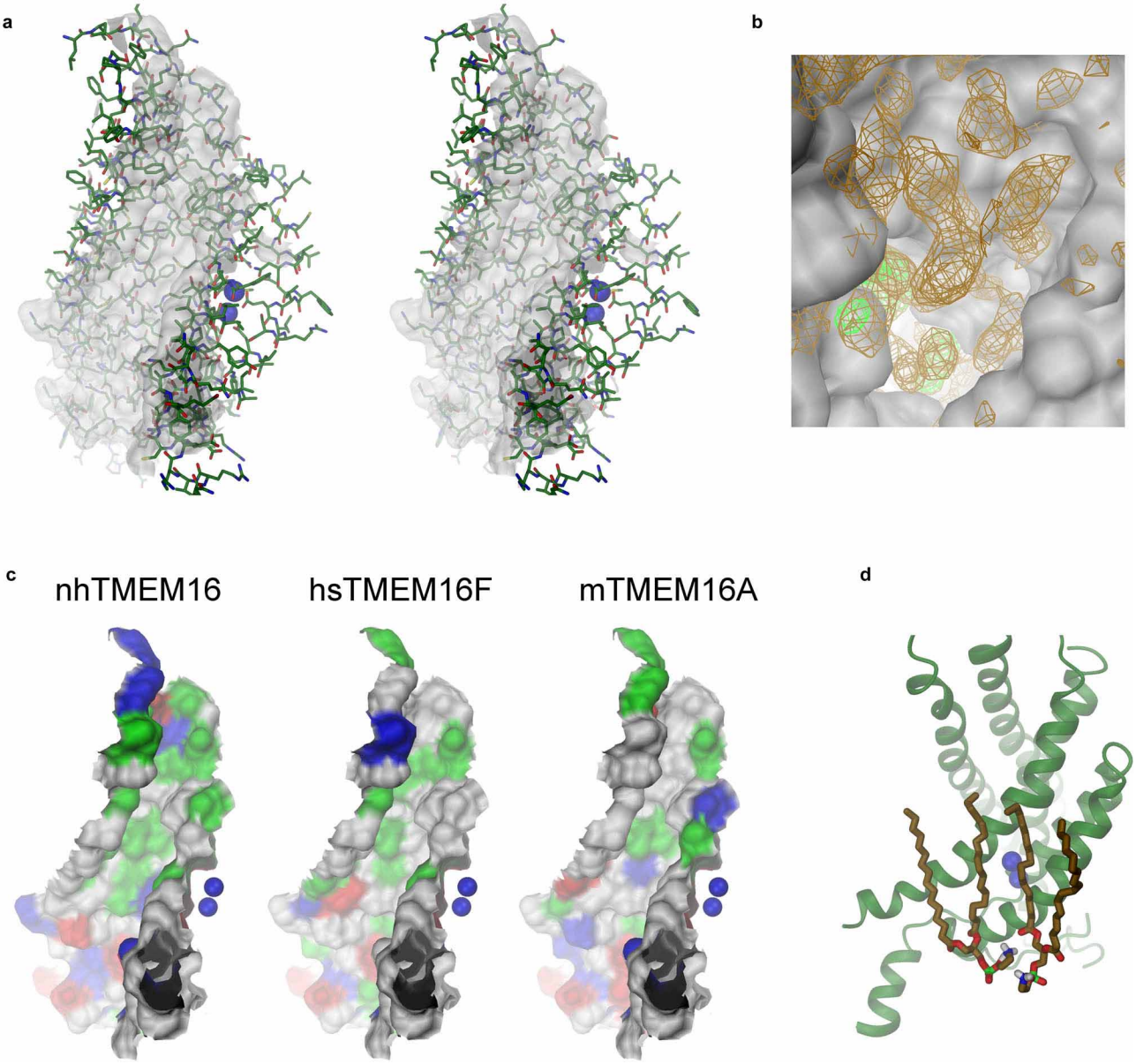

Extended Data Figure 8 | Subunit cavity and Ca^{2+}-binding site. **a**, Stereo view of the subunit cavity viewed from within the membrane. Protein residues and the molecular surface are shown. **b**, Residual density in the subunit cavity. The molecular surface of the protein is shown. $2F_o - F_c$ density (CF2, contoured at 1σ after sharpening with $b = 50$, orange) and $F_o - F_c$ density (contoured at 3σ, green) are displayed. **c**, Model of the subunit cavity in different TMEM16 proteins. The molecular surface is coloured according to the properties of contacting residues (red, acidic; blue, basic; green, polar). Putative surface-exposed residues were obtained from a sequence alignment with nhTMEM16. **d**, Location of the Ca^{2+}-binding site in relation to the lipid bilayer. Modelled lipids of the inner leaflet of the bilayer are shown as sticks.

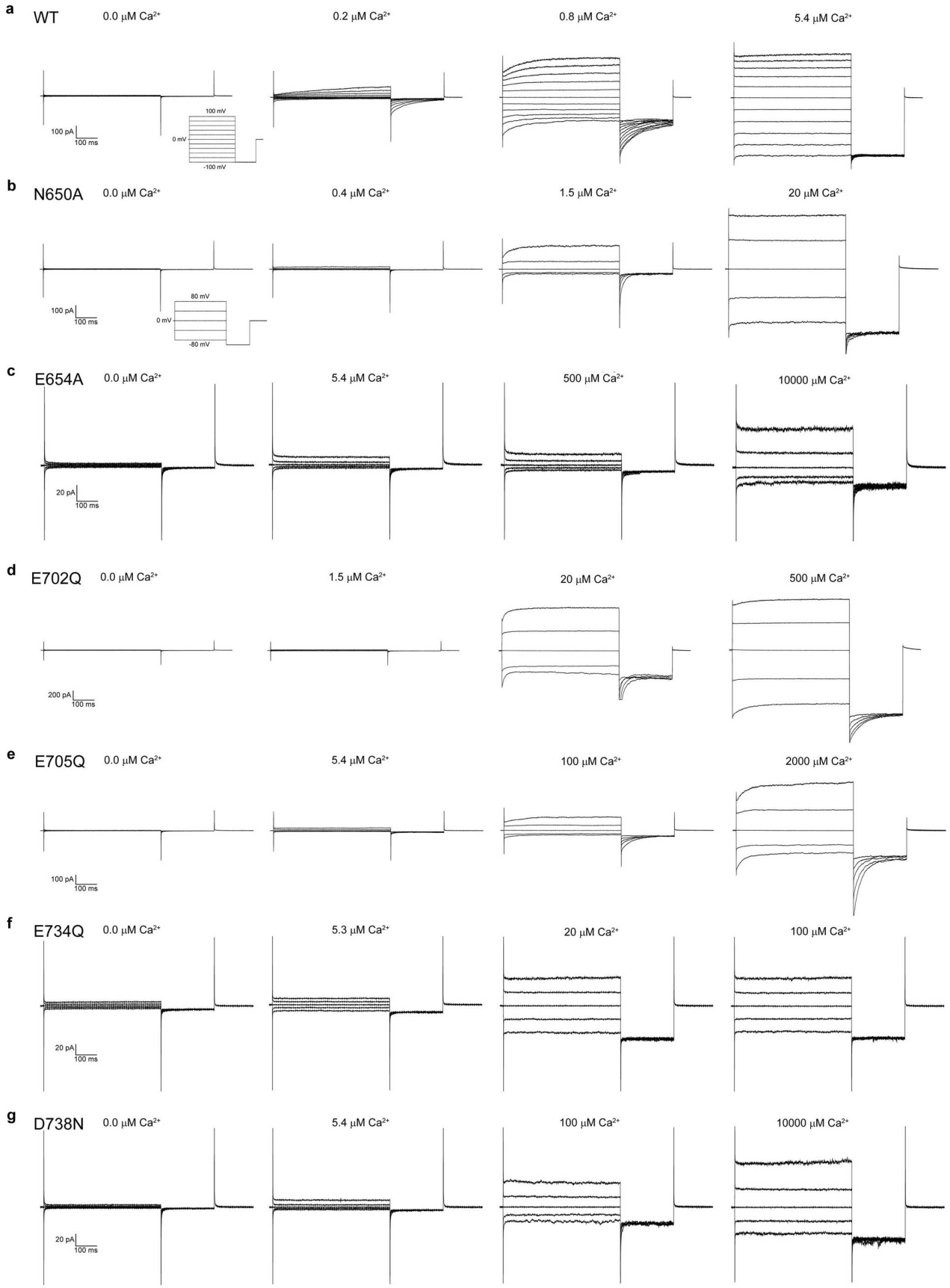

Extended Data Figure 9 | Electrophysiology. Current response in HEK293T cells overexpressing mTMEM16A–YFP and point mutants of the Ca^{2+}-binding site. All recordings were measured from single excised patches in the inside-out configuration after changing to intracellular solutions containing the indicated Ca^{2+} concentrations. **a**, WT, with voltage protocol shown as inset. **b**, Mutant N650A, with the voltage protocol shown as inset. **c**–**g**, Recordings of mutants E654A, **c**, E702Q, **d**, E705Q, **e**, E634Q, **f**, and mutant D738N, **g**.

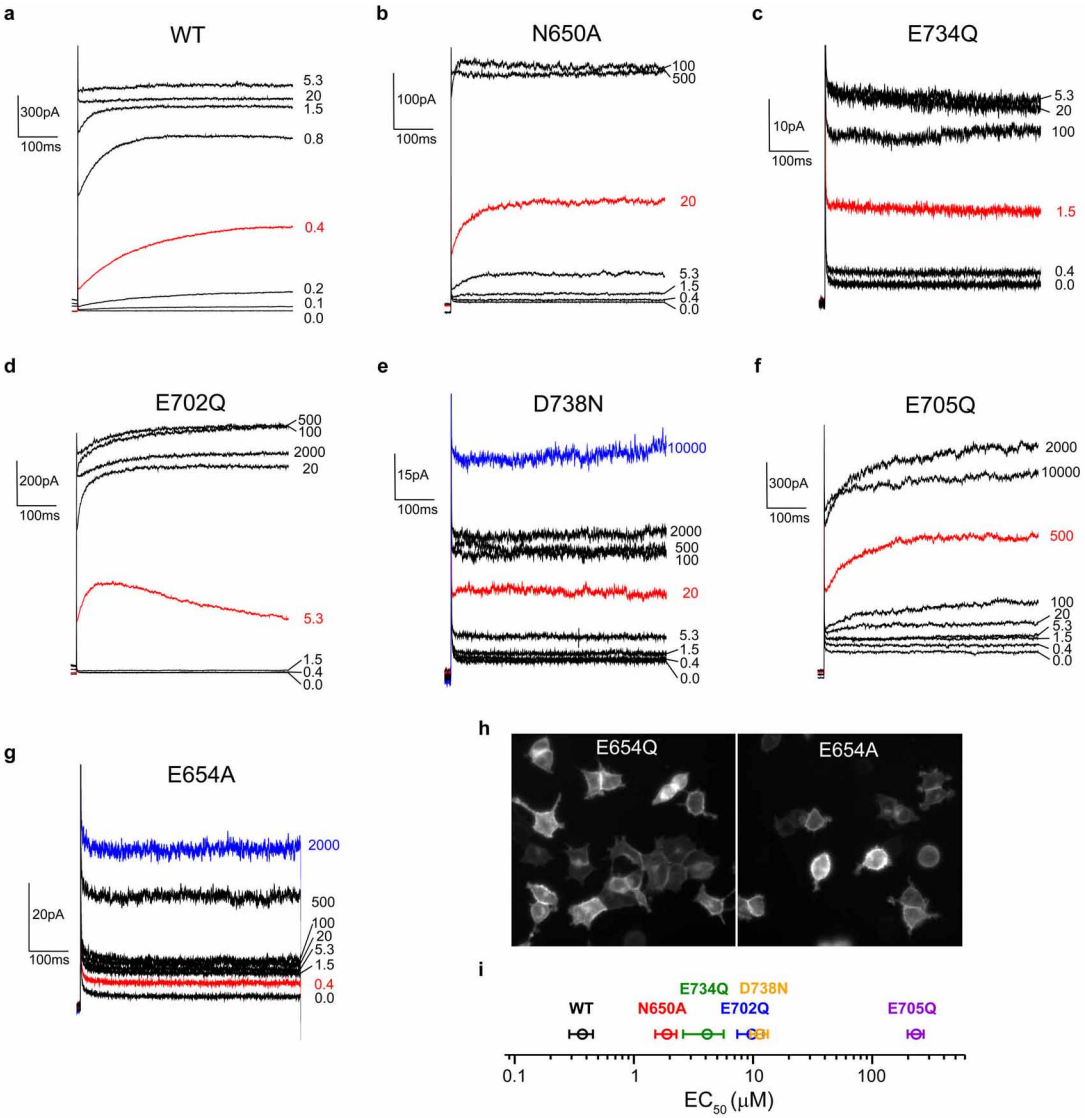

Extended Data Figure 10 | Ca^{2+} activation of mTMEM16A. Representative current traces of mTMEM16A and mutants of the Ca^{2+}-binding site. Currents were measured from excised inside-out patches of HEK293T cells expressing the respective protein at 80 mV. The Ca^{2+} concentration is indicated, selected traces are shown in colour. **a**, WT, **b**, N650A, **c**, E734Q, **d**, E702Q, **e**, D738N **f**, E705Q and **g**, E654A. **h**, Fluorescence microscopy image of mTMEM16A mutants expressed in HEK293T cells. Expression of fluorescently labelled protein is shown for mutants E654Q (left) and E654A (right). **i**, Analysis of the EC_{50} of Ca^{2+} activation for different binding site mutants. The data show averages of fits to 3–4 independent recordings. Errors are s.d.

3. Discussion

At the start of this thesis (early 2010), the knowledge about TMEM16 proteins was extremely limited, a fact that was reflected in the low number of available publications (19) at that time. The main focus of the field was and is still put on the functional characterization of TMEM16A, one of the first members to be identified at the molecular level [4-6]. In only few reports the topology of TMEM16 proteins was explored using epitope mapping methods and hydrophobicity analyses [11, 176, 218]. Owing to the lack of available structural information on TMEM16 proteins, this thesis aimed at drawing a detailed molecular picture of the first member of this family.

As part of the results of this work, the structure determination of a fungal homologue from *Nectria haematococca*, nhTMEM16, has permitted first insight into the architecture of TMEM16 proteins, which share a structural organization that was not described before. Furthermore, for the first time, the structure of a scramblase was revealed and the study of scrambling processes is now facilitated with a model near atomic resolution. As observed in the structure, nhTMEM16 is organized as homodimer with ten transmembrane spanning helices per monomer and cytosolic amino- and carboxy termini. While the dimeric arrangement of TMEM16 proteins was already previously predicted [177, 178], the topology was not very accurately anticipated. Whereas the topology established based on epitope mapping and hydrophobicity analysis predicted only eight transmembrane domains [11, 218, 219, 290, 291] nhTMEM16 spans the membrane ten times. Essentially, these differences arose from difficulties to identify transmembrane helix 6 at all and transmembrane helices 7 and 8 as separate entities (Figure 12). Besides the novel architecture of the transmembrane domain, the structure of nhTMEM16 has revealed a couple of very interesting structural features. These features include the amino- and carboxy termini and the dimer interface within the transmembrane part, which potentially all contribute to the dimeric arrangement, the constitution and localization of the Ca^{2+} binding site within the hydrophobic membrane-inserted part, and the nearby subunit cavity, a crevice of uncommon hydrophilic character, that traverses the entire membrane and is presumably linked to Ca^{2+} activation and lipid scrambling. The following chapters aim at describing these unusual features in detail and drawing potential conclusions on functional consequences. In addition, scrambling processes, which were investigated using purified nhTMEM16 protein reconstituted into liposomes, are analyzed, quantified and put in context with the scrambling processes described in other TMEM16 family members. At the same time, efforts are made to link functional aspects with the structure. Then, the dual- functionality of TMEM16 proteins, phospholipid scrambling and ion conductance, is thoroughly discussed. Furthermore, the next chapters aim at giving insight into the mode of Ca^{2+} activation in TMEM16 proteins. Based on experiments on Ca^{2+} activated chloride channels (CaCCs) [1, 136, 292-294], TMEM16A [4-6] and F [10, 111], scrambling experiments in blood cells [13, 14], afTMEM16 [170], nhTMEM16 [295] and using the structure obtained in the course of this work [295], suggestions are provided on the mechanism of ion conduction and lipid scrambling.

3.1. The N- and C- termini: A potential role in dimerization

As observed in the structure, the carboxy terminus of nhTMEM16 consists of three alpha helical regions of a total length of 100 amino acids. The C- terminus of one subunit in the dimer wraps around the amino-terminus of the other subunit, presumably interacting with each other. While the carboxy terminus of TMEM16 family members is in most cases short only containing 50- 100 amino acids, the amino-terminus is longer and ranges between 170- 350 amino acids for most TMEM16 homologues. Interactions between equivalent helices of the two amino- termini of the dimer, that were proposed to be required for dimerization [179], as indicated in Figure 13, are not observed in the structure. In fact, the N-termini are located in a mutual distance of 20 Å, which is unlikely to be close enough for interaction, assuming that other TMEM16 proteins share a similar organization in this part of the structure.

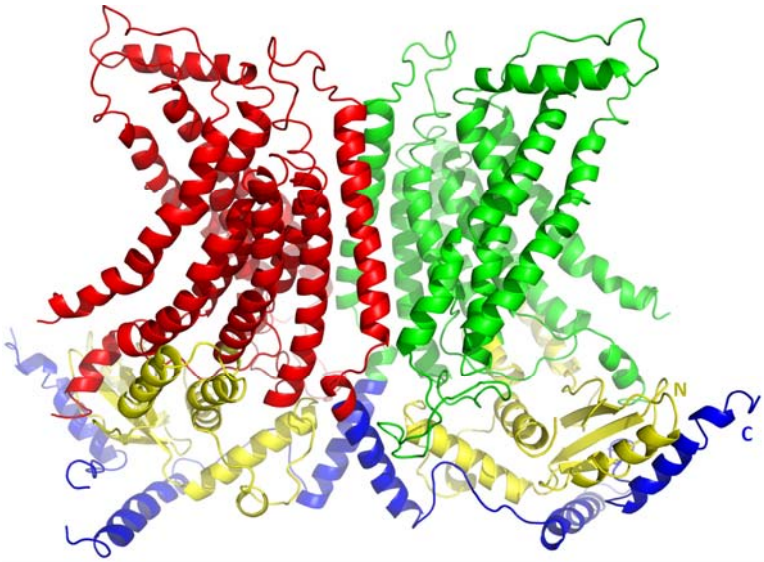

Figure 64 Interaction between termini

nhTMEM16 structure. While the N- and C- termini are displayed in yellow and blue, respectively, the trans-membrane part of the dimer is shown in red/green.

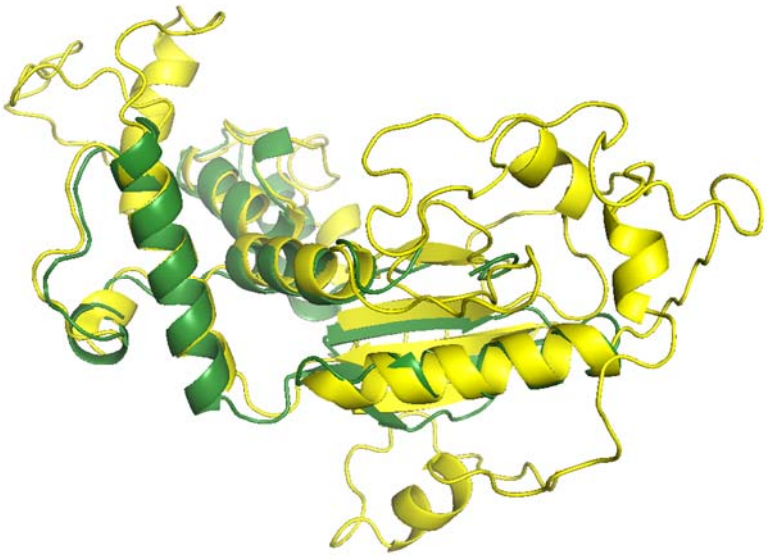

Figure 65 Structural conservation of the N-terminus in TMEM16 proteins

The N-termini of nhTMEM16 (green) and mTMEM16A (yellow) are superimposed. The structure of the N-terminus of mTMEM16A was predicted by the Phyre2 server [296].

Clearly, a crystal structure represents a snapshot and may reflect only one particular state among several possible ones. An interaction between helices of the amino- termini for establishing the dimeric arrangement in a different conformation of the protein can therefore not be completely excluded, although in the experiments postulating an interaction between N-termini mainly pull-down approaches with small fragments of the N-termini of investigated TMEM16 proteins were applied. Thus, an interaction, which might occur between these isolated fragments and full-length TMEM16 proteins, might not be relevant in a dimer formed by two full-length subunits. In the structure a large interface is created rather through various alpha helical contact sites between the N-terminus of one subunit and the C- terminus of the adjacent subunit and between the C- termini (Figure 51a, Figure 52a and Figure 64). Although, appropriate experiments are still missing, it appears more conceivable that the organization as a dimer is regulated largely through interactions involving the amino- and carboxy termini and through interactions in the transmembrane domain (see also chapter 3.2).

The N-termini of various distantly related TMEM16 proteins do not show a high degree of conservation. But, as already suggested from secondary structure predictions (Figure 13), the N- termini were expected to be nevertheless structurally related. Figure 65 illustrates the relationship of the amino- termini of nhTMEM16 and a structure of the N- terminus of mTMEM16A modeled by Phyre2 [296]. To prevent bias, the input sequence was the N- terminus only, not the full- length protein. The much longer N-terminus of mTMEM16A compared to the N- terminus of nhTMEM16 (330 vs. 180 amino acids) is reflected by various insertions, that presumably contain unstructured sequences.

3.2. The dimer interface: A role in dimerization

While TMEM16A and B were concordantly described as Ca^{2+}- activated chloride channels, other mammalian TMEM16 family members were proposed to have a role in ion transport [9] and phospholipid scrambling [10, 111], with both functions depending on Ca^{2+}. This functional diversity is usually referred to as ‘dual- functionality’ in TMEM16 proteins, and denotes the classification of TMEM16 proteins either into chloride channels or channels/scramblases. However, the underlying criteria that are associated with these functional differences are not known at a molecular level.

In the structure of nhTMEM16, additional inter- subunit contacts are observed besides the interactions between the amino- and carboxy termini. A significant part of the interface is generated through hydrophobic interactions between the two subunits of the dimer, mostly by transmembrane helices 10 (α10), the dimer interface. Within this hydrophobic interface, a pair of salt bridges is formed between equivalent residues of transmembrane helix α10 involving mutual interactions between glutamates and histidines, as illustrated in Figure 46 and Figure 53a and b. Due to the location of these salt bridges within a largely hydrophobic environment in the transmembrane part, the interaction between these residues is thought to be much stronger as it would be the case in an aqueous environment (Table 11, page 128) [297]. Interestingly, this pair of salt-bridges is conserved among most TMEM16 family members, except for TMEM16A and B homologues, where a pair of glutamines (Gln) and asparagines (Asn) is found at

equivalent positions (Figure 53c). Assuming that these Gln and Asn would face each other in a similar way as observed for the residues in the salt bridge, they would most likely form hydrogen bonds between oxygen and hydrogen atoms attached to the amide nitrogen in the respective side chains. Compared to the salt bridge found in nhTMEM16 the Gln and Asn could be at a larger distance from each other. For these reasons, the interaction is presumably weaker (Figure 66 and Figure 68a and b). This circumstance raises the question, whether the type of interaction in the dimer interface is in some way associated with the classification of TMEM16 proteins into chloride channels and channels/scramblases.

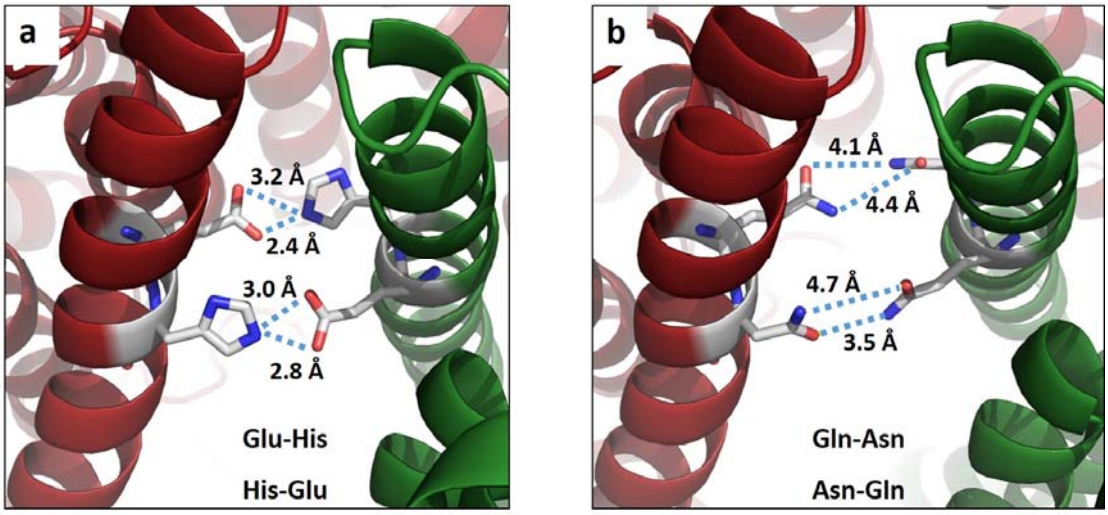

Figure 66 Dimer interface: Electrostatic vs. hydrogen bond interactions

Detailed view of the dimer interface. Mutual interactions between residues of adjacent subunits located on transmembrane helices α10 are shown. Distances between the interacting atoms are denoted. a, As observed in the structure of nhTMEM16, a pair of salt bridges is formed between a glutamate and a histidine. It is likely, that most TMEM16 members share these interactions. b, In TMEM16A and B the interactions are presumably established between glutamines and asparagines. Mutations were modeled in Pymol [298].

It is conceivable, that a mechanism had to be developed to prevent hetero-dimerization of functionally different types of TMEM16 proteins during dimer assembly, e.g. the dimerization of the cation channel/scramblase TMEM16F with the chloride channel TMEM16A.

The tissue expression of TMEM16A and B proteins was well studied, suggesting that while TMEM16 A is expressed abundantly, TMEM16B was mainly detected in certain neurons, and few overlaps in the expression were reported [8, 155]. The tissue distribution of TMEM16F proteins, for example, was not examined, but from the analysis of mRNA content of various organs and tissues from mouse, both TMEM16A and F mRNA were detected abundantly, partially in the same tissues [111], as seen in Figure 67. The dimerization of TMEM16 proteins was reported to occur in the endoplasmic reticulum (ER) [179], therefore the encounter and co-localization of different TMEM16 proteins in the ER is likely to take place. After assembly, TMEM16A, B and F were reported to be targeted to the plasma membrane [4-6, 10, 111, 112] (and observations from the present study). The hetero-dimerization of the comparably

similar proteins TMEM16A and B is possible [179], and protein co-localization was reported (as described above). The currents of such hetero-dimers investigated by patch-clamp methods were classified as intermediate compared to the currents of the particular homo-dimers, when overexpressed in HEK cells [149].

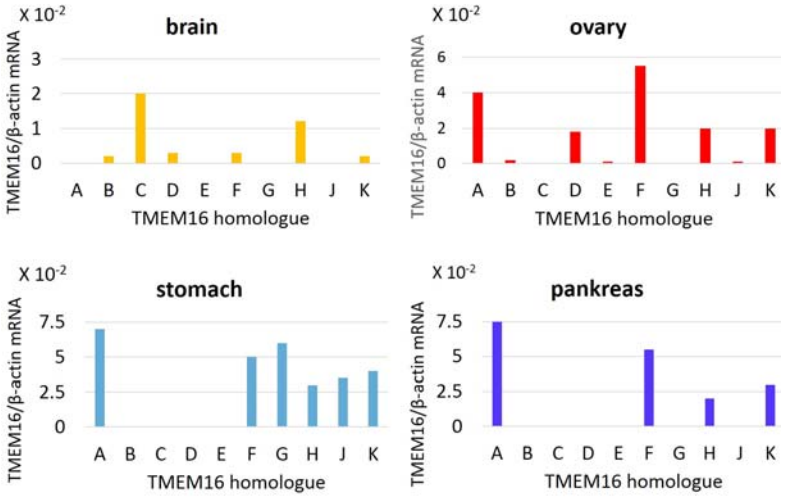

Figure 67 mRNA level of TMEM16 family members in murine tissues

mRNA levels were measured for TMEM16 family members in various tissues from mouse and normalized to the β-actin mRNA level. Data extracted and adapted from [111]. For most organs and tissues investigated in that study, mRNA was detected for several TMEM16 homologues.

However, dimers consisting of subunits from TMEM16A or B with TMEM16F were not observed [179]. Although currently speculative, it appears conceivable that TMEM16 proteins, owing to similar tissue distribution, circumvent the association of dimers with mixed functions through the formation of two different types of interactions in the dimer interface, see Figure 66. A contact between residues on transmembrane helix 10 of TMEM16F (Glu and His) with residues from TMEM16A (Gln and Asp) would presumably be less favorable. Furthermore the interaction of the salt bridges between two subunits of TMEM16F (Glu and His) is much stronger, so that the formation of such hetero-dimers (TMEM16A-TMEM16F) would be largely prevented (Figure 68c). In such a theoretical arrangement (TMEM16A-TMEM16F) the distance of the mutual His and Gln of mixed hetero-dimers would be too close, so that the Gln might turn away thus lowering the strength of the interaction. Although appropriate experiments are still missing, the existence of such a mechanism to control the formation of 'proper' dimers appears plausible.

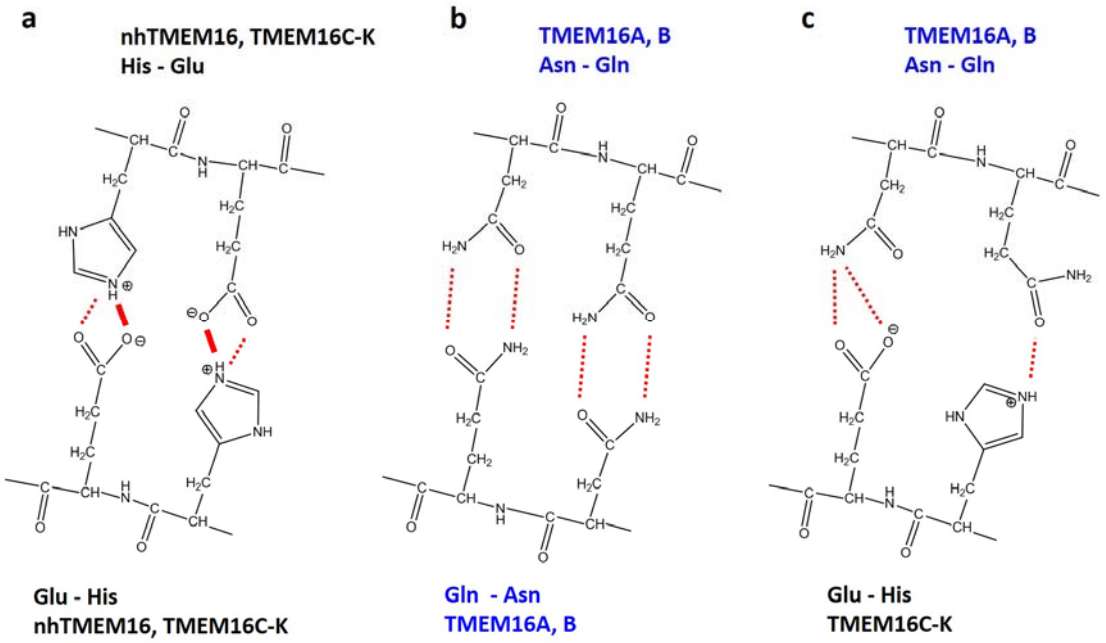

Figure 68 Mutual interactions between TM helices 10

Close-up view illustrating interacting residues residing on transmembrane helices α10. Intermolecular interactions based on the nhTMEM16 structure. Potential interactions (electrostatic attractions and hydrogen bonds) are indicated by full and dashed lines in red. a, In nhTMEM16 and TMEM16C-K a pair of salt bridges is formed involving glutamines and histidines. b, TMEM16A and B have a pair of glutamines and asparagines at the respective position. The glutamines and asparagines may interact with each other via hydrogen bonds. c, Mutual interactions in a hetero-dimer consisting of mixed subunits of TMEM16A and F. This type of interaction was not observed so far. Amino acids drawn in ChemDraw Pro 12.0.

3.3. The Ca^{2+} binding site

The nhTMEM16 structure has revealed the location of a Ca^{2+} binding site per subunit by exploiting the anomalous scattering properties of Ca^{2+} in data collected at long wavelength (Figure 54). Interestingly, the Ca^{2+} binding site is embedded within the transmembrane part of the membrane, thus offering an explanation for the voltage-dependence of ion conduction in various family members [4-6, 12, 150, 156]. The Ca^{2+} binding site was generally expected to be a component of the cytoplasmic part of the protein, but from data obtained by a number of patch-clamp experiments on CaCCs, whose main component is most likely TMEM16A, it was suggested that the site may reside within the membrane [299, 300]. As seen in Figure 69, the Ca^{2+} binding site is located within the hydrophobic core at one third of the membrane, closer to the cytoplasmic than the luminal side. Ca^{2+} coordination is established by six residues from three different transmembrane helices (α6-8) and involves an asparagine, three glutamates and two aspartates (N448, E452, D503, E506, E535 and D539). These residues are found at equivalent positions in other TMEM16 family members thus underlining the conservation of the Ca^{2+} binding site between TMEM16 proteins (Figure 54d).

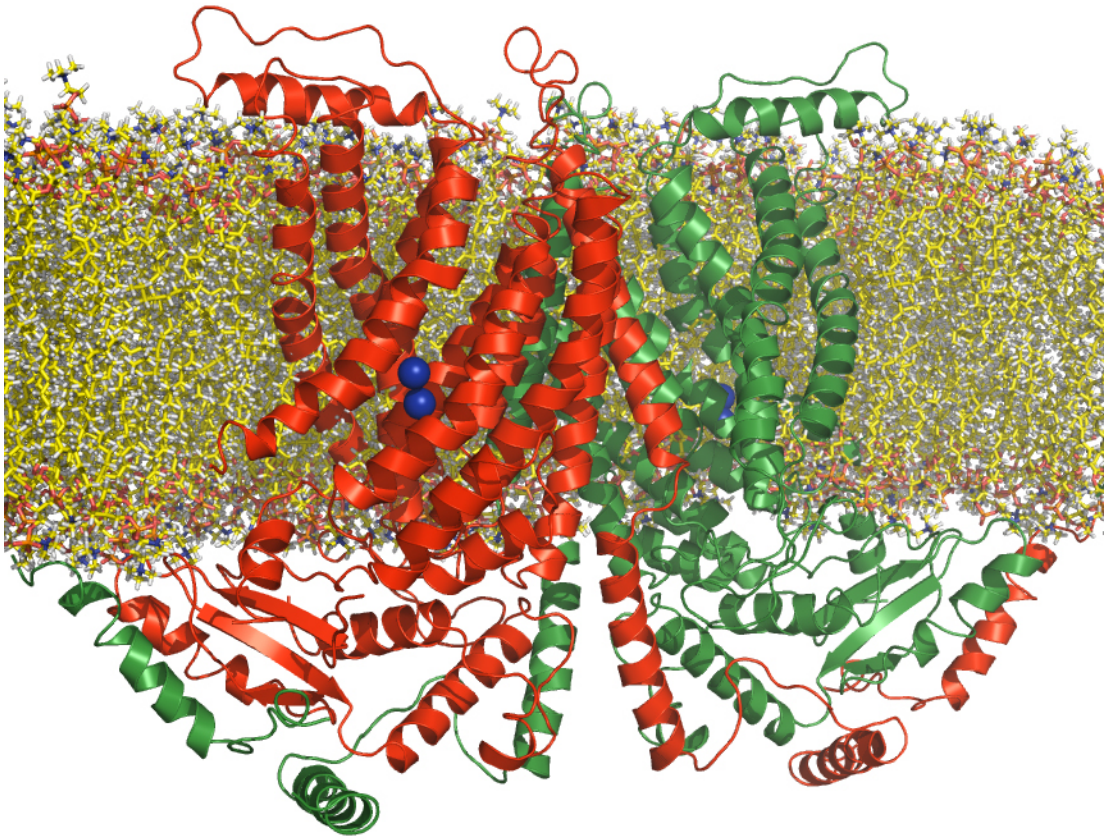

Figure 69 nhTMEM16 in a bilayer model

nhTMEM16 placed into a model of di-palmotoyl- phosphatidylcholine (DPPC) obtained from http:// www.lobos.nih.gov/mbs/coords.shtml. The dimer is colored in red/ green and the Ca^{2+} ions are marked as blue spheres. Alpha helices in loop regions that connect the transmembrane helices on the luminal side of the protein and the amino- and carboxy termini appear to define the boundaries within the bilayer.

In previous work applying electrophysiological methods, two residues that are part of the identified site, were proposed to be involved in Ca^{2+} sensing in TMEM16A [12], which is now confirmed by the results of the present work. A function in Ca^{2+} activation of these two residues could later also be confirmed for TMEM16F [9] and purified afTMEM16 [170]. Recently, three more equivalent residues were linked to Ca^{2+} activation in TMEM16A [182] and in a study accompanying the structural characterization of nhTMEM16 [295]. All five residues predicted to be involved in Ca^{2+} sensing in TMEM16A are part of the Ca^{2+} binding site as observed in the structure of nhTMEM16. Neither the localization of the Ca^{2+} binding site within the membrane nor the organization shares close resemblance with previously described Ca^{2+} binding motifs such as EF hands or C2 domains found in other Ca^{2+} binding proteins.

An anomalous difference density map calculated from data collected at long wavelength identified two strong peaks for Ca^{2+} per binding site. Since in X-ray crystallography, the molecular picture that is obtained reflects an average of many copies of a crystal, it was initially not clear, whether the observed two peaks originate from two Ca^{2+} ions, that bind simultaneously to one Ca^{2+} binding site, or whether the sites may be occupied only partially. Crystallographic parameters that may clarify this question are

the occupancy, a measure of how frequently an atom is found at a particular position, and the B-factors, indicative for the flexibility at a certain position.

During the refinement of both parameters evidence was accumulating, that two Ca^{2+} ions are coordinated in a distance of 4.2 Å of each other by six residues in one Ca^{2+} binding site. The Ca^{2+} coordination number would therefore be presumably around 5 (+/- 1) for both Ca^{2+} ions (see Figure 70a). Simultaneous occupancy appears plausible since the comparison of available structural data on different types of Ca^{2+} binding sites revealed an average coordination number for Ca^{2+} of 6 (+/- 1) for continuous and 4 (+/- 2) for discontinuous types [301]. Discontinuous types summarize all different Ca^{2+} binding sites in which Ca^{2+} coordinating residues are distant in the primary sequence, while in the tertiary or quarternary structure these residues come close together.

Hence, as illustrated in Figure 70a, nhTMEM16 belongs to the group of Ca^{2+} binding proteins with discontinuous Ca^{2+} binding sites involving three transmembrane helices (α6-8), that are connected by loops of variable length, and each of the transmembrane helices contributing two binding residues. Somewhat resembling the situation in nhTMEM16, the structure from thermolysin from *Bacillus thermoproteolyticus* (pdb protein data base entry: 1FJ3), a protease, revealed the coordination of two Ca^{2+} ions by three glutamates and two aspartates. Four residues are provided by a loop and adjacent α-helix, while the fifth residue participates in Ca^{2+} coordination from another α-helix far away in the primary sequence. Similar to nhTMEM16, the two Ca^{2+} ions are separated from each other at a distance of 3.8 Å (Figure 70b). Thus, the presence of four Ca^{2+} ions per dimer as seen in the structure of nhTMEM16 appears reasonable from a structural viewpoint.

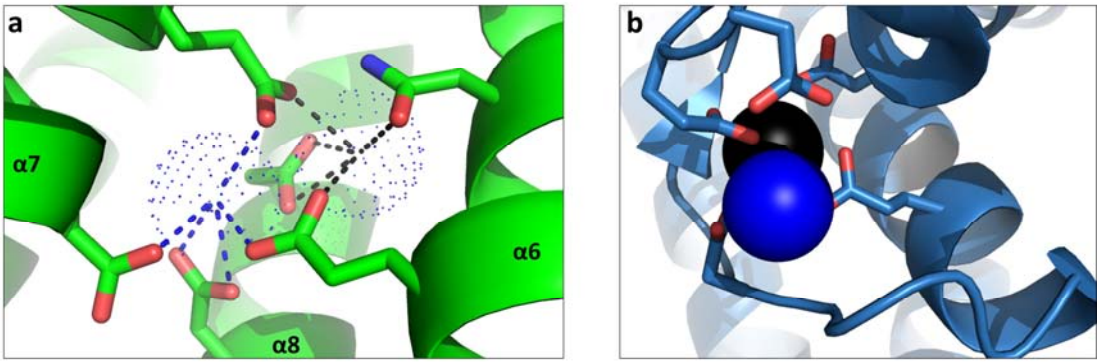

Figure 70 Ca^{2+} binding site of nhTMEM16 and thermolysin

The discontinuous Ca^{2+} binding sites of nhTMEM16 and thermolysin (pdb protein data base entry: 1FJ3) from *Bacillus thermoproteolyticus* are compared. a, In nhTMEM16, three Glu, two Asp and an Asn coordinate two Ca^{2+} ions at a distance of 4.2 Å. Ca^{2+} ions are displayed as dotted spheres and the potential interactions between the Ca^{2+} ions and the coordinating residues are indicated by dashed lines. The participating α-helices are labeled. b, Close-up of the Ca^{2+} binding site of thermolysin. Two Ca^{2+} ions are separated at a distance of 3.8 Å. Four interacting residues point into the binding site from a loop and connecting α-helix and the fifth residue involved in coordination resides on a discontinuous α-helix far in a different region of the protein sequence.

3.4. The subunit- cavity: Potential site of lipid flip-flop

In close proximity to the Ca^{2+} binding site, a 10- 14 Å wide crevice spans the entire transmembrane part in a diagonal direction, thereby resembling a spiral staircase. Remarkably, despite facing the hydrophobic environment of the membrane, the solvent- accessible surface of this crevice is highly hydrophilic. When equivalent residues of TMEM16A and F are mapped on the nhTMEM16 structure based on a sequence alignment, it appears that this characteristic is well conserved among various TMEM16 family members (Figure 71). 20 years earlier, before TMEM16F was proposed to have a role in Ca^{2+} dependent phospholipid scrambling required for blood coagulation after injury [10], scrambling processes were already investigated in platelets using fluorescently labeled NBD-lipids. Phospholipid transport was observed for many different lipid substrates with variable head groups ranging from serine, choline to various bulky sugar moieties. Based on the kinetics measured in these experiments, different lipid translocation models were established. A working hypothese assumed that phospholipids would be moved with their head groups interacting with residues of the scramblase along an aqueous or hydrophilic path through the membrane, while the phospholipid acyl chain would diffuse through hydrophobic interfaces [14, 302]. Further, it was concluded that rather the size of the head group than its chemical composition would dictate, which molecule is permitted to move through this path and which one is not.

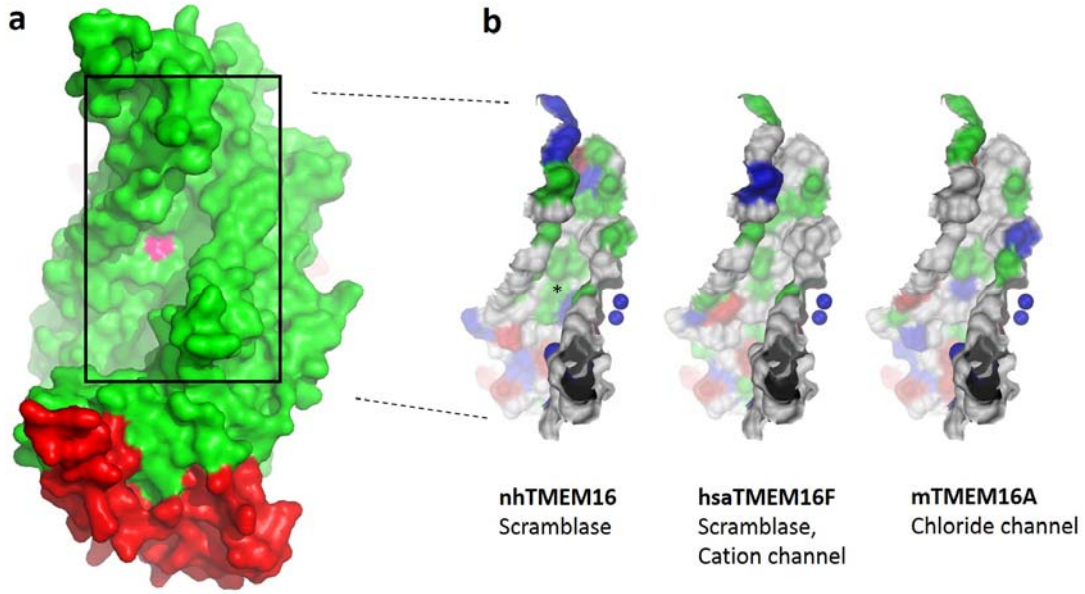

Figure 71 The subunit- cavity of TMEM16F contains a functionally important residue

Side view of the nhTMEM16 structure showing details of the subunit- cavity. The position of a residue in nhTMEM16 that in TMEM16F was reported to influence the ion selectivity is colored in magenta and marked with an asterisks (*). a, The dimer is displayed in red/green. b, The subunit cavities of nhTMEM16, human TMEM16F (hsaTMEM16F) and mTMEM16A are colored according to the properties of the surface exposed residues (red: acidic, green: polar, blue: basic). Equivalent, potentially surface- exposed residues were identified based on a sequence alignment. Ca^{2+} ions are indicated as blue spheres.

During the last years TMEM16F gained increasing attention, since it was related to phospholipid scrambling and the loss of TMEM16F was associated with Scott-syndrome, a rare bleeding disorder [10]. Further investigation of TMEM16F revealed a role in the transport of cations [9]. In TMEM16F, a glutamine (Q559) was identified that influenced the cation- over- anion- selectivity towards a larger selectivity for anions, when replaced by a lysine. Interestingly, a lysine is present at equivalent position in all TMEM16A chloride channels from various species. Using a sequence alignment to find the equivalent amino acid in nhTMEM16, the structure has revealed the location of this residue to be part of the surface-exposed area of the subunit- cavity. Its position within the subunit- cavity is shown in Figure 71b.

In the chloride channel TMEM16A several residues were discovered that belong to a putative pore entry [12]. In this elegant study, TMEM16A and mutants were investigated by patch-clamp experiments. Residues at a certain region of the protein that were replaced by cysteines abolished currents. Remarkably, these currents were restored after modifying these cysteines with a positively charged $MTSET^+$ reagent, thus indicating a potential role in ion conduction. In Figure 72, the identified residues were mapped on a TMEM16A homology model, that was prepared using Phyre2 [296]. Two residues (TMEM16A(ac): G628 and G629 corresponding to the nhTMEM16 residues T423 and R424) reside near the entry to the subunit- cavity on an extracellular loop upstream of transmembrane helix α6. Four residues (TMEM16A(ac): M632, I636, Q637 and K645 corresponding to nhTMEM16: P429, N434, Q435 and T442) are located on transmembrane helix 6 (α6) within the transmembrane part on the surface-exposed area of the subunit- cavity. Recently, four more residues were identified in TMEM16A that had an influence on the lyotropic permeability sequence of larger anions over chloride ions (TMEM16A: R515, K603, R618, R788 corresponding to nhTMEM16: T307, Y392, R407, A577). Also in this case, all four residues map to the subunit- cavity or its vicinity (Figure 72).

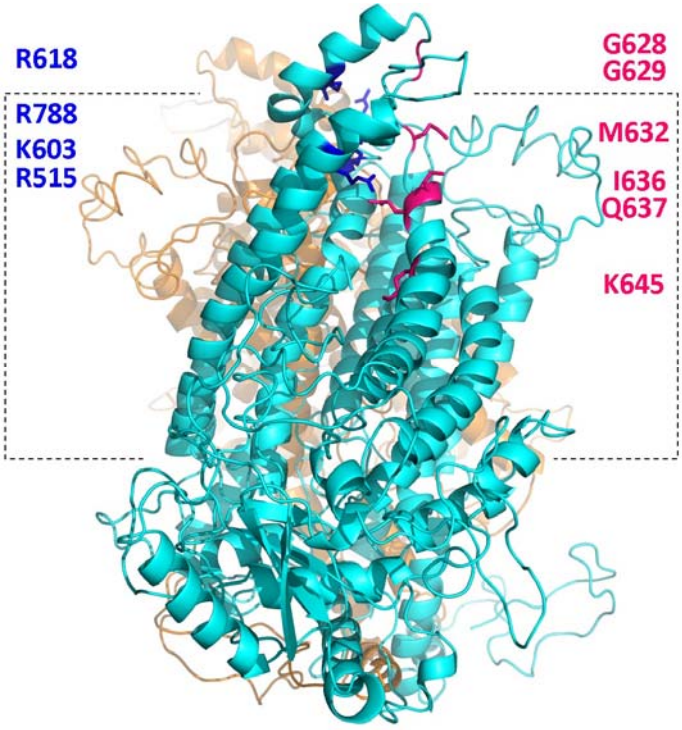

Figure 72 Mutations in the putative pore in TMEM16A

Homology model of TMEM16A prepared with Phyre2 [296]. Side view of the dimer in red/green is shown. The subunit- cavity is indicated with dashed lines. Residues that were identified in TMEM16A to be part of the putative pore and pore entry are shown. Residues that, when mutated, affect the conductance or selectivity are highlighted in magenta or blue, respectively, and the corresponding numbering in TMEM16A is indicated.

TMEM16E, one of the less studied mammalian TMEM16 proteins, was associated with autosomal recessive diseases of the muscular and skeletal apparatus. Approximately 46 mutations in TMEM16E are known to date by gene sequencing, and these mutations lead to distinct phenotypes of gnathodiaphyseal dysplasia and muscular dystrophy in human [201, 303-306]. The mutations are summarized in Table 10.

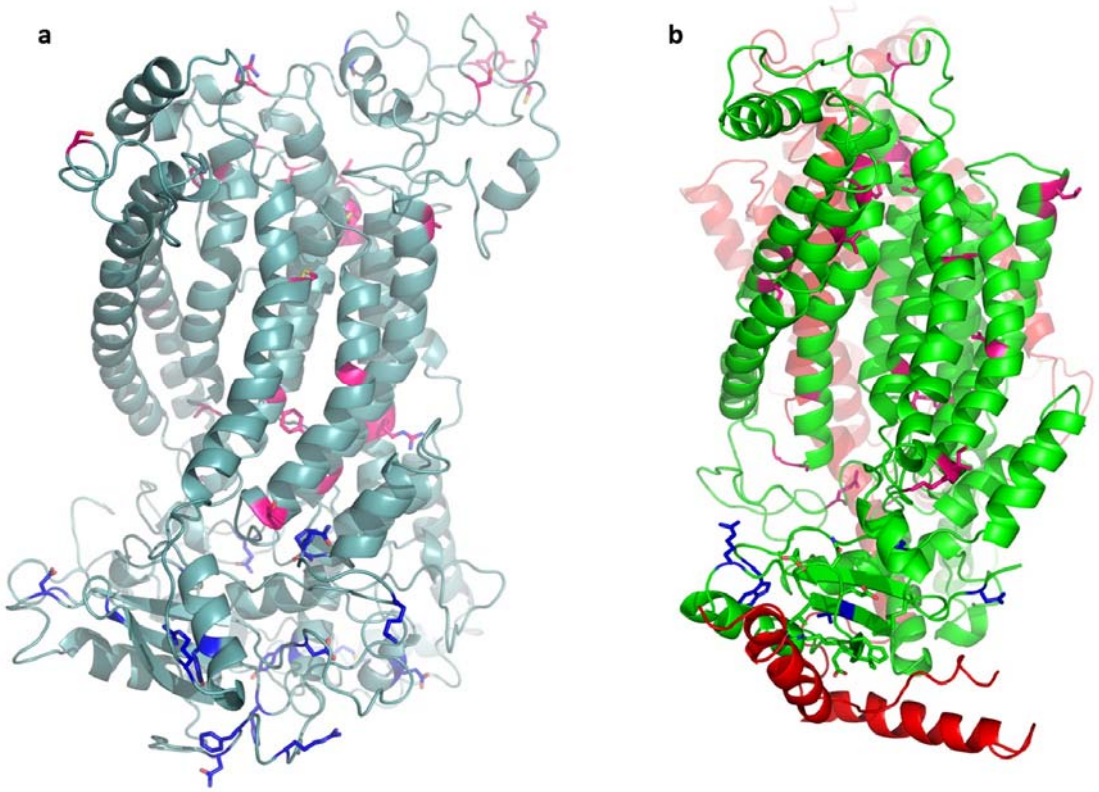

Figure 73 TMEM16E mutations mapped to the structure

Side view on the subunit- cavity. TMEM16E mutations that lead to gnathodiaphyseal dysplasia or muscular dystrophy are shown. Mutated residues are displayed in magenta, when they map to the subunit- cavity, associated loop regions and dimer interface, or blue, when they locate to the cytoplasmic part. a, A homology model of TMEM16E obtained by the Phyre2 server [296] is shown. Note that only one subunit of TMEM16E is shown, therefore the C- terminus, which in the structure of nhTMEM16 forms contact sites with the N-terminus of the adjacent subunit, is not present. Note further that sequences, of which equivalent positions do not exist in nhTMEM16, cannot be predicted accurately in the homology model of TMEM16E. b, Corresponding positions of TMEM16E mutations mapped on the nhTMEM16 structure. Residues were identified using a sequence alignment Since several of the mutations are located within parts of the molecule, where no equivalent sequences exist in nhTMEM16, they could not be mapped on the structure.

While both, biochemical and functional characterizations of TMEM16E are still missing, the close relationship of with TMEM16F (i.e. a sequence identity of 50%) might hint at a similar function in phospholipid scrambling (and perhaps also in ion transport). In Figure 73 the mutations were mapped on a TMEM16E homology model generated by the Phyre2 server [296], while in Figure 73b the same

mutations were transferred to the structure of nhTMEM16 using a sequence alignment. 21 of the known mutations reside in parts of the protein that are located within the cytosol. Most of them concern polar or charged amino acids, which may form hydrogen bonds or salt bridges. These residues are presumably essential for intra- and intermolecular interaction and stability. Most of the remaining 25 mutations are located on helices that are part of the subunit- cavity, thus adding further supporting evidence for a relationship between the function of TMEM16 proteins and the subunit- cavity. Further, some of these mutations map to the dimer interface and loop regions. The loop regions are significantly longer in TMEM16E than in nhTMEM16 and therefore neither their location nor their interactions in TMEM16E could be accurately predicted by the Phyre2 server. Considering the length of these loops they might potentially contribute to the entry of the subunit- cavity. Alternatively, similarly as residues in the dimer interface they might form intermolecular contact sites, which are important for the dimer assembly and mutations in these regions might presumably interfere with dimerization and thus impair the function of TMEM16E. In TMEM16 proteins, the cytoplasmic parts and the ferredoxin-like fold is likely structurally conserved, but the functional relevance of this region is completely obscure. The fact that mutations in cytoplasmic parts of TMEM16E lead to disease might further point to a relevance of this part of the protein for its function.

In summary, residues that influence the ion selectivity in TMEM16A as well as TMEM16F and that alter ion conduction in TMEM16A map to the subunit- cavity in the structure of nhTMEM16. It was also found, that approximately half of the known TMEM16E mutations are located in helices forming this cavity.

1 Asn52Ser	13 Pro266Leu	25 Thr548Ile	37 Ser796Leu
2 Phe54Ser	14 Thr267Ser	26 Ser555Ile	38 Cys804Ser
3 Arg58Trp	15 Ala249Gly	27 Phe578Ser	39 Tyr806Cys
4 Asp81Gly	16 Gly301Val	28 Met618Ile	40 Tyr811X
5 Asp93Glu	17 Ala323Gly	29 Arg642Leu	41 Ala830Val
6 His134Tyr/Arg	18 Asn366Ser	30 Tyr652Cys	42 Met833Lys
7 Tyr143Cys	19 Arg404Leu	31 Tyr673Cys	43 Met839Arg
8 Gly126Val	20 Gln405X	32 Asn701Asp	44 His841Asp
9 Glu202Lys	21 Gln421X	33 ΔAsn701	45 Ile865Leu
10 Gly231Val	22 Ala464Asp	34 Tht714Ser	46 Met900Leu
11 Lys259Asn	23 Ser506Gly	35 Arg758Cys	
12 Asn265Ser	24 Arg547Gln	36 Leu781Pro	

Table 10 TMEM16E mutations at a glance

TMEM16E mutation revealed by genotype sequencing. In blue mutations are listed that concern the cytoplasmic part in TMEM16E, while mutations in magenta indicate a location on helices of the subunit- cavity, within extracellular loops or within the dimer cavity.

Thus, most likely the subunit- cavity is implicated in ion transport as well as phospholipid translocation in TMEM16 proteins. In a previous work, a model was elaborated that explains, how lipids would overcome the energy barrier that is associated with lipid flip-flop. It was proposed that the scrambling of phospholipids would be facilitated by an aqueous or hydrophilic path. Such a path would provide an interface for interaction with the polar phospholipid head groups along the scramblase through the hydrophobic barrier of the membrane. Strikingly, the subunit- cavity is open to the lipid environment,

highly hydrophilic and, due to the close proximity to the Ca^{2+} binding site, likely linked to Ca^{2+} activation. Furthermore, as illustrated in Figure 74, the subunit- cavity provides enough space to accommodate different types of lipids (model of the lipids obtained from http://www.lobos.nih.gov/mbs /cords.shtml). The subunit- cavity thus meets all the requirements that were suggested to be relevant for enabling lipid flip-flop.

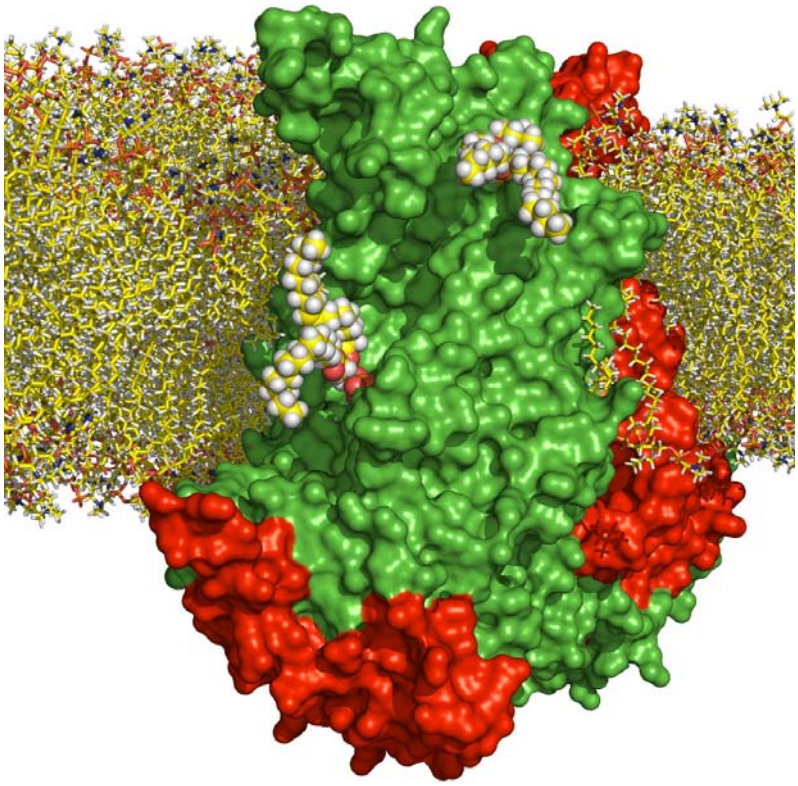

Figure 74 Modelled lipids fit into the subunit- cavity

Surface representation of nhTMEM16 placed into a bilayer model of di-palmotoyl-phosphatidyl-choline (DPPC). Lipids are modelled into the subunit- cavity of nhTMEM16.

3.5. Mode of Ca^{2+} activation

3.5.1. Location of the Ca^{2+} binding site within the membrane

The location of the Ca^{2+} binding site within the membrane gives reason to a couple of questions. How, for example, do the Ca^{2+} ions reach the Ca^{2+} binding site? Clearly, Ca^{2+} binds from the cytoplasmic side, as revealed by numerous experiments and as expected for Ca^{2+} signaling cascades. In excised outside-out patching experiments, for example, currents are only induced if Ca^{2+} is contained in the cytoplasmic solution [307]. Intriguingly, in the Ca^{2+} bound structure no obvious Ca^{2+} path could be discovered. However, as displayed in Figure 75, several negatively charged amino acids are located on an intracellular loop at the membrane boundary in close proximity to the Ca^{2+} binding site. As seen from the representation of the potentially surface-exposed residues, these negatively charged amino acids are clearly accessible from the cytoplasm and thus may have a function in guiding the Ca^{2+} ions towards the binding site. Indeed, there is partial conservation of these residues in TMEM16 proteins. Interestingly, a

residue at an equivalent position in TMEM16A (E686) was demonstrated to have a significant higher EC_{50} value when replaced by an alanine (Ala), indicating a nearly ten-fold lower affinity for Ca^{2+} [182]. Although at that time no conclusions were drawn, this might suggest that E686 in TMEM16A interacts with Ca^{2+} and potentially is part of a Ca^{2+} path. However, appropriate experiments confirming this hypothesis are still lacking. Alternatively, in the absence of bound Ca^{2+} ions, such a Ca^{2+} path might be generated or become accessible from the cytoplasmic side due to local rearrangements in the protein.

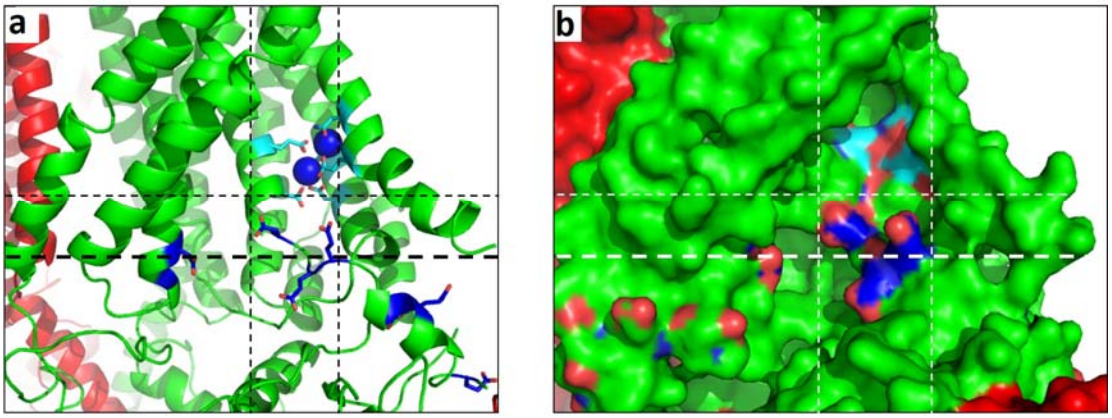

Figure 75 Potential Ca^{2+} path in nhTMEM16

Close-up view of the subunit- cavity and Ca^{2+} binding site. Subunits of the dimer are shown in green/red, the Ca^{2+} binding site in cyan and bound Ca^{2+} ions as blue spheres. Negatively charged residues at the membrane boundary in close vicinity to the Ca^{2+} binding site are indicated in blue. These residues might potentially play a role in guiding the Ca^{2+} ions towards the Ca^{2+} binding site. Dashed lines are shown to mark equivalent parts in the two representations. The thicker dashed line indicates the expected membrane boundary at the cytoplasmic side. a, Cartoon representation of the structure. b, Representation of the molecular surface.

The question arise why the location of the Ca^{2+} binding site within the membrane is relevant for the activity and the activation mechanism. As demonstrated in electrophysiological recordings, TMEM16A is synergistically gated by $Ca^{2+}$and voltage [147]. By clamping the voltage at different potentials using patch-clamp methods, it was noticed that at low Ca^{2+} concentrations TMEM16 proteins (TMEM16A, B and F) elicit higher currents at positive than at negative potentials [1, 5, 6, 12, 136, 147]. This was interpreted as a higher affinity for Ca^{2+} at positive potentials, although in one report it was claimed that these differences might be a consequence of the run-down effect, which is well-known to happen during electrophysiological recordings with TMEM16A [308]. It was further suggested that the voltage-dependence of the Ca^{2+} affinity might be related to the fact that for reaching the binding site, the Ca^{2+} ion has to cross parts of the electric field of the membrane [1]. At low Ca^{2+} concentrations channel activation occurs time-dependent with outward rectification, meaning by convention that chloride ion flow is preferably inwardly directed. At higher Ca^{2+} levels (above 25 µM) both the time- dependence and rectification disappear [1, 4, 147, 309]. The time- dependence reflects a lag period that likely correspond to multi-step opening of the channel, suggesting that Ca^{2+} binding is the rate limiting step [147]. Channel opening occurring in several steps appears plausible, potentially reflecting Ca^{2+} ions on

the way in stages through the membrane to enter the Ca^{2+} binding site or the sequential binding of the first and second Ca^{2+} ion to one Ca^{2+} binding site. It appears that the time- dependence of Ca^{2+} activation is associated with the position of the binding site deep in the membrane. The localization of the Ca^{2+} binding site within the membrane and thus potential impeded accessibility might account for the time-dependence of the currents at low Ca^{2+} concentrations as observed for TMEM16A activation. The loss of the time- dependence at higher Ca^{2+} concentrations might reflect a transition step that cause structural changes, which then subsequently allows Ca^{2+} ions to freely access the binding site.

3.5.2. Occupancy in the Ca^{2+} binding site

In patch-clamp experiments of TMEM16A, the Hill-coefficient with a value between 2 and 4 points to a positive cooperativity involving the binding of multiple Ca^{2+} ions [6, 308, 310]. A group investigating CaCCs, whose currents most likely arose from TMEM16A, developed a model for the mechanism of activation based on a set of electrophysiological recordings [299]. Briefly, this model claimed that each channel (the oligomeric state of the protein was not known at that time) contains two identical binding sites involving the subsequent binding of at least two, but perhaps three, Ca^{2+} ions. However, these Hill coefficients are only estimates for the number of ions that bind.

In the nhTMEM16 structure, most likely four Ca^{2+} ions are coordinated per dimer. For purification and crystallization experiments, nhTMEM16 (and other TMEM16 proteins as well) needed 3-5 mM Ca^{2+} for stabilization (chapter 2.6). If these amounts of Ca^{2+} were left away, the final yield dropped to about 1/10 due to instability of the protein. Thus, to increase the yields and obtain crystals of sufficient dimension and quality for structure determination, it was crucial to add high concentrations of Ca^{2+} to any buffer during purification and crystallization. However, if the protein was purified in the presence of high Ca^{2+}, similarly as for crystallization, the protein was no longer active in the liposome-based scrambling assay. Removal of Ca^{2+} by dialysis did not restore the activity. Therefore, for functional characterization of nhTMEM16 the protein was usually purified in the absence of Ca^{2+}. Protein obtained in that way for reconstitution was found to be functionally integer. In order to understand the reasons for this discrepancy, but also aiming for a structure of nhTMEM16 in a potentially Ca^{2+}-free conformation, nhTMEM16 was crystallized in the absence of Ca^{2+} and buffers were prepared to contain EGTA wherever possible, similarly as done in preparation for functional assays. For crystallization itself EDTA or EGTA was not included, since it prevented the formation of crystals.

Importantly, the structures determined in the presence and absence of Ca^{2+} suggested very similar conformations. It is noteworthy, that in the 'Ca^{2+}-free' structure a peak of anomalous difference density of Ca^{2+} was nevertheless detected in the Ca^{2+} binding site, indicating the presence of bound Ca^{2+} ions even in crystals grown under apparently Ca^{2+}-free conditions (Figure 50 and Figure 76). Although in these cases EDTA was present in most parts of the purification and no Ca^{2+} was included during the harvest of the cells, membrane preparation, purification and crystallization of nhTMEM16, bound Ca^{2+} ions point towards a relatively high affinity for Ca^{2+}. An explanation for that might be found in the localization of the Ca^{2+} binding site within the hydrophobic environment of the membrane or the detergent micelle. A hydrophobic environment is known to potentiate electrostatic interactions, that

approach the strength of covalent bonds in a low dielectric environment [297]. Table 11 summarizes the strength of covalent and non-covalent interactions in water and vacuum, which would resemble the low dielectric environment of the membrane.

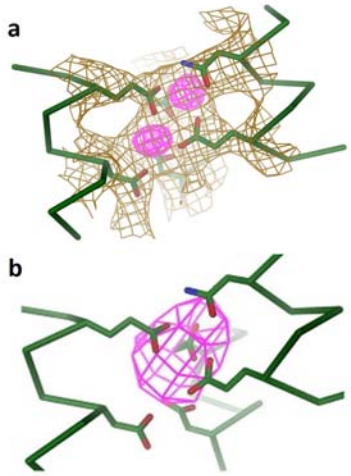

Figure 76 Anomalous difference density maps (Ca^{2+} vs. ' Ca^{2+}-free')

Close-up view of the Ca^{2+} binding site.
a, Data obtained in the presence of high amounts of Ca^{2+}. The $2F_0$-F_c map (brown, at 3.5 Å, contoured at 1σ) is superimposed in the refined structure of CF2, shown as stick model. The anomalous difference density map is indicated in magenta (at 3.8 Å, contoured at 5σ).
b, Data from protein purified and crystallized in the absence of additional Ca^{2+}. Anomalous difference density in magenta is depicted (calculated at 6 Å and contoured at 4σ).

The lower resolution of the data (4.2 Å) and decreased anomalous signal caused the anomalous difference density maps to be less well resolved compared to data of higher resolution obtained in the presence of Ca^{2+} (Figure 76a and b). In these maps, only a single blurry peak is found in the Ca^{2+} binding site. It is not possible to assign from this low resolution, whether there would be two Ca^{2+} ions being coordinated in a single binding site.

Bond type		Length [nm]	Strength in [kJ/mole] In vacuum	In water
Covalent		0.15	377 (90)	377 (90)
Non- covalent	Ionic	0.25	335 (80)	12.6 (3)
	hydrogen	0.3	16.7 (4)	4.2 (1)
	van der Waals attraction (per atom)	0.35	0.4 (0.1)	0.4 (0.1)

Table 11 Covalent and non- covalent chemical bonds

Covalent and non- covalent bond strengths are compared in an environment of water or vacuum. In water the ionic and hydrogen bond interactions are greatly decreased. The numbers in parenthesis indicate how much stronger an interaction is compared to the strength of a hydrogen bond in water. Adapted from [297].

Various Ca^{2+} binding sites were analyzed with respect to the Ca^{2+} coordination number, which describes how many ligand atoms are involved in Ca^{2+} coordination in a binding site [301]. In a variety of structurally distinct Ca^{2+} binding sites, the coordination number of Ca^{2+} was found to range between two and six for discontinuous binding sites [301]. Hence, both scenarios appear plausible, the binding of one

or two Ca^{2+} ions per binding site in nhTMEM16. Clearly, the presence of 3-5 mM Ca^{2+} is physiologically not authentic, as it is 3000-5000 fold higher than the intracellular Ca^{2+} levels, when Ca^{2+} enters the cell or is released from intracellular stores (~1 µM) [311]. Remarkably, whereas the protein was inactive, when purified in the presence of such high Ca^{2+} concentrations, besides the two peaks in the binding site no additional peaks corresponding to Ca^{2+} ions were identified in the anomalous difference density that may explain, why the protein has lost its activity. Perhaps, the protein is irreversibly changed, once it encounters high concentrations of Ca^{2+}, which may also account for the considerable higher stability at high Ca^{2+} concentration. The question thus remains, whether two Ca^{2+} ions are required for proper function of nhTMEM16 in scrambling processes. It is however certain, that both structures, 'Ca^{2+}- free' and Ca^{2+}- bound, revealed very similar conformations.

3.6. Ion conduction in TMEM16F and afTMEM16

After TMEM16A and B were identified as constituents of the long sought-after Ca^{2+}- activated chloride channels (CaCCs), it was assumed that other members of the family would encode proteins with similar properties. Thereafter, various reports from different groups have related TMEM16F with a function in ion transport. Based on electrophysiological recordings TMEM16F was proposed to be conductive for chloride ions in response to different stimuli [158, 160-162, 164], but also for cations with preference for Ca^{2+} [9, 165], while no currents were detected by another group [111]. Taken together, TMEM16F was proposed to constitute a channel with permeability and selectivity for cations, but also for anions, depending on the study. Further, TMEM16F was described to display different current- voltage relationships and was suggested to contain different kinetics for activation and inactivation, while activation was achieved by Ca^{2+}, volume changes and hyperpolarization. It appears unlikely, that a single protein can carry out all described functions. Additionally, in the work that proposed TMEM16F as a cation channel, comparably high levels of Ca^{2+} (100 µM) were applied and the EC_{50} was determined to be around 10 µM. However, several reports claimed, that the intracellular free Ca^{2+} concentration in a resting state would be around 100 nM, which during Ca^{2+}- signaling increases to about 1 µM [311, 312]. This concentration would be insufficient for the activation of TMEM16F currents, unless a high local concentration would be obtained in micro- domains containing a high density of proximal Ca^{2+} channels.

However, a role of TMEM16F in phospholipid scrambling was assigned prior to the cation conductance [10, 111]. Patients with Scott-syndrome, a rare congenital bleeding disorder, have impaired Ca^{2+} dependent phosphatidylserine exposure in platelets, which is needed for efficient blood coagulation [10, 105, 118, 203, 313]. It was discovered in one of these patients, that the gene encoding TMEM16F carries a point mutation leading to premature termination of the protein [10]. In support of its role as scramblase, TMEM16F knock-out mice had a similar phenotype with decreased blood clotting paired with defective exposure of phosphatidylserine [9].

Similarly to TMEM16F, purified afTMEM16 was shown to constitute a dual-function protein with phospholipid scrambling activity and currents of high conductance and low selectivity as characterized

in a liposome-based assays [170]. Furthermore, phospholipid scrambling was also confirmed for nhTMEM16 [295], while a potential function in ion transport remains to be tested.

Taken together, these data strongly indicate a function as phospholipid scramblase for afTMEM16, nhTMEM16, TMEM16F and presumably other TMEM16 family members such as TMEM16C, D, G and J [10, 111, 170, 295]. The different currents measured for TMEM16F might be a consequence of membrane distortion during the transbilayer movement of the lipids, since in an activated scramblase 10'000 lipids are believed to be transported within one second from one leaflet to the other [170]. On the other hand, it is well known that poly-cations are attracted by the negative charge of phosphatidylserine. Thus, the manifold currents detected for TMEM16F might underlay unselective binding of ions to the polar head groups of lipids during the scrambling process. Assuming that an aqueous or hydrophilic path is formed by residues that facilitate the lipid transport by interacting with the polar head group of a particular phospholipid, the concern was raised that a scramblase might also be permeable for small molecules that resemble the head groups of its lipid substrates [13].

In TMEM16F, the exchange of a glycine with an aspartate (G409D) lowered the Ca^{2+} -induced currents and the Ca^{2+} sensitivity of activation when examined in HEK cells [9], while the rate of phospholipid scrambling and Ca^{2+} sensitivity of scrambling was strongly increased in blood cells [10]. In these blood cells phospholipid scrambling was constitutive and could be detected at cytoplasmic Ca^{2+} concentrations as low as occurring normally in resting cells (~20-50 nM) [10]. This rather indicates that ions and lipids might compete for binding sites along the translocation path in a Ca^{2+} dependent manner and suggests that the increased scrambling activity attenuates ion transport. However, in these experiments the different cell types used to investigate both functions may also play a role.

Clearly, for TMEM16F more experiments are required to address questions concerning the mechanism of ion conduction and lipid translocation, including the use of purified TMEM16F in a reconstituted system. It further remains to be clarified, whether or not the observed currents may originate from membrane distortion or unspecific binding of ions to lipid head groups.

3.7. Phospholipid scrambling in TMEM16 family members

The scrambling of phospholipids by nhTMEM16 was analyzed in a cell-free system using liposomes that contained small amounts of NBD-labelled lipids, as previously described [170]. The subsequent addition of dithionite allowed the selective reduction of NBD-groups on the outside of the liposomes. While a drop in the fluorescence of 50 % indicated no scrambling activity, a total loss in fluorescence suggested rapid transbilayer movement of lipids, which is indicative for the presence of a lipid translocator in the liposomes.

In the present work, the scrambling properties of isolated nhTMEM16 was investigated using NBD-phosphatidylethanolamine (NBD-PE) and NBD-phosphatidylserine (NBD-PS), as illustrated in Figure 57 and Figure 60. The scrambling activity was demonstrated to depend on Ca^{2+} and activation was observed with concentrations as low as 250 nM (Figure 59). Sr^{2+} was capable of inducing scrambling as efficiently as Ca^{2+}, whereas Mg^{2+} did not activate the protein (Figure 61). Similar findings concerning

activation by divalent cations were reported for afTMEM16 [170] using isolated protein in the scrambling assay, but also for TMEM16A as revealed by electrophysiological recordings [308]. It was reported, that Mg^{2+} is not able to activate neither TMEM16A nor CaCCs, but that it may bind to the Ca^{2+} binding site to antagonize activation by Ca^{2+} [136, 308]. The failure to activate TMEM16A (as well as afTMEM16 and nhTMEM16) by Mg^{2+} might be due to the inability to induce the transition between the binding of Mg^{2+} and opening or activation of the channel [308].

Interestingly, even in the absence of Ca^{2+}, nhTMEM16 still exhibited measurable scrambling activity (Figure 59). For this reason, experiments were repeated using buffers including reasonable amounts of EGTA and chemicals as well as water of very high purity to avoid traces of Ca^{2+} in the solutions, with similar results. The same effect was previously reported for afTMEM16 [170]. The residual activity of nhTMEM16 could suggest that, due to comparably high affinity for Ca^{2+}, trace amounts of free Ca^{2+}, that would still be present in these buffers are sufficient to promote activation. When aiming for a Ca^{2+}-free conformation, most of the purification steps were carried out using EDTA, and no Ca^{2+} was added at any time. Nevertheless, bound Ca^{2+} ions were detected in the Ca^{2+} binding site, supporting the idea of a high affinity for Ca^{2+}. Alternatively, the residual activity observed in the scrambling assay may imply that the protein retained a basal activity even in the absence of Ca^{2+}. In cellular assays used to measure scrambling processes in TMEM16C, D, F, G and J, no significant scrambling activity was detected for wild- type (WT) TMEM16F in the absence of Ca^{2+} [10, 111]. However, such a basal activity of the scramblase in the absence of Ca^{2+} could escape detection, because of the activity of lipid flippases and floppases, which continuously transport lipids in opposite direction compared to the scramblase to maintain membrane asymmetry (see also chapter 1.4 Proteins that modulate the lipid asymmetry in eukaryotes). Therefore, it cannot be ruled out that a potential residual activity of TMEM16F in the absence of Ca^{2+} is masked by the concerted action of flippases and floppases [170].

It is noteworthy that the scrambling assay is not completely quantitative. The curves obtained in the scrambling assay can be fitted to exponential functions. In the presence of 300 µM Ca^{2+}, the time-dependent fluorescence decay of the protein-free and proteoliposomes containing nhTMEM16 is well described by single exponential functions, with time constants of 15 and 22 seconds, respectively (Figure 77). In both cases, the kinetics reflect the reduction of the NBD-group by dithionite, which becomes rate-limiting at high Ca^{2+} concentrations, as already previously discussed [170] and illustrated in Figure 59. There, the activity of nhTMEM16 in the presence of 2.5 µM or 300 µM Ca^{2+} appears very similar, underlining that the reduction by dithionite represents the rate-limiting step above Ca^{2+} concentrations of 2.5 µM. This further implies that the real activity of nhTMEM16 observed in the presence of 300 µM Ca^{2+} (in fact starting at values above 2.5 µM), is masked due to the slow reduction process. Thus, the activity of fully activated nhTMEM16 cannot be measured quantitatively using this assay. In contrast, the time dependence of proteoliposomes containing WT nhTMEM16 in the apparent absence of Ca^{2+} can be described by a sum of two exponential functions with time constants of 25 and 175 seconds. While the first time constant represents the rate-liming reduction by dithionite similarly as observed in the presence of high Ca^{2+}, the second time constant derives from scrambling processes that are comparably slow (which are slow enough to be resolved during the process of dithionite reduction). Unfortunately,

the scrambling rates of nhTMEM16 in the absence or presence of high Ca^{2+} levels cannot be compared, since no 'Slow' time constants could be calculated for the scrambling at high Ca^{2+} concentrations.

a

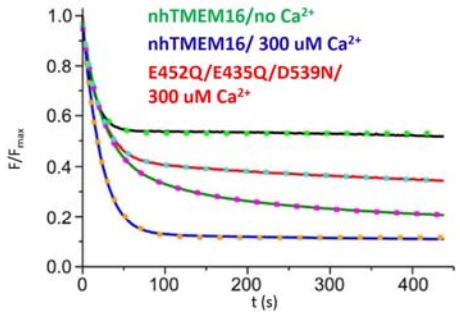

b

		Time constants [s]	
	Ca^{2+} [µM]	Fast	Slow
no protein	300	15	n.d.
WT	0	25	175
WT	300	22	n.d. (7)
E452Q/E535Q/D539N	0	21	803
E452Q/E535Q/D539N	300	21	803

Figure 77 Kinetics of lipid scrambling

a, Scrambling assay. The fluorescence decay (F/F_{max}) is plotted against the time (s). The curves can be fitted by exponential functions. b, Table of corresponding time constants. The curves can either be described by a single exponential function (termed Fast) or by the sum of two exponential functions (Fast and Slow). In the presence of 300 µM Ca^{2+} (i.e. under saturating conditions), no time constants could be measured for the Slow component in protein-free and proteoliposomes containing nhTMEM16 (denoted as n.d.). The time constant for the Slow component for scrambling of afTMEM16 in the presence of saturating Ca^{2+} concentrations was estimated [170] and is displayed in blue. Fits are shown as dotted lines.

A triple mutant combining the conservative mutations E452Q/E535Q/D539N was shown to be slightly active as well in the absence of Ca^{2+} (Figure 63). Interestingly, the scrambling activity of this mutant could no longer be enhanced by Ca^{2+}. The time dependence for the mutant was characterized by time constants of 21 and 803 seconds respectively, thus suggesting that the activity of the mutant was five times lower than the activity of the WT nhTMEM16 in the absence of Ca^{2+}. Also here, the scrambling rates by WT and mutant nhTMEM16 cannot be compared in the presence of Ca^{2+}, due to the lack of the appropriate time constants (Figure 77b, Slow).

For afTMEM16 the rates between the Ca^{2+}- free and saturating conditions were estimated, assuming that 10^6 lipids would be present in an average liposome [314] containing five copies of a scramblase. In this case, the rates for lipid flip-flop would be 400 lipids per second in the absence and 10^4 lipids per second in the presence of saturating Ca^{2+} concentrations [170]. This would indicate an approximate 25 fold increase in scrambling rates for afTMEM16, which presumably also applies for nhTMEM16, whose properties in the scrambling assay are very similar. According to that, nhTMEM16 would be about 25 times more active at saturating Ca^{2+} concentrations compared to zero Ca^{2+}. This would further imply that the mutant nhTMEM16 would be more than 100 times less active than WT nhTMEM16 in the presence of saturating Ca^{2+} levels.

Using a cellular assay, TMEM16C, D, F, G and J were associated with scrambling of NBD-galactosylceramide (NBD-GalCer) and NBD-phosphatidylcholine (NBD-PC) while TMEM16D, F, G and J were additionally shown to be involved in translocation of NBD-phosphatidylserine (NBD-PS) [10, 111]. For afTMEM16 the substrate specificity was analyzed using purified protein reconstituted into NBD-containing liposomes. Phospholipid scrambling was confirmed for substrates as diverse as NBD-PS, NBD-phosphatidylethanolamine (NBD-PE), NBD-PC and NBD-Glucosylceramide (NBD-GluCer). For nhTMEM16, two phospholipids were tested, NBD-PS and NBD-PE, but most probably, other lipids may be substrates of this scramblase, too. For afTMEM16, one experiment compared the flipping rates in liposomes containing different amounts of NBD-PE (0.05, 0.5 and 5 %). Since no significant differences in the kinetics could be observed, it was concluded that the observed scrambling is not specific for NBD-labelled lipids [170]. Although not investigated in detail for nhTMEM16, it is likely that, due to the functional similarity and the high degree of sequence conservation (i.e. 48%) between the two fungal proteins, these properties apply to nhTMEM16 as well. Thus, most probably nhTMEM16 does not only transport NBD-labelled lipid derivatives but also their native forms likewise with similar flipping rates. The transport of many different lipids indicates a low substrate specificity and that rather the size or a particular charge than its specific chemical interactions with the protein determines, whether a particular molecule is a substrate or not.

Altogether, the scrambling assay used in this work permitted to draw semi-quantitative conclusions on phospholipid scrambling of nhTMEM16. The assay was sensitive enough to detect activation of scrambling at sub-micromolar Ca^{2+} concentrations and it was suitable to investigate the Ca^{2+} dependence as well as the activation by different divalent cations. The scrambling rates could partially be quantified and allowed the comparison of the scrambling rates between WT and mutant nhTMEM16. Furthermore, as shown in Figure 62, the scrambling assay served to evaluate potential inhibitors. Using this assay, any lipid substrate can be assessed, provided that it is available with an NBD- group attached to the head group of the lipid, and findings likely apply to the corresponding lipids not containing any NBD-modification. This at least was shown for NBD- PE and PE, respectively. In this work, nhTMEM16, one of two TMEM16 family members in the fungus *Nectria haematococca* was demonstrated to catalyze the bidirectional transport of phospholipids between the two leaflets of the membrane in a Ca^{2+} dependent manner, while for activation Ca^{2+} can be replaced by Sr^{2+}, but not by Mg^{2+}.

3.8. Mechanism of ion conduction and lipid scrambling

Before Ca^{2+}- activated chloride channels (CaCCs) were discovered at a molecular level, their function was thoroughly studied by electrophysiological methods [1, 135, 136, 147, 294, 315, 316]. In 2008, three groups independently demonstrated [4-6] that currents elicited by TMEM16A in CaCC- free systems strikingly resembled these CaCC currents. The experiments on CaCCs allowed drawing conclusions on the channel properties of TMEM16A, which might also apply to other TMEM16 family members.

As already discussed above, TMEM16A activation occurs synergistically by Ca^{2+} and voltage, presumably involving two or three Ca^{2+} ions, as deduced from the Hill- coefficient. These were calculated

to bind to a Ca^{2+} binding site located within the membrane [1]. The affinity for Ca^{2+} was monitored to change not only at higher membrane potentials, but it was also depended on the type of the conducting anion [136, 147]. According to the Goldman-Hodgkin-Katz equation, the reversal potential E_{rev} of +44 mV in the presence of a 10-fold NaCl gradient, suggests that the channel is ten times more selective for chloride than for sodium ions, and the apparent chloride affinity of 73 mM indicates a weak interaction of the permeating chloride with the protein [136]. By comparing different anions, the permeability sequence and conductance was determined. Whereas the permeability refers to the ability of a particular anion to enter the channel pore, the conductance reflects the ability of an anion to go through the pore.

The permeability (P_X/P_{Cl} which was determined from the E_{rev} by the GHK equation from bi-ionic conditions) followed the sequence:

$C(CN)_3^-$ > SCN^- > $N(CN)_2^-$ > ClO_4^- > I^- > N_3^- > Br^- > Cl^- > COOH.

However, the conductance (determined as G_X/G_{Cl} between E_{rev} and E_{rev}-50 mV) followed the sequence**:**

N_3^- > Br^- > Cl^- > $N(CN)_2^-$ > I^- > SCN^- > COOH > ClO_4^- > $C(CN)_3^-$.

These findings indicated that particular anions unhesitantly entered the pore, but did not readily traverse the path through the pore, and inversely, other anions did not enter easily, but once they have entered the pore they travelled comparably fast through it [136]. These differences were suggested to arise due to different affinities of a permeant anion for the pore. The order of the relative affinities for such anion binding sites in the pore were measured to resemble the sequence for permeability (see above). It was found that the permeabilities depended on the size and charge distribution of the anion. The radius of anions with equally distributed charge is inversely proportional to the hydration energy, which defines the strength of the anion- water interaction [136, 292, 293]. Thus, the hydration energy is a relevant property to discern between anions in CaCCs (or TMEM16A) implying that the larger the anion, the easier the water molecules can be peeled off and the more permeant it is (termed as lyotropic).

In CFTR (Cystic Fibrosis Transmembrane Conductance Regulator) the permeability of anions was determined to be lyotropic as well, with higher affinities for larger anions. In CFTR the anion permeation is believed to proceed in three steps [293, 317]: In a first step the anions enter the pore and strip off at least part of the hydration shell. In the second step dehydrated anions are stabilized by the channel and translocate through the pore. In the last step the ions leave the pore and get rehydrated in the aqueous environment on the other side. The strength of the interaction of residues within the pore with a particular anion (defined as solvation energy) is reflected in the dielectric constant of the polarizable interior of a channel and the radius of the anion. For CaCCs and CFTR, these dielectric constants were, with a value of 20 and 19, respectively, estimated to be very similar, thus indicating similar polarizabilities within the pore [136, 292, 294, 317]. Similarly as demonstrated for CFTR, it was found in CaCCs (or TMEM16A) that the reciprocal relationship between permeability and conductibility of particular anions is caused by

the affinity they exhibit towards the polarizable interior of the channel. This is further reflected in the fact that larger anions such as SCN^- or $C(CN)_3^-$ block the chloride conductance in both, CFTR [292] and CaCCs. In CFTR, but perhaps also in CaCCs, permeability and binding might underlie the selectivity mechanism to form a chloride filter [292]. Larger anions than chloride, which take less energy to strip off their hydration shell, readily enter the pore, but are retained within the channel due to their relatively high affinities for residues along the path. In contrast to that, anions with smaller radius than chloride dehydrate reluctantly due to their high hydration energy and their entry into the pore is thus unfavorable. The pore diameter was estimated to be at least 8 Å, based on the fact, that large ions such as $C(CN)_3^-$ or $NMDG^+$ with a mean diameter of 7.2 Å are able to permeate through the channel, while the observed average diameter of the subunit- cavity in the structure of nhTMEM16 was determined to be around 10-14 Å.

Whereas for characterization of ion conduction and channel properties many different and often direct methods are applied, and different types of channels can be distinguished using appropriate electrophysiological methods, only few approaches exist to measure scrambling processes. Scrambling assays carried out in cellular systems are often not reliably quantitative, so that they only allow qualitative conclusions. Additionally, the detection of scrambling processes is indirect and requires visualization of the substrate based on fluorophores. Similar limitations concerning the quantification of scrambling processes also exist in liposome-based scrambling assays, as discussed above. Altogether, considerably larger progress was made in the study of ion channels over the past decades, while the mechanistic understanding of lipid flip-flop in scramblases (and partially also in flippases and floppases) resisted any detailed characterization and is still in its infancy.

Ca^{2+}- activated scrambling processes were already described years before TMEM16F was proposed to constitute the Ca^{2+}- activated scramblase in blood cells. In red blood cells, scrambling was measured for NBD- lipids labelled at their fatty acid chains to follow the sequence: NBD- PC > NBD- PE > NBD- PS > NBD- phosphatidylgalactose (NBD-PGal) > NBD- phosphotidylmaltose (NBD-PMal) > NBD- phosphatidyltriose (NBD-PTriose), where NBD-PTriose is barely transported [13]. These observations indicated that the scrambling efficiency might be related to the size of the head group. A similar relationship of head group labelled NBD- lipids was assessed for afTMEM16 [170]: PC > NBD- PE > NBD- PS ~ NBD- glucosylceramide (NBD- GluCer) > NBD- trimethylammonium propane (NBD-DOTAP).

A model was established to explain how the transport of lipids is catalyzed by scramblases. In this model, an aqueous path allows the polar head groups to traverse the membrane, while the lipophilic fatty acid chains diffuse through hydrophobic interfaces [14]. As already discussed above, such an aqueous path might be formed by the subunit- cavity in TMEM16 scramblases, which contains a high amount of charged and polar residues and is likely linked to Ca^{2+} activation (Figure 78). The scrambling rates were compared between glycerophospholipids with identical head groups, but either containing a glycerophospho- or a sphingosine backbone. Interestingly, the sequence of such lipids was determined to be: NBD- PC > NBD- PGal > NBD- galactosylceramide (NBD- GalCer) > NBD- sphingomyelin (NBD- SM) [13]. These results suggested that the rate of scrambling is not exclusively determined by

the head group size of the transported lipid. For example, PGal scrambling was more efficient that GalCer scrambling, despite the fact that the head group of GalCer is smaller in size, since it does not contain a phosphate group (Figure 1) [13]. A similar relationship was observed for PC and SM. This suggests that interactions with the phosphate group might play a role during the flip-flop. Alternatively, the reduced scrambling of ceramide lipids might also be due to their preferential localization within lipid rafts [318].

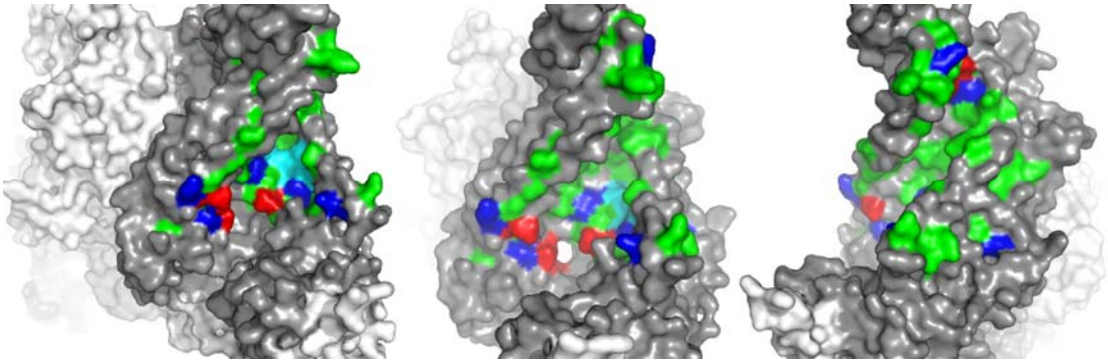

Figure 78 subunit- cavity: Potential lipid and ion translocation path

View of the subunit- cavity of nhTMEM16. The dimer is illustrated in grey (dark/light). Residues located in the subunit- cavity are colored according to their properties (red: acidic, blue: basic, green: polar) and the Ca^{2+} binding site is shown in cyan.

The possibility of a non- aqueous polar path was considered as well. There, the different scrambling rates might result from distinct hydration energies for the various lipids that, similarly as ions, have to be stripped from interacting water molecules before they can enter the path [13]. From the structure of nhTMEM16 it cannot be concluded, whether the subunit- cavity is polarized or aqueous, but both mechanism appear plausible. Besides the size of the head group, additional factors might play a role in determining the substrate specificity. Particularly, it is conceivable that the different charges of a certain lipid might be of importance. Altogether, considering the many different types of lipid substrates, it appears that in TMEM16 scramblases not only few specific amino acids, but rather many residues distributed over the entire subunit- cavity may contribute to lipid scrambling (and the observed ion conduction) and that the type of lipid substrate defines to which degree individual residues may contribute. Figure 79 shows schematically, how lipid scrambling might occur along the hydrophilic (or polarized) surface of the subunit- cavity. The distribution of many charged and polar residues within the subunit- cavity, as seen in Figure 78, might explain the broad substrate specificity in TMEM16 proteins.

It appears possible, that in TMEM16 proteins the transport of ions and lipids might in part be regulated electrostatically. The net charge within the Ca^{2+} binding site might be a determinant for gating. In the absence of Ca^{2+}, the negative charge within the empty Ca^{2+} binding site might prevent the passage of chloride ions and lipids, due to strong electrostatic interaction or repulsion in such a low di-electric environment. The binding of Ca^{2+} ions to the Ca^{2+} binding site might neutralize the negative charge of the glutamates and aspartates within the binding site. Ca^{2+} binding would thus abrogate the electrostatic

barrier and the transport of ions and lipids may be enabled. In an electrostatic gate, the binding of Ca^{2+} does not necessarily induce a conformational change, but the neutralization of the electrostatic block might be sufficient to promote ion conductance or lipid translocation.

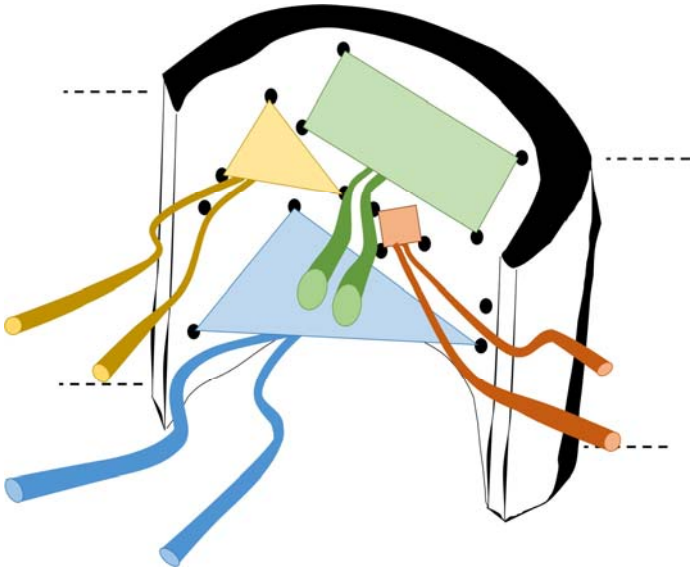

Figure 79 Fictive lipid path

View of the subunit- cavity. Schematic representation of the lipid path within the subunit- cavity of one monomer (black/ white). The putative membrane boundaries are indicated by dashed lines and different types of lipids are schematically drawn. While the polar head groups are indicated as triangles and squares, the acyl chains are shown as tubes. Residues of the subunit- cavity that may be involved in interactions with the lipid head groups (fictive) are indicated as black dots.

The nhTMEM16 structure has not only revealed the architecture and certain concepts of TMEM16 proteins, but it has also provided a first detailed view of a scramblase. Besides TMEM16 proteins, other known scramblases, i.e. the phospholipid (PL) scramblase of the ER (chapter 1.5) and scramblases of the Xk- related family of proteins (chapter 1.6.1) at the plasma membrane, catalyze the rapid breakdown of the lipid asymmetry. This is reflected in a broad substrate specificity that allows the transport of different types of phospholipids. Such a performance requires the formation of an interface that allows interactions with different types of lipid substrates at the same time. Therefore, it is likely, that other scramblases exploit similar strategies like TMEM16 proteins to facilitate rapid, bidirectional lipid translocation between the two leaflets of a membrane. It is thus conceivable, that the concept of the subunit- cavity is not only a feature of TMEM16 proteins, but may presumably also be found in a similar form in other scramblases.

3.9. Alternative arrangement of TMEM16A and B

Several TMEM16 family members, namely afTMEM16 [170], nhTMEM16 [295], TMEM16C, D, F, G and J [10, 111] were suggested to be involved in phospholipid scrambling processes, while TMEM16A and B were shown to be devoid of such a function [111, 112, 170, 295]. In addition, afTMEM16 and TMEM16F appear to mediate ion transport in a Ca^{2+} dependent manner. While channel activity of afTMEM16 was proposed to be non-selective with high conductance [170], TMEM16F was associated with cation-selective currents of small-conductance with highest preference for Ca^{2+} [9]. In contrast, TMEM16A was related to Ca^{2+} dependent chloride transport [5, 6, 186]. In TMEM16A and F the subunit-

cavity might provide the ion conduction path, as indicated by point mutations that influence the conductance in TMEM16A [12, 188] and selectivity in TMEM16F [9].

Although TMEM16 proteins combine different functions, it is generally assumed that they would share a similar fold [15, 167, 168, 230, 295]. It is therefore intriguing, how TMEM16F would catalyze the transport of ions and lipids, while in TMEM16A and B only ion transport occurs. In TMEM16A and B the question arise, how the subunit- cavity might form a hydrophilic aqueous path required for ion conduction and, on the other hand, how scrambling of lipids would be precluded in these proteins. Since in the structure of nhTMEM16 the subunit- cavity is formed by an open 10-14 Å wide crevice that faces the hydrophobic environment of the membrane (Figure 80a), it appears conceivable that in TMEM16A and B sufficient shielding of the ion path is achieved by local structural rearrangements in this region in an overall assembly as seen in nhTMEM16.

Alternatively, it is inviting to speculate that in TMEM16A and B both subunits might be reoriented by a 180° turn to allow interaction of the two monomers via their subunit cavities (Figure 80b, front view). In contrast to the two subunit cavities as observed in the assembly of nhTMME16, in this alternative arrangement perhaps only a single pore is formed. In such an inverted orientation the pore would be completely shielded from the membrane and any access to lipids would be prevented. Remarkably, a model of this alternative arrangement generated with Pymol [298] is largely compatible with the structure of the monomer with no significant superposition or clashes produced (Figure 80b, top and bottom view). The two opposite assemblies formed by structurally similar subunits would result in two distinct proteins (with different shapes and properties) that conceivably fulfill disparate tasks. Such an assembly would not only offer a plausible explanation to the dual-functionality in TMEM16 proteins, but also why and how in TMEM16A and B the scrambling of lipids consequently would be precluded. Supporting evidence for this proposal may also come from a strong salt bridge, which is formed at the dimer interface in most TMEM16 family members, while it is absent in TMEM16A and B (Figure 53c and Figure 66).

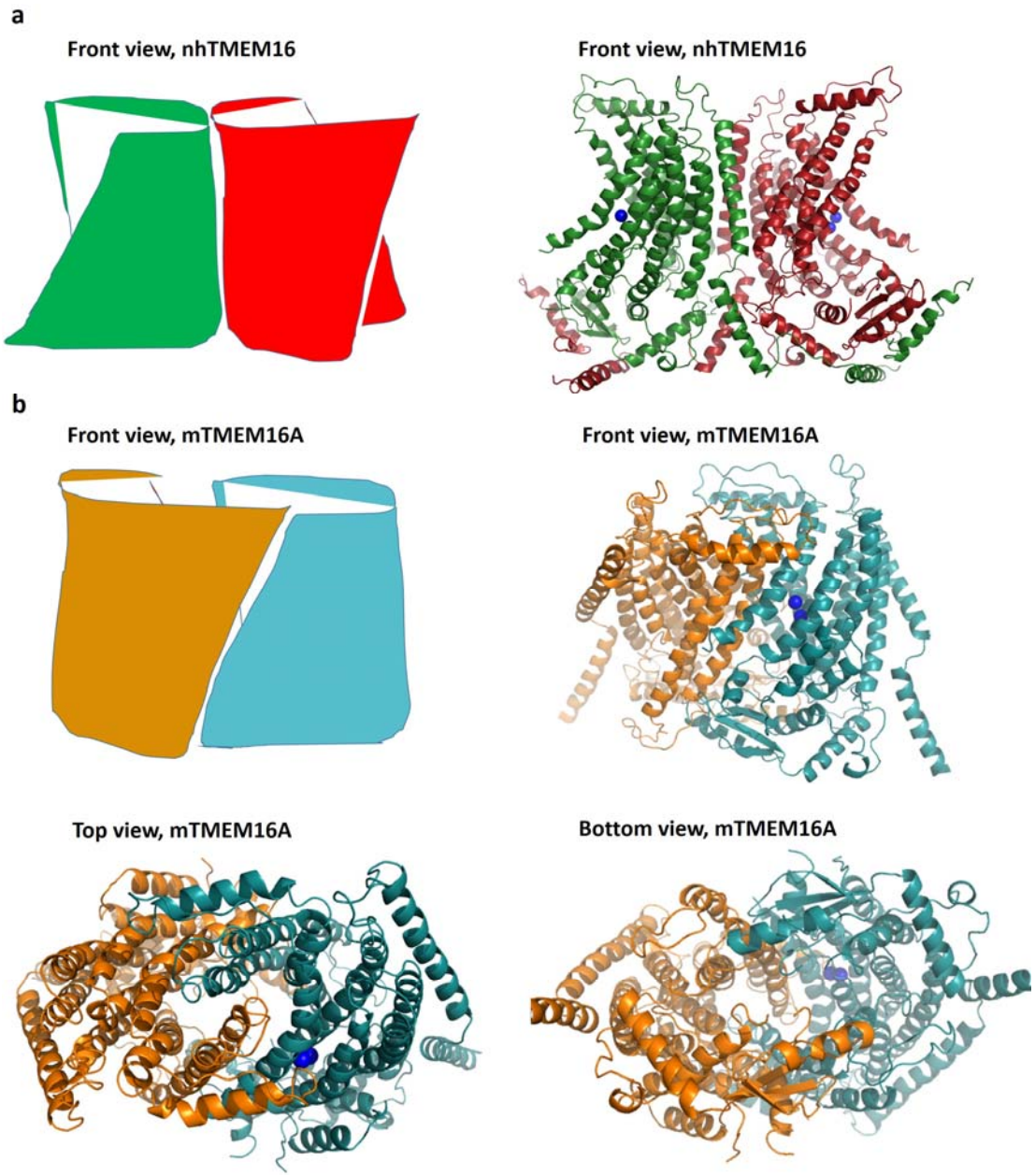

Figure 80 Possible dimer arrangements in TMEM16 proteins

Possible dimeric organization in TMEM16 proteins. a, Front view of the arrangement observed in nhTMEM16. Inter-subunit contacts occur in the dimer interface created by helix α-10 and the two subunit cavities are located far away from each other. b, An alternative assembly is illustrated for TMEM16A and B. There, the dimer would interact via the subunit cavities. In such an arrangement perhaps a single pore is formed, as seen from top and bottom views.

With the alternative dimeric arrangement for TMEM16A and B a plausible suggestion was provided, that might contribute to understand and explain the dual- functionality in TMEM16 proteins. However, this hypothesis now requires experimental data to either be confirmed or contradicted.

3.10. Outlook

The structure of nhTMEM16 allowed detailed insight into a family that so far has resisted any deeper structural characterization. For the first time the architecture of a TMEM16 family member was revealed, that permits a mechanistic view on the diverse transport processes catalyzed by TMEM16 proteins and on the mode of activation in these proteins. Although the structure of nhTMEM16 provides many answers, it also raises more questions.

While TMEM16A and B were characterized as Ca^{2+}- activated chloride channels, other members were associated with a function in lipid scrambling, along with a potential function in ion transport. The structure by itself is insufficient to explain this functional discrepancy between different members of the family. It does, however, provide an intuitive mechanism for lipid scrambling, as it significantly deviates from the architecture of known ion channels. The candidate region for ion transport and lipid translocation is formed by an open 10-14 Å wide crevice, the subunit- cavity, which faces the hydrophobic environment of the membrane. In light of the structural organization of the subunit- cavity, it appears now even more puzzling, how lipid scrambling is promoted in nhTMEM16, afTMEM16 and presumably in TMEM16C, D, F, G and J [10, 111, 112, 170, 295], while some of these proteins may at the same time be permeable for ions [9, 170]. Similarly, it is unclear how ion transport is permitted in TMEM16A and B [4-7], while lipid scrambling is prevented [111, 170, 295]. It is conceivable that slight local structural rearrangement in the subunit- cavity would preclude lipids from entering. However, in the present work, a plausible explanation was offered by the assembly of two distinctly oriented dimers (Figure 80). Such an alternative assembly might result in the formation of a single pore, which would be inaccessible to lipids since it is shielded from the membrane. This important question could be addressed by strategically placed mutations within TMEM16A and nhTMEM16 in order to cross- link the respective dimer arrangement using subsequent SDS-PAGE for analysis.

Hetero- dimers between subunits of the functionally related TMEM16A and TMEM16B [179], and co-localization of these proteins was both confirmed [8, 155], which raises the question, whether there might exist mechanisms to prevent the formation of hetero- dimers with mixed functions, for example consisting of TMEM16 A and F monomers. Indeed, no mixed dimers of TMEM16F and either TMEM16A or B were detected in biochemical experiments [179]. As discussed in chapter 3.2, a possible mechanism to circumvent hetero- dimers with heterogeneous function might be controlled by the formation of two different types of interactions in the dimer interface. While in most TMEM16 family members an obligate pair of salt bridges is formed by interactions between a histidine and a glutamate, in TMEM16A and B homologues usually a pair of glutamine and asparagine residues are found at equivalent places. A potential incompatibility of the respective residues due to weaker interactions and potential steric hindrance at that position might account for the absence of dimer assemblies with mixed functions. Mutations in TMEM16F that transform the histidine and aspartate residues into a glutamine and asparagine might lower the dimeric interaction with WT TMEM16F. Similarly, it might occur that such mutations suddenly increase the likelihood that TMEM16F would assemble with TMEM16A or B

monomers. Clarity about this question could be gained by quantifying the monomer- dimer proportion in these proteins after unspecific cross-linking and subsequent SDS-PAGE and Western blot analysis.

Clearly, the high- resolution structure of nhTMEM16 represents only one snapshot of a particular situation in which Ca^{2+} was bound to the protein. In order to increase the understanding of the role of Ca^{2+} for activation and to characterize potential conformational changes that might occur during the process of lipid scrambling, attempts were undertaken in the course of this work to crystallize nhTMEM16 in the absence of Ca^{2+}. However in the 'Ca^{2+} -free' structure of nhTMEM16 bound Ca^{2+} ions were nevertheless detected. Clearly, one challenge would be to obtain a structure in a conformation, where no Ca^{2+} ions are bound within the Ca^{2+} binding site. Two factors complicates such an endeavor, the apparent high affinity for Ca^{2+} and the low stability of the protein in the absence of Ca^{2+}. The existence of a completely Ca^{2+}- free conformation under physiological conditions is in fact plausible, but not certain.

In the scrambling assay, nhTMEM16 was demonstrated to facilitate the transbilayer movement of lipids such as PS and PE between the two leaflets of the membrane in a Ca^{2+} dependent manner. Interestingly, the protein still exhibited residual scrambling activity towards these substrates even in the absence of Ca^{2+}. Similar results were previously obtained for the related scramblase afTMEM16 [170]. The question remains unanswered, whether the residual activity is a consequence of traces of Ca^{2+} ions still present as impurities in the solutions used for purification and the scrambling assay, or whether the protein is constitutively active, albeit at lower rate in the absence of Ca^{2+}. Towards the clarification of this important question, a five or six-fold alanine mutant replacing residues in the Ca^{2+} binding site, or mutations within the subunit- cavity that potentially alter protein-lipid interactions, might be considered and evaluated in the scrambling assay. Alternatively, since for the liposome- based scrambling assay used in this work, large amounts of purified protein is required, the establishment of a cellular scrambling assay, as previously described [53, 93, 106, 107, 111], might be considered for mutational studies of TMEM16F, for example.

Although substantial evidence was provided that TMEM16F and other family members function as phospholipid scramblases, a definitive conclusion on that is still missing. Such an activity was so far only detected in cells, but not in an assay based on purified and reconstituted protein. The main reason for the lack of in-vitro experiments is the low expression level and the poor stability of the protein after extraction with detergents (observations from the present work and [167, 170]). The generation of sufficient yields of stable TMEM16F for reconstitution into liposomes in order to quantify its scrambling activity would be a large breakthrough. Although a role of TMEM16F in ion transport was proposed, the different types of currents that were attributed to TMEM16F prevent a definite assignment. It will thus be of great interest to address questions concerning the mechanism of ion conduction and lipid scrambling in this protein. The structure will thereby be of help to identify appropriate residues for mutations. It will also be of importance to contrive experiments that may allow to distinguish between currents of physiological relevance from potential artifacts.

4. Methods

4.1. Sequence search

The murine TMEM16A protein (mTMEM16A) sequence obtained from the Uniprot K database was used as a query in the basic local alignment tool [319] (Blastp, http://blast.ncbi.nlm.nih.gov/Blast.cgi) applying standard settings to identify homologous genes from different eukaryotic kingdoms. Around 80 genes were thereafter obtained as cDNAs (from ImaGenes) or as synthetic genes (from GenScript).

4.2. Cloning

The genes were modified by standard PCR procedures (with Fusion HF DNA polymerase, NEB) to contain flanking *SapI* sites upstream (5'TATATAGCTCTTCTAGT3') and downstream (5'GCATGAAGAGCTAATA3') of the coding sequence to make them compatible for *SapI* dependent sub-cloning [240]. The expression vectors were modified to be compatible with FX-cloning [240]. Figure 81 shows a schematic representation of the different constructs that are described in this chapter. Gel purified PCR products (prepared with the Agarose gel DNA extraction kit, Roche Life Science) of the respective full-length genes containing flanking *SapI* sites were cloned into different expression vectors.

For expression screening in HEK tsA201 cells, the PCR products of the full-length genes were cloned into a modified [240] pcDNA3.1 vector (Invitrogen), bearing a 5' UTR of hVEGF (from pcDNA4/HisMax, Invitrogen) upstream of the start codon. Constructs were generated as N- or C-terminal fusion to a cassette encoding an SBP- [320] and a Myc-tag, Venus-yellow fluorescent protein [257] (Venus-YFP) and a HRV-3C cleavage site. Once a construct proved to be expressed during HEK expression screening it was cloned into a modified pcDNA3.1 vector that lacked the Venus-YFP and contained only an N- or C-terminal fusion to an SBP-tag, a Myc-tag and the HRV-3C cleavage site.

For expression in the insect cell lines Sf9 and Sf21 a modified [240] pFastBac vector (pFastBac dual expression vector, Invitrogen) bearing an N- or C-terminal SBP-tag, Myc-tag and a HRV-3C cleavage site was employed. For cloning of the genes into the pFastBac vectors and further site-specific transposition of the gene of interest into the bacmid DNA, procedures described in the Invitrogen manual [321] were followed.

For expression in *S. cerevisiae* the full-length genes were cloned into a modified [240] pYES2/CT plasmid (Life technologies) as C-terminal fusion to a cassette encoding enhanced GFP (EGFP), preceded by a His_{10}-tag and followed by a HRV-3C cleavage site.

For the scramblase assay the modified [240] pYES2/CT plasmid was adapted so that the gene of interest was fused to an N- or C-terminal SBP- and a Myc- tag flanked by a HRV-3C cleavage site.

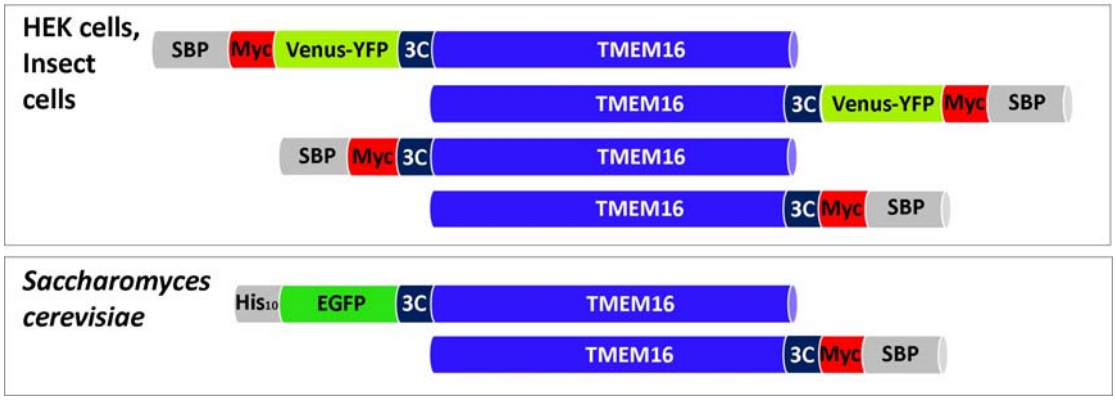

Figure 81 Schematic representation of the constructs used in this work

Various constructs for the expression of TMEM16 proteins were generated. Constructs were adapted depending on the experimental purpose and expression host. Where highest purity was required (i.e. in the scramblase assay) or in case of low expression and challenging production (in HEK and insect cells) constructs generally contained an SBP-tag that facilitated purification. Hence, there were four different constructs for the expression and crystallization screening in HEK and insect cell lines, depending on the location of the SBP-tag and the absence or presence of a Venus-YFP. One construct with a C-terminal SBP-tag was generated for expression in *Saccharomyces cerevisiae* for protein used in the scrambling assay. All crystallization constructs generated in *S.cerevisiae* were purified by means of a His_{10}-tag. A Myc-tag was used for Western blot detection. All constructs contained a HRV-3C cleavage site to be able to remove any fusion protein tag.

4.3. Protein expression

For expression in mammalian cells, tsA201 cells (Cat # 96121229, Sigma-Aldrich) with a confluency of 40-60% were transfected with plasmid DNA containing the respective genes as described [322], except that the transfection buffer was prepared with 2.8 mM Na_2HPO_4. Expression was carried out in 10 cm dishes (10 ml, Corning) at 37 °C and 2.2% CO_2 for 1–2 days. For small scale expression screening only 1-2 dishes per construct were needed. The expression level and the cellular localization of Venus-YFP tagged proteins was monitored by fluorescence microscopy.

For virus generation in Sf9 and expression in Sf9 or Sf21 cells (Gibco) the descriptions of the Invitrogen manual [321] were followed. Briefly, low passage cells at 10^6 ml^{-1} were transfected in 6-well plates with a mix of Cellfectin II reagent (Invitrogen) and 1.5 µg bacmid DNA containing the gene of interest. After 5 h the transfection media was replaced with Sf-900 II SFM media and incubated in a humidified incubator at 27°C for 5-6 days. When the transfected cells started to detach, they were collected for later analysis (small scale purification, FSEC) and the supernatant containing the virus P_0 was used for infection of low passage Sf9 cells. After 5-6 days the supernatant comprising virus P_1 was isolated to infect a larger volume of Sf9 cell suspension. Cells were harvested after 4 days. The amount of virus P_1 used for expression depended on the virulence of the virus and was determined for each new virus batch in small scale expression tests. For expression of TMEM16 proteins it was crucial to add protease inhibitors (Sigma-Aldrich, 1:800) into the media to prevent proteolysis of the proteins in response to the inevitable lysis of the Sf9 cells.

For expression in yeast the pYES2/CT vectors carrying the respective full-length genes were transformed into *S. cerevisiae* FGY217 cells carrying an URA deletion for positive selection as described [252]. Cells were grown at 30 °C in small scale (50ml) or fermentation culture (35 l) in yeast nitrogen base (w/o amino acids, Sigma) supplemented with Synthetic Complete drop-out medium without URA (Formedium) and 0.1% glucose. Protein expression was induced with 2% galactose for 40 h at 25 °C at an OD_{600} of 0.8. For generation of seleno-methionine labeled protein, BY4741 cells (*MAT**a** his3Δl leu2Δ0 met15Δ0 ura3Δ0*) were grown at 30 °C to an OD_{600} of 2-3, centrifuged and washed to remove residual methionine prior to induction. The cells were subsequently suspended in yeast nitrogen base without amino acids (Sigma), supplemented with Synthetic Complete drop-out medium without Met/URA (Formedium), 0.01% raffinose and 100 mg l^{-1} seleno-methionine (Acros Organics), grown for 1 h, induced and expressed as described before.

4.4. Expression screening in HEK, insect cells and yeast

Protein expression screening in HEK tsA201 and Sf9 or Sf21 cells was carried out as described above with two dishes per construct or in a 6-well plate (2ml per well). The cells were subsequently harvested and proteins were extracted in buffer A (50 mM Hepes pH 7.6, 150 mM NaCl) containing 0.5 mM $CaCl_2$, 5% glycerol, protease inhibitors (Complete, Roche) and 2% n-Dodecyl-β-D-Maltopyranoside (DDMβ, Anatrace) for 1.5 h. After removal of the cell debris by centrifugation a sample for analysis by Western blotting was taken and the supernatant was either directly loaded on a fluorescent size exclusion column (GF450, Agilent Zorbax or G3000SWxl, Tosoh Bioscience LLC) for analysis of the elution profile (excitation 480 nm, emission 515 nm) or applied to Pierce Streptavidin plus UltraLink Resin and bound for 1.5 h to assess the stability of protein. The bound protein was washed with buffer A containing 3-5 mM $CaCl_2$, 5% glycerol and 0.025% DDMβ and subsequently eluted with buffer A containing 3-5 mM $CaCl_2$, 5% glycerol, 0.025% DDMβ and 2% Biotin. A sample was saved for SDS-PAGE analysis. The rest of the eluate was subjected to fluorescent size exclusion analysis connected to either a GF450 column (Agilent Zorbax) or a G3000SWxl (Tosoh Bioscience LLC) column. Whereas fusion proteins bearing a Venus-YFP tag were detected by GFP-fluorescence (ex. 480 nm, em. 515 nm) constructs only fused to the purification tag were detected by tryptophan fluorescence (ex. 280 nm, em. 320-350 nm). All steps were carried out on ice or at 4°C.

Screening in yeast was performed in small scale using a volume of 50 ml or 1 l by two protocols. For the screening of different nhTMEM16 constructs (such as protein truncations, methionine point mutants, mutants of the calcium binding site and others) it was sufficient to compare the fluorescence level in whole cell with the fluorescence in wild type protein. A decreased fluorescence indicated either a lower expression level or decreased stability of the protein. Cells were harvested at an OD_{600} of 4.5-6 and resuspended to an OD_{600} of 60 in buffer A containing 0.5 mM CaCl2, 1% glycerol, protease inhibitors, DNaseI and 1 mM $MgCl_2$. In protocol 1, 3 x 550 µl per construct were transferred into screw cap Eppendorfer tubes that were loaded with glass beads (425-600 µm size, Sigma). The cells were subsequently broken in a FastPrep-24 (MP Biomedicals) with the settings 6 x 40 s and 5.5 m s^{-1}. A 30 s spin at 10,000 g separated the glass beads and cell debris from the supernatant containing the membranes.

In protocol 2, the 1 l culture was harvested and resuspended in 40 ml buffer A containing 0.5 mM $CaCl_2$, 1% glycerol, protease inhibitors, DNaseI and 1 mM $MgCl_2$. Cells were lysed in a custom-made pressure-based cell disruptor at 40 kpsi. Cell debris was removed by low-spin centrifugation and membranes were collected using an ultracentrifuge. All membranes independent of the protocol were extracted in buffer A containing 0.5 mM $CaCl_2$, 5% glycerol, protease inhibitors and 1% DDMβ for 1.5 h. The supernatant that was obtained after a 15 min spin at 200,000 g was applied to fluorescent size exclusion as described before. All steps except the FastPrep lysis were carried out on ice or at 4°C.

4.5. Western blotting

Western blot analysis was performed by standard procedures using 5% milk powder dissolved in phosphate buffered saline at pH 7.2 containing 0.1% Tween-20 (PBS-T) for blocking and incubation with antibody and PBS-T for the washing steps. Constructs bearing only a His_{10}tag were detected by an αHis-antibody (Roche) at a ratio of 1:1000. Constructs expressed in HEK cells contained a Myc-tag and were detected by an αMyc-antibody (rabbit, ABcam, ab9106) in a ratio of 1:10,000 which was recognized by an αRabbit-antibody (goat, BioRad, Herkules California, 172-1019) used at the same ratio. Constructs carrying a fusion to EGFP were detected by an αGFP-antibody (rabbit, Synaptic Systems, 132 002) at a ratio of 1:1,000 followed by an αRabbit-antibody (goat, BioRad, Herkules California, 172-1019). The αHis-antibody and the secondary antibody were conjugated to horseradish peroxidase.

4.6. Limited proteolysis

Limited proteolysis was performed at 4-8°C with several proteases at different concentrations and time points. Trypsin and LysC were used at a molar ratio of 1:10, 1:100, 1:1,000 and 1:2,000 and samples were taken after 2 h, 4 h and 24 h. The fragments were TCA precipitated, washed with acetone and subsequently analyzed by electrospray ionization mass spectrometry to determine fragment size and identity. N- and C-terminal truncations of ppaTMEM16, gzeTMEM16 and nhTMEM16 were subsequently generated based on the outcome of the limited proteolysis experiments or prepared by systematic truncations at both termini and cloned as described in the cloning section.

4.7. Protein purification for crystallization

Once a construct proved to be stable and monodisperse during the initial characterization, it was used for large scale expression and purification in either HEK tsA201, Sf9 or Sf21 cells or in *S.cerevisiae*.

HEK tsA201 expression culture was scaled up by collecting 1,700 10 cm dishes for ppaTMEM16 or >2000 dishes per purification for gzeTMEM16 with a confluency of 40-60% each. Protein expressed in insect cells was either purified from 7 l of Sf9 cells or 2.5 l of Sf21 suspension culture. Purification was performed as described before for small scale, except that the SBP- and Myc-tag used for purification was cleaved off by HRV-3C enzyme and the constructs lacked the Venus-YFP tag used in the screening.

The cleaved protein was concentrated (Amicon, 100 kDa Cut-off) and injected to a Superdex-200 column that was previously equilibrated with buffer C containing 3 mM $CaCl_2$ and 0.025% DDMβ. Peak fractions were pooled and concentrated. Crystallization was initially screened in a variety of crystallization screens in sitting drops with a crystallization robot at 100 nl volumes with the help of the protein crystallization center (PCC) at the Department of Biochemistry. Crystallization conditions were usually refined manually in 1 µl volume in sitting drops.

S. cerevisiae expressing the protein of interest was harvested by centrifugation and resuspended in buffer A containing 0.5 mM $CaCl_2$, protease inhibitors, DNaseI and 1 mM $MgCl_2$ and lysed in a custom-made pressure-based cell disruptor at 40 kpsi. Cell debris was removed by low-spin centrifugation. Membranes were harvested by ultracentrifugation with a 45 TI rotor (Beckmann) at 40,000 rpm for 1.5 h. All steps were carried out on ice or at 4 °C. Protein was extracted in buffer A containing 0.5 mM $CaCl_2$, 1% DDMβ and protease inhibitors for 1.5 h. Insoluble parts were removed by centrifugation for 30 min at 40,000 rpm with a 45 TI rotor (Beckmann). After addition of 15 mM Imidazole the protein was bound in batch to NiNTA for 1.5 h, washed with buffer B (10 mM Hepes 7.6, 150 mM NaCl, 5 % glycerol, 0.025% DDMβ) containing 5 mM $CaCl_2$ and 50 mM Imidazole and eluted in buffer B containing 5 mM $CaCl_2$ and 400 mM Imidazole. The eluted fraction was cleaved with HRV 3C-protease for 2 h and dialyzed against buffer B containing 5 mM $CaCl_2$. The GFP-His_{10} fragment was removed by binding to NiNTA resin, the flow-through was concentrated and applied to a Superdex 200 column (GE healthcare) equilibrated in buffer C containing 0.025% DDMβ and 3 mM $CaCl_2$. The peak fraction was concentrated and crystallization was initially screened in a variety of crystallization screens with a robot in 100 nl volumes (with the help of the PCC). Crystallization conditions were refinement manually as described before. For crystallization nhTMEM16 was concentrated to 8–14 mg/ml. A 35 l fermentation culture harvested at an OD_{600} of 4.5 typically yielded about 5 mg of pure nhTMEM16.

4.8. Protein purification for the scramblase assay

For reconstitution into liposomes the protein of interest containing an SBP-tag was either purified from *S. cerevisiae* or HEK tsA201 cells with similar results. HEK tsA201 cells or membranes of *S. cerevisiae* expressing the respective protein were collected and treated with buffer A containing 5 mM EDTA, 5% glycerol, protease inhibitors and 2% DDMβ. Cell debris was removed by centrifugation. The supernatant was incubated with Streptavidin resin (Pierce Streptavidin plus UltraLink Resin) for 1.5 h and washed with buffer B. Protein was eluted with buffer B containing 2 mM Biotin. Initially, the protein was cleaved to remove the purification tag and subjected to size-exclusion chromatography on a Superdex 200 column prior to reconstitution. In later stages, the protein was reconstituted after affinity purification at 1 mg ml^{-1} with very similar results. For reconstitution, an 18 l fermentation culture of *S. cerevisiae* typically yielded 400 µg of nhTMEM16. All buffers used during reconstitution were made with calcium free water (Merck Milipore) and chemicals extra low in calcium.

4.9. Thermal stability

Several additives were probed for their ability to stabilize gzeTMEM16, edeTMEM16 and nhTMEM16 in a modified thermal stability assay [323]. The protein of interest was purified as described, the purification tag was cut off and the protein was run on a size exclusion column to remove soluble aggregates. For assaying its thermal stability, purified protein was mixed with additives and incubated for 10 min at different temperatures (e.g. 4 °C as control, 20 °C, 30 °C, 40 °C, 50 °C and 60 °C). The emerging precipitate was subsequently removed by centrifugation and the supernatant was subjected to fluorescent size exclusion chromatography (GF450, Agilent Zorbax) and detected by tryptophan fluorescence (excitation 280 nm, emission 320-350 nm).

4.10. Crystallization and structure determination

Initially, gzeTMEM16 was concentrated to 2-8 mg ml^{-1}, which depended on the amount of protein that could be obtained from either HEK tsA201, Sf9, Sf21 or *S.cerevisiae* expression cultures. After broad screening of several hundreds of conditions promising crystals were identified in only few conditions condition. In later stages of this work, after identification of stabilizing conditions for purification, the protein yield was no longer limiting and crystals have been identified in several conditions. After cryo-protection crystals were investigated at the PXI beamline of the SLS. Crystals diffracted to 5 Å.

For crystallization of nhTMEM16, a similar approach as described for gzeTMEM16 was successful and has allowed the identification of many initial crystals. The initial low resolution of two particular crystal forms was improved by screening crystallization additives including detergents, lipids and many others. hTMEM16 (containing two additional residues on the N-terminus from the protease cleavage site) was crystallized in sitting drops at 4 °C. Prior to crystallization 0.2% n-Undecyl-α-D-Maltopyranoside (Anatrace), 50 µg ml^{-1} yeast polar lipid extract (solubilized in 1% DDMβ, Avanti Polar Lipids) and 2% 1,2,3-Heptanetriol were added to the protein (crystallization additives). Crystals were prepared by mixing protein at a concentration of 8-14 mg ml^{-1} in a 1:1 ratio with reservoir containing either 100 mM Capso pH 9.4, 100 mM $MgCl_2$, 100 mM NaCl and 21-23% PEG400 (CF1) or 50 mM Hepes pH 7.4, 100 mM Ammonium Sulfate, 21-23% PEG400 (CF2). Crystals were harvested after 2–3 weeks (CF1) or 1 week (CF2), cryo-protected by increasing the PEG400 concentration to 36% and flash-frozen in liquid propane. Cryo- protected crystals were measured at the X06SA beamline at the Swiss Light Source (SLS) of the Paul Scherrer Institute (PSI) on a PILATUS 6M detector (Dectris). Indexing, integration and scaling of the data was done using XDS [272] and further processing with CCP4 programs [324]. Both crystal forms were of space group $P2_12_12_1$. The structure of the nhTMEM16 (CF2) was determined by the single wavelength anomalous dispersion (SAD) method with data collected from crystals containing a seleno- methionine derivatized protein. Identification of the Se-sites was achieved with SHELX C and D [273] and these were refined in SHARP [325]. Initial phases at low resolution were improved by solvent flattening and 2-fold NCS averaging in DM [326]. A coarse model was built in O [327] and used as search model in molecular replacement in CF1 using PHASER [328]. Phases could then be extended

to 3.3 Å by NCS and cross-crystal averaging with DM [329]. Models were built with O and COOT [279]. The correct register of the protein was confirmed with the help of 13 methionine positions defined in the Se-Met dataset and from sulfur anomalous data collected for mutants F612M and L624M where methionine residues were inserted in regions of the protein that lack this amino acid. The structure was initially refined maintaining strict 2-fold NCS constraints in CNS [330]. In later stages, the strict constraints were loosened and restraint individual B-factors and TLS parameters were refined in PHENIX [280]. R and R_{free} were monitored throughout. R_{free} was calculated by selecting 5% of the reflection data that were omitted in refinement. The final model (CF1) contains 654 out of 735 residues per subunit, has R/R_{free} values of 23.7% and 28.2%, good geometry and no outliers in the Ramachandran plot (Extended Data Table 1). Regions not defined in the electron density include residues 1-18, 130-140, 465-482, 586-593, 657-659, 685-691 and 720-735. The structure of nhTMEM16 in CF2 was refined in PHENIX as described for CF1. Both structures show very similar conformations. Ca^{2+} positions were identified from data collected at 1.95 Å to improve the anomalous scattering of the bound ions and included in the refinement (Extended Data Table 1).

4.11. Liposome preparation and scrambling assay

Liposomes were prepared as 3:1 mixture of *E.coli* polar lipids/egg PC (Avanti Polar Lipids). For scramblase assays lipids were supplemented with either 0.5% NBD-PE or NBD-PS (Avanti Polar Lipids). For control experiments approximately 20 µM NBD-dextran (prepared following manufacturers instruction, Life technologies) was added during liposome preparation instead of NBD labeled lipids. Liposomes were suspended in buffer D (20 mM Hepes pH 7.4, 300 mM KCl) containing either 2 mM EGTA (for Ca^{2+}-free conditions), or 2 mM EGTA and the concentration of Ca^{2+} or other divalent cations (made from the respective nitrate salts) as calculated by MAXCHELATOR (maxchelator.stanford.edu/CaMgATPEGTA-TS.htm) to reach the indicated free divalent ion concentration. Liposomes were prepared as described [285, 286]. Briefly, liposomes were subjected to three freeze-thaw cycles, subsequently extruded through a 400 nm polycarbonate filter (Avestin) and destabilized with Triton-X-100. Purified protein (5 µg per mg lipid) was added and detergent was removed by stepwise addition of SM-2 adsorbent biobeads (BioRad). Proteoliposomes were formed at 4 °C under gentle agitation, incubated for 40 h, collected by ultracentrifugation, resuspended in buffer D containing the above-mentioned concentrations of EGTA and divalent ions at a lipid concentration of 20 mg ml^{-1}, flash frozen in liquid N_2 and stored at –80 °C. All buffers were prepared with calcium-free water (Merck Milipore) using highly pure chemicals low in calcium. The scramblase assay was performed similarly as previously described [170]. After three freeze-thaw cycles and extrusion (400 nm filter), 20 µl of proteo-liposome suspension was diluted in 2 ml buffer D (with HEPES pH 7.4 concentration increased to 60 mM) containing either 2 mM EGTA, or 2mM EGTA and the calculated concentrations of divalent ions, in a stirred cuvette at 23 °C. Sodium dithionite was added after 1 min to a final concentration of 30 mM unless stated otherwise and fluorescence decay was recorded on a

Fluoromax-4 spectrofluorimeter (Horiba, excitation 470 nm, emission 530 nm). For analysis the fluorescence intensity was normalized to F/F_{max}.

5. Curriculum Vitae

CURRICULUM VITAE

BRUNNER Janine Denise

Date of Birth	01.10.1980
Native place	Ebnat- Kappel SG
Nationality	Swiss
Adress	Dorflindenstrasse 6, 8050 Zürich
E-mail	j.brunner@bioc.uzh.ch

Education

April 2010- July 2015 **PhD thesis in the group of Prof. Raimund Dutzler**

Department of Biochemistry, University of Zurich, Switzerland

Title: Insight into Ca^{2+} dependent lipid scrambling from the crystal structure of a TMEM16 family member

Member in the PhD program of the University and ETH of Zurich 'Biomolecular structure and mechanism'

2008 **Master thesis in Human Biology**

Group of Prof. Michael Arand

Institute of Pharmacology and Toxicology, University of Zurich, Switzerland

Title: Biochemical characterization of PEG1/MEST, a potential epoxide hydrolase

2005 **Bachelor in Biology**

University of Zurich, Switzerland

2002- 2008 **Study of Biology**

University of Zurich, Switzerland

2001	**Matura Typus C** (mathematisch- naturwissenschaftlich)
	Kantonsschule in Oerlikon (KSOe), Zurich, Switzerland

Publication List

2014	X-ray structure of a calcium-activated TMEM16 lipid scramblase
	Brunner JD, Lim NK, Schenck S, Duerst A, Dutzler R
	Nature. 2014 Dec 11. 516(7530). 207-12

List of Talks

2015	
New and Notable	Principles of Lipid Scrambling: Structural Insight from a TMEM16 Family
invited speaker	Member
	10th European Biophysics Congress (EBSA 2015), Dresden, Germany
2015	
New and Notable	Principles of Lipid Scrambling: Structural Insights from a TMEM16 Family Member
	Biophysical Society 59th Annual Meeting, Baltimore, Maryland, USA
2014	Structural Studies of Anoctamins, a new Class of Calcium Activated Chloride Channels (CaCC)
	Research seminar, University of Zurich, Switzerland

Work Experience

May- November 2009	Scientific employee in the group of Prof. Michael Arand Institute of Pharmacology and Toxicology, University of Zurich, Switzerland
May– July 2009	Scientific employee Institute of Integrative Biology, ETH Zurich, Switzerland
December 2008- May 2009	Scientific employee Institute of Environmental Sciences, University of Zurich, Switzerland
July- September 2008	Scientific employee in the group of Prof. Michael Arand Institute of Pharmacology and Toxicology, University of Zurich, Switzerland
2005- 2006	Job as a paragliding instructor to raise funds for my studies
2001- 2002	Job to raise funds for my studies

6. Bibliograhpy

1. Arreola, J., J.E. Melvin, and T. Begenisich, *Activation of calcium-dependent chloride channels in rat parotid acinar cells.* The Journal of General Physiology, 1996. **108**(1): p. 35-47.
2. Romanenko, V.G., et al., *Tmem16A Encodes the Ca2+-activated Cl− Channel in Mouse Submandibular Salivary Gland Acinar Cells.* Journal of Biological Chemistry, 2010. **285**(17): p. 12990-13001.
3. Jang, W., et al., *The Anoctamin Family Channel Subdued Mediates Thermal Nociception in Drosophila.* Journal of Biological Chemistry, 2015. **290**(4): p. 2521-2528.
4. Caputo, A., et al., *TMEM16A, A Membrane Protein Associated with Calcium-Dependent Chloride Channel Activity.* Science, 2008. **322**(5901): p. 590-594.
5. Schroeder, B.C., et al., *Expression Cloning of TMEM16A as a Calcium-Activated Chloride Channel Subunit.* Cell, 2008. **134**(6): p. 1019-1029.
6. Yang, Y.D., et al., *TMEM16A confers receptor-activated calcium-dependent chloride conductance.* Nature, 2008. **455**(7217): p. 1210-1215.
7. Pifferi, S., V. Cenedese, and A. Menini, *Anoctamin 2/TMEM16B: a calcium-activated chloride channel in olfactory transduction.* Experimental Physiology, 2012. **97**(2): p. 193-199.
8. Billig, G.M., et al., *Ca2+-activated Cl- currents are dispensable for olfaction.* Nat Neurosci, 2011. **14**(6): p. 763-769.
9. Yang, H., et al., *TMEM16F Forms a Ca(2+)-Activated Cation Channel Required for Lipid Scrambling in Platelets during Blood Coagulation.* Cell, 2012. **151**(1): p. 111-122.
10. Suzuki, J., et al., *Calcium-dependent phospholipid scrambling by TMEM16F.* Nature, 2010. **468**(7325): p. 834-838.
11. Das, S., et al., *Topology of NGEP, a Prostate Specific Cell:Cell Junction Protein Widely Expressed in Many Cancers of Different Grade Level.* Cancer research, 2008. **68**(15): p. 6306-6312.
12. Yu, K., et al., *Explaining Calcium-Dependent Gating of Anoctamin-1 Chloride Channels Requires a Revised Topology.* Circulation Research, 2012. **110**(7): p. 990-999.
13. Dekkers DW, C.P., Bevers EM, Zwaal RF., *Comparison between Ca2+-induced scrambling of various fluorescently labelled lipid analogues in red blood cells.* Biochem J, 2002. **362(Pt 3)**: p. 741-7.
14. Zwaal, R.F.A. and A.J. Schroit, *Pathophysiologic Implications of Membrane Phospholipid Asymmetry in Blood Cells*. Vol. 89. 1997. 1121-1132.
15. Pedemonte, N. and L.J.V. Galietta, *Structure and Function of TMEM16 Proteins (Anoctamins)*. Vol. 94. 2014. 419-459.
16. Singer SJ, N.G., *The fluid mosaic model of the structure of cell membranes.* Science, 1972. **175**((4023)): p. 720-31.
17. Lemmon, M.A., *Membrane recognition by phospholipid-binding domains.* Nat Rev Mol Cell Biol, 2008. **9**(2): p. 99-111.
18. Schick, P.K., K.B. Kurica, and G.K. Chacko, *Location of phosphatidylethanolamine and phosphatidylserine in the human platelet plasma membrane.* The Journal of Clinical Investigation, 1976. **57**(5): p. 1221-1226.
19. Higgins, J.A. and W.H. Evans, *Transverse organization of phospholipids across the bilayer of plasma-membrane subfractions of rat hepatocytes.* Biochemical Journal, 1978. **174**(2): p. 563-567.
20. Devaux, P.F. and R. Morris, *Transmembrane Asymmetry and Lateral Domains in Biological Membranes.* Traffic, 2004. **5**(4): p. 241-246.

21. Boumann, H.A., et al., *Depletion of Phosphatidylcholine in Yeast Induces Shortening and Increased Saturation of the Lipid Acyl Chains: Evidence for Regulation of Intrinsic Membrane Curvature in a Eukaryote.* Molecular Biology of the Cell, 2006. **17**(2): p. 1006-1017.
22. Sprong, H., P. van der Sluijs, and G. van Meer, *How proteins move lipids and lipids move proteins.* Nat Rev Mol Cell Biol, 2001. **2**(7): p. 504-513.
23. McMahon, H.T. and E. Boucrot, *Membrane curvature at a glance.* Journal of Cell Science, 2015. **128**(6): p. 1065-1070.
24. Leventis, P.A. and S. Grinstein, *The Distribution and Function of Phosphatidylserine in Cellular Membranes.* Annual Review of Biophysics, 2010. **39**(1): p. 407-427.
25. Magalhaes, M.A.O. and M. Glogauer, *Pivotal Advance: Phospholipids determine net membrane surface charge resulting in differential localization of active Rac1 and Rac2.* Journal of Leukocyte Biology, 2010. **87**(4): p. 545-555.
26. Bach R., G.R., Nemerson Y., *Factor VII binding to tissue factor in reconstituted phospholipid vesicles: induction of cooperativity by phosphatidylserine.* Biochemistry., 1986. **25**((14)): p. 4007-20.
27. Majumder, R., et al., *A phosphatidylserine binding site in factor Va C1 domain regulates both assembly and activity of the prothrombinase complex*. Vol. 112. 2008. 2795-2802.
28. Andree HA, N.Y., *Tissue factor: regulation of activity by flow and phospholipid surfaces.* Blood Coagul Fibrinolysis, 1995. **6**((3)): p. 189-97.
29. Bevers, E.M., et al., *Generation of Prothrombin-Converting Activity and the Exposure of Phosphatidylserine at the Outer Surface of Platelets.* European Journal of Biochemistry, 1982. **122**(2): p. 429-436.
30. Ow, Y.-L.P., et al., *Cytochrome c: functions beyond respiration.* Nat Rev Mol Cell Biol, 2008. **9**(7): p. 532-542.
31. Luthi, A.U. and S.J. Martin, *The CASBAH: a searchable database of caspase substrates.* Cell Death Differ, 2007. **14**(4): p. 641-650.
32. Martin, S.J. and D.R. Green, *Protease activation during apoptosis: Death by a thousand cuts?* Cell, 1995. **82**(3): p. 349-352.
33. Martin, S.J., et al., *Phosphatidylserine Externalization during CD95-induced Apoptosis of Cells and Cytoplasts Requires ICE/CED-3 Protease Activity.* Journal of Biological Chemistry, 1996. **271**(46): p. 28753-28756.
34. Fadok, V.A., et al., *Exposure of phosphatidylserine on the surface of apoptotic lymphocytes triggers specific recognition and removal by macrophages.* The Journal of Immunology, 1992. **148**(7): p. 2207-16.
35. Yoshida, H., et al., *Phosphatidylserine-dependent engulfment by macrophages of nuclei from erythroid precursor cells.* Nature, 2005. **437**(7059): p. 754-758.
36. A.P. Harrison, R. and B.M. Gadella, *Bicarbonate-induced membrane processing in sperm capacitation.* Theriogenology, 2005. **63**(2): p. 342-351.
37. van den Eijnde, S.M., et al., *Transient expression of phosphatidylserine at cell-cell contact areas is required for myotube formation.* Journal of Cell Science, 2001. **114**(20): p. 3631-3642.
38. Hochreiter-Hufford, A.E., et al., *Phosphatidylserine receptor BAI1 and apoptotic cells as new promoters of myoblast fusion.* Nature, 2013. **497**(7448): p. 263-267.
39. Czuczman M. A., F.R., van Rijn J. M., Canadien V., Osborne S., Muise A. M., Kuchroo V. K. Higgins D. E. & Brumell J. H., *Listeria monocytogenens exploits efferocytosis to promote cell-to-cell spread.* Nature, 2014. **509**: p. 230-234.
40. Feng, D., et al., *Cellular Internalization of Exosomes Occurs Through Phagocytosis.* Traffic, 2010. **11**(5): p. 675-687.
41. Miyanishi, M., et al., *Identification of Tim4 as a phosphatidylserine receptor.* Nature, 2007. **450**(7168): p. 435-439.
42. Alberti-Segui C., G.K.R., Higgins D. E., *Differential function of Listeria monocytogenes listeriolysin O and phospholipases C in vacuolar dissolution following cell-to-cell spread.* Cell Microbiol, 2007. **9**: p. 179-195.

43. Gedde M. M., H.E.E., Tilnez L. G. & Portnoz D. A., *Role of listeriolysin O in cell-to-cell spread of Listeria monocytogenes.* Infect Immun, 2000. **68**: p. 999-1003.
44. Hamon M. A., R.D., Stavru F. & Cossart P., *Listeriolysin O: the Swiss army knife of Listeria.* Trends Microbiol, 2012. **20**: p. 360-368.
45. Föller, M., et al., *Induction of Suicidal Erythrocyte Death by Listeriolysin from <italic>Listeria monocytogenes</italic>.* Cellular Physiology and Biochemistry, 2007. **20**(6): p. 1051-1060.
46. D., F.B.X., *The ins and outs of phospholipid asymmetry in the plasma membrane: roles in health and disease.* Crit Rev Biochem Mol Biol, 2009. **44**: p. 264-277.
47. Bevers EM, T.R., Senden JM, Comfurius P, Zwaal RF, *Exposure of endogenous phosphatidylserine at the outer surface of stimulated platelets is reversed by restoration of aminophospholipid translocase activity.* Biochemistry, 1989. **28**((6)): p. 2382-7.
48. Zhou, X. and T.R. Graham, *Reconstitution of phospholipid translocase activity with purified Drs2p, a type-IV P-type ATPase from budding yeast.* Proceedings of the National Academy of Sciences, 2009. **106**(39): p. 16586-16591.
49. Paterson, J.K., et al., *Lipid Specific Activation of the Murine P4-ATPase Atp8a1 (ATPase II)†.* Biochemistry, 2006. **45**(16): p. 5367-5376.
50. Coleman, J.A., M.C.M. Kwok, and R.S. Molday, *Localization, Purification, and Functional Reconstitution of the P4-ATPase Atp8a2, a Phosphatidylserine Flippase in Photoreceptor Disc Membranes.* Journal of Biological Chemistry, 2009. **284**(47): p. 32670-32679.
51. Pomorski, T., et al., *Drs2p-related P-type ATPases Dnf1p and Dnf2p Are Required for Phospholipid Translocation across the Yeast Plasma Membrane and Serve a Role in Endocytosis.* Molecular Biology of the Cell, 2003. **14**(3): p. 1240-1254.
52. Baldridge, R.D., P. Xu, and T.R. Graham, *Type IV P-type ATPases Distinguish Mono- versus Diacyl Phosphatidylserine Using a Cytofacial Exit Gate in the Membrane Domain.* Journal of Biological Chemistry, 2013. **288**(27): p. 19516-19527.
53. Takatsu, H., et al., *Phospholipid Flippase Activities and Substrate Specificities of Human Type IV P-type ATPases Localized to the Plasma Membrane.* Journal of Biological Chemistry, 2014. **289**(48): p. 33543-33556.
54. Groen, A., et al., *Complementary Functions of the Flippase ATP8B1 and the Floppase ABCB4 in Maintaining Canalicular Membrane Integrity.* Gastroenterology, 2011. **141**(5): p. 1927-1937.e4.
55. Zachowski, A., J.-P. Henry, and P.F. Devaux, *Control of transmembrane lipid asymmetry in chromaffin granules by an ATP-dependent protein.* Nature, 1989. **340**(6228): p. 75-76.
56. Seigneuret, M. and P.F. Devaux, *ATP-dependent asymmetric distribution of spin-labeled phospholipids in the erythrocyte membrane: relation to shape changes.* Proceedings of the National Academy of Sciences, 1984. **81**(12): p. 3751-3755.
57. Ding, J., et al., *Identification and Functional Expression of Four Isoforms of ATPase II, the Putative Aminophospholipid Translocase: EFFECT OF ISOFORM VARIATION ON THE ATPase ACTIVITY AND PHOSPHOLIPID SPECIFICITY.* Journal of Biological Chemistry, 2000. **275**(30): p. 23378-23386.
58. Mouro, I., et al., *Cloning, Expression, and Chromosomal Mapping of a Human ATPase II Gene, Member of the Third Subfamily of P-Type ATPases and Orthologous to the Presumed Bovine and Murine Aminophospholipid Translocase.* Biochemical and Biophysical Research Communications, 1999. **257**(2): p. 333-339.
59. Quazi, F., S. Lenevich, and R.S. Molday, *ABCA4 is an N-retinylidene-phosphatidylethanolamine and phosphatidylethanolamine importer.* Nat Commun, 2012. **3**: p. 925.
60. Smriti, et al., *ABC transporters Cdr1p, Cdr2p and Cdr3p of a human pathogen Candida albicans are general phospholipid translocators.* Yeast, 2002. **19**(4): p. 303-318.

61. Borst, P., N. Zelcer, and A. van Helvoort, *ABC transporters in lipid transport.* Biochimica et Biophysica Acta (BBA) - Molecular and Cell Biology of Lipids, 2000. **1486**(1): p. 128-144.
62. Sune A, B.-B.P., Bienvenüe A, Fellmann P, Devaux PF, *Selective outside-inside translocation of aminophospholipids in human platelets.* Biochemistry, 1987. **26**((11)): p. 2972-8.
63. Zachowski, A., et al., *Phospholipid outside-inside translocation in lymphocyte plasma membranes is a protein-mediated phenomenon.* Biochimica et Biophysica Acta (BBA) - Biomembranes, 1987. **897**(1): p. 197-200.
64. Julien, M., J.-F. Tournier, and J.-F. Tocanne, *Differences in the Transbilayer and Lateral Motions of Fluorescent Analogs of Phosphatidylcholine and Phosphatidylethanolamine in the Apical Plasma Membrane of Bovine Aortic Endothelial Cells.* Experimental Cell Research, 1993. **208**(2): p. 387-397.
65. Pomorski, T., et al., *Transbilayer movement of fluorescent and spin-labeled phospholipids in the plasma membrane of human fibroblasts: a quantitative approach.* Journal of Cell Science, 1996. **109**(3): p. 687-698.
66. Cribier, S., J. Sainte-Marie, and P.F. Devaux, *Quantitative comparison between aminophospholipid translocase activity in human erythrocytes and in K562 cells.* Biochimica et Biophysica Acta (BBA) - Biomembranes, 1993. **1148**(1): p. 85-90.
67. Muller, P., et al., *Transverse movement of spin-labeled phospholipids in the plasma membrane of a hepatocytic cell line (HepG2): Implications for biliary lipid secretion.* Hepatology, 1996. **24**(6): p. 1497-1503.
68. Müller K, P.T., Müller P, Zachowski A, Herrmann A, *Protein-dependent translocation of aminophospholipids and asymmetric transbilayer distribution of phospholipids in the plasma membrane of ram sperm cells.* Biochemistry, 1994. **33**((33)): p. 9968-74.
69. Zachowski A, G.-T.Y., *Phospholipid transverse diffusion in synaptosomes: evidence for the involvement of the aminophospholipid translocase.* J. Neurochem., 1990. **55**((4)): p. 1352-6.
70. Bryde, S., et al., *CDC50 Proteins Are Critical Components of the Human Class-1 P4-ATPase Transport Machinery.* Journal of Biological Chemistry, 2010. **285**(52): p. 40562-40572.
71. van der Velden, L.M., et al., *Heteromeric Interactions Required for Abundance and Subcellular Localization of Human CDC50 Proteins and Class 1 P4-ATPases.* Journal of Biological Chemistry, 2010. **285**(51): p. 40088-40096.
72. Lenoir, G., et al., *Cdc50p Plays a Vital Role in the ATPase Reaction Cycle of the Putative Aminophospholipid Transporter Drs2p.* Journal of Biological Chemistry, 2009. **284**(27): p. 17956-17967.
73. Olesen, C., et al., *The structural basis of calcium transport by the calcium pump.* Nature, 2007. **450**(7172): p. 1036-1042.
74. Dupont Y, L.J., *Transient kinetics of sarcoplasmic reticulum CA2+ + Mg2+ ATPase studied by fluorescence.* Nature, 1978. **273(5661)**: p. 396-8.
75. Takisawa H, M.M., *Occluded bound calcium on the phosphorylated sarcoplasmic transport ATPase.* Nature, 1981. **290(5803)**: p. 271-3.
76. MacLennan DH, B.C., Korczak B, Green NM., *Amino-acid sequence of a Ca2+ + Mg2+-dependent ATPase from rabbit muscle sarcoplasmic reticulum, deduced from its complementary DNA sequence.* Nature, 1985. **316(6030)**: p. 696-700.
77. Kawakami K, N.S., Noda M, Takahashi H, Ohta T, Kawamura M, Nojima H, Nagano K, Hirose T, Inayama S, et al., *Primary structure of the alpha-subunit of Torpedo californica (Na+ + K+)ATPase deduced from cDNA sequence.* Nature, 1985. **316(6030)**: p. 733-6.
78. Reyes, N. and D.C. Gadsby, *Ion permeation through the Na+,K+-ATPase.* Nature, 2006. **443**(7110): p. 470-474.
79. Morth, J.P., et al., *Crystal structure of the sodium-potassium pump.* Nature, 2007. **450**(7172): p. 1043-1049.

80. Kanai, R., et al., *Crystal structure of a Na+-bound Na+,K+-ATPase preceding the E1P state.* Nature, 2013. **502**(7470): p. 201-206.
81. van Veen, H.W., et al., *A bacterial antibiotic-resistance gene that complements the human multidrug-resistance P-glycoprotein gene.* Nature, 1998. **391**(6664): p. 291-295.
82. Gerlach, J.H., et al., *Homology between P-glycoprotein and a bacterial haemolysin transport protein suggests a model for multidrug resistance.* Nature, 1986. **324**(6096): p. 485-489.
83. Hyde, S.C., et al., *Structural model of ATP-binding proteing associated with cystic fibrosis, multidrug resistance and bacterial transport.* Nature, 1990. **346**(6282): p. 362-365.
84. Hohl, M., et al., *Crystal structure of a heterodimeric ABC transporter in its inward-facing conformation.* Nat Struct Mol Biol, 2012. **19**(4): p. 395-402.
85. Parcej, D. and R. Tampe, *ABC proteins in antigen translocation and viral inhibition.* Nat Chem Biol, 2010. **6**(8): p. 572-580.
86. Higgins, C.F., *Multiple molecular mechanisms for multidrug resistance transporters.* Nature, 2007. **446**(7137): p. 749-757.
87. van den Brûle S, M.A., Fleming AJ, Smart CC., *The ABC transporter SpTUR2 confers resistance to the antifungal diterpene sclareol.* Plant J, 2002. **30**((6)): p. 649-62.
88. Rommens JM, I.M., Kerem B, Drumm ML, Melmer G, Dean M, Rozmahel R, Cole JL, Kennedy D, Hidaka N, et al, *Identification of the cystic fibrosis gene: chromosome walking and jumping.* Science, 1989. **245**((4922)): p. 1059-65.
89. Riordan JR, R.J., Kerem B, Alon N, Rozmahel R, Grzelczak Z, Zielenski J, Lok S, Plavsic N, Chou JL, et al., *Identification of the cystic fibrosis gene: cloning and characterization of complementary DNA.* Science, 1989. **245**((4922)): p. 1066-73.
90. Gadsby, D.C., P. Vergani, and L. Csanady, *The ABC protein turned chloride channel whose failure causes cystic fibrosis.* Nature, 2006. **440**(7083): p. 477-483.
91. Bitbol, M., et al., *Ion regulation of phosphatidylserine and phosphatidylethanolamine outside-inside translocation in human erythrocytes.* Biochimica et Biophysica Acta (BBA) - Biomembranes, 1987. **904**(2): p. 268-282.
92. Segawa, K., J. Suzuki, and S. Nagata, *Flippases and scramblases in the plasma membrane.* Cell Cycle, 2014. **13**(19): p. 2990-2991.
93. Segawa, K., et al., *Caspase-mediated cleavage of phospholipid flippase for apoptotic phosphatidylserine exposure.* Science, 2014. **344**(6188): p. 1164-1168.
94. Backer, J.M. and E.A. Dawidowicz, *Reconstitution of a phospholipid flippase from rat liver microsomes.* Nature, 1987. **327**(6120): p. 341-343.
95. Buton, X., et al., *Ultrafast Glycerophospholipid-selective Transbilayer Motion Mediated by a Protein in the Endoplasmic Reticulum Membrane.* Journal of Biological Chemistry, 1996. **271**(12): p. 6651-6657.
96. Sanyal, S. and A.K. Menon, *Flipping Lipids: Why an' What's the Reason for?* ACS Chemical Biology, 2009. **4**(11): p. 895-909.
97. Vidugiriene, J. and A.K. Menon, *The GPI anchor of cell-surface proteins is synthesized on the cytoplasmic face of the endoplasmic reticulum.* The Journal of Cell Biology, 1994. **127**(2): p. 333-341.
98. Sanyal, S., C.G. Frank, and A.K. Menon, *Distinct Flippases Translocate Glycerophospholipids and Oligosaccharide Diphosphate Dolichols across the Endoplasmic Reticulum†.* Biochemistry, 2008. **47**(30): p. 7937-7946.
99. Menon, A.K., W.E. Watkins Iii, and S. Hrafnsdóttir, *Specific proteins are required to translocate phosphatidylcholine bidirectionally across the endoplasmic reticulum.* Current Biology, 2000. **10**(5): p. 241-252.
100. Helenius, J., et al., *Translocation of lipid-linked oligosaccharides across the ER membrane requires Rft1 protein.* Nature, 2002. **415**(6870): p. 447-450.

101. Haselbeck, A. and W. Tanner, *Dolichyl phosphate-mediated mannosyl transfer through liposomal membranes.* Proceedings of the National Academy of Sciences, 1982. **79**(5): p. 1520-1524.
102. Frank, C.G., et al., *Does Rft1 flip an N-glycan lipid precursor?* Nature, 2008. **454**(7204): p. E3-E4.
103. Rush, J.S., et al., *Suppression of Rft1 Expression Does Not Impair the Transbilayer Movement of Man5GlcNAc2-P-P-Dolichol in Sealed Microsomes from Yeast.* Journal of Biological Chemistry, 2009. **284**(30): p. 19835-19842.
104. Zimmerman, J.W. and P.W. Robbins, *The hydrophobic domain of dolichyl-phosphate-mannose synthase is not essential for enzyme activity or growth in Saccharomyces cerevisiae.* Journal of Biological Chemistry, 1993. **268**(22): p. 16746-16753.
105. Williamson, P., et al., *Phospholipid Scramblase Activation Pathways in Lymphocytes†.* Biochemistry, 2001. **40**(27): p. 8065-8072.
106. Suzuki, J., et al., *Xk-Related Protein 8 and CED-8 Promote Phosphatidylserine Exposure in Apoptotic Cells.* Science, 2013. **341**(6144): p. 403-406.
107. Suzuki, J., E. Imanishi, and S. Nagata, *Exposure of Phosphatidylserine by Xk-related Protein Family Members during Apoptosis.* Journal of Biological Chemistry, 2014. **289**(44): p. 30257-30267.
108. Comfurius, P., et al., *Reconstitution of Phospholipid Scramblase Activity from Human Blood Platelets.* Biochemistry, 1996. **35**(24): p. 7631-7634.
109. Henseleit, U., G. Plasa, and C. Haest, *Effects of divalent cations on lipid flip-flop in the human erythrocyte membrane.* Biochimica et Biophysica Acta (BBA) - Biomembranes, 1990. **1029**(1): p. 127-135.
110. Dekkers DW, C.P., Bevers EM, Zwaal RF, *Comparison between Ca2+-induced scrambling of various fluorescently labelled lipid analogues in red blood cells.* Biochem J, 2002. **362**((Pt 3)): p. 741-7.
111. Suzuki, J., et al., *Calcium-dependent Phospholipid Scramblase Activity of TMEM16 Protein Family Members.* Journal of Biological Chemistry, 2013. **288**(19): p. 13305-13316.
112. Suzuki, T., J. Suzuki, and S. Nagata, *Functional Swapping between Transmembrane Proteins TMEM16A and TMEM16F.* Journal of Biological Chemistry, 2014. **289**(11): p. 7438-7447.
113. Weiss HJ, V.W., Lages BA, Rogers J, *Isolated deficiency of platelet procoagulant activity.* Am J Med, 1979. **67**((2)): p. 206-13.
114. Sims, P.J., et al., *Assembly of the platelet prothrombinase complex is linked to vesiculation of the platelet plasma membrane. Studies in Scott syndrome: an isolated defect in platelet procoagulant activity.* Journal of Biological Chemistry, 1989. **264**(29): p. 17049-17057.
115. Bevers, E., et al., *Defective Ca(2+)-induced microvesiculation and deficient expression of procoagulant activity in erythrocytes from a patient with a bleeding disorder: a study of the red blood cells of Scott syndrome*. Vol. 79. 1992. 380-388.
116. Weiss, H.J., *Scott syndrome: a disorder of platelet coagulant activity.* Semin Hematol, 1994. **31**((4)): p. 312-9.
117. Toti, F., et al., *Scott syndrome, characterized by impaired transmembrane migration of procoagulant phosphatidylserine and hemorrhagic complications, is an inherited disorder*. Vol. 87. 1996. 1409-1415.
118. Zwaal, R.F.A., P. Comfurius, and E.M. Bevers, *Scott syndrome, a bleeding disorder caused by defective scrambling of membrane phospholipids.* Biochimica et Biophysica Acta (BBA) - Molecular and Cell Biology of Lipids, 2004. **1636**(2–3): p. 119-128.
119. Ehlen, H.W.A., et al., *Inactivation of anoctamin-6/Tmem16f, a regulator of phosphatidylserine scrambling in osteoblasts, leads to decreased mineral deposition in skeletal tissues.* Journal of Bone and Mineral Research, 2013. **28**(2): p. 246-259.

120. Wuthier RE, L.G., *Matrix vesicles: structure, composition, formation and function in calcification.* Front Biosci (Landmark Ed), 2011. **16**: p. 2812-902.
121. Zhou, Q., et al., *Molecular Cloning of Human Plasma Membrane Phospholipid Scramblase: A PROTEIN MEDIATING TRANSBILAYER MOVEMENT OF PLASMA MEMBRANE PHOSPHOLIPIDS.* Journal of Biological Chemistry, 1997. **272**(29): p. 18240-18244.
122. Bassé, F.o., et al., *Isolation of an Erythrocyte Membrane Protein that Mediates Ca2+-dependent Transbilayer Movement of Phospholipid.* Journal of Biological Chemistry, 1996. **271**(29): p. 17205-17210.
123. Zhou, Q., P.J. Sims, and T. Wiedmer, *Identity of a Conserved Motif in Phospholipid Scramblase That Is Required for Ca2+-Accelerated Transbilayer Movement of Membrane Phospholipids.* Biochemistry, 1998. **37**(8): p. 2356-2360.
124. Wiedmer, T., et al., *Identification of three new members of the phospholipid scramblase gene family.* Biochimica et Biophysica Acta (BBA) - Biomembranes, 2000. **1467**(1): p. 244-253.
125. Zhou, Q., et al., *Normal hemostasis but defective hematopoietic response to growth factors in mice deficient in phospholipid scramblase 1*. Vol. 99. 2002. 4030-4038.
126. Zhou, Q., P.J. Sims, and T. Wiedmer, *Expression of Proteins Controlling Transbilayer Movement of Plasma Membrane Phospholipids in the B Lymphocytes From a Patient With Scott Syndrome*. Vol. 92. 1998. 1707-1712.
127. Milenkovic, V., et al., *Evolution and functional divergence of the anoctamin family of membrane proteins.* BMC Evolutionary Biology, 2010. **10**(1): p. 319.
128. Barish, M.E., *A transient calcium-dependent chloride current in the immature Xenopus oocyte.* The Journal of Physiology, 1983. **342**(1): p. 309-325.
129. R., M., *A calcium-dependent transient outward current in Xenopus laevis oocytes.* Proc R Soc Lond B Biol Sci., 1982. **215**((1201)): p. 491-7.
130. Firestein, S. and G.M. Shepherd, *Interaction of anionic and cationic currents leads to a voltage dependence in the odor response of olfactory receptor neurons*. Vol. 73. 1995. 562-567.
131. Boucher, R.C., *Human airway ion transport. Part one.* American Journal of Respiratory and Critical Care Medicine, 1994. **150**(1): p. 271-281.
132. Wagner, J.A., et al., *Activation of chloride channels in normal and cystic fibrosis airway epithelial cells by multifunctional calcium/calmodulin-dependent protein kinase.* Nature, 1991. **349**(6312): p. 793-796.
133. Koumi, S., R. Sato, and T. Aramaki, *Characterization of the calcium-activated chloride channel in isolated guinea-pig hepatocytes.* The Journal of General Physiology, 1994. **104**(2): p. 357-373.
134. Reisert, J., et al., *The Ca-activated Cl Channel and its Control in Rat Olfactory Receptor Neurons.* The Journal of General Physiology, 2003. **122**(3): p. 349-364.
135. Kuruma, A. and H.C. Hartzell, *Bimodal Control of a Ca2+-Activated Cl− Channel by Different Ca2+ Signals.* The Journal of General Physiology, 2000. **115**(1): p. 59-80.
136. Qu, Z. and H.C. Hartzell, *Anion Permeation in Ca2+-Activated Cl− Channels.* The Journal of General Physiology, 2000. **116**(6): p. 825-844.
137. Evans, M.G. and A. Marty, *Calcium-dependent chloride currents in isolated cells from rat lacrimal glands.* The Journal of Physiology, 1986. **378**(1): p. 437-460.
138. Huang, F., et al., *Studies on expression and function of the TMEM16A calcium-activated chloride channel.* Proceedings of the National Academy of Sciences, 2009. **106**(50): p. 21413-21418.
139. Sievers, F. and D. Higgins, *Clustal Omega, Accurate Alignment of Very Large Numbers of Sequences*, in *Multiple Sequence Alignment Methods*, D.J. Russell, Editor. 2014, Humana Press. p. 105-116.
140. O'Driscoll, K.E., R.A. Pipe, and F.C. Britton, *Increased complexity of Tmem16a/Anoctamin 1 transcript alternative splicing.* BMC Molecular Biology, 2011. **12**: p. 35-35.

141. Ferrera, L., et al., *Regulation of TMEM16A Chloride Channel Properties by Alternative Splicing.* Journal of Biological Chemistry, 2009. **284**(48): p. 33360-33368.
142. Teardo, E., et al., *Alternative splicing-mediated targeting of the plant glutamate receptor AtGLR3.5 to mitochondria affects organelle morphology.* Plant Physiology, 2014: p. pp.114.242602v1-pp.114.242602.
143. Oberwinkler, J., et al., *Alternative Splicing Switches the Divalent Cation Selectivity of TRPM3 Channels.* Journal of Biological Chemistry, 2005. **280**(23): p. 22540-22548.
144. Putney, J.W., *Chapter Five - Alternative Forms of the Store-Operated Calcium Entry Mediators, STIM1 and Orai1*, in *Current Topics in Membranes*, P. Murali, Editor. 2013, Academic Press. p. 109-123.
145. Lipscombe, D., A. Andrade, and S.E. Allen, *Alternative splicing: Functional diversity among voltage-gated calcium channels and behavioral consequences().* Biochimica et biophysica acta, 2013. **1828**(7): p. 1522-1529.
146. Mittendorf, K.F., et al., *Tailoring of Membrane Proteins by Alternative Splicing of Pre-mRNA.* Biochemistry, 2012. **51**(28): p. 5541-5556.
147. Xiao, Q., et al., *Voltage- and calcium-dependent gating of TMEM16A/Ano1 chloride channels are physically coupled by the first intracellular loop.* Proceedings of the National Academy of Sciences, 2011. **108**(21): p. 8891-8896.
148. Cenedese, V., et al., *The voltage dependence of the TMEM16B/anoctamin2 calcium-activated chloride channel is modified by mutations in the first putative intracellular loop.* The Journal of General Physiology, 2012. **139**(4): p. 285-294.
149. Ponissery Saidu, S., et al., *Channel properties of the splicing isoforms of the olfactory calcium-activated chloride channel Anoctamin 2.* The Journal of General Physiology, 2013. **141**(6): p. 691-703.
150. Pifferi, S., M. Dibattista, and A. Menini, *TMEM16B induces chloride currents activated by calcium in mammalian cells.* Pflügers Archiv - European Journal of Physiology, 2009. **458**(6): p. 1023-1038.
151. Ryu, R.H., et al., *Cloning and heterologous expression of new xANO2 from Xenopus laevis.* Biochemical and Biophysical Research Communications, 2011. **408**(4): p. 559-565.
152. Stephan, A.B., et al., *ANO2 is the cilial calcium-activated chloride channel that may mediate olfactory amplification.* Proceedings of the National Academy of Sciences, 2009. **106**(28): p. 11776-11781.
153. Betto, G., et al., *Interactions between permeation and gating in the TMEM16B/anoctamin2 calcium-activated chloride channel.* The Journal of General Physiology, 2014. **143**(6): p. 703-718.
154. Scudieri P, S.E., Caci E, Ravazzolo R, Galietta LJ, *TMEM16A-TMEM16B chimaeras to investigate the structure-function relationship of calcium-activated chloride channels.* Biochem J, 2013. **452**((3)): p. 443-55.
155. Amjad, A., et al., *Conditional knockout of TMEM16A/anoctamin1 abolishes the calcium-activated chloride current in mouse vomeronasal sensory neurons.* The Journal of General Physiology, 2015.
156. Stöhr, H., et al., *TMEM16B, A Novel Protein with Calcium-Dependent Chloride Channel Activity, Associates with a Presynaptic Protein Complex in Photoreceptor Terminals.* The Journal of Neuroscience, 2009. **29**(21): p. 6809-6818.
157. Dauner, K., et al., *Expression patterns of anoctamin 1 and anoctamin 2 chloride channels in the mammalian nose.* Cell and Tissue Research, 2012. **347**(2): p. 327-341.
158. Tian, Y., R. Schreiber, and K. Kunzelmann, *Anoctamins are a family of Ca2+-activated Cl− channels.* Journal of Cell Science, 2012. **125**(21): p. 4991-4998.
159. Kunzelmann, K., et al., *Expression and function of epithelial anoctamins.* Experimental Physiology, 2012. **97**(2): p. 184-192.

160. Schreiber, R., et al., *Anoctamins support calcium-dependent chloride secretion by facilitating calcium signaling in adult mouse intestine.* Pflügers Archiv - European Journal of Physiology, 2014: p. 1-11.
161. Martins, J.R., et al., *Anoctamin 6 is an essential component of the outwardly rectifying chloride channel.* Proceedings of the National Academy of Sciences, 2011. **108**(44): p. 18168-18172.
162. Almaça, J., et al., *TMEM16 Proteins Produce Volume-regulated Chloride Currents That Are Reduced in Mice Lacking TMEM16A.* Journal of Biological Chemistry, 2009. **284**(42): p. 28571-28578.
163. Szteyn, K., et al., *Expression and Functional Significance of the Ca²⁺-Activated Cl⁻ Channel ANO6 in Dendritic Cells.* Cellular Physiology and Biochemistry, 2012. **30**(5): p. 1319-1332.
164. Kmit, A., et al., *Calcium-activated and apoptotic phospholipid scrambling induced by Ano6 can occur independently of Ano6 ion currents.* Cell Death Dis, 2013. **4**: p. e611.
165. Ousingsawat, J., et al., *Anoctamin-6 Controls Bone Mineralization by Activating the Calcium Transporter NCX1.* Journal of Biological Chemistry, 2015. **290**(10): p. 6270-6280.
166. Duran, C., et al., *ANOs 3–7 in the anoctamin/Tmem16 Cl− channel family are intracellular proteins*. Vol. 302. 2012. C482-C493.
167. Picollo, A., M. Malvezzi, and A. Accardi, *TMEM16 Proteins: Unknown Structure and Confusing Functions.* Journal of Molecular Biology, 2015. **427**(1): p. 94-105.
168. Duran, C. and H.C. Hartzell, *Physiological roles and diseases of tmem16/anoctamin proteins: are they all chloride channels?* Acta Pharmacol Sin, 2011. **32**(6): p. 685-692.
169. Kunzelmann, K., et al., *Molecular functions of anoctamin 6 (TMEM16F): a chloride channel, cation channel, or phospholipid scramblase?* Pflügers Archiv - European Journal of Physiology, 2014. **466**(3): p. 407-414.
170. Malvezzi, M., et al., *Ca2+-dependent phospholipid scrambling by a reconstituted TMEM16 ion channel.* Nat Commun, 2013. **4**.
171. van Kruchten, R., et al., *Both TMEM16F-dependent and TMEM16F-independent pathways contribute to phosphatidylserine exposure in platelet apoptosis and platelet activation*. Vol. 121. 2013. 1850-1857.
172. Bera, T.K., et al., *NGEP, a gene encoding a membrane protein detected only in prostate cancer and normal prostate.* Proceedings of the National Academy of Sciences of the United States of America, 2004. **101**(9): p. 3059-3064.
173. Das, S., et al., *NGEP, a Prostate-Specific Plasma Membrane Protein that Promotes the Association of LNCaP Cells.* Cancer Research, 2007. **67**(4): p. 1594-1601.
174. Huang, F., et al., *TMEM16C facilitates Na+-activated K+ currents in rat sensory neurons and regulates pain processing.* Nat Neurosci, 2013. **16**(9): p. 1284-1290.
175. Gadotti, V.M. and G.W. Zamponi, *TMEM16C cuts pain no SLACK.* Nat Neurosci, 2013. **16**(9): p. 1165-1166.
176. Hartzell, H.C., et al., *Anoctamin/TMEM16 family members are Ca2+-activated Cl− channels.* The Journal of Physiology, 2009. **587**(10): p. 2127-2139.
177. Sheridan, J.T., et al., *Characterization of the Oligomeric Structure of the Ca2+-activated Cl− Channel Ano1/TMEM16A.* Journal of Biological Chemistry, 2011. **286**(2): p. 1381-1388.
178. Fallah, G., et al., *TMEM16A(a)/anoctamin-1 Shares a Homodimeric Architecture with CLC Chloride Channels.* Molecular & Cellular Proteomics, 2011. **10**(2).
179. Tien, J., et al., *Identification of a dimerization domain in the TMEM16A calcium-activated chloride channel (CaCC).* Proceedings of the National Academy of Sciences, 2013. **110**(16): p. 6352-6357.
180. Ertongur-Fauth, T., et al., *A novel TMEM16A splice variant lacking the dimerization domain contributes to calcium-activated chloride secretion in human sweat gland epithelial cells.* Experimental Dermatology, 2014. **23**(11): p. 825-831.

181. Yu, K., et al., *Activation of the Ano1 (TMEM16A) chloride channel by calcium is not mediated by calmodulin.* The Journal of General Physiology, 2014. **143**(2): p. 253-267.
182. Tien, J., et al., *A comprehensive search for calcium binding sites critical for TMEM16A calcium-activated chloride channel activity*, ed. R. Aldrich. Vol. 3. 2014.
183. Tian, Y., et al., *Calmodulin-dependent activation of the epithelial calcium-dependent chloride channel TMEM16A.* The FASEB Journal, 2011. **25**(3): p. 1058-1068.
184. Jung, J., et al., *Dynamic modulation of ANO1/TMEM16A HCO3− permeability by Ca2+/calmodulin.* Proceedings of the National Academy of Sciences, 2013. **110**(1): p. 360-365.
185. Vocke, K., et al., *Calmodulin-dependent activation and inactivation of anoctamin calcium-gated chloride channels.* The Journal of General Physiology, 2013. **142**(4): p. 381-404.
186. Terashima, H., A. Picollo, and A. Accardi, *Purified TMEM16A is sufficient to form Ca2+-activated Cl− channels.* Proceedings of the National Academy of Sciences, 2013. **110**(48): p. 19354-19359.
187. Peters, C.J., et al., *Four basic residues critical for the ion selectivity and pore blocker sensitivity of TMEM16A calcium-activated chloride channels.* Proceedings of the National Academy of Sciences, 2015.
188. Peters, C.J., et al., *Four basic residues critical for the ion selectivity and pore blocker sensitivity of TMEM16A calcium-activated chloride channels.* Proceedings of the National Academy of Sciences, 2015. **112**(11): p. 3547-3552.
189. Bill, A., et al., *Variomics Screen Identifies the Re-entrant Loop of the Calcium-activated Chloride Channel ANO1 That Facilitates Channel Activation.* Journal of Biological Chemistry, 2015. **290**(2): p. 889-903.
190. Liu, W., et al., *Inhibition of Ca2+-activated Cl− channel ANO1/TMEM16A expression suppresses tumor growth and invasiveness in human prostate carcinoma.* Cancer Letters, 2012. **326**(1): p. 41-51.
191. Mazzone, A., et al., *Inhibition of cell proliferation by a selective inhibitor of the Ca2+-activated Cl− channel, Ano1.* Biochemical and Biophysical Research Communications, 2012. **427**(2): p. 248-253.
192. Qu, Z., et al., *The Ca2+-activated Cl− channel, ANO1 (TMEM16A), is a double-edged sword in cell proliferation and tumorigenesis.* Cancer Medicine, 2014. **3**(3): p. 453-461.
193. West, R.B., et al., *The Novel Marker, DOG1, Is Expressed Ubiquitously in Gastrointestinal Stromal Tumors Irrespective of KIT or PDGFRA Mutation Status.* The American Journal of Pathology, 2004. **165**(1): p. 107-113.
194. Rock, J.R., C.R. Futtner, and B.D. Harfe, *The transmembrane protein TMEM16A is required for normal development of the murine trachea.* Developmental Biology, 2008. **321**(1): p. 141-149.
195. Firestein, S., *How the olfactory system makes sense of scents.* Nature, 2001. **413**(6852): p. 211-218.
196. Kleene, S.J., *The Electrochemical Basis of Odor Transduction in Vertebrate Olfactory Cilia.* Chemical Senses, 2008. **33**(9): p. 839-859.
197. Rasche, S., et al., *Tmem16b is Specifically Expressed in the Cilia of Olfactory Sensory Neurons.* Chemical Senses, 2010. **35**(3): p. 239-245.
198. Hengl, T., et al., *Molecular components of signal amplification in olfactory sensory cilia.* Proceedings of the National Academy of Sciences, 2010. **107**(13): p. 6052-6057.
199. Bolduc, V., et al., *Recessive Mutations in the Putative Calcium-Activated Chloride Channel Anoctamin 5 Cause Proximal LGMD2L and Distal MMD3 Muscular Dystrophies.* The American Journal of Human Genetics, 2010. **86**(2): p. 213-221.
200. Penttilä S, P.J., Udd B., *ANO5-Related Muscle Diseases.* GeneReviews, 2012.

201. Marconi, C., et al., *A novel missense mutation in ANO5/TMEM16E is causative for gnathodiaphyseal dyplasia in a large Italian pedigree.* Eur J Hum Genet, 2013. **21**(6): p. 613-619.
202. Mizuta, K., et al., *Molecular characterization of GDD1/TMEM16E, the gene product responsible for autosomal dominant gnathodiaphyseal dysplasia.* Biochemical and Biophysical Research Communications, 2007. **357**(1): p. 126-132.
203. Lhermusier, T., H. Chap, and B. Payrastre, *Platelet membrane phospholipid asymmetry: from the characterization of a scramblase activity to the identification of an essential protein mutated in Scott syndrome.* Journal of Thrombosis and Haemostasis, 2011. **9**(10): p. 1883-1891.
204. Vermeer, S., et al., *Targeted Next-Generation Sequencing of a 12.5 Mb Homozygous Region Reveals ANO10 Mutations in Patients with Autosomal-Recessive Cerebellar Ataxia.* The American Journal of Human Genetics, 2010. **87**(6): p. 813-819.
205. Balreira, A., et al., *ANO10 mutations cause ataxia and coenzyme Q10 deficiency.* Journal of Neurology, 2014. **261**(11): p. 2192-2198.
206. Stricker, S.A., *Comparative Biology of Calcium Signaling during Fertilization and Egg Activation in Animals.* Developmental Biology, 1999. **211**(2): p. 157-176.
207. Busa WB, N.R., *An elevated free cytosolic Ca2+ wave follows fertilization in eggs of the frog, Xenopus laevis.* The Journal of Cell Biology, 1985. **100**(4): p. 1325-1329.
208. A., J.L., *Fast block to polyspermy in sea urchin eggs is electrically mediated.* Nature, 1976. **261**((5555)): p. 68-71.
209. Grey, R.D., et al., *An electrical block is required to prevent polyspermy in eggs fertilized by natural mating of Xenopus laevis.* Developmental Biology, 1982. **89**(2): p. 475-484.
210. Miledi, R. and I. Parker, *Chloride current induced by injection of calcium into Xenopus oocytes.* The Journal of Physiology, 1984. **357**(1): p. 173-183.
211. Kline, D., *Calcium-dependent events at fertilization of the frog egg: Injection of a calcium buffer blocks ion channel opening, exocytosis, and formation of pronuclei.* Developmental Biology, 1988. **126**(2): p. 346-361.
212. Machaca K., Q.Z., Kuruma A., Hartzell H. C., McCarty N., *The endogenous calcium-activated Cl channel in Xenopus oocytes: a physiologically and biophysically rich model system.* Calcium Activated Chloride Channels. Academic Press, San Diego, 2001: p. 3-39.
213. P., E.R., *Fertilization in amphibians: the ancestry of the block to polyspermy.* Int Rev Cytol, 1986. **101**: p. 59-100.
214. Wong, X.M., et al., *Subdued, a TMEM16 family Ca2+-activated Cl− channel in Drosophila melanogaster with an unexpected role in host defense*, ed. U. Banerjee. Vol. 2. 2013.
215. Bonnay, F., et al., *big bang gene modulates gut immune tolerance in Drosophila.* Proceedings of the National Academy of Sciences, 2013. **110**(8): p. 2957-2962.
216. Kuraishi, T., et al., *Genetic evidence for a protective role of the peritrophic matrix against intestinal bacterial infection in Drosophila melanogaster.* Proceedings of the National Academy of Sciences, 2011. **108**(38): p. 15966-15971.
217. Kramer, J. and R.S. Hawley, *The spindle-associated transmembrane protein Axs identifies a membranous structure ensheathing the meiotic spindle.* Nat Cell Biol, 2003. **5**(3): p. 261-263.
218. Kramer, J. and R.S. Hawley, *The Spindle-Associated Transmembrane Protein Axs Identifies a New Family of Transmembrane Proteins in Eukaryotes.* Cell Cycle, 2003. **2**(3): p. 173-175.
219. Whyte, W.L., et al., *The genetic analysis of achiasmate segregation in Drosophila melanogaster. III. The wild-type product of the Axs gene is required for the meiotic segregation of achiasmate homologs.* Genetics, 1993. **134**(3): p. 825-35.
220. Pichler, H., et al., *A subfraction of the yeast endoplasmic reticulum associates with the plasma membrane and has a high capacity to synthesize lipids.* European Journal of Biochemistry, 2001. **268**(8): p. 2351-2361.

221. West, M., et al., *A 3D analysis of yeast ER structure reveals how ER domains are organized by membrane curvature.* The Journal of Cell Biology, 2011. **193**(2): p. 333-346.
222. Carrasco, S. and T. Meyer, *STIM Proteins and the Endoplasmic Reticulum-Plasma Membrane Junctions.* Annual Review of Biochemistry, 2011. **80**(1): p. 973-1000.
223. Toulmay, A. and W.A. Prinz, *Lipid transfer and signaling at organelle contact sites: the tip of the iceberg.* Current Opinion in Cell Biology, 2011. **23**(4): p. 458-463.
224. Wolf, W., et al., *Yeast Ist2 Recruits the Endoplasmic Reticulum to the Plasma Membrane and Creates a Ribosome-Free Membrane Microcompartment.* PLoS ONE, 2012. **7**(7): p. e39703.
225. Fischer, M.A., et al., *Binding of Plasma Membrane Lipids Recruits the Yeast Integral Membrane Protein Ist2 to the Cortical ER.* Traffic, 2009. **10**(8): p. 1084-1097.
226. Maass, K., et al., *A signal comprising a basic cluster and an amphipathic α-helix interacts with lipids and is required for the transport of Ist2 to the yeast cortical ER.* Journal of Cell Science, 2009. **122**(5): p. 625-635.
227. Ercan, E., Momburg, F., Engel, U., Temmerman, K., Nickel, W. and Seedorf, M., *Lipid-Mediated Sorting Mechanism of Yeast Ist2 and Mammalian STIM Proteins to the Peripheral ER.* Traffic, 2009. **10**: p. 1802–1818.
228. Franz, A., K. Maass, and M. Seedorf, *A complex peptide-sorting signal, but no mRNA signal, is required for the Sec-independent transport of Ist2 from the yeast ER to the plasma membrane.* FEBS Letters, 2007. **581**(3): p. 401-405.
229. Manford, Andrew G., et al., *ER-to-Plasma Membrane Tethering Proteins Regulate Cell Signaling and ER Morphology.* Developmental Cell, 2012. **23**(6): p. 1129-1140.
230. Galietta, L.J.V., *The TMEM16 Protein Family: A New Class of Chloride Channels?* Biophysical Journal, 2009. **97**(12): p. 3047-3053.
231. Sievers, F., et al., *Fast, scalable generation of high-quality protein multiple sequence alignments using Clustal Omega.* Molecular Systems Biology, 2011. **7**: p. 539-539.
232. Fei, H., et al., *Membrane topology of the Drosophila vesicular glutamate transporter.* Journal of Neurochemistry, 2007. **101**(6): p. 1662-1671.
233. Halestrap, A. and D. Meredith, *The SLC16 gene family—from monocarboxylate transporters (MCTs) to aromatic amino acid transporters and beyond.* Pflügers Archiv, 2004. **447**(5): p. 619-628.
234. Pope, A., et al., *Amino acid conservation and interactions in rhodopsin: Probing receptor activation by NMR spectroscopy.* Biochimica et Biophysica Acta (BBA) - Bioenergetics, 2014. **1837**(5): p. 683-693.
235. Kwong, P.D., et al., *Probability Analysis of Variational Crystallization and Its Application to gp120, The Exterior Envelope Glycoprotein of Type 1 Human Immunodeficiency Virus (HIV-1).* Journal of Biological Chemistry, 1999. **274**(7): p. 4115-4123.
236. Chang, G. and C.B. Roth, *Structure of MsbA from E. coli: A Homolog of the Multidrug Resistance ATP Binding Cassette (ABC) Transporters.* Science, 2001. **293**(5536): p. 1793-1800.
237. Chang, G., et al., *Structure of the MscL Homolog from Mycobacterium tuberculosis: A Gated Mechanosensitive Ion Channel.* Science, 1998. **282**(5397): p. 2220-2226.
238. Wang, D.-N., et al., *Practical aspects of overexpressing bacterial secondary membrane transporters for structural studies.* Biochimica et Biophysica Acta (BBA) - Biomembranes, 2003. **1610**(1): p. 23-36.
239. Kendrew, J.C. and R.G. Parrish, *The Crystal Structure of Myoglobin. III. Sperm-Whale Myoglobin.* Proceedings of the Royal Society of London. Series A. Mathematical and Physical Sciences, 1957. **238**(1214): p. 305-324.
240. Geertsma, E.R. and R. Dutzler, *A Versatile and Efficient High-Throughput Cloning Tool for Structural Biology.* Biochemistry, 2011. **50**(15): p. 3272-3278.
241. Kabsch, W., *XDS.* Acta Crystallographica Section D, 2010. **66**(2): p. 125-132.

242. He, Y., K. Wang, and N. Yan, *The recombinant expression systems for structure determination of eukaryotic membrane proteins.* Protein & Cell, 2014. **5**(9): p. 658-672.
243. Brocchieri, L. and S. Karlin, *Protein length in eukaryotic and prokaryotic proteomes.* Nucleic Acids Research, 2005. **33**(10): p. 3390-3400.
244. Doyle, D.A., et al., *The Structure of the Potassium Channel: Molecular Basis of K+ Conduction and Selectivity.* Science, 1998. **280**(5360): p. 69-77.
245. Galindo BE, V.V., *Phylogeny of the TMEM16 protein family: some members are overexpressed in cancer.* Int J Mol Med, 2005 **(5)**: p. 919-24.
246. Kabsch, W., *XDS.* Acta Crystallographica Section D: Biological Crystallography, 2010. **66**(Pt 2): p. 125-132.
247. Eshaghi, S., et al., *An efficient strategy for high-throughput expression screening of recombinant integral membrane proteins.* Protein Science, 2005. **14**(3): p. 676-683.
248. Geisse, S., et al., *Eukaryotic Expression Systems: A Comparison.* Protein Expression and Purification, 1996. **8**(3): p. 271-282.
249. Bernaudat, F., et al., *Heterologous Expression of Membrane Proteins: Choosing the Appropriate Host.* PLoS ONE, 2011. **6**(12): p. e29191.
250. Locher, K.P., A.T. Lee, and D.C. Rees, *The E. coli BtuCD Structure: A Framework for ABC Transporter Architecture and Mechanism.* Science, 2002. **296**(5570): p. 1091-1098.
251. Drew, D., et al., *Optimization of membrane protein overexpression and purification using GFP fusions.* Nat Meth, 2006. **3**(4): p. 303-313.
252. Drew, D., et al., *GFP-based optimization scheme for the overexpression and purification of eukaryotic membrane proteins in Saccharomyces cerevisiae.* Nat. Protocols, 2008. **3**(5): p. 784-798.
253. Kawate, T. and E. Gouaux, *Fluorescence-Detection Size-Exclusion Chromatography for Precrystallization Screening of Integral Membrane Proteins.* Structure, 2006. **14**(4): p. 673-681.
254. L, E., *Catalysis of disulphide bond formation in the endoplasmic reticulum.* Biochem Soc Trans, 2004 **32**((Pt 5)): p. 663-7.
255. Braakman, I. and N.J. Bulleid, *Protein Folding and Modification in the Mammalian Endoplasmic Reticulum.* Annual Review of Biochemistry, 2011. **80**(1): p. 71-99.
256. Tate, C.G., *Overexpression of mammalian integral membrane proteins for structural studies.* FEBS Letters, 2001. **504**(3): p. 94-98.
257. Nagai, T., et al., *A variant of yellow fluorescent protein with fast and efficient maturation for cell-biological applications.* Nat Biotech, 2002. **20**(1): p. 87-90.
258. Chen, C. and H. Okayama, *High-efficiency transformation of mammalian cells by plasmid DNA.* Molecular and Cellular Biology, 1987. **7**(8): p. 2745-2752.
259. Ikonomou, L., Y.J. Schneider, and S.N. Agathos, *Insect cell culture for industrial production of recombinant proteins.* Applied Microbiology and Biotechnology, 2003. **62**(1): p. 1-20.
260. Smith, G.E., M.D. Summers, and M.J. Fraser, *Production of human beta interferon in insect cells infected with a baculovirus expression vector.* Molecular and Cellular Biology, 1983. **3**(12): p. 2156-2165.
261. Contreras-Gómez, A., et al., *Protein production using the baculovirus-insect cell expression system.* Biotechnology Progress, 2014. **30**(1): p. 1-18.
262. Arachea, B.T., et al., *Detergent selection for enhanced extraction of membrane proteins.* Protein Expression and Purification, 2012. **86**(1): p. 12-20.
263. Hattori, M., R.E. Hibbs, and E. Gouaux, *A fluorescence-detection size-exclusion chromatography-based thermostability assay to identify membrane protein expression and crystallization conditions.* Structure (London, England : 1993), 2012. **20**(8): p. 1293-1299.
264. Strop, P. and A.T. Brunger, *Refractive index-based determination of detergent concentration and its application to the study of membrane proteins.* Protein Science : A Publication of the Protein Society, 2005. **14**(8): p. 2207-2211.

265. Hendrickson, W.A., J.R. Horton, and D.M. LeMaster, *Selenomethionyl proteins produced for analysis by multiwavelength anomalous diffraction (MAD): a vehicle for direct determination of three-dimensional structure.* The EMBO Journal, 1990. **9**(5): p. 1665-1672.
266. Laurila, M.R.L., et al., *Gene silencing pathway RNA-dependent RNA polymerase of Neurospora crassa: yeast expression and crystallization of selenomethionated QDE-1 protein.* Journal of Structural Biology, 2005. **149**(1): p. 111-115.
267. Bellizzi JJ, W.J., Kemp CW, Clardy J, *Producing selenomethionine-labeled proteins with a baculovirus expression vector system.* Structure, 1999. **7**((11)).
268. Carlson, C.B., et al., *Structure of the calcium-rich signature domain of human thrombospondin-2.* Nat Struct Mol Biol, 2005. **12**(10): p. 910-914.
269. Aricescu, A.R., et al., *Molecular analysis of receptor protein tyrosine phosphatase μ - mediated cell adhesion*. Vol. 25. 2006. 701-712.
270. Baker Brachmann, C., et al., *Designer deletion strains derived from Saccharomyces cerevisiae S288C: A useful set of strains and plasmids for PCR-mediated gene disruption and other applications.* Yeast, 1998. **14**(2): p. 115-132.
271. Kitajima, T., Y. Jigami, and Y. Chiba, *Cytotoxic Mechanism of Selenomethionine in Yeast.* Journal of Biological Chemistry, 2012. **287**(13): p. 10032-10038.
272. Kabsch, W., *Automatic Processing of Rotation Diffraction Data from Crystals of Initially Unknown Symmetry and Cell Constants.* J Appl Crystallogr, 1993. **26**: p. 195-800.
273. Schneider, T.R. and G.M. Sheldrick, *Substructure solution with SHELXD.* Acta Crystallographica Section D, 2002. **58**(10 Part 2): p. 1772-1779.
274. Pape, T.S., T. R., *HKL2MAP: a graphical user interface for phasing with SHELX programs.* J. Appl. Crystallogr, 2004. **37**: p. 843–844.
275. De la Fortelle, E., Bricogne, G., *Macromolecular Crystallography Part A.* Elsevier, 1997.
276. Cowtan, K., *'dm': An automated procedure for phase improvement by density modification.* Joint CCP4 and ESF-EACBM Newsletter on Protein Crystallography, 1994. **31**(34–38).
277. Jones, T.A., Zou, J. Y., Cowan,S. W.&Kjeldgaard, M., *Improved methods for building proteinmodels in electron densitymaps and the location of errors in thesemodels.* Acta Crystallogr. A 47, 110–119 (1991). 1991. **47**: p. 110–119.
278. McCoy, A.J.e.a., *Phaser crystallographic software.* J.Appl. Crystallogr, 2007. **40**: p. 658–674.
279. Emsley, P. and K. Cowtan, *Coot: model-building tools for molecular graphics.* acta Crystallogr D Biol Crystallogr, 2004. **60**: p. 2126-2132.
280. Adams, P.D.e.a., *PHENIX: building new software for automated crystallographic structure determination* Acta Crystallogr D Biol Crystallogr, 2002. **58**: p. 1948-1954.
281. Hinkle, P.C., J.J. Kim, and E. Racker, *Ion Transport and Respiratory Control in Vesicles Formed from Cytochrome Oxidase and Phospholipids.* Journal of Biological Chemistry, 1972. **247**(4): p. 1338-1339.
282. Racker, E., *Reconstitution of a Calcium Pump with Phospholipids and a Purified Ca++Adenosine Triphosphatase from Sarcoplasmic Reticulum.* Journal of Biological Chemistry, 1972. **247**(24): p. 8198-8200.
283. Rigaud JL, P.M., Bluzat A, *Mechanisms of membrane protein insertion into liposomes during reconstitution procedures involving the use of detergents. 2. Incorporation of the light-driven proton pump bacteriorhodopsin.* Biochemistry, 1988. **27(8)**: p. 2677-88.
284. Paternostre MT, R.M., Rigaud JL, *Mechanisms of membrane protein insertion into liposomes during reconstitution procedures involving the use of detergents. 1. Solubilization of large unilamellar liposomes (prepared by reverse-phase evaporation) by triton X-100, octyl glucoside, and sodium cholate.* biochemistry. **27**((8)): p. 2668-77.

285. Rigaud, J.-L. and D. Lévy, *Reconstitution of Membrane Proteins into Liposomes*, in *Methods in Enzymology*, D. Nejat, Editor. 2003, Academic Press. p. 65-86.
286. Geertsma, E.R., et al., *Membrane reconstitution of ABC transporters and assays of translocator function.* Nat. Protocols, 2008. **3**(2): p. 256-266.
287. McIntyre JC, S.R., *Fluorescence assay for phospholipid membrane asymmetry.* Biochemistry, 1991. **30(51)**: p. 11819-27.
288. Williamson P1, B.E., Smeets EF, Comfurius P, Schlegel RA, Zwaal RF., *Continuous analysis of the mechanism of activated transbilayer lipid movement in platelets.* Biochemistry, 1995. **34(33)**: p. 10448-55.
289. Namkung, W., et al., *Inhibition of Ca2+-activated Cl− channels by gallotannins as a possible molecular basis for health benefits of red wine and green tea.* The FASEB Journal, 2010. **24**(11): p. 4178-4186.
290. Tsutsumi, S., et al., *The Novel Gene Encoding a Putative Transmembrane Protein Is Mutated in Gnathodiaphyseal Dysplasia (GDD).* The American Journal of Human Genetics, 2004. **74**(6): p. 1255-1261.
291. Jüschke, C., et al., *SEC18/NSF-independent, protein-sorting pathway from the yeast cortical ER to the plasma membrane.* The Journal of Cell Biology, 2005. **169**(4): p. 613-622.
292. Liu, X., S.S. Smith, and D.C. Dawson, *CFTR: What's it like inside the pore?* Journal of Experimental Zoology Part A: Comparative Experimental Biology, 2003. **300A**(1): p. 69-75.
293. DAWSON, D.C., S.S. SMITH, and M.K. MANSOURA, *CFTR: Mechanism of Anion Conduction*. Vol. 79. 1999. S47-S75.
294. Perez-Cornejo, P., J.A. De Santiago, and J. Arreola, *Permeant Anions Control Gating of Calcium-dependent Chloride Channels.* The Journal of Membrane Biology, 2004. **198**(3): p. 125-133.
295. Brunner, J.D., et al., *X-ray structure of a calcium-activated TMEM16 lipid scramblase.* Nature, 2014. **516**(7530): p. 207-212.
296. Kelley, L.A. and M.J.E. Sternberg, *Protein structure prediction on the Web: a case study using the Phyre server.* Nat. Protocols, 2009. **4**(3): p. 363-371.
297. Alberts, B., Johnson A., Lewis J., Morgan D., Raff M., Roberts K., Walter P., *Molecular biology of the cell (6th edition).* Garland Science, 2015: p. 45.
298. Baugh, E.H., et al., *Real-Time PyMOL Visualization for Rosetta and PyRosetta.* PLoS ONE, 2011. **6**(8): p. e21931.
299. Arreola J, M.J., Begenisich T, *Activation of Calcium-dependent Chloride Channels in Rat Parotid Acinar Cells.* J Gen Physiol, 1996. **108(1)**: p. 35-47.
300. Hartzell, C., I. Putzier, and J. Arreola, *CALCIUM-ACTIVATED CHLORIDE CHANNELS.* Annual Review of Physiology, 2005. **67**(1): p. 719-758.
301. Wang, X., et al., *Towards predicting Ca2+-binding sites with different coordination numbers in proteins with atomic resolution.* Proteins: Structure, Function, and Bioinformatics, 2009. **75**(4): p. 787-798.
302. David W. C. DEKKERS , P.C., Edouard M. BEVERS and Robert F. A. ZWAAL, *Comparison between Ca2+-induced scrambling of various fluorescently labelled lipid analogues in red blood cells.* Biochem. J. , 2002. **362**: p. 741–747.
303. Anneke J. van der Kooi, L.t.D., Wendy S. Frankhuizen, Chiara S.M. Straathof, Pieter A. van Doorn, Marianne de Visser, Ieke B. Ginjaa, *ANO5 mutations in the Dutch limb girdle muscular dystrophy population.* Neuromuscul Disord. 2013 Jun;23, 2013. **23(6)**: p. 456-60.
304. Penttilä S, P.J., Suominen T, Raheem O, Evilä A, Muelas Gomez N, Tasca G, Waddell LB, Clarke NF, Barboi A, Hackman P, Udd B., *Eight new mutations and the expanding phenotype variability in muscular dystrophy caused by ANO5.* Neurology 2013. **78(12)**: p. 897-903.
305. Sarkozy A1, H.D., Hudson J, Laval SH, Barresi R, Hilton-Jones D, Deschauer M, Harris E, Rufibach L, Hwang E, Bashir R, Walter MC, Krause S, van den Bergh P, Illa I, Pénisson-Besnier I, De Waele L, Turnbull D, Guglieri M, Schrank B, Schoser

B, Seeger J, Schreiber H, Gläser D, Eagle M, Bailey G, Walters R, Longman C, Norwood F, Winer J, Muntoni F, Hanna M, Roberts M, Bindoff LA, Brierley C, Cooper RG, Cottrell DA, Davies NP, Gibson A, Gorman GS, Hammans S, Jackson AP, Khan A, Lane R, McConville J, McEntagart M, Al-Memar A, Nixon J, Panicker J, Parton M, Petty R, Price CJ, Rakowicz W, Ray P, Schapira AH, Swingler R, Turner C, Wagner KR, Maddison P, Shaw PJ, Straub V, Bushby K, Lochmüller H., *ANO5 gene analysis in a large cohort of patients with anoctaminopathy: confirmation of male prevalence and high occurrence of the common exon 5 gene mutation.* Hum Mutat, 2013. **34(8)**: p. 1111-8.

306. Savarese, M., et al., *Next generation sequencing on patients with LGMD and nonspecific myopathies: Findings associated with ANO5 mutations.* Neuromuscular Disorders, (0).
307. Taleb O, F.P., Bossu JL, Feltz A., *Small-conductance chloride channels activated by calcium on cultured endocrine cells from mammalian pars intermedia.* Pflugers Arch, 1988. **412(6)**: p. 641-6.
308. Ni, Y.-L., A.-S. Kuan, and T.-Y. Chen, *Activation and Inhibition of TMEM16A Calcium-Activated Chloride Channels.* PLoS ONE, 2014. **9**(1): p. e86734.
309. Galietta LJ, Z.-M.O., Mastrocola T, Wöhrle C, Rugolo M, Romeo G., *Activation of Ca(2+)-dependent K+ and Cl- currents by UTP and ATP in CFPAC-1 cells.* Pflugers Arch., 1994. **426(6)**: p. 534-41.
310. Yang, H., et al., *TMEM16F Forms a Ca2+-Activated Cation Channel Required for Lipid Scrambling in Platelets during Blood Coagulation.* Cell, 2012. **151**(1): p. 111-122.
311. Clapham, D.E., *Calcium Signaling.* Cell, 2007. **131**(6): p. 1047-1058.
312. Dubovsky, S.L., E. Daurignac, and K.E. Leonard, *Increased platelet intracellular calcium ion concentration is specific to bipolar disorder.* Journal of Affective Disorders, 2014. **164**(0): p. 38-42.
313. Castoldi, E., et al., *Compound heterozygosity for 2 novel TMEM16F mutations in a patient with Scott syndrome*. Vol. 117. 2011. 4399-4400.
314. Mimms LT, Z.G., Nozaki Y, Tanford C, Reynolds JA., *Phospholipid vesicle formation and transmembrane protein incorporation using octyl glucoside.* Biochemistry, 1981 **20(4)**: p. 833-40.
315. Kuruma, A. and H.C. Hartzell, *Dynamics of calcium regulation of chloride currents inXenopus oocytes*. Vol. 276. 1999. C161-C175.
316. Callamaras, N. and I. Parker, *Ca2+-dependent activation of Cl−currents in Xenopus oocytes is modulated by voltage*. Vol. 278. 2000. C667-C675.
317. Smith, S.S., et al., *Cystic Fibrosis Transmembrane Conductance Regulator: Physical Basis for Lyotropic Anion Selectivity Patterns.* The Journal of General Physiology, 1999. **114**(6): p. 799-818.
318. Brown, D.A. and E. London, *Structure and Function of Sphingolipid- and Cholesterol-rich Membrane Rafts.* Journal of Biological Chemistry, 2000. **275**(23): p. 17221-17224.
319. Altschul, S.F., et al., *Gapped BLAST and PSI-BLAST: a new generation of protein database search programs.* Nucleic Acids Research, 1997. **25**(17): p. 3389-3402.
320. Keefe, A.D., et al., *One-Step Purification of Recombinant Proteins Using a Nanomolar-Affinity Streptavidin-Binding Peptide, the SBP-Tag.* Protein Expression and Purification, 2001. **23**(3): p. 440-446.
321. Invitrogen, *Bac-to-Bac Baculovirus expression system (http://tools.lifetechnologies.com/content/sfs/manuals/bactobac_man.pdf)* Publication Nr MAN0000414.
322. Schenck, S., et al., *A chloride conductance in VGLUT1 underlies maximal glutamate loading into synaptic vesicles.* Nat Neurosci, 2009. **12**(2): p. 156-162.
323. Hattori, M., Ryan E. Hibbs, and E. Gouaux, *A Fluorescence-Detection Size-Exclusion Chromatography-Based Thermostability Assay for Membrane Protein Precrystallization Screening.* Structure, 2012. **20**(8): p. 1293-1299.

324. CCP4, *Collaborative Computational Project Nr. 4. The CCP4 Suite: Programs for X-ray Crystallography.* Acta Crystallogr, 1994. **58**: p. 17772-17779.
325. de La Fortelle, E. and G. Bricogne, Methods in enzymology, 1997: p. 492-494.
326. Cowtan, K., *An automated procedure for phase imporvement by density modification.* Joint CCP4 and ESF-EACBM Newsletter on Protein Crystallography, 1994. **31**: p. 34-38.
327. Jones, T., et al., *Improved methods for building protein models in electron density maps and the location of errors in these models.* Acta Crystallogr, 1991. **47 (Pt 2)**: p. 110-119.
328. McCoy, A.J., et al., *Phaser crystallographic software.* Journal of Applied Crystallography, 2007. **40**(4): p. 658-674.
329. Cowtan, K., *An automated procedure for phase imporvement by density modification.* Joint CCP4 and ESF-EACBM Newsletter on Protein Crystallography, 1994. **31**: p. 34-38.
330. Brunger, A.T.e.a., *Crystallography & NMR system: A new software suite for macromolecular structure determination.* Acta Crystallogr D Biol Crystallogr, 1998. **54**: p. 905-921.